An investigation of the electronic structure and structural stability of pyrochlore-type oxides and glass-ceramic composites

A Thesis Submitted to the

College of Graduate Studies and Research

In Partial Fulfillment of the Requirements

For the Degree of Doctor Philosophy

In the Department of Chemistry

University of Saskatchewan

Saskatoon

By

ESTER RANI ALURI

Permission to Use

In presenting this thesis/dissertation in partial fulfillment of the requirements for a degree of Doctor of Philosophy from the University of Saskatchewan, I agree that the Libraries of this University may make it freely available for inspection. I further agree that permission for copying of this thesis/dissertation in any manner, in whole or in part, for scholarly purposes may be granted by the professor or professors who supervised my thesis/dissertation work or, in their absence, by the Head of the Department or the Dean of the College in which my thesis work was done. It is understood that any copying or publication or use of this thesis/dissertation or parts thereof for financial gain shall not be allowed without my written permission. It is also understood that due recognition shall be given to me and to the University of Saskatchewan in any scholarly use which may be made of any material in my thesis/dissertation.

Requests for permission to copy or to make other uses of materials in this thesis/dissertation in whole or part should be addressed to:

Head of the Department of Chemistry

University of Saskatchewan

Saskatoon, Saskatchewan S7N 5C9

Canada

Acknowledgement

I owe my gratitude to all the people who have contributed to my thesis production. First of all, I would like to thank my parents for their constant source of love, strength, encouragement, and support throughout these years. I would like to thank my elder sisters and brother-in-laws, who strengthened me in difficult situations and have been the back bone in my personal and academic life.

I would especially thank to my advisor Dr. Andrew P. Grosvenor for his immense support and guidance throughout my PhD study. I would really grateful to his motivation, enthusiasm, and immense knowledge. Further, I am also thankful for encouraging the use of correct grammar and consistent notation in my writings and for carefully reading and commenting on countless revisions of the manuscripts. Besides my advisor, I would like to thank the advisory committee Dr. Matthew Paige, Dr. Steve Reid, and Dr. Derek Peak for their guidance and insightful comments. I would thank my past and present group members for sharing their knowledge, giving guidance, and especially for sharing the synchrotron beam time. Without Grosvenor group; John R. Hayes, James D. Walker, Michelle N. Revoy, Mohamad Ruwaid Rafiuddin, and Dr. Peter Blanchard, it would not be possible to complete my thesis work. I would especially like to thank John Hayes and James Walker, who helped me to collect micro-XRD and glancing angle X-ray absorption spectroscopy data presented in Chapter 5. I would like to thank all my friends who cherish my graduate life.

Dr. Robert Gordon is thanked for his assistance in carrying out XANES and GA-XANES/EXAFS data presented in Chapter 3, 4, and 5 at 20BM facility (CLS/XSD, APS). Dr. Yongfeng Hu is thanked for his support in carrying out XANES experiments (Chapter 2, 4,

and 6) using the SXRMB beamline (06B1-1) at the CLS. Dr. Lucia Zuin is thanked for her support in carrying out XANES experiments (Chapter 6) using the VLS-PGM (11ID-2) beamline at the CLS. Dr. Ning Chen and Mr. Tom Regier of the CLS are thanked for their support in carrying out XANES experiments (Chapter 2) at beamlines HXMA (06ID-1) and VLS-SGM (11ID-1). Mr. Jack Hendrix is thanked for carrying out the ion implantation studies (presented in Chapter 4, 5, and 6) using the Tandetron accelerator located at Interface Science Western, University of Western Ontario. Mr. Blaine Novakovski (Department of Geology, U of S) is thanked for his help in polishing the surface of the glass-ceramic composite materials presented in Chapter 6. Mr. Tom Bonli (Department of Geology, U of S) is thanked for his help in performing the electron microprobe experiments from the samples that presented in Chapter 6. I have carried out all the experimental work (*e.g.*, synthesis, characterization, electronic calculations, sample preparation, data collection), interpretation, and writing presented in this thesis, except where noted otherwise. Dr. Andrew Grosvenor has revised and edited the written material, and also provided guidance throughout the course of the work described in this thesis.

Finally, I would like to thank all the funding agencies who funded the work in this thesis. The thesis projects were funded by the Natural Sciences and Engineering Research Council (NSERC) of Canada through a discovery grant awarded to Dr. Andrew P Grosvenor. I would like thank to the University of Saskatchewan for financial support. The Canadian Foundation for Innovation (CFI) is thanked for providing funds to purchase the PANalytical Empyrean powder X-ray diffractometer that was used in this project. The 20BM facilities at the APS are supported by the US Department of Energy - Basic Energy Sciences, the National Sciences and Engineering Research Council (NSERC), the Canadian Light Source (CLS), the University of Washington, and the APS. Use of the APS, an Office of Science User Facility operated for the

U.S. Department of Energy (DOE) Office of Science by Argonne National Laboratory, was supported by the U.S. DOE under Contract No. DE-AC02-06CH1135. *The CLS is supported by the Canada* Foundation for Innovation, the Natural Sciences and Engineering Research Council, Western Economic Diversification Canada, the National Research Council of Canada, the Canadian Institutes of Health Research, and the Government of Saskatchewan, and the University of Saskatchewan.

Abstract

Pyrochlore-type oxides ($A_2B_2O_7$) and glass-ceramic materials have received considerable attention for nuclear waste sequestration applications because of the remarkable compositional diversity and structural flexibility of the materials. These properties can enhance the incorporation of radioactive waste elements and resistance to radiation induced damage of incorporated nuclear waste. For the materials to be a potential nuclear wasteform, it is very important to understand how the electronic structure of these materials changes depending upon composition and to study the structural stability of these materials upon irradiation. The objective of this thesis was to investigate how the metal-oxygen bond covalency, cationic radii ratio (r_A/r_B), and oxygen vacancies of pyrochlore-type oxides affect their resistance to radiation induced damage. X-ray absorption near-edge spectroscopy (XANES) can be used to investigate the electronic structure (i.e., local coordination number (CN), oxidation state, bonding environment, etc.) of the element of interest in the materials. Radiation induced structural damage of these materials can be simulated by bombarding with high-energy ion beams. Surface sensitive glancing angle XANES (GA-XANES) spectra can be used to study the damaged surface of the materials, as the high energy ions can only implant in the near-surface region of the pellets.

In Chapter 2, the effect of substituting lower oxidation state metals in the A^{3+} or B^{4+}-site of pyrochlore-type oxides has been investigated using XANES. A series of $Yb_2Ti_{2-x}Fe_xO_{7-\delta}$ ($0 \leq x \leq 0.2$) have been investigated to understand the effect of cation substitution on the local CN and oxidation state of the transition metal. Examination of transition metal K- and $L_{2,3}$-edge XANES spectra has shown that Ti and Fe CN decreases with increasing Fe content, and Fe

adopts the 3+ state rather than 4+ throughout the series in $Yb_2Ti_{2-x}Fe_xO_{7-\delta}$ ($0 \leq x \leq 0.2$). The results of this study confirms the presence of only Fe^{3+} and a decrease in Ti and Fe CN in $Yb_2Ti_{2-x}Fe_xO_{7-\delta,}$ which makes these compounds oxygen deficient materials. The generation of oxygen vacancies by the substitution of Ti^{4+} for Fe^{3+} may affect the resistance to radiation induced structural damage and this will be discussed in Chapter 4.

A series of $Gd_2Ti_{2-x}Sn_xO_7$ have been investigated to understand the effect of bond covalency on the electronic structure of these materials using XANES and discussed in Chapter 3. Examination of changes in energy and/or line shape of Ti K-, Sn L_3- and Gd L_3-edge XANES spectra from $Gd_2Ti_{2-x}Sn_xO_7$ has shown that the ionic character of Ti-O and Gd-O bonds increases while the Sn-O bond becomes more covalent with increasing Sn content. Partial density of states calculations have also been performed to understand the spectral line shape changes and energy shifts in the spectra. This study has shown that the bonding interactions between metal and oxygen vary depending on the composition, which may affect the resistance to radiation induced structural damage of these materials.

In order to understand the radiation induced structural damage in the pyrochlore-type oxides, structural damage has been simulated by implanting with 2 MeV Au^- ions. These high-energy heavy ions can only implant in the surface region (few hundred nm) of the pellets. The objective of Chapter 4 was to demonstrate the ability of surface sensitive glancing-angle XANES (GA-XANES) and total electron yield XANES (TEY-XANES) techniques to selectively probe the damaged surface layer of rare-earth titanates ($RE_2Ti_2O_7$; RE (rare-earth)=La-Lu, and Y). $RE_2Ti_2O_7$ crystallites have already been examined previously using transmission electron microscopy (TEM) before and after implantation, and reported that the resistance to radiation induced structural damage increases with decreasing radius of the RE ion (La-Lu). GA-XANES

and TEY-XANES techniques have successfully probed the damaged surface of $RE_2Ti_2O_7$, and have shown that the local CN of Ti decreased (i.e., damage occurs in the structure) after implantation. The study has also shown that the ion induced structural damage decreases with decreasing radius of the RE ion (Sm-Yb), which is in agreement with the previous TEM studies of $RE_2Ti_2O_7$. The ability to reduce ion induced structural damage has also investigated in oxygen deficient pyrochlore-type materials ($Yb_{1.85}Ca_{0.15}Ti_2O_{7-\delta}$ and $Yb_2Ti_{1.85}Fe_{0.15}O_{7-\delta}$) along with stoichiometric materials.

Further, the $Gd_2Ti_{2-x}Sn_xO_7$ materials were implanted to study how the metal-oxygen bond covalency affect the ion-induced structural damage. This is discussed in Chapter 5. Glancing-angle XANES (GA-XANES) spectra, glancing-angle extended X-ray absorption fine structure (GA-EXAFS), and micro (μ)-powder XRD have been used to probe the damaged surface layer of $Gd_2Ti_{2-x}Sn_xO_7$ pellets after being implanted with 2 MeV Au^- ions. Analysis of Ti K- and Sn $L_{2,3}$-edge GA-XANES/EXAFS spectra from the $Gd_2Ti_{2-x}Sn_xO_7$ materials have shown that Ti- and Sn-sites become distorted after ion implantation in terms of decrease in CN and a change in bonding environment. The study has shown that the $Gd_2Ti_{2-x}Sn_xO_7$ materials become more susceptible to ion induced structural damage with increasing the Sn content because of the increased covalency between O and Sn in $Gd_2Ti_{2-x}Sn_xO_7$.

After investigating the ceramic materials, the composite materials containing $Gd_2Ti_2O_7$ pyrochlore-type crystallites in a glass have been investigated in Chapter 6. Borosilicate- and Fe-Al-borosilicate glass-ceramic composites containing pyrochlore-type $Gd_2Ti_2O_7$ crystallites were synthesized at different annealing temperatures. The study has shown how the $Gd_2Ti_2O_7$ crystallites interact within a glass matrix and how these materials change as a result of ion implantation. Examination of backscattered electron (BSE) images and XANES spectra from the

composite materials have shown that the $Gd_2Ti_2O_7$ crystallites are dissolved in the glass matrix depending on the annealing temperature and the glass composition of composite materials. The examination of Fe K-edge from Fe-Al-borosilicate glass-ceramic composites have shown that Fe in the composite materials was reduced to Fe^{2+} when annealed at 1100 ^oC and oxidized to Fe^{3+} when the composites were annealed at 750 ^oC. Further, these glass-ceramic composite materials have shown similar response to ion implantation as $Gd_2Ti_2O_7$.

The studies in this thesis have shown that the metal-oxygen bond covalence and cationic radii of the pyrochlore-type oxides plays important role to resist the ion beam induced damage. Along with this, this study has also demonstrated the ability of surface sensitive techniques such as GA-XANES/EXAFS and TEY-XANES techniques to probe only the damaged surface layer of ion implanted materials. These studies and techniques will be useful for the development of materials for nuclear waste sequestration applications.

Contents

1. Introduction 1

1.1. Nuclear waste generation and manangement 1
1.2. Nuclear wasteforms 3

1.2.1 Radiation effects on nuclear wasteforms. 3
1.2.2 Glass wasteforms. 4
1.2.3 Ceramic wasteforms 6
1.2.3.1 Pyrochlore-type crystal oxides. 7
1.2.4 Multi-phase ceramic wasteforms 9
1.2.5 Glass-ceramic waste forms 10

1.3. Ion beam implantation studies 11
1.4. Powder X-ray diffraction 12
1.5. Synchrotron radiation techniques 14

1.5.1 Beamline set up. 18
1.5.2 XAS experiemental set-up. 20
1.5.3 An Overview on XAS: XANES and EXAFS. 23
1.5.4 Glancing angle XAS. 28

1.6. Thesis Objectives 29

2. An investigation of pyrochlore-type oxides ($Yb_2Ti_{2-x}Fe_xO_{7-\delta}$) by XANES 33

2.1. Introduction 33
2.2. Experimental 35

2.2.1 Synthesis and X-ray diffraction. 35
2.2.2 XANES. 36

2.3. Results and Discussions 37

2.3.1 Structure. 37
2.3.2 Fe K-edge XANES. 40
2.3.3 Fe $L_{2,3}$-edge XANES 44
2.3.4 Ti K-edge XANES. 46
2.3.5 Ti $L_{2,3}$-edge XANES. 48

2.4. Conclusions 49

3. An X-ray absorption spectroscopic study of the effect of bond covalency on the electronic structure of $Gd_2Ti_{2-x}Sn_xO_7$ 51

3.1. Introduction 51
3.2. Experimental 52

3.2.1 Synthesis. 52
3.2.2 XANES. 53
3.2.3 Electronic structure calculations. 54

3.3. Results and Discussions 55

3.3.1 Structure. 55
3.3.2 Ti K-edge XANES. 57
3.3.3 Sn L_3-edge XANES. 66
3.3.4 Sn K-edge XANES. 72
3.3.5 Gd L_3-edge XANES. 73

3.4. Conclusions 74

4. An investigation of the electronic structure and structural stability of $RE_2Ti_2O_7$ by glancing angle and total electron yield XANES 75

4.1. Introduction 75
4.2. Experimental 78

4.2.1 Synthesis. 78
4.2.2 Ion beam implantation. 78
4.2.3 Micro powder X-ray diffraction. 79
4.2.4 XANES. 80

4.3. Results and Discussions 83

4.3.1 Powder X-ray diffraction before and after ion implantaion. 83
4.3.2 Ti K-edge XANES of the undamaged materials. 87
4.3.3 Ti K-edge XANES from ion implanted materials. 89
4.3.3.1 GA-XANES. 90
4.3.3.2 TEY-XANES. 95

4.4. Conclusions 99

5. Investigation of the structural stability of ion-implanted $Gd_2Ti_{2-x}Sn_xO_7$ pyrochlore-type oxides by glancing angle X-ray absorption spectroscopy 100

5.1. Introduction 100
5.2. Experimental 102

5.2.1 Synthesis. 102
5.2.2 Ion beam implantation. 103

5.2.3 Micro X-ray diffraction..... 104
5.2.4 XANES/EXAFS. 104
5.3. Results and Discussions..... 107
5.3.1 Powder X-ray diffraction before and after ion implantaion..... 107
5.3.2 GA-XANES and GA-EXAFS. 112
5.3.2.1 Ti K-edge GA-XANES..... 113
5.3.2.2 Ti K-edge GA-EXAFS. 120
5.3.2.3 Sn L_3-edge GA-XANES. 121
5.3.2.4 Gd L_3-edge GA-XANES..... 126
5.3.3 The effect of Sn substitution on ion beam induced structural damage in $Gd_2Ti_{2-x}Sn_xO_7$ 127
5.4. Conclusions..... 128

6. A study of the electronic structure and structural stability of $Gd_2Ti_2O_7$ based glass-ceramic composites 129
6.1. Introduction..... 129
6.2. Experimental..... 131
6.2.1 Synthesis. 131
6.2.2 Electron microprobe analysis..... 133
6.2.3 Ion beam implantation. 133
6.2.4 XANES. 134
6.3. Results and Discussions..... 136
6.3.1 Powder X-ray diffraction. 136
6.3.2 Electron microscopy. 140
6.3.3 XANES analysis from as-synthesized materials..... 142
6.3.3.1 Ti K-edge XANES..... 142
6.3.3.2 Si $L_{2,3}$-edge XANES. 147
6.3.3.3 Fe K-edge XANES. 151
6.3.3.4 Al $L_{2,3}$-edge XANES..... 153
6.3.4 Ti K-edge GA-XANES of the ion-implated materials. 155
6.4. Conclusions..... 157

7. Conclusions and directions for future research 159
7.1. Summary of factors affecting resistance to radiation induced damge 159
7.1.1 Effect of composition on electronic properties..... 160
7.1.2 Effect of changes in composition on structural stability..... 161
7.1.3 Effect of combining the ceramics with glass materials. 162

7.2. Significance and implications 163
7.3. Directions for future research 164

8. References 167

Appendix 1. Supporting information for Chapter 3 187
Appendix 2. Supporting information for Chapter 4 188
Appendix 3. Supporting information for Chapter 5 193
Appendix 4. Supporting information for Chapter 6 197

List of Tables

Table 2.1 Lattice parameters from the $Yb_2Ti_{2-x}Fe_xO_{7-\delta}$ system 40

Table 3.1 Lattice constants from the $Gd_2Ti_{2-x}Sn_xO_7$ series 57

Table 3.2 Ti-O and Sn-O bond lengths from $RE_2Ti_2O_7$ (RE = Y and Gd) and $RE_2Sn_2O_7$ (RE = Y, Gd, and La) determined using previously reported crystallographic information 64

Table 4.1 Calculated glancing angles required to give specific X-ray attenuation depths for photons having energies of 4966 eV (Ti K-edge) 82

Table 4.2 Lattice constants from the undamaged and damaged materials along with the full width at half maximum (FWHM) of the (222) diffraction peak 85

Table 5.1 Calculated glancing angles required to give specific X-ray attenuation depths for photons having energies of 3929 eV (Sn L_3-edge), 4966 eV (Ti K-edge), and 7243 eV (Gd L_3-edge) 107

Table 5.2 Lattice constants and along with the full width at half maximum (FWHM) of the (222) peak from the diffraction pattern of the undamaged $Gd_2Ti_{2-x}Sn_xO_7$ and $Gd_2Zr_2O_7$ materials 112

Table 6.1 Compositions of the different glasses synthesized 132

Table 6.2 Labels used to name the glasses and glass-ceramic composites studied 132

Table 6.3 Calculated glancing angles required to give specific X-ray attenuation depths in $Gd_2Ti_2O_7$ for photons having energies of 4966 eV (Ti K-edge) 135

List of Figures

Figure 1.1 A portion of the unit cell (1/8) of the pyrochlore-type structure of $A_2B_2O_7$ ($Gd_2Ti_2O_7$) is shown 8

Figure 1.2 Schematic diagram of the Tandetron accelerator along with the ion implantation chamber located at the Interface Science Western (ISW), University of Western Ontario 12

Figure 1.3 Schematic diagram of Bragg`s law 14

Figure 1.4 Schematic diagram for a modern synchrotron (3^{rd} generation) source is shown 15

Figure 1.5 Schematic of a bending magnet, wiggler, and undulator are shown 18

Figure 1.6 Schematic diagram of XAS experimental set-up for different detection methods 23

Figure 1.7 A representative energy diagram for K- and L-edge transitions in the XAS process and transition metal (Ti) K-edge XANES along with EXAFS are shown 26

Figure 1.8 Ti K-edge XANES speactra from materials with varying coordination number and oxidation state 27

Figure 1.9 Experimental set up for the glancing angle XANES measurements are shown 29

Figure 2.1 A powder XRD pattern from phase pure $Yb_2Ti_{1.85}Fe_{0.15}O_{7-\delta}$ 39

Figure 2.2 Fe K-edge XANES spectra from the $Yb_2Ti_{2-x}Fe_xO_{7-\delta}$ system 42

Figure 2.3 Fe K-edge XANES spectra from the $La_{1-x}Sr_xFeO_{3-\delta}$ system 43

Figure 2.4 The pre-edge region from the Fe K-edge XANES spectra for $Yb_2Ti_{2-x}Fe_xO_{7-\delta}$ (x=0.05, 0.10), $LaFeO_3$, and $SrFeO_3$ are presented 44

Figure 2.5 Fe L_3-edge XANES spectra from the $Yb_2Ti_{2-x}Fe_xO_{7-\delta}$ series 46

Figure 2.6 Ti K-edge spectra from the $Yb_2Ti_{2-x}Fe_xO_{7-\delta}$ series 47

Figure 2.7 Ti L_3-edge XANES spectra from $Yb_2Ti_{2-x}Fe_xO_{7-\delta.}$ 49

Figure 3.1 XRD patterns from the $Gd_2Ti_{2-x}Sn_xO_7$ series are shown 56

Figure 3.2 Ti K-edge XANES spectra from the $Gd_2Ti_{2-x}Sn_xO_7$ system 60

Figure 3.3 Ti K-edge XANES spectra from $Y_2Ti_2O_7$ and Y_2TiSnO_7 are shown 62

Figure 3.4 The partial DOS calculations of the Ti 4p and 3d states from $Y_2Ti_{2-x}Sn_xO_7$ are presented, and have been plotted relative to the Fermi level (0 eV) 63

Figure 3.5 Ti K-edge XANES spectra from $Y_2Ti_2O_7$ and $Gd_2Ti_2O_7$ are shown 65

Figure 3.6 Sn L_3-edge spectra from the $Gd_2Ti_{2-x}Sn_xO_7$ series 67

Figure 3.7 Sn L_3-edge spectra from $RE_2Sn_2O_7$ (RE= Y, Gd, and La) are shown 69

Figure 3.8 Sn L_3-edge spectra from $Y_2Ti_{2-x}Sn_xO_7$ are shown 70

Figure 3.9 The partial DOS calculations of the Sn 5d and Sn 5s states from $Y_2Ti_{2-x}Sn_xO_7$ 71

Figure 3.10 Sn K-edge XANES spectra from the $Gd_2Ti_{2-x}Sn_xO_7$ system are presented 72

Figure 3.11 Gd L_3-edge spectra from $Gd_2Ti_{2-x}Sn_xO_7$ 73

Figure 4.1 A plot of the ion beam implantation depth profile from $Yb_2Ti_2O_7$ and the number of vacancies produced per Au- ion (defect per ion profile) in $Yb_2Ti_2O_7$ 80

Figure 4.2 Bulk and micro powder XRD patterns from $RE_2Ti_2O_7$ (RE= Sm, Eu, Gd, Ho, Y, and Yb, respectively) are shown before and after the materials were implanted by Au^- ions to a dose of 5×10^{14} ions/cm^2 86

Figure 4.3 Ti K-edge XANES spectra from the $RE_2Ti_2O_7$, $Yb_2Ti_{1.85}Fe_{0.15}O_{7-\delta}$, and $Yb_{1.85}Ca_{0.15}Ti_2O_{7-\delta}$ systems 88

Figure 4.4 Ti K-edge GA-XANES spectra collected at various glancing angles from $Sm_2Ti_2O_7$, $Gd_2Ti_2O_7$, $Yb_2Ti_2O_7$, $Yb_2Ti_{1.85}Fe_{0.15}O_{7-\delta}$, and $Yb_{1.85}Ca_{0.15}Ti_2O_{7-\delta}$ implanted to a dose of 5×10^{14} ions/cm^2 91

Figure 4.5 Ti K-edge GA-XANES spectra from the implanted $(Sm,Gd,Yb)_2Ti_2O_7$, $Yb_2Ti_2O_7$, $Yb_2Ti_{1.85}Fe_{0.15}O_{7-\delta}$, and $Yb_{1.85}Ca_{0.15}Ti_2O_{7-\delta}$ materials at a glancing angle providing an X-ray attenuation depth of 450 nm are shown 94

Figure 4.6 Ti K edge TEY-XANES spectra from $Sm_2Ti_2O_7$, $Gd_2Ti_2O_7$, $Ho_2Ti_2O_7$, $Yb_2Ti_2O_7$, $Yb_2Ti_{1.85}Fe_{0.15}O_{7-\delta}$, and $Yb_{1.85}Ca_{0.15}Ti_2O_{7-\delta}$ implanted to a dose of 5×10^{14} ions/cm^2 96

Figure 4.7 Ti K edge TEY-XANES spectra before normalization from an implanted pellet of $Sm_2Ti_2O_7$ and connected to the sample holder using only carbon tape or using carbon tape *and* silver paint. 97

Figure 4.8 Ti K edge TEY-XANES spectra from the implanted $Yb_2Ti_2O_7$, $Yb_2Ti_{1.85}Fe_{0.15}O_{7-\delta}$, and $Yb_{1.85}Ca_{0.15}Ti_2O_{7-\delta}$ materials 98

Figure 5.1 An ion beam implantation depth profile and vacancies per ion depth profile of $Gd_2Ti_2O_7$ calculated using SRIM-2013 106

Figure 5.2 Bulk and micro powder XRD patterns from $Gd_2Ti_2O_7$, Gd_2TiSnO_7, $Gd_2Sn_2O_7$, $Gd_2Sn_2O_7$ and $Gd_2Zr_2O_7$samples are shown before and after the materials were implanted to a dose of 1×10^{15} ions/cm^2 or 5×10^{15} ions/cm^2 by a beam of Au^- ions 111

Figure 5.3 Ti K-edge GA-XANES spectra collected at various glancing angles from $Gd_2Ti_2O_7$ implanted to a dose of 1×10^{15} ions/cm^2 or 5×10^{15} ions/cm^2 116

Figure 5.4 Ti K-edge GA-XANES spectra collected at various glancing angles from Gd_2TiSnO_7 implanted to a dose of 1×10^{15} ions/cm^2 or 5×10^{15} ions/cm^2 117

Figure 5.5 Ti K-edge GA-XANES spectra collected at different glancing angles from an undamaged pellet of $Yb_2Ti_2O_7$ and measured in fluorescence mode 118

Figure 5.6 Ti K-edge GA-XANES spectra from ion implanted $Gd_2Ti_2O_7$ and Gd_2TiSnO_7 implanted to a dose of 5×10^{15} ions/cm^2 or 1×10^{15} ions/cm^2 at a glancing angle providing an X-ray attenuation depth of 450 nm 119

Figure 5.7 Ti K-edge GA-EXAFS spectra from $Gd_2Ti_2O_7$ and Gd_2TiSnO_7 implanted to a dose of 1×10^{15} ions/cm^2 or 5×10^{15} ions/cm^2 are shown 121

Figure 5.8 Sn L_3-edge GA-XANES spectra from Gd_2TiSnO_7 implanted to a dose of 1×10^{15} ions/cm^2 or 5×10^{15} ions/cm^2 are shown 123

Figure 5.9 Sn L_3-edge GA-XANES spectra from $Gd_2Sn_2O_7$ implanted to a dose of 1×10^{15} ions/cm^2 or 5×10^{15} ions/cm^2 are shown 124

Figure 5.10 Sn L_3-edge GA-XANES spectra from ion implanted Gd_2TiSnO_7 and $Gd_2Sn_2O_7$ implanted to a dose of 1×10^{15} ions/cm^2 or $\times10^{15}$ ions/cm^2 at a glancing angle providing an X-ray attenuation depth of 450 nm 125

Figure 5.11 Gd L_3-edge XANES spectra from the undamaged $Gd_2Sn_2O_7$ material collected in fluorescence and transmission modes 126

Figure 6.1 XRD patterns from the Borosilicate glass (BG) and the BG-ceramic composite materials, and Fe-Al-borosilicate glass (FABG) and the FABG-ceramic composite materials (20 wt%, 40 wt%, and 80 wt% loading of $Gd_2Ti_2O_7$) annealed at 1100^{o}C 138

Figure 6.2 XRD patterns from the Borosilicate and its composite materials and Fe-Al-borosilicate glass and its composite materials (10 wt%, 20 wt%, 40 wt%, and 80 wt% loading of $Gd_2Ti_2O_7$) annealed at 750^{o}C 139

Figure 6.3 Backscattered images from the borosilicate glass composite materials annealed at 750^{o}C or at 1100^{o}C 141

Figure 6.4 Ti K-edge XANES spectra from BG-$Gd_2Ti_2O_7$-1100^{o}C and FABG-$Gd_2Ti_2O_7$-1100^{o}C containing 20 wt% , 50 wt%, and 80 wt% loading of $Gd_2Ti_2O_7$ 144

Figure 6.5 Ti K-edge XANES spectra from BG-$Gd_2Ti_2O_7$-750^{o}C and FABG-$Gd_2Ti_2O_7$-750^{o}C containing 20 wt% , 50 wt%, and 80 wt% loading of $Gd_2Ti_2O_7$ 145

Figure 6.6 Ti K-edge XANES spectra from BG- and FABG- composite materials (50 wt% $Gd_2Ti_2O_7$) annealed at 1100^{o}C or 750^{o}C are shown 146

Figure 6.7 Si $L_{2,3}$-edge XANES spectra from the borosilicate glass annealed at 1100^{o}C or 750^{o}C are shown 148

Figure 6.8 Si $L_{2,3}$-edge XANES spectra from BG-$Gd_2Ti_2O_7$-1100^oC and FABG-$Gd_2Ti_2O_7$-1100^oC containing 20 wt% , 50 wt%, and 80 wt% loading of $Gd_2Ti_2O_7$ 149

Figure 6.9 Si $L_{2,3}$-edge XANES spectra from BG-$Gd_2Ti_2O_7$-750^oC and FABG-$Gd_2Ti_2O_7$-750^oC containing 80 wt% , 50 wt%, and 20 wt% loading of $Gd_2Ti_2O_7$ 150

Figure 6.10 The Fe K-edge XANES spectrum from FABG, FABG-$Gd_2Ti_2O_7$-1100^oC and FABG-$Gd_2Ti_2O_7$-750^oC are shown. 153

Figure 6.11 Al $L_{2,3}$-edge XANES spectra from FABG-$Gd_2Ti_2O_7$-1100^oC and FABG-$Gd_2Ti_2O_7$-750^oC are shown 154

Figure 6.12 Ti K-edge GA-XANES spectra from BG-$Gd_2Ti_2O_7$-1100^oC and BG-$Gd_2Ti_2O_7$-750^oC implanted using Au^- ions to a dose of 5×10^{14} ions/cm^2 are shown 156

Figure 6.13 Ti K-edge GA-XANES spectra from BG-$Gd_2Ti_2O_7$-750^oC (40 wt% loading of $Gd_2Ti_2O_7$) and $Gd_2Ti_2O_7$ implanted to a dose of 5×10^{14} ions/cm^2 are shown 157

List of Abbreviations

APS	Advanced Photon Source
ABG	Al-borosilicate Glass
BG	Borosilicate Glass
BSE	Backscattered Electron
CANDU	Canada deuterium uranium
CLS	Canadian Light Source
CN	Coordination Number
DOS	Density of States
d	Lattice spacing
E_c	Bending magnet Critical Energy
EDX	Energy Dispersive X-ray spectroscopy
EXAFS	Extended X-ray Absorption Fine Structure
FBG	Fe-borosilicate Glass
FABG	Fe-Al-borosilicate Glass
FWHM	Full Width at Half Maximum
GA	Glancing Angle
HXMA	Hard X-ray Micro Analysis
I_0	Intensity of incident X-ray beam
I_t	Intensity of transmitted X-ray beam
I_f	Intensity of fluorescent photons
I_{TEY}	Intensity of total electron yield
ISW	Interface Science Western
l	Angular momentum

N	Total number of magnetic periods
NMR	Nuclear Magnetic Resonance
PNC/XSD	Pacific Northwest Consortium/X-ray Science Division
RE	Rare-Earth
RF	Radio Frequency
SGM	Spherical Grating Monochromator
SRIM	Stopping and Range of Ions in Matter
SXRMB	Soft X-ray Microcharacterization Beamline
SYNROC	Synthetic Rock
t	Sample thickness
TB-LMTO	Tight-Binding Linear-Muffin-Tin Orbital model
TEM	Transmission Electron Microscopy
TEY	Total Electron Yield
TFY	Total Fluorescence Yield
VLS-PGM	Variable Line Spacing-Plane Grating Monochromator
XANES	X-ray Absorption Near-Edge Spectroscopy
XAS	X-ray Absorption Spectroscopy
XPS	X-ray Photoelectron Spectroscopy
XRD	X-ray Diffraction
μ-XRD	Micro-X-ray Diffraction
μ	Absorption Coefficient
γ	Storage ring energy
λ	Wavelength

Chapter 1

Introduction

The demand for energy is increasing with the growing population of our society, increasing the need for reliable energy sources. Nuclear energy has been considered a clean energy source that provides huge amounts of energy, which can meet industrial and societal energy needs.[1-5] Canada produces 15 % of its electricity from nuclear reactors, as of 2010 statistics.[6] The growing demand for nuclear energy has resulted in the production of a considerable stock-pile of hazardous radioactive nuclear waste.[7-8] The safe and effective disposal of radioactive nuclear waste has become an issue in our globalized and industrialized society.[8-11] Therefore, it is important to investigate strategies for the safe disposal of fissile Pu (from dismantled nuclear weapons) and minor actinides (Np, Am, Cm) as the demand and development of nuclear power increases.[8,12-16] This thesis has been focused on investigating and developing materials that can sequester actinides in a crystalline structure.

1.1 Nuclear waste generation and management

The nuclear industry has been producing a significant amount of radioactive nuclear waste. The risk of this hazardous nuclear waste depends upon its radioactivity, half-life, and the amount.[12-14] Canada has been producing nuclear waste since the early 1930's, when uranium mining operations started in the Northwest Territories to support nuclear fuel and military applications.[17,18] Over the years, a significant amount of nuclear waste has been accumulated because of the growing demand for nuclear energy. Nuclear waste is generated from a number of

sources, such as spent nuclear fuel rods, reprocessing of nuclear fuel waste, dismantlement of nuclear weapons, etc.[12-15] The accumulated nuclear waste from used fuel (measured by volume) and uranium mill tailings were 9079 m^3 and 214,000,000 tonnes, respectively, in Canada to the end of 2010.[17] It is important to immobilize the hazardous nuclear waste materials from the environment safely and securely.

The generated nuclear waste has been safely managed and stored at nuclear reactor sites in past years.[19-23] Spent nuclear fuel rods discharged from nuclear reactors are stored in specially designed pools called spent fuel storage pools. In this method, the spent fuel rods are placed under water (~ 20 feet of water) to reduce the heat generated from the radioactive elements. The pool water is continually monitored to reduce the heat produced by the spent fuel rod assemblies. After cooling for a number of years (~5-10 years), these spent fuel rods are sent to dry cask storage sites.[19,23] In this method, spent fuel rods are surrounded by inert gas (typically He) inside a container called dry casks. These casks are closed cylinders made of steel/copper. Each cylinder is again covered by steel/copper layer and then concrete layers to protect waste from environment.[19,23]

In Canada, nuclear waste is stored in either storage pools or dry cask storage.[20] However, these sites are short term storage methods to immobilize the nuclear waste elements having longer half-lives. There is growing need to permanently dispose of accumulated nuclear waste.[24,25] It has been proposed to dispose the nuclear waste deep under the ground (i.e., below sea level for long term storage up to ~10^6 years), which is called geological sequestration.[24-26] The disposal of nuclear waste is one of the factors that is responsible for the decline of the number of nuclear energy sites worldwide over the past few years (other factors like nuclear accidents are also responsible for this decline too).[27-29] Geological sequestration is still under

consideration because of the role of public policies and political issues involved in resolving the issue of nuclear waste.[26,29,30] A key consideration for nuclear waste management is the development of highly durable materials that can ensure the long-term stability and isolation of the radioactive waste elements.[8,16]

1.2 Nuclear wasteforms

A number of nuclear wasteforms have been proposed to immobilize the nuclear waste for geological sequestration and a significant amount of research has been done in this area over the last 50 years.[9,11,12,14,16] Nuclear wasteforms are materials that can safely and securely incorporate various radioactive nuclear waste elements. The functions of a nuclear wasteform are to immobilize the radioactive waste and provide physically, chemically, thermally, and mechanically stable protection, and resist radiation induced damage over a thousand years.[8,30,32,33] Nuclear wasteforms have been proposed based on the high waste loading, easy processing, radiation stability, and physical and chemical durability over thousands of years.[8,32-37]

1.2.1 Radiation effects on nuclear wasteforms

A key concern for the nuclear wasteform materials are long-term stability and durability issues, which may be affected by the radioactive decay of incorporated nuclear waste elements.[16,38-43] During the radioactive decay (i.e., α- or β-decay) process, the incorporated radioactive nuclear waste elements may release α- or β-particles over a period of time and transform to daughter products. These α- or β-decay events can cause radiation damage to the nuclear wasteform through various processes i.e., collisions between the α- or β-particles, ionization effects associated with these particles, and atomic displacements in the structure. The

major effect that can influence long-term stability of nuclear wasteforms is the atomic displacements in the structure i.e., the daughter products having a sufficient recoil energy can displace the other atoms in the structure. This can lead the structure to become metamict (i.e. the structure becomes amorphous).[8,16,33,41,43-45] For example, the long lived radioactive actinide ^{239}Pu releases energetic 5.2 MeV α-particles and is transformed to ^{235}U with recoil energy of 86 keV. The daughter product with its recoil energy can displace more atoms (~ 10^3 atomic displacements) in the structure of the material compared to the α-particle (~ 10-10^2 atomic displacements).[41,46] This process can result in the development of defects, swelling, and cracking of the structure and can affect the long-term chemical durability of the nuclear wasteform.[43-46] It is very important to study how the structure behaves when exposed to radiation and the structural damage caused by incorporated nuclear waste.[33,41,46] Therefore, studying how the material responds to the radioactive decay of the incorporated nuclear waste elements is a crucial step to develop nuclear wasteforms. Radiation induced structural damage can be simulated by bombardment (implantation) of the materials using high-energy ion beams (e.g., Au^-, Kr^+, and Xe^+), which will be discussed in Section 1.3.[33,45-47] A number of wasteforms have been proposed based on their long-term stability to radiation damage such as glass wasteforms, ceramic wasteforms, glass-ceramic wasteforms, and multiphase systems (SYNROC: Synthetic rock).[30-36] Each nuclear wasteform offers unique features to incorporate nuclear waste elements, which will be discussed below.[30-36]

1.2.2 Glass wasteforms

Glass was the first wasteform that was proposed and developed as a host material for nuclear waste via vitrification process.[15,36,48-50] Vitrification involves loading of waste elements within glass matrix at low melting temperatures. Various glass wasteforms have been proposed

for the immobilization of nuclear waste based on chemical durability, thermal, mechanical, and radiation stability.[34,50-52] Glass wasteforms can incorporate a wide range of waste compositions (i.e., over 30 different nuclear fission and activation products, and minor actinides) because of the amorphous silicate structure of glasses and can easily be modified to optimize its properties.[15,33,34,38,50] Borosilicate, phosphate, and rare-earth glasses are the proposed wasteforms to immobilize fission products and actinides.[33,36,38] Although phosphate and rare-earth glasses have been considered for the immobilization of selected nuclear waste elements, most research has focused on various borosilicate glass compositions.[36,38,52,53]

Previous investigations on borosilicate glasses have shown how the chemical durability, thermal, and mechanical stability can vary with changing the composition.[11,15,36,38,51-54] The oxides in the glass are divided into three categories based on the role of forming or modifying the silicate networks: network formers (B, P, Fe, etc), modifiers (Na, K, Li, Al, Ca, etc.), and intermediates (Ca, Ti, Zr, Al, etc).[11,34,40,38,55-56] Durability of these glasses for nuclear waste immobilization can be achieved by adding different compositions of these oxides.[11,15,36,38,51-53] The radioactive nuclear waste elements can bind to glass-forming elements (e.g. Si, B, and alkali elements) via bridging bonds in a glass matrix.[33,34] Previous investigations on borosilicate glasses have shown that the loadings of nuclear waste, the resistance to radiation damage, and swelling can depend on the glass composition.[34,38,50-53,55] It was reported that most actinide elements (e.g., Pu) can only dissolve in the glass network at very low loading (3-10 wt %).[21,50] Although these borosilicate glasses can accommodate a wide range of waste elements, these materials have some disadvantages as nuclear wasteforms such as small fraction of loading of actinide elements and the volatility of some fission products during vitrification.[33,36,50,51,52]

1.2.3 Ceramic wasteforms

Ceramic materials have been proposed as nuclear wasteforms as they are naturally occurring mineral analogues that contain actinides and are preserved in nature over millions of years.[57-62] Over the last few decades, a number of chemically durable, stable, and flexible ceramic materials have been developed and proposed as potential nuclear wasteform such as zirconolites ($CaZrTi_2O_7$), monazite ($(Ce,La,Nd,Th)PO_4$), hollandite ($BaAl_2Ti_6O_{16}$), Zircon ($ZrSiO_4$), perovskites (ABO_3, where A and B are cations occupied in different atomic positions of crystal structure), fluorites (AO_4), and pyrochlores ($A_2B_2O_7$).[32,40,41,57,62] After several decades of research on ceramic materials, investigations have shown how the variations in long-range structural arrangements (edge/face/corner sharing) and electronic properties can affect the waste loading, stability, chemical durability and resistance to radiation damage.[32,33,39-42] The main drawback of using ceramic materials as a nuclear wasteforms is that, compared to glass, they can only incorporate a limited number of radioactive waste elements in specific atomic positions of the crystal structure.[32,33] In this thesis, the pyrochlore-type crystal structure has been studied due to its unique features, which may make these materials viable as a nuclear wasteform.

1.2.3.1 Pyrochlore-type crystalline oxides

The fluorite and fluorite-related oxides, such as pyrochlore-type oxides, have received substantial interest for the immobilization of actinides.[8,32,48,54,56,63,64] Pyrochlore is a mineral ore of Nb and Ta in the Earth's crust and can contain small amounts of lanthanide and actinide (Th and U) elements in the Earth's crust.[65] The pyrochlore-type crystal structure shows remarkable compositional diversity with over 500 compositions being known up to date.[66-67] The diverse chemistry of the pyrochlore-type oxides is coupled to a remarkable variation of chemical and

physical properties, and these materials have technological applications such as catalysis, piezoelectricity, ferro- and ferri-magnetism, luminescence, giant magneto resistance and ionic conductivity.[68-73] The advantages of using these materials as nuclear wasteforms are the high compositional diversity, structural flexibility, and chemical durability.[32,41,64,66,67] This can enhance the incorporation of nuclear waste elements (actinides) into the structure and the resistance of these materials to radiation induced structural damage.[32,41,64,66,67,74]

The general stoichiometry of pyrochlore-type oxides can be written as $A_2B_2O_7$ (Space group: $Fd\bar{3}m$) and the pyrochlore-type crystal structure is related to the fluorite structure (AO_2, Space group: $Fm\bar{3}m$), except that it has two cation sites and one eighth fewer oxygen vacancies.[41,64,66,67,75] The pyrochlore-type structure is shown in Figure 1.1.[76] The A-site atoms (A = La to Lu, Ca, Y, etc) are generally larger trivalent cations and the B-site atoms (B = Ti, Sn, Ta, Zr, Hf, etc.) are smaller tetravalent cations (it is also possible for the A- and B-site cations to have oxidation states other than 3+ and 4+, respectively).[41,64,75,77] In the 3D framework of pyrochlore-type crystal structure, the A-site cation is in an eight coordinate-site within a distorted cubic polyhedral and the B-site cation occupies a distorted octahedral environment. The structure has three distinct oxygen anion sites within tetrahedral interstices and one of the anion sites is vacant when the pyrochlore structure is perfectly ordered.[41,64,75,78] The local environments for each oxygen anion site are OA_4, OB_4, and OA_2B_2. The pyrochlore-type crystal oxides lend themselves to a wide variety of chemical substitutions at the A and B sites, and the crystal structure can tolerate the presence of additional oxygen vacancies to a certain extent.[64,75,78-80]

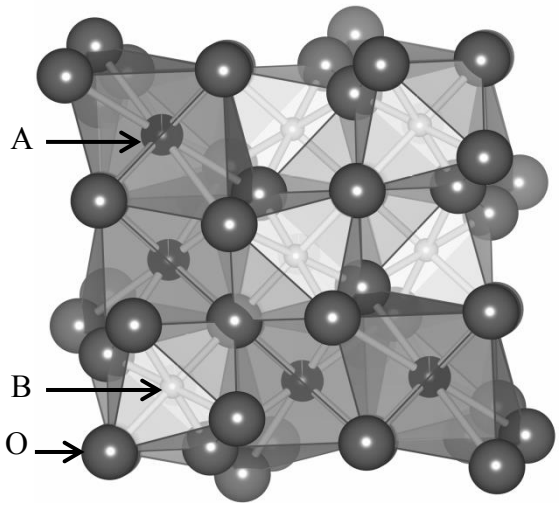

Figure 1.1 A portion of the unit cell (1/8) of the pyrochlore-type structure of $A_2B_2O_7$ ($Gd_2Ti_2O_7$) is shown. The structure consists of AO_8 in distorted cubic polyhedra (dark grey), distorted BO_6 octahedra (light grey), and O atoms (dark grey spheres) occupy tetrahedral interstitial sites. The pyrochlore-type structure was generated using the VESTA program.[76]

In pyrochlore-type oxide materials, anti-site disorder can occur among cations and anions depending on the composition and the method used to synthesize the materials.[79,81] Anti-site disorder can also be driven by thermal treatment, the application of an external pressure, or implanting the material with an ion beam.[79,82,83] The driving force for the degree of cation anti-site disorder is generally dependant on the ratio A- and B-site ionic radii (r_A/r_B). As the ionic radius ratio (r_A/r_B) decreases and approaches ~1.46, the ordered pyrochlore structure can transform to the defect fluorite structure (i.e., order-disorder phase transition) by disordering of A- and B-site cations.[41,81,83-84] Anion anti-site disorder generally accompanies the disordering of the cation lattice.[84] Other factors such as the covalency of the metal-oxygen bond interactions and electronic structure can also influence the transformation of ordered pyrochlore-type structure to disordered defect fluorite-type structure.[41,87-89] The order-disorder phase transition would greatly affect the resistance to radiation induced structural damage of the pyrochlore-type

oxides.[41,86-88] Pyrochlore-type materials can exhibit a wide range of properties and applications depending on composition, and most of these properties depend on the extent of disordering among the A-site and B-site cations in the structure, bond covalency, and presence of oxygen vacancies.[41,87-89] Therefore, it is very important to understand how the electronic and structural properties of pyrochlore-type materials change depending on composition and how the variation in electronic properties can affect the structural stability of the materials upon irradiation.

1.2.4 Multi-phase ceramic wasteforms

Multiphase ceramic materials have been proposed and designed to incorporate a wide range of complex nuclear waste elements.[32,37,57,90-92] SYNROC (i.e., synthetic rock), a multi-ceramic material, has been designed based on the stable natural titanate minerals that have immobilized uranium and thorium for a long time. Synroc is a combination of zirconolites, perovskite, hollandite and rutile phases.[90-92] Zirconolite and perovskite crystal phases can incorporate long lived actinides (e.g., Pu) and hollandite crystal phases can immobilize Cs along with K, Rb, and Ba. Various forms of SYNROC have been developed to immobilize various nuclear waste elements and these wasteforms have been examined under lab conditions.[57,92] Waste loading range of 50-70 wt % with high durability has been demonstrated in Synroc materials.[90-92] Pyrochlore ($(Ca,Gd,U,Pu,Hf)_2Ti_2O_7$) enriched synroc (Synroc-F) has been developed for the disposal of nuclear waste from CANDU (Canada deuterium uranium) reactors.[92-95] The pyrochlore-rich synroc has been observed to be efficient for the immobilization of nuclear waste with a loading of 50 wt % U/PuO_2.[57,92,95,96]

1.2.5 Glass-ceramic wasteforms

Glass and ceramic materials have unique features for the immobilization of nuclear waste. The combination of these two materials can enhance the incorporation and effective immobilization of various nuclear waste elements.[32,33,50,53,97] Glass-ceramic composite materials have been considered as a potential nuclear wasteforms because of the stable and flexible structure of these materials. This can increase the ability of these materials to incorporate actinides and various fission products in either the crystalline structure or the glass matrix.[33,50,53,55] Further, in these composite materials, the glass can also act as a secondary barrier for the incorporated radioactive actinides in the crystalline material.[98,99] Different glass-ceramic composite materials have been examined in the past.[32,33,50,53,99] These investigations have shown that the degree of immobilization vary with the glass composition and/or crystalline structure of the composite material.

Recently, rare-earth pyrochlore based glass-ceramic materials have been investigated for immobilization applications. The studies on $Gd_2Zr_2O_7$ and $La_2Zr_2O_7$ based glass-ceramic composite materials have shown that the distribution and interaction of pyrochlore-type oxides within the glass matrix plays an important role in stabilizing the composite materials when exposed to radiation.[98-100] These studies have also shown how the mechanical stability and the interaction of ceramics within the material changes depending on glass/ceramic composition. [98-100] A better understanding of compositional study and its structural stability upon radiation will help to develop and design this potential nuclear wasteform.

1.3 Ion beam implantation studies

Investigation of radiation induced structural damage (i.e., metamiction) of a material is not possible in a real time scale (i.e., 10^3-10^6 years).[35,38,41] However, this can be simulated by bombarding the materials with high energy heavy ion beams. In previous studies, heavy ions (i.e. Au^-, Kr^+, and Xe^+) at various doses (10^{12}-10^{15} ions/cm^2) have been used to mimic the daughter products and long-term radiation damage.[41,63,83,84,86-88]

An ion beam implantation chamber from a Tandetron accelerator (located at the University of Western Ontario, London) is shown in Figure 1.2.[101] A typical ion beam implantation chamber consists of a sputter ion source, accelerator, and a target chamber. The sputter ion source is a heavy ion source that produces high intensity ion beams from the desired heavy element. The ion beams are boosted to higher energies (MeV) using accelerator tubes. A uniform amount of ions with a specific velocity and charge are transferred to the target chamber (where the sample was placed) using high-energy magnets and slits. During implantation, the ion beam is aligned approximately normal to the surface of a thick material (i.e., pellet).[47,102] A uniform amount of ions are implanted on a target material, generally measured in terms of dose or flux (Ions/cm^2). The high-energy ion beam can penetrate to a maximum depth of 450-1000 nm. The penetration depth can depend on the composition, energy of ion beam, and the ion species. Ion beam implantation can effectively simulate radiation induced structural damage, which can help to develop materials that resist radiation-induced structural damage.[41,63,83,84,86-88,102]

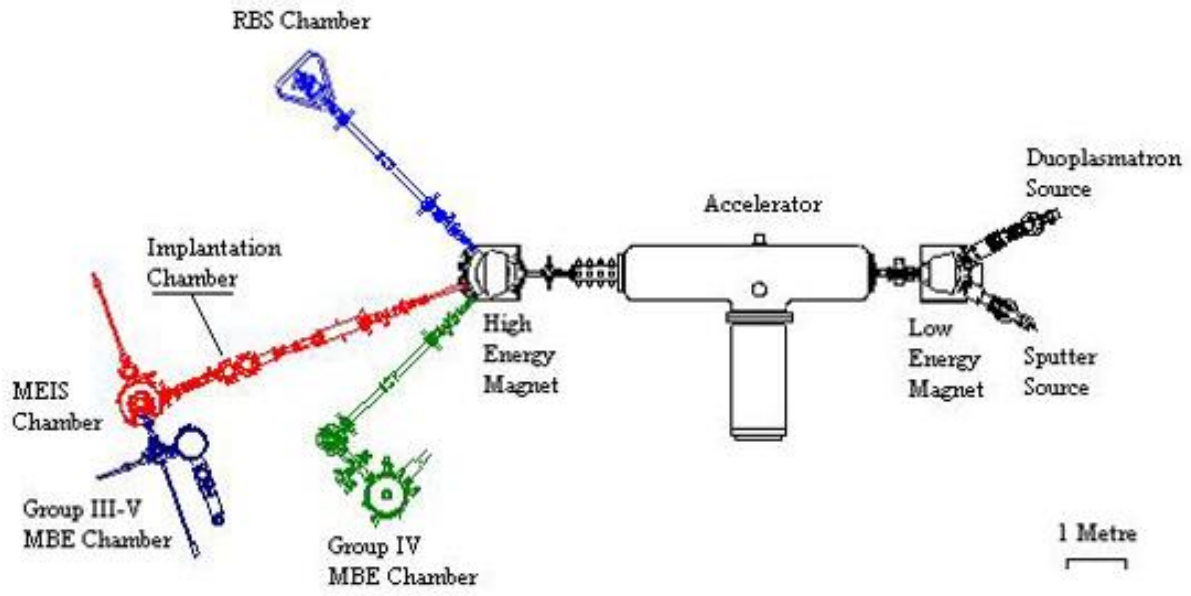

Figure 1.2 Schematic diagram of the Tandetron accelerator along with the ion implantation chamber located at the Interface Science Western (ISW), University of Western Ontario is shown.[101] The diagram was retrieved from the ISW website.[101] High energy (MeV) heavy ions are generated from a sputter source, accelerated through an accelerator, and transferred to implantation chamber. The samples were placed normal to the ion flow.

1.4 Powder X-ray diffraction

Powder X-ray diffraction (XRD) is one of the primary techniques that can be used for identification and quantitative determination of various crystalline structures in a material.[103] As the name suggests, the sample is in a powder (or solid) form consisting of fine grains of crystalline domains oriented randomly in the material. This diffraction technique provides information on phase purity, lattice parameters, atomic site positions, and crystallite size.[103] Due to its versatility, powder XRD has been used in a wide variety of fields such as geology, material science, environmental science, etc.[103,104]

Due to the periodic array of atoms in a crystalline solid, the structure can be described as a series of lattice planes (hkl) with equal inter-planer distance (d_{hkl}).[103] When the monochromatic

X-rays interact with the electron cloud of atoms in a lattice plane, some of the X-rays undergo coherent scattering without loss in energy. Diffraction occurs only when the distance travelled by these scattered X-rays from successive lattice planes differs by an integer wavelength of X-rays. This can be explained by applying Bragg's law of diffraction (shown in Figure 1.3).[103] This law states that the path length difference ($2d_{hkl}\sin\theta$) of the incident and the scattered X-rays of each lattice plane is an integral multiple of the wavelength (λ) of the incident X-rays.

$$2d_{hkl}\sin\theta = n\lambda \qquad (1.1)$$

Where `θ` is the angle between the incident (or diffracted) beam and the lattice plane, `n` is an integer, `λ` is the wavelength, and `$d_{hkl}$` is the spacing between the successive lattice planes. Constructive interference of diffracted photons from different lattice planes produces a pattern, which contains the information about the atomic arrangement within a crystal. For a fixed wavelength, the inter-planar distance of various lattice planes in a crystalline material can be measured by varying the angle between the diffracted beam and the lattice plane. The diffractogram from a poly-crystalline material can be formed by the addition of individual diffraction patterns from different crystalline structures of a material.[104] The number and position of each diffraction peak depends on the lattice spacing, lattice type, and lattice parameters whereas the peak intensity depends on the type and position of the atoms.[103,104] The width of the diffraction peaks from a particular crystalline structure provides information of the average crystallite size and the presence of defects in the material.[104,105]

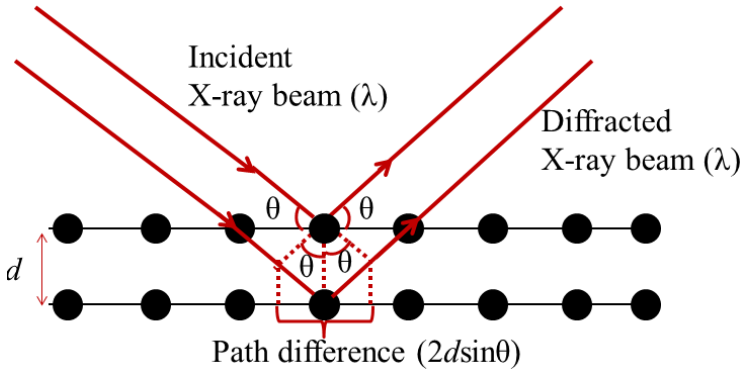

Figure 1.3 Schematic diagram of Bragg`s law. When X-rays (wavelength, λ) are incident on a lattice plane at an angle θ, some of the X-rays undergo constructive interference. This occurs when the path difference of the incident and diffracted beams is an integral multiple of the wavelengths of the incident X-rays.

1.5 Synchrotron radiation techniques

In this work, synchrotron facilitated X-ray absorption spectroscopy (XAS) experiments have been used to probe the electronic structure of the constituent elements in a material. When the electrons are moving at relativistic speed (~speed of light) and are forced by the applied magnetic fields to move along curved trajectories, the electrons emits radiation tangential to the direction of their path known as synchrotron radiation. The synchrotron radiation is a highly polarized, narrow monochromatic beam with a high intensity and provides a broad and continuous energy band (i.e., infrared to hard X-ray energy region).[106-108] Because of these properties, synchrotron radiation is a beneficial tool for studying the electronic and structural properties of materials in different fields.[106]

Tantalus (Wisconsin, US) was the world's first light source dedicated to synchrotron radiation research.[109] The Aladdin storage ring, also located in Wisconsin, with energy of 1 GeV was the second synchrotron source.[109] A schematic diagram of modern synchrotron radiation source is shown in Figure 1.4. In synchrotron radiation facilities, the charged particles (i.e.,

electrons) from an electron gun are injected to a linear accelerator (linac) and accelerated to high velocity and energy (MeV). These electrons are injected in bunches and accelerated to a relativistic speed and high-energy (GeV) in an evacuated booster ring. The accelerated electrons in the booster ring are then injected into the polygon shaped closed loop called a storage ring.[106]

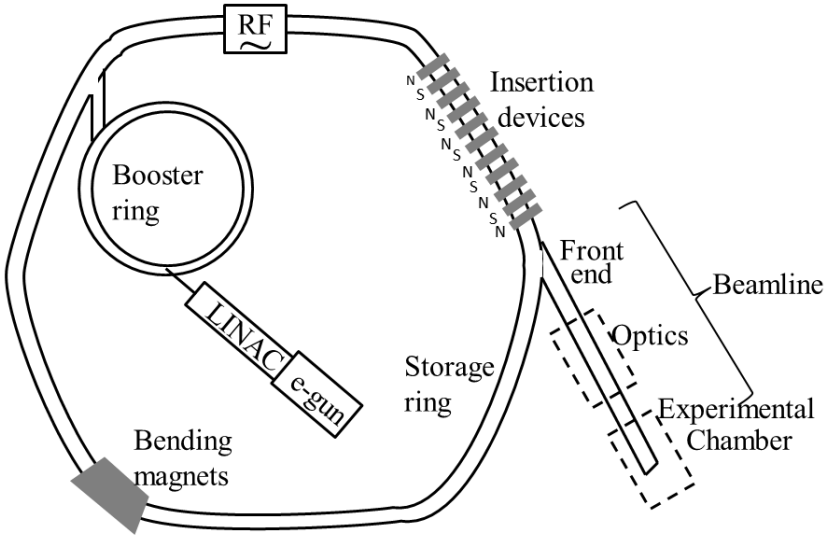

Figure 1.4 Schematic diagram of a modern synchrotron (3rd generation) source is shown. The electrons are accelerated with a relativistic speed using a series of accelerators: LINAC, booster ring, and storage ring, respectively. The storage ring consists of bending magnets and insertion devices, which are responsible for the generation of most intense synchrotron radiation. The beamlines bring the synchrotron radiation to the experimental chamber using various optical devices.

The storage ring maintains the electrons with a relativistic speed in a closed path by magnetic lattice (arc sections of bending magnets and straight sections of insertion devices). Bending magnets are large dipole magnets used to bend the electron beam around the corner of the polyhedral storage ring.[106,107,110] The insertion devices are continuous array of magnets,

categorized as wigglers and undulators based on magnetic field strength (and number of magnetic periods), built into a straight section of the storage ring.[106-108,111] Schematic diagram for bending magnets and insertion devices are shown in Figure 1.5. The electrons in the storage ring circulate over a million times each second and generate very intense electromagnetic radiation.[106] The beamline stations are tangential to the storage ring in order to transfer the emitted radiation into the experimental chamber.[106] The beamlines are the stations where the emitted radiation is transferred to the experimental chamber using optics (mirrors, monochromators, and gratings). The lost energy of the accelerated electrons due to the emission of synchrotron radiation can be regained using a radio frequency (RF) supply.[106]

As the electrons are accelerated close to the speed of light (at operating energy) along the bending magnets, the radiation emitted by these relativistic electrons is highly collimated (narrow) into a forward facing cone (i.e., in a pencil-like beam). The opening angle of the emitted radiation cone is of the order $1/\gamma$ (~ mrad), where γ is the storage ring energy (~GeV).[106-108] The emitted radiation from a bending magnet covers a broad range of energy. The important parameter that characterizes the emission spectrum output from a bending magnet is the critical energy, E_c.[106] The critical energy is the energy below which half of the total radiative power of a beam that is emitted and is taken as the high energy cut off of a synchrotron source. The critical energy of a source varies with the magnetic field strength and storage ring energy, which can be increased by increasing the magnetic field strength (e.g., by placing super bend magnets) for a specific synchrotron source.[106] The flux (generally referred as to the brilliance in the units of photons/s/mm^2/mrad^2/0.1% bandwidth) emitted by the relativistic electrons is proportional to γ^4 (i.e., high energy synchrotron sources produce high brilliance).[106]

Insertion devices (wigglers or undulators) placed in the straight sections of the storage ring can be optimized to produce radiation specifically tailored to different experimental needs.[106,110,111] They can produce significantly higher fluxes (and higher critical photon energies) than the bending magnets. An insertion device is an array of magnets arranged in alternating dipoles of a straight section, which can cause the electrons to oscillate sinusoidally in the plane of the ring. Insertion devices are categorized into wigglers and undulators based on the number of magnets and the magnetic field strength that caused by these magnetic arrays.[106,111]

An undulator is an array of a large number of permanent magnets (shown in Figure 1.5c) where angular divergence of the electron beam is smaller.[106] The electron beam is periodically deflected by a weak magnetic field with small amplitude. The small amplitude oscillations creates constructive and destructive interference, resulting in the emission spectrum with a narrow bands of radiation (because only the wavelengths with constructive interference adds up) and a higher photon flux (proportional to N^2 times, N-total number of magnetic periods). Undulators are often used for soft X-ray beamlines which require a relatively limited range in energy and demand for high photon flux.[112] A wiggler is a smaller array of powerful permanent magnets, which deflect the electron beam with larger amplitude oscillations.[106,110] This can cause a broad emission spectrum (similar to bending magnet spectrum) over a large opening angle of radiation. Wigglers are just like bending magnet, but produces higher photon flux and higher critical energies (because of number of strong magnetic periods). Wigglers are often used for hard X-ray beamlines, where broad range of X-ray energies are required.[112]

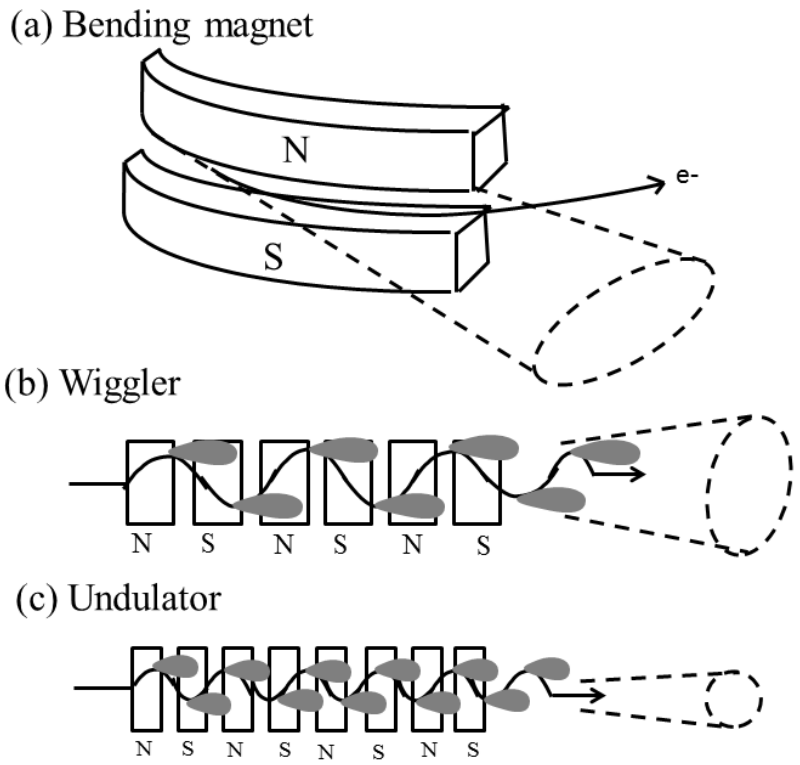

Figure 1.5 Schematic of a bending magnet, wiggler, and undulator are shown. (a) Bending magnets are used to change the trajectory of electron and generated wide span of radiation (b,c) Wigglers and Undulators are a series of magnets arranged in an alternative way. Wigglers can produce very wide band of energy whereas undulators can produce a narrow energy band of radiation because of the variations in magnetic field strength.

1.5.1 Beamline set-up

The generated synchrotron radiation in the storage ring can be delivered to the experimental chamber through a beamline. A beamline consists of a front end aperture (to bring the beam from the storage ring), an optics section (to select the wavelength of a beam), and an experimental chamber.[106] To perform X-ray absorption spectroscopy experiments, it is necessary to focus the monochromated beam on the sample with good energy resolution and optimized photon flux.[106,112] Various optical instruments have been designed for the beamlines to produce

collimated, monochromated, and focused beams, which depend on the X-ray energy range and the measurement method (i.e., scattering, imaging, or spectroscopic methods).[106]

The most important components for hard X-ray (above 2000 eV) optics are monochromators and mirrors.[107,113] Monochromators are used to produce single wavelength (i.e., energy) radiation whereas mirrors are used for collimating and focusing the X-ray beam onto the sample. Double crystal monochromators have been used for hard X-rays (i.e., the energy above 2 keV) to select and scan the energy.[107,113] Double crystal monochromators have two single crystals mounted parallel to each other with one used to select the energy and the other to attain the position of beam spot on the sample (since beam position is energy dependant, which can be tracked by a second crystal). For a fixed lattice spacing (d) and a fixed angle between the incident beam and the crystal face, these crystals can separate energy (i.e., wavelength) of photon beam using Bragg diffraction ($n\lambda = 2d\sin\theta$) and scan through the energy with good resolution.[107] Energies that satisfy the Bragg equation with n>1 are called harmonics and can be removed from the beam using harmonic rejection mirrors (e.g., Rh coated mirrors can absorb high harmonics) and/or detuning the monochromatic crystal.[114] Generally for XAS experiments, Si (111) vs Si (220) faces have been used at the cost of high flux *vs* high resolution.[112,115]

The wavelengths of soft X-rays (below 2 keV, ~0.5 nm to few nanometers) match the length scales in the materials well. For these wavelengths, there is no need to use single crystal monochromators like for the hard X-ray region. Monochromatic gratings can cause dispersion (i.e., separation of light with different wavelengths) due to its well-defined line spacing and size.[116] Large dispersion and small focus can bring high energy resolution to the soft X-rays. The resolving power of a particular monochromatic grating depends on the line spacing and total number of grooves in the grating.[116] The photon beam emitted from the soft X-ray optics has a

small spot size due to small interaction cross section of soft X-rays and a high resolving power. The end stations for a beamline vary with the measurement method (i.e., spectroscopy, scattering, and imaging).[106] Since X-ray absorption experiments have been the interest of study of this thesis, the end stations will be explained below.

1.5.2 XAS experimental set-up

Generally, the X-ray absorption spectrum (XAS) records the absorption intensity as a function of the incoming photon energy.[112,117,118] The absorption coefficient can be determined either directly by measuring the intensities of incoming and transmitted beam (transmission mode) or indirectly by measuring the intensity of incoming beam and of the decay products (i.e., decay of excited state accompanied by the emission of fluorescent photons, photo-electrons, Auger electrons, or secondary electrons).[112,118] A schematic diagram of the different X-ray absorption spectroscopy detection methods is shown in Figure 1.6. The selection of a detection method varies with the absorption-edge energy and sample environment.[120]

Transmission experiments are designed for high energy XAS experiments because the high energy beam can transmit and penetrate easily through the sample.[112,117] In transmission mode, the incident beam of X-rays (I_0) passes through a sample of thickness (t), and the transmitted beam (I_t) is measured (Figure 1.6a). The change in intensity of incident and transmitted photons is related to the absorption coefficient (μ) of a sample, which can be explained by Beer-Lambert law for linear absorption.

$$\ln\left(\frac{I_t}{I_0}\right) = -\mu t \tag{1.2}$$

Where 'I_0' is the incident X-ray beam intensity, 'I_t' is the intensity transmitted through the sample, and 't' is the sample thickness.[112,117,118] Since 'μ' is the sum of the absorption coefficients of all components in a material, a sharp increase in absorption coefficient can be achieved using a sufficiently concentrated sample. The intensity of incident (I_0) and transmitted beams (I_t) is measured using ionization chambers.[112,117,118] Ionization chambers consist of compartments filled with gas and is connected between two oppositely charged parallel plates.[112,117,119] Some of the X-rays ionize gas when they pass through these chambers, releasing ions and electrons that are collected at the plates in form of current. The current is proportional to the intensity of X-ray beam.[119] The selection of a gas for these ionization chambers varies depending on the energy of X-ray photon beam. Heavier gases (e.g., Ar, Xe) have been used for high energy (above 10 keV) XAS experiment due its large absorption cross section and it ability to absorb large number of X-ray photons.[120] Low atomic number gas (e.g., He and/or N_2) are used for low energy (~3 keV-5 keV) and medium energy (~5-10 keV) XAS experiments.

For the absorption-edge energies in soft X-ray region, the transmission experiments are not possible and absorption is monitored by measuring either the emission of fluorescence photons or electrons.[119-121] The emission of fluorescence photons or electrons (i.e. direct emission of Auger or photoelectrons or indirect emission of secondary electrons) occurs by the decay of excited state and the intensity of these decay products are generally proportional to X-ray absorption.[121] The emitted fluorescence photon flux (I_f) from a sample is collected using a detector and the total electron yield (I_{TEY}) is measured in the form of a drain current to replace electrons that lost from emission. The absorption spectra measured is the ratio of detected fluorescent (or electron yield) signal and incident photon (i.e., μ proportional to I_f/I_o (or I_{TEY}/I_o)), which is similar to the transmission spectra.[112,121] However, the detected signal intensity in

fluorescent measurements can be strongly attenuated by absorption effects (i.e., fluorescent photons absorbed by the same atom) or saturation effects when measuring thick or concentrated samples.[112,122,123] As for the electron yield measurements, charging effects are also problematic for electron yield from thick insulating materials.[120] Charging effects obstruct the transfer of electrons from electrically grounded sample holder to the sample surface (to replace the lost electrons during emission). These problems can be reduced using an effective mounting procedure and sample preparation (or concentration).[120,124] Therefore, care should be taken when measuring the spectra using these detection methods.

Transmission, florescence, and electron yield experiments have different sampling depths because of the variation in the penetrating depths of photons vs electrons (i.e., because of the different interaction cross sections of photons vs electrons with matter).[112,120,124] Transmission and fluorescence measurements are inherently bulk sensitive whereas electron yield measurements are surface sensitive.[117,120,122] The subtracted photon beam is measured in the transmission since the beam passes through the entire thickness of sample and, for the fluorescence mode, the (fluorescent) photons sufficiently penetrates through the medium (small interaction with the matter) and the collected fluorescence photons escape from the bulk of the sample.[120,122] These make the transmission and fluorescence measurements bulk sensitive. For the electron yield experiments, the electrons lose energy rapidly via scattering or absorption (larger interaction cross section) and the signal recorded is only from the electrons that escaped from the surface (in nm).[120,124]

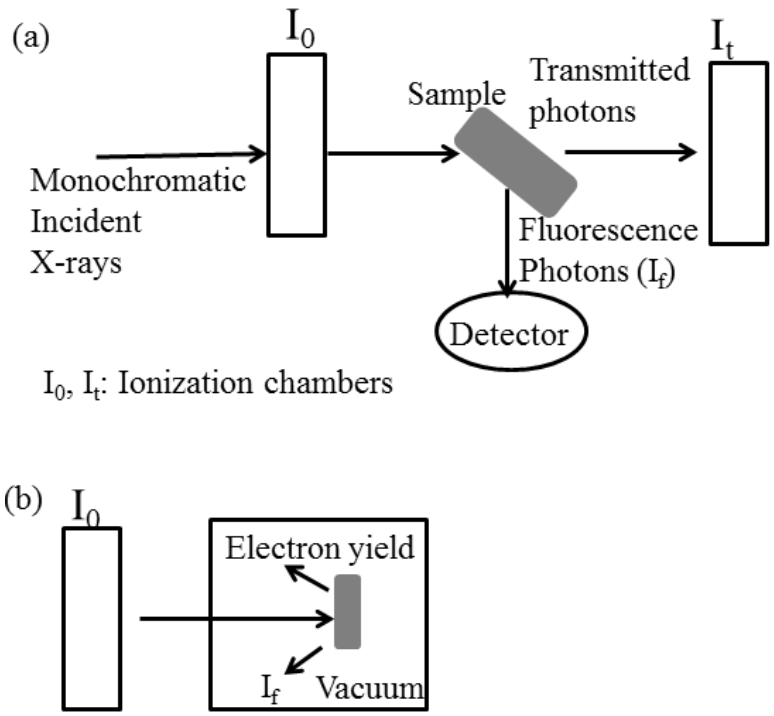

Figure 1.6 Schematic diagram of XAS experimental set-up for different detection methods. (a) For Hard X-ray transmission and fluorescence set-up, the X-ray photon beam from the ionization chamber (I_0) is transmitted through the sample and the transmitted beam is measured using an ionization chamber (I_t). The released fluorescence photons (I_f) are collected using fluorescence detector. (b) Soft X-ray electron yield (EY) experiments are done in vacuum. The incident X-ray photon beam (I_0) interacts with matter and creates a core-hole. The core-hole decays by emission of electrons (EY) and fluorescence photons (I_f). A total electron yield spectrum along with the fluorescence spectrum can be collected simultaneously to get accurate XANES spectra.

1.5.3 An overview on XAS: XANES and EXAFS

X-ray absorption spectroscopy (XAS) is a powerful tool to study the electronic structure and local environment of the element of interest in materials.[121,125] XAS can be applied not only to crystalline but also amorphous systems like glasses, liquids, metalloproteins, nanoscale materials, etc.[121,125,126] Due to its elemental selectivity, XAS has been used in a wide variety of fields such as material sciences, environmental sciences and life sciences.[121,125,126]

In X-ray absorption experiments, a core electron (electron in occupied state) is excited into unoccupied atomic/molecular orbitals above the Fermi level (conduction and/or continuum state) by the absorption of an X-ray photon having sufficient energy to excite the electron.[112,125-127] Since the absorption process is a core electron excitation, the XAS technique is element specific and sensitive to the oxidation state, bonding environment, and local geometry around the absorbing atom.[112,125-127] As the incident photon energy increases, the X-ray absorption coefficient (μ, generally referred as the absorbing power of a material) has been interrupted by a sharp rise when the photon energy that is equal to the binding energy of a core electron shell (K, L, M, etc) for a given absorbing atom (referred to as an absorption-edge).[112,118,125-127] The transitions just below and above the absorption-edge energy region (e.g., ~ 10 eV-30 eV energy range for K-edge spectra) in the spectrum are referred to as X-ray absorption near-edge spectroscopy (XANES). As the scanning energy increases (generally 30 eV above from edge energy) above the absorption-edge energy, the electron enters into a continuum states, and can be back scattered by neighbouring atoms in coordination shells surrounding the absorbing atom, resulting in constructive and destructive interference that creates structured oscillations in the spectrum.[112,118,125-127] These oscillations are from multi-scattering and then single scattering resonances. Multi-scattering resonances overlap with the high-energy region of XANES spectra and can occur due to the multiple scattering events of an excited core-electron with neighbouring atoms. Single scattering resonances occur when the core electron with high kinetic energy and small scattering path-length is back-scattered by neighbouring atoms in a single scattering event. These resonances are referred as extended X-ray absorption fine structure (EXAFS) and are sensitive to the bond distance, coordination number, and identity of the scattering atoms from the absorbing atom.[112,126]

If the excitation of an electron is from a K-shell (i.e., excitation of 1s electrons) then the XAS spectrum is labeled as K-edge. The electronic transitions in the absorption process mainly follows the conservation of angular momentum (i.e., $\Delta l = \pm 1$). In this thesis, the materials have been investigated using K-edge XAS spectra (excitation of 1s electrons) and L-edge XAS spectra (excitation of 2p electrons).[112,118,125-127] Schematic diagram for representative K-edge and L-edge transitions are shown in Figure 1.7a. The L_1-edge consists of 2s→np transitions whereas $L_{2,3}$-edge consists of 2p→(n-1)d transitions. As in K-edge, the prominent transitions are from dipolar transitions (1s→np), however, quadrupolar (i.e., $\Delta l = \pm 2$) transitions (1s→(n-1)d) are also possible in the spectra.[112,118,125-127] The transition metal (i.e., Ti) K-edge XANES spectrum is shown in Figure 1.7b, which consists of a low intensity pre-edge (A) feature (1s→3d; quadrupolar transitions) and very high intensity main edge (B,C) feature (1s→4p; dipolar transitions). The weak intensity pre-edge region (A) probes the d-states of a transition metal and is sensitive to the chemical environment.[128-131] The probability of the quadrupolar transitions (i.e., the intensity of pre-edge peak) can be increased by the addition of dipolar character through the overlap of d- and p-states. The p-d mixing can occur by varying the coordination environment (e.g., octahedral to tetrahedral geometry) of the absorbing atom.[128-131] As illustrated in Figure 1.8a, decreasing the coordination number ($Ti^{[6]} \rightarrow Ti^{[5]} \rightarrow Ti^{[4]}$) can increase the intensity of pre-edge feature (A). Further, the absorption energy of pre-edge peak is sensitive to the oxidation state and CN of an absorbing atom.[128-132] Similar to the pre-edge feature, the high intense main-edge features (B,C) can depend on coordination number, bonding environment, and oxidation state of the metal atom.[121,128-132] Figure 1.8b shows a shift to higher energies in the main-edge region with increasing oxidation state. Unlike other techniques such as diffraction, solid-state NMR or Raman spectroscopy, XANES gives qualitative information on the electronic

structure and bonding environment of the absorbing atom.[118,126] In this work, X-ray absorption spectroscopy experiments have been used to probe the electronic structure of the constituent elements in a material.

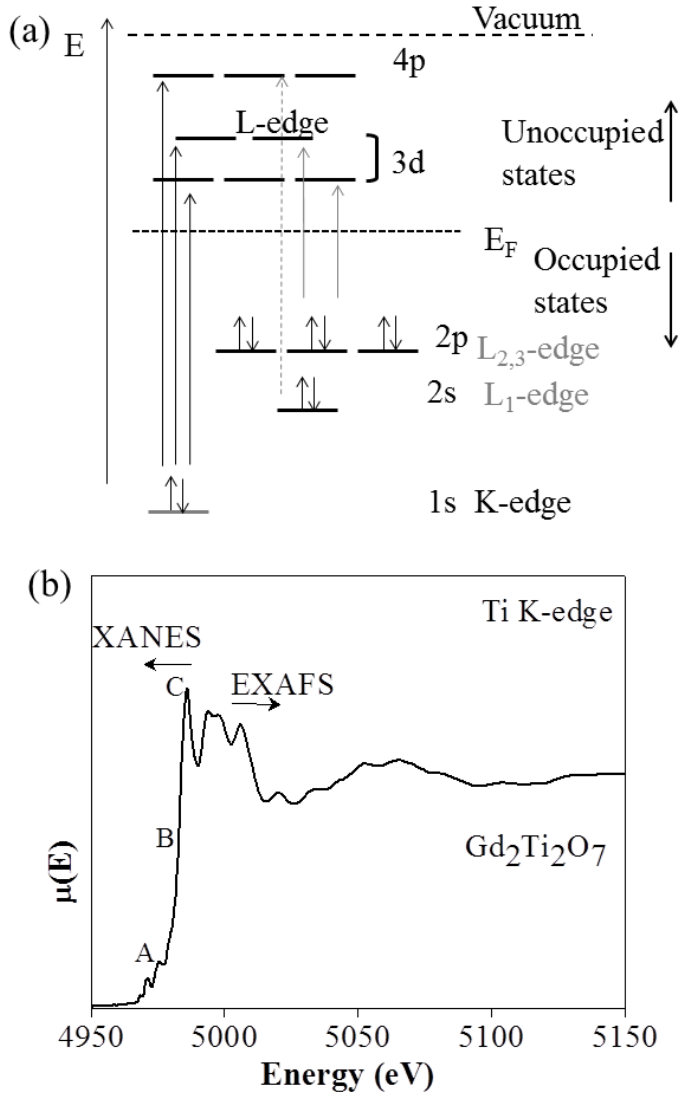

Figure 1.7 (a) A representative energy diagram for K- and L-edge transitions in the XAS process. Metal K-edge transitions not only include dipole allowed 1s→np transitions but also quadrupole transitions (1s→(n-1)d). In the L-edge, the dipole allowed electronic transitions are 2s→np (L_1-edge) and 2p→(n-1)d ($L_{2,3}$-edge). (b) Transition metal (Ti) K-edge XANES along with EXAFS are shown. The XANES spectrum is further divided into pre-edge (A:1s→3d) and main-edge (B,C:1s→np) regions.

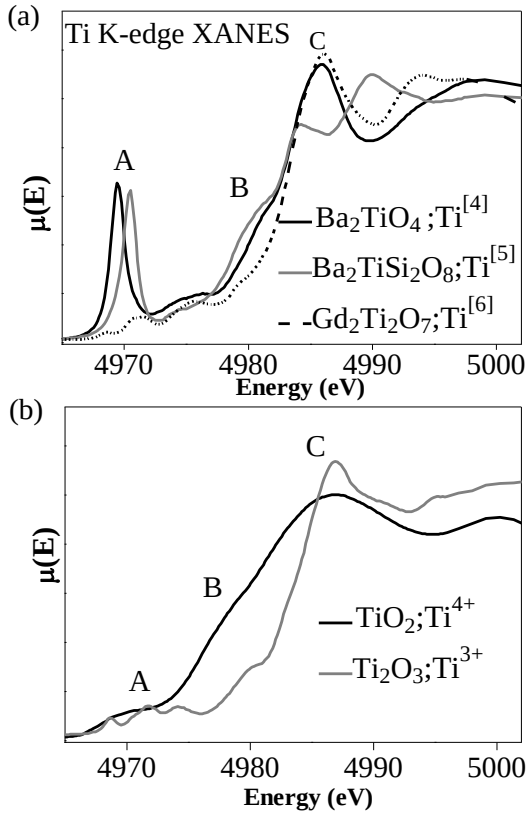

Figure 1.8 (a) Ti K-edge XANES speactra from materials having 4-coordinate, 5-coordinate, and 6-coordinate Ti atoms. The intensity and energy of pre-edge peak (A) are observed to change significantly with varying CN. These changes are also accompanied by changes in the main-edge features (B,C). (b) Ti K-edge XANES speactra from TiO_2 (Ti^{4+})and Ti_2O_3 (Ti^{3+}) are presented. A large high energy shift in main-edge region (B) are observed with increasing the oxidation state of Ti ($Ti^{3+} \rightarrow Ti^{4+}$).

1.5.4 Glancing angle XAS

In order to investigate the resistance to radiation induced structural damage from materials, it is necessary to select a technique that can probe only the damaged surface layer (typically only a few hundred nm) produced by ion beam implantation of a thick material.[86-88,102] Transmission and/or fluorescence methods are generally employed to measure hard X-ray XANES and these measurements are not surface sensitive. The surface sensitivity of these hard X-ray XANES measurements can be achieved using the glancing angle method to probe only the damaged surface layer.[102,133-136] A schematic diagram for a glancing angle XANES (GA-XANES) experimental set-up is shown in Figure 1.9. In a glancing angle experiment, the incident X-ray beam angle (generally called the glancing angle) is set to be just above the critical angle of total reflection in order to selectively probe the surface layer. When the incident X-ray angle is less than the critical angle, total external reflection occurs and X-rays propagate parallel to the surface of the material. Therefore, it is necessary to select the angle just above the critical angle to probe the amorphous surface layer (few hundreds of nm thick) of an implanted surface. Surface sensitivity generally increases with decreasing glancing angle (i.e., the X-ray beam angle of incidence on the surface of a pellet decreases and result in the spectra becoming more surface sensitive).[102,133-136] The monochromatic X-ray beam angle of incidence (θ) and its X-ray attenuation depths depend on the density of a material and the fixed excitation energy (i.e., absorption-edge energy).[134]

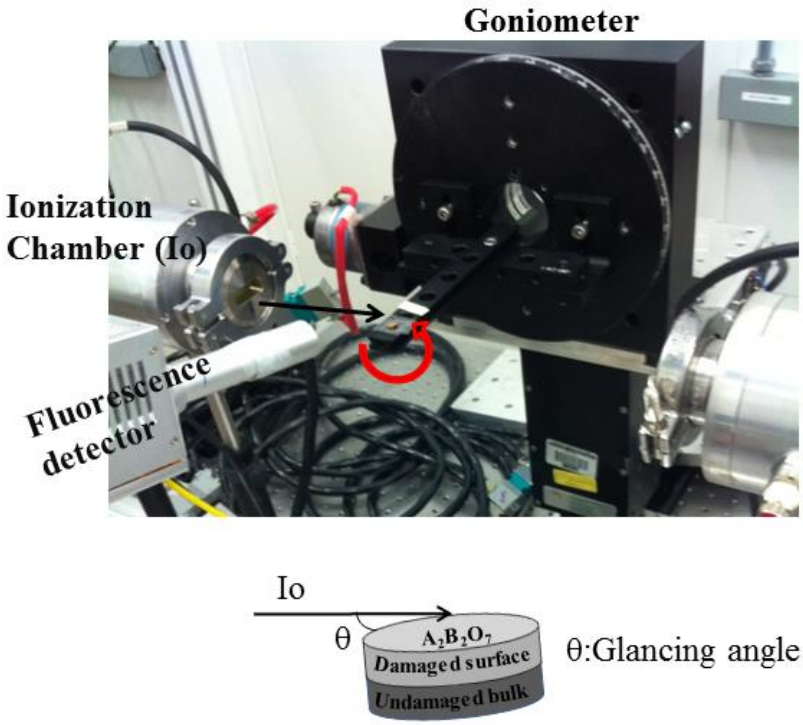

Figure 1.9 Experimental set up for the glancing angle XANES measurements are shown, where the sample (pellet) surface is irradiated with incident X-ray beam (I_0). The X-ray beam angle of incidence (θ) on a surface of a pellet can be achieved by a goniometer (moving motor). The spectra are collected using fluorescence mode because of the thick pellet and because of only wanting to probe the near-surface region.

1.6 Thesis Objectives

In order to develop potential nuclear wasteforms, it is necessary to understand how the changes in electronic and structural properties of a material can influence the chemical durability and its resistance to radiation induced structural damage. The work presented in the thesis was designed to provide this knowledge through the study of pyrochlore-type materials. The initial study of this thesis will focus on investigating the electronic structure and local coordination environment of the stoichiometric and non-stoichiometric pyrochlore-type oxides depending on composition. The later step of this work will contribute to a better understanding of how these electronic properties can affect the structural stability of the materials upon irradiation.

The first objective of this thesis is to investigate the changes in electronic and structural properties (i.e., changes in local coordination environment or changes in the covalency of bonds or changes in the oxidation states) of pyrochlore-type materials depending on composition. The benefit of using XANES in this study is that it allows qualitative insight into slight variations in the electronic properties of the materials resulting from elemental substitution. The composition for pyrochlore-type materials has been deliberately chosen for these investigations, which has not been investigated previously using XANES. Chapter 2 addresses how the reduced A or B-site cations of pyrochlore-type oxides can affect the local coordination environment of the metals and oxygen deficiency of pyrochlore-type oxide system. The $Yb_2Ti_{2-x}Fe_xO_{7-\delta}$ ($0 \leq x \leq 0.2$) series have been investigated in this study to understand how a lower oxidation state cation in the B-site can affect the local CN and oxidation state of the transition metal. Transition metal (Ti and Fe) K- and $L_{2,3}$-XANES spectra were collected and analysed for this study. The next step of this objective was to study how the substitution of metals of different electronegativity can influence the bonding interactions between the metal and oxygen, and this is discussed in Chapter 3. The $Gd_2Ti_{2-x}Sn_xO_7$ ($0 \leq x \leq 2.0$) series has been investigated to study the metal-oxygen bond covalency with increasing Sn substitution. Ti K-, Sn L_3-, Sn K-, and Gd L_3-edge XANES spectra from the $Gd_2Ti_{2-x}Sn_xO_7$ system have been collected and analysed carefully.

After completing the preliminary objective of studying the electronic structure of the pyrochlore-type oxides depending on composition, the next objective of this thesis was to understand the effects of radiation induced structural damage in these materials. The materials were bombarded with high energy Au^- ions to mimic radiation induced structural damage. Various techniques have been previously used to probe the response of the materials upon ion beam implantation,[86,88,89] In this work, surface sensitive glancing angle and total electron yield

XANES experiments have been used to probe only the damaged surface layer of the ion implanted pellets. The benefit of using these techniques is that they provide for a high level of sensitivity to slight atomic distortions resulting from ion beam implantation. Since very few studies have used GA-XANES (and no studies on TEY-XANES) to study the damaged surface layer of materials, the objective of Chapter 4 was to demonstrate how these techniques can be used to investigate the radiation induced damage of the materials.[102,136] $RE_2Ti_2O_7$ (RE (rare-earth)=La-Lu, and Y) was chosen for this purpose to demonstrate the effect of the cationic radii ratio (r_A/r_B) on the structural stability. Ti K-edge TEY-XANES and GA-XANES spectra of $RE_2Ti_2O_7$ were collected and analyzed for this purpose. Chapter 4 has also focused on how oxygen vacancies can affect the resistance of pyrochlore-type oxides to radiation-induced structural damage. Oxygen-deficient $Yb_{1.85}Ca_{0.15}Ti_2O_{7-\delta}$ and $Yb_2Ti_{1.85}Fe_{0.15}O_{7-\delta}$ materials have been examined to investigate the response to ion beam implantation using TEY-XANES and GA-XANES. Through careful analysis and successful demonstration of surface sensitive GA-XANES, Chapter 5 will focus on understanding the effects of metal-oxygen bond covalency on the structural stability of ion implanted $Gd_2Ti_{2-x}Sn_xO_7$ materials using Ti K- and Sn L_3-edge GA-XANES (and GA-EXAFS) spectra.

The final objective of this thesis (Chapter 6) was to combine the pyrochlore-type materials with glasses, and to develop a better understanding of glass-ceramic composite materials with varying composition. The feasibility of producing glass-ceramic materials from borosilicate (and Fe-Al-borosilicate) glass and pyrochlore-type oxides ($Gd_2Ti_2O_7$) has been demonstrated by a simple solid state method at different annealing temperatures. The chemistry and distribution (and also interaction) of ceramic materials within the glasses has been thoroughly investigated by electron microprobe and (Ti K-, Al $L_{2,3}$-edge and Fe K-edge)

XANES. This Chapter also includes an investigation on the response of the ceramic materials within the glass matrix to ion beam implantation.

The thesis work has investigated pyrochlore-type oxides as well as glass-ceramic composites depending on composition and also the stability of these materials upon irradiation. This thesis has also demonstrated the ability of surface sensitive techniques such as GA-XANES/EXAFS and TEY-XANES techniques to probe only the damaged surface layer of ion implanted pellets. These studies will contribute to a better understanding of how the changes in electronic properties can influence the structural stability of the materials after implantation.

Chapter 2

An investigation of pyrochlore-type oxides ($Yb_2Ti_{2-x}Fe_xO_{7-\delta}$) by XANES*

2.1 Introduction

Oxides with the pyrochlore-type structure have been considered for nuclear waste immobilization applications during the last few decades because of their exceptionally high compositional diversity and structural flexibility.[64,79,137,138] The general formula of materials adopting the pyrochlore-type structure can be written as $A_2B_2O_7$ (Space group: $Fd\bar{3}m$) and is shown in Figure 1.1. The structural arrangements were discussed in Section 1.2.3.1. The structure contains a distorted BO_6 octahedra and the A-site is eight coordinate within a distorted cubic polyhedral.[64,75] There are three distinct anion sites within tetrahedral interstices, and one of the anion sites is vacant.[41,64,75] Anti-site disorder between the A- and B-sites can also occur depending on the composition[79,81] The driving force for anti-site disordering in the pyrochlore-type system is generally the relative size of the A- and B-site cations, with a lower A/B radius ratio resulting in greater disorder (other factors can also affect this too; see Section 1.2.3.1).[64,81] Pyrochlore-type materials lend themselves to a wide variety of chemical substitutions at the A and B sites, and the crystal structure can tolerate the presence of O-vacancies to a certain extent.[139-141]

$Yb_2Ti_2O_7$ exhibits remarkable physiochemical properties along with potential applications in different fields.[140-143] The potential for developing chemically durable $Yb_2Ti_2O_7$ and its ability to reduce radiation induced structural damage can be changed by introduction of

* A version of this Chapter has been published. Reprinted with permission from Aluri, E. R.; Grosvenor, A. P. *J. Phys. Chem. Solids* **2013**, 74, 830–836 © 2013 Elsevier Ltd. doi:10.1016/j.jpcs.2013.01.026

O-vacancies.[141,143] According to the charge neutrality condition, O-deficiency can be achieved by the partial substitution of the A^{3+} or B^{4+} cations for metals that have a similar size and lower oxidation state. The number of oxygen vacancies generated by lower oxidation state metal substitution could affect the chemical durability and the resistance to radiation induced damage of a material. The $Yb_2Ti_{2-x}Fe_xO_{7-\delta}$ materials have been examined previously for oxygen ionic conduction applications.[142] In particular, these studies have assumed that only Fe^{3+} is present, even though Fe^{4+} can be stable in some materials.[142,144-146] The investigations of $SrFe_xTi_{1-x}O_{3-\delta}$, $CaFe_xTi_{1-x}O_{3-\delta}$, and $La_{1-x}Sr_xFeO_{3-\delta}$ have shown that Fe substitutes for Ti^{4+}, partly as Fe^{4+} and partly as Fe^{3+}.[144-146] The presence of Fe^{4+} in $Yb_2Ti_{2-x}Fe_xO_{7-\delta}$ would affect the number of O-vacancies present, and the ionic conductivity and the resistance to radiation damage by this material.[147,148] Therefore, it is important to better understand the effect of cation substitution and oxygen deficiency on the local coordination and oxidation state of the metal. The presence of O-defects (O-vacancy; positive charge carriers) in the $Yb_2Ti_{2-x}Fe_xO_{7-\delta}$ system makes the material viable for solid oxide fuel cell applications.[142]

X-ray absorption near-edge spectroscopy (XANES) is a very useful tool to investigate changes in the electronic and crystal structure of materials.[121] It is element-specific, and the coordination number (CN), charge, and bonding of the element of interest with neighboring atoms can be determined through the analysis of the absorption-edge energy and line shape of the spectra.[125] In this Chapter, transition-metal K-edge and $L_{2,3}$-edge XANES spectra have been investigated, providing a chance to assess the local environment around the Fe and Ti centres throughout the whole $Yb_2Ti_{2-x}Fe_xO_{7-\delta}$ series ($0 \leq x \leq 0.2$). Fe K-edge XANES spectra have been collected from this system to examine how the CN and oxidation state varies with Fe content. The oxidation state of Fe in the $Yb_2Ti_{2-x}Fe_xO_{7-\delta}$ system has been examined by comparison to

spectra from $La_{1-x}Sr_xFeO_{3-\delta}$.[149] The change in CN of Fe and Ti is also discussed through the examination of Fe $L_{2,3}$-, Ti K-, and Ti $L_{2,3}$-edge XANES spectra.

2.2 Experimental

2.2.1 Synthesis and X-ray diffraction

The $Yb_2Ti_{2-x}Fe_xO_{7-\delta}$ (x=0.00, 0.05, 0.10, 0.15, 0.20) system was synthesized by a conventional ceramic method.[142] Powders of Yb_2O_3 (Alfa Aesar, 99.9%), TiO_2 (Alfa Aesar, 99.9%), and Fe_2O_3 (Alfa Aesar, 99.945%) were mixed in stoichiometric amounts and pressed uniaxially into pellets at 6 MPa. The pellets were heated in air at 1400 ^oC for 6-12 days, and then quench cooled in air. Intermediate grinding and repelleting of the materials was performed to produce homogeneous materials.

$La_{1-x}Sr_xFeO_{3-\delta}$ (x=0.0, 0.5, 1) samples were synthesized to aid in the interpretation of the Fe K-edge XANES spectra from the $Yb_2Ti_{2-x}Fe_xO_{7-\delta}$ system.[146,149] Stoichiometric amounts of La_2O_3 (Alfa Aesar, 99.99%), $SrCO_3$ (Alfa Aesar, 99%), and Fe_2O_3 (Alfa Aesar, 99.945%) were mixed and heated in air at 1100 ^oC to decompose the carbonate. The resulting powders were pressed uniaxially into pellets at 6 MPa and heated in air at 1300 ^oC over 5 days before being quenched in air. Portions of the samples were also annealed in $O_{2(g)}$ at 1200 ^oC for 4 days and cooled slowly to room temperature over 8 hours to improve the oxygen stoichiometry.

X-ray diffraction (XRD) was performed to confirm that the pyrochlore-type structure had formed. XRD patterns from each sample were collected at room temperature using a PANalytical Empyrean X-ray diffractometer and a Co $K\alpha_{1,2}$ X-ray source operating at 40 kV and 45 mA. Diffraction data was collected in the 2θ range of 10-110^o. The lattice constants were determined

using the HighScore Plus software package.[150] All materials were determined to be phase-pure, except for $Yb_2Ti_{1.80}Fe_{0.20}O_{7-\delta}$.

2.2.2 XANES

2.2.2.1 Fe K-edge XANES

The Fe K-edge XANES spectra from $Yb_2Ti_{2-x}Fe_xO_{7-\delta}$ and $La_{1-x}Sr_xFeO_{3-\delta}$ were collected using the Hard X-ray Micro Analysis (HXMA, 06ID-1) beamline at the Canadian Light Source (CLS).[113] A Si (111) double crystal monochromator was used, and the radiation generated from a superconducting wiggler was detuned to 50% to remove higher harmonics. All spectra were recorded in transmission mode using ionization chambers filled with 100% $N_{2(g)}$ to achieve optimal absorption and signal to noise ratios. The flux was ~10^{12} photons/s and the spectral resolution was 0.7 eV at 7112 eV (Fe K-edge).[113] Energy calibration was performed by simultaneously collecting spectra from a Fe metal foil and fixing the absorption-edge energy to 7112 eV.[151] The data were collected using a 0.15 eV step through the absorption edge. Finely ground powders of the samples were spread on (and sealed between) Kapton tape to perform this experiment. The thickness of the sample was varied by adding or removing layers of the tape to maximize the adsorption-edge step height. Background reduction, normalization, and calibration of all spectra collected in this study was performed using the Athena software program.[152]

2.2.2.2 Ti K-edge XANES

Ti K-edge XANES spectra from the $Yb_2Ti_{2-x}Fe_xO_{7-\delta}$ system was measured using the Soft X-ray Microcharacterization Beam line (SXRMB, 06B1-1) at the CLS.[153] A Si(111) monochromator was used, providing a photon flux of >10^{11} photons/s and a resolution of 0.5 eV at 4966 eV (Fe K-edge). Samples were prepared by placing finely ground powders on carbon tape. The spectra were calibrated against the K-edge spectrum from Ti metal with a set

absorption-edge energy of 4966 eV.[151] Total electron yield (TEY) spectra were collected using a step size of 0.2 eV through the absorption-edge.

2.2.2.3 Ti $L_{2,3}$- and Fe $L_{2,3}$-edge XANES

The Ti $L_{2,3}$-edge and Fe $L_{2,3}$-edge spectra from $Yb_2Ti_{2-x}Fe_xO_{7-\delta}$ were recorded at the CLS using the Spherical Grating Monochromator (SGM) undulator beam line 11ID-1.[115] The flux is ~10^{11} photons/s at 1900 eV and increases to 10^{12} photons/s at 250 eV. The resolution of the beamline is 0.2 eV at 706.8 eV (Fe L_3-edge) and 0.1 eV at 453.8 eV (Ti L_3-edge).[115] Finely ground samples were spread on carbon tape prior to measurement. The spectra were collected simultaneously in both total fluorescence yield (TFY) and TEY modes. The spectra were collected from 30 eV below the absorption edge to 50 eV (Ti) or 70 eV (Fe) above the edge. The data were collected using a step size of 0.10 eV (Fe $L_{2,3}$-edge) and 0.05 eV (Ti $L_{2,3}$-edge) through the absorption-edge. The Fe L_3-edge spectra were calibrated using Cr metal powder as a standard with an L_3-edge energy of 543.1 eV, and the Ti L_3-edge spectra were calibrated against the L_3-edge spectrum from Ti metal with a set absorption-edge energy of 453.8 eV.[151] TFY spectra of Cr and Ti metal powders were used for calibration due to the surface sensitivity of TEY spectra, and the influence of surface oxidation.

2.3 Results and Discussion

2.3.1 Structure

Powder XRD was performed to gain information about the crystal structure of $Yb_2Ti_{2-x}Fe_xO_{7-\delta}$, and to determine how the lattice parameters of the unit cell changed depending on composition. The XRD patterns from these materials (Figure 2.1) compared well to the calculated pattern produced using the crystal structure of $Yb_2Ti_2O_7$, which has the pyrochlore-type structure.[154] All samples were pure-phase, except for $Yb_2Ti_{1.80}Fe_{0.20}O_{7-\delta}$. Small

amounts of Fe_2O_3 and Yb_2O_3 impurities were detected in the powder XRD pattern from $Yb_2Ti_{1.80}Fe_{0.20}O_{7-\delta}$ and suggests that the limit of Fe solubility in the $Yb_2Ti_{2-x}Fe_xO_{7-\delta}$ system occurs when $x<0.2$. However, these phase impurities are not considered to be large enough to adversely influence the XANES spectra. It was found that the lattice constant decreased slightly upon substitution of Fe in the $Yb_2Ti_{2-x}Fe_xO_{7-\delta}$ system (Table. 2.1). It might be expected that the lattice constants would increase if Fe^{3+} replaced Ti^{4+}, if the ionic radii of 6-coordinate Fe^{3+} (0.645Å) and Ti^{4+} (0.585Å) were compared.[155] The observed slight decrease in the lattice constant was first assumed to be a result of the presence of Fe^{4+} (r_{Fe4+}=0.585Å), but it was later determined to be a result of the decrease in the CN of Ti^{4+} and Fe^{3+} with increasing Fe incorporation after examination of the Fe K-edge XANES spectra (*vide infra*).[155]

As stated earlier, anti-site disorder can influence the site occupancies of the metal sites. However, previous studies of $Yb_2Ti_2O_7$ have shown that the amount of anti-site disorder experienced in this material is low (~4.5% of Ti atoms were found in the Yb site).[141,154,156] Generally, a decrease in the intensity of the super structural reflections (e.g., (311), (331)) in the powder XRD patterns is indicative of anti-site disorder in compounds adopting the pyrochlore-type structure.[154] In the case of $Yb_2Ti_{2-x}Fe_xO_{7-\delta}$, the intensity ratio of the super structural peaks ((311) or (331)) to the (222) reflection was found to remain relatively constant regardless of the Fe concentration (including when x=0). This suggests that the amount of anti-site disorder present is low in the $Yb_2Ti_{2-x}Fe_xO_{7-\delta}$ systems, and relatively invariant.

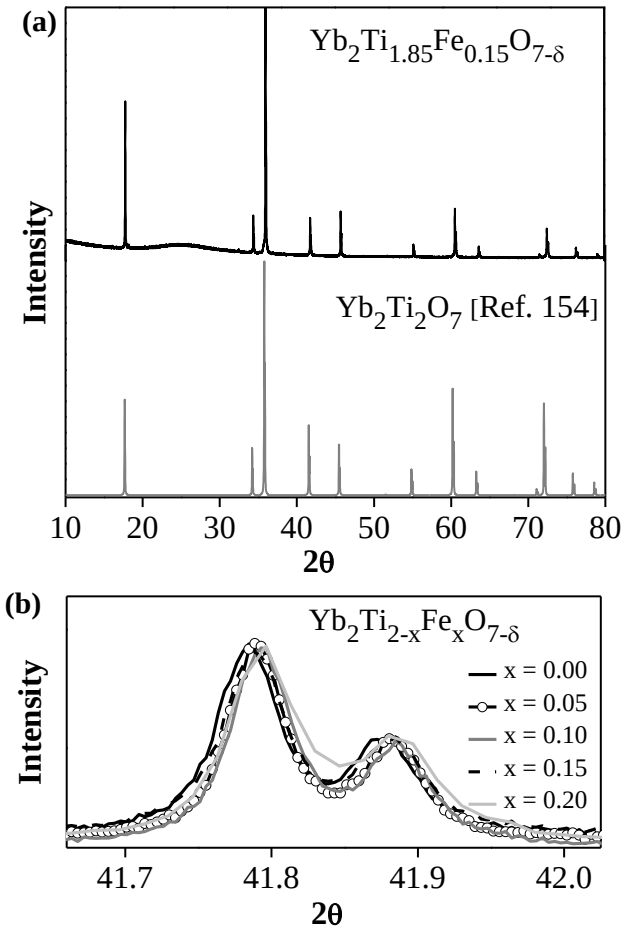

Figure 2.1 (a) A powder XRD pattern from phase pure $Yb_2Ti_{1.85}Fe_{0.15}O_{7-\delta}$ is shown and the lattice constants are calculated from the pattern produced using the crystal structure of $Yb_2Ti_2O_7$.[154] (b). The (400) reflections from the $Yb_2Ti_{2-x}Fe_xO_{7-\delta}$ series ($0.00 \leq x \leq 0.20$) are shown. The diffraction peaks shift very slightly to higher 2θ with increasing Fe incorporation.

Table 2.1 Lattice parameters from the $Yb_2Ti_{2-x}Fe_xO_{7-\delta}$ system.

$Yb_2Ti_{2-x}Fe_xO_{7-\delta}$	
x	a (Å)
0.00	10.0302(1)
0.05	10.0283(1)
0.10	10.0270(1)
0.15	10.0268(1)
0.20	10.0267(5)

2.3.2 Fe K-edge XANES

XANES is sensitive to the oxidation state and local order around an absorbing atom, and has been widely used to analyze the structure and electronic properties of materials.[121,125] The normalized Fe K-edge spectra from $Yb_2Ti_{2-x}Fe_xO_{7-\delta}$ are shown in Figure 2.2. The spectra can be subdivided into two regions, the pre-edge region (feature A) and the main edge region (features B and C). All three features change in intensity or energy in a systematic way as the CN is changed.[130,157,158] As will be discussed below by comparison to the spectra from $La_{1-x}Sr_xFeO_{3-\delta}$, the spectral changes observed in Figure 2.2 are not due to a change in the Fe oxidation state.

The pre-edge peak (feature A) results from the excitation of 1s electrons to 3d states.[128,157,159,160] Since this is a quadrupolar transition, it is much less intense than the higher energy dipolar transition.[157] The intensity of the pre-edge peak increases upon substitution of Fe for Ti and is a result of a decrease in CN. As the CN decreases, inversion symmetry is lost and the metal 4p states mix with 3d states, which provides some dipole allowed character to the transition and leads to an increase in the intensity of the pre-edge peak.[128,129,146,157] The more

intense main-edge region (features B and C in Figure 2.2) located at higher energy than the pre-edge region results from the dipolar transition of 1s electrons to 4p states.[127,161] The energy of feature B (and C) can shift because of changes in CN and/or oxidation state.[133,161] Feature B (and C) can shift to higher energy with increasing oxidation because of reduced screening of the nuclear charge. Fewer electrons are available to screen the nuclear charge with increasing oxidation state, requiring more energy to remove core electrons.[133,161] Feature B can also shift because of a change in CN. For example, a lower CN results in greater final state relaxation effects because of the presence of fewer electrons in the first coordination-shell that are available to screen the core-hole, which leads to a shift down in absorption energy.[130,131] Feature C results from a dipolar transition of 1s electrons to 4p states that are hybridized with O 2p states and changes with CN.[130,131,158] As the CN decreases, the number of Fe 4p-O 2p final states available for 1s electrons to be excited to also decreases, resulting in a decrease in the intensity of feature C.[130,131,162,163] (This feature can also shift in energy because of a change in oxidation state.)

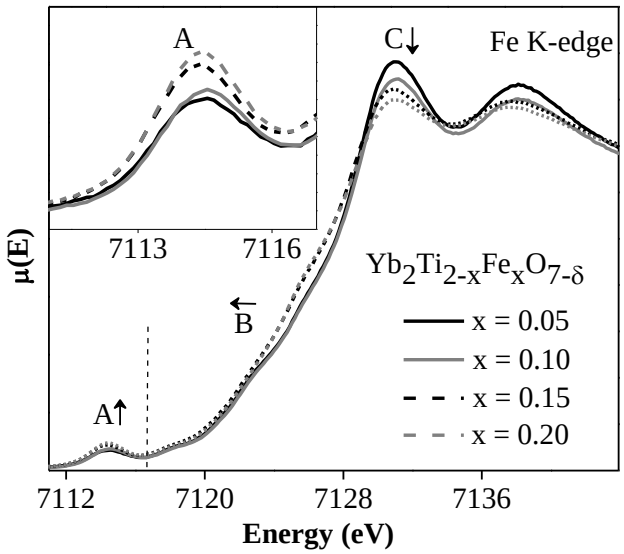

Figure 2.2 Fe K-edge XANES spectra from the $Yb_2Ti_{2-x}Fe_xO_{7-\delta}$ system. Feature A represents the pre-edge region and arises from 1s→3d excitations. Features B and C represent the main-edge region and result from 1s→4p transitions. (The separation between the pre- and main-edge regions is represented by a dashed-line.) The pre-edge region (Feature A) of the spectra from $Yb_2Ti_{2-x}Fe_xO_{7-\delta}$ is shown in the inset. The changes in intensity or energy of features A, B and C with increasing Fe content are marked by arrows.

The oxidation state of Fe in $Yb_2Ti_{2-x}Fe_xO_{7-\delta}$ was studied by comparing the Fe K-edge spectra to those from $La_{1-x}Sr_xFeO_{3-\delta}$ annealed in $O_{2(g)}$ (Figure 2.3 and 2.4).[146,164] In the $La_{1-x}Sr_xFeO_{3-\delta}$ series, the intensity and absorption energy of the three features (A, B and C) found in the Fe K-edge XANES spectra vary with composition. A systematic shift of the pre-edge peak (feature A) by ~0.5 eV was observed in the Fe K-edge spectra from $La_{1-x}Sr_xFeO_{3-\delta}$ as Sr^{2+} was substituted for La^{3+} (Figure 2.3). Previous examinations of the pre-edge region of Fe K-edge XANES spectra have shown that the energy of this feature shifts because of variations in Fe oxidation state and that it is not affected by changes in CN, unlike the Ti K-edge pre-edge peak (*vide infra*).[128-130,165] The shift in energy of the pre-edge peak in the Fe K-edge spectra from

$La_{1-x}Sr_xFeO_{3-\delta}$ is a result of the increased oxidation state of Fe (from Fe^{3+} to Fe^{4+}) with greater Sr^{2+} incorporation. The intensity of feature A was also observed to increase with greater Sr^{2+} incorporation, suggesting that the material is oxygen deficient and that not all Fe^{3+} is oxidized to Fe^{4+} (i.e., the Fe CN decreases with greater Sr incorporation).[144,147] Features B and C (Figure 2.3) were also observed to shift to higher energy with increasing Sr content, which is expected if the oxidation state of Fe increases.[165]

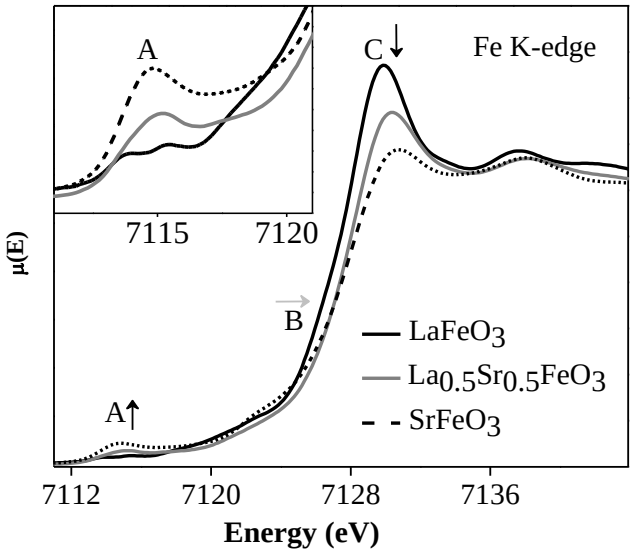

Figure 2.3 Fe K-edge XANES spectra from the $La_{1-x}Sr_xFeO_{3-\delta}$ system. Feature A represents the pre-edge region and arises from 1s→3d excitations. Features B and C represent the main-edge region and result from 1s→4p transitions. (The separation between the pre-edge and main-edge regions is represented by a dashed-line.) The pre-edge region is shown in the inset. Arrows mark the changes observed in the spectra with increasing Sr content.

The pre-edge peak positions from the spectra from the $Yb_2Ti_{2-x}Fe_xO_{7-\delta}$ series were compared to the pre-edge peak energies from the $O_{2(g)}$-annealed $LaFeO_3$ and $SrFeO_3$ samples

(*cf.* Figure 2.4). The centroid of the pre-edge peak for all $Yb_2Ti_{2-x}Fe_xO_{7-\delta}$ compositions was in good agreement with that for $LaFeO_3$, implying that all Fe ions have a 3+ oxidation state in this pyrochlore-type system. As has been explained earlier, the increase in intensity of feature A and the decrease in intensity of feature C in the Fe K-edge spectra from $Yb_2Ti_{2-x}Fe_xO_{7-\delta}$ (Figure 2.3) with increasing Fe incorporation implies that the Fe CN decreases. The shift of feature B to lower energy with increasing Fe content is also a result of a decrease in the CN of Fe with increasing Fe content.[130,131]

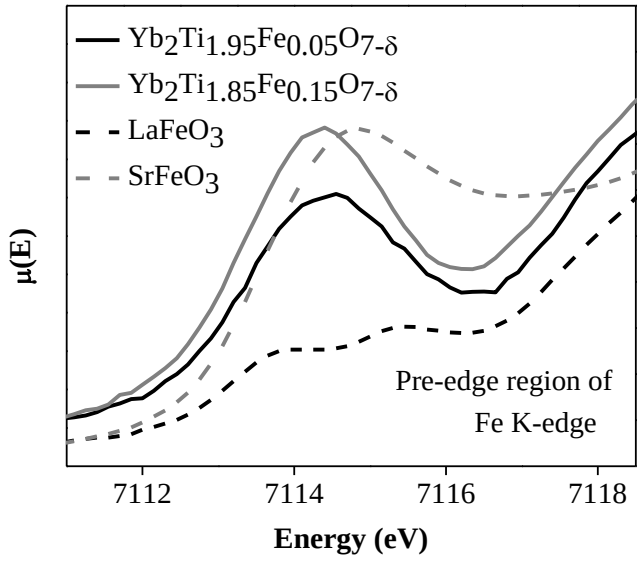

Figure 2.4 The pre-edge region from the Fe K-edge XANES spectra for $Yb_2Ti_{2-x}Fe_xO_{7-\delta}$ (x=0.05, 0.10), $LaFeO_3$, and $SrFeO_3$ are presented. The centroid of the pre-edge peak for all $Yb_2Ti_{2-x}Fe_xO_{7-\delta}$ compositions coincides with that of $LaFeO_3$.

2.3.3 Fe $L_{2,3}$-edge XANES

Fe $L_{2,3}$-edge XANES spectra were collected to better understand how the Fe CN changes in the $Yb_2Ti_{2-x}Fe_xO_{7-\delta}$ system depending on substitution. According to dipole selection rules, the

Fe $L_{2,3}$ absorption edges correspond to excitations of Fe 2p core level electrons into unoccupied Fe 3d or 4s states, although the 2p→3d excitations dominate.[166] The intensity, peak shape, and energy of the metal $L_{2,3}$ absorption edge is sensitive to the chemical environment, valence state, crystal-field splitting energy, and electronic effects (multiplet effects).[166-169] The Fe L_3-edge XANES spectra are shown in Figure 2.5. The line shape and energy of the Fe L_3-edge spectrum from $Yb_2Ti_{1.95}Fe_{0.05}O_{7-\delta}$ is very similar to that from Fe_2O_3, confirming that Fe has a 3+ oxidation state.[166] When Fe^{3+} is in an octahedral environment, feature D is a result of excitations to 3d t_{2g} states while feature E results from excitations to 3d e_g* states.[171-173] The intensity of these two features changes upon changing CN.[169,174,175] As Fe^{3+} goes from occupying an octahedral environment to a tetrahedral environment, the ratio of unoccupied 3d states changes from 3:2 (t_{2g}:e_g^*; low energy:high energy) to 2:3 (e:t_2^*). This change in distribution of unoccupied 3d states results in a decrease in intensity of peak D and an increase in intensity of peak E.[175] The decrease in intensity of feature D and the increase in intensity of feature E in the spectra presented in Figure 2.5 with increasing Fe incorporation in $Yb_2Ti_{2-x}Fe_xO_{7-\delta}$ imply that the Fe CN decreases with greater x. This suggestion is further corroborated by the shift of feature E to lower energy by ~0.1 eV as Fe was substituted for Ti in $Yb_2Ti_{2-x}Fe_xO_{7-\delta}$. This shift is attributed to the lower crystal field splitting energy of 3d states in a tetrahedral geometry *vs.* when Fe is in octahedral environment.[176] These observations indicate that the average CN of Fe decreases from 6 to a mixture of 4 and 6 with greater Fe content (*i.e.*, the Fe L_3-edge results are in good agreement with the Fe K-edge spectra).

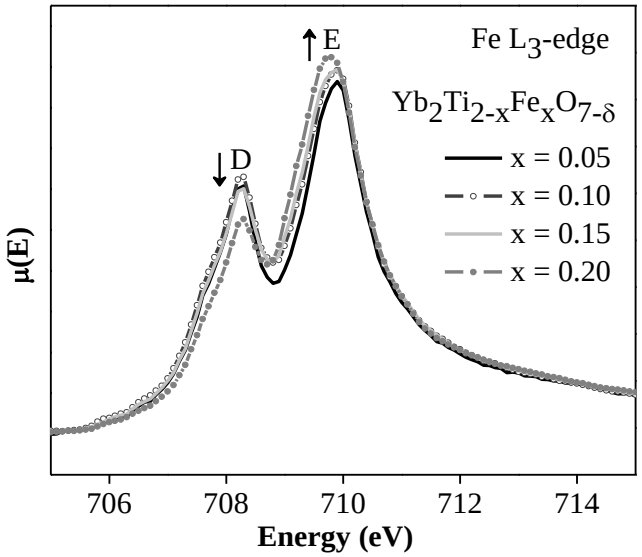

Figure 2.5 Fe L_3-edge XANES spectra from the $Yb_2Ti_{2-x}Fe_xO_{7-\delta}$ series. The changes in intensity of features D and E with increasing Fe content are marked by arrows.

2.3.4 Ti K-edge XANES

The normalized Ti K-edge spectra from $Yb_2Ti_{2-x}Fe_xO_{7-\delta}$ ($0 \leq x \leq 0.2$) are shown in Figure 2.6 and contain both pre-edge ($1s \rightarrow 3d$) and main-edge ($1s \rightarrow 4p$) excitations.[159,177] Three features are observed in the pre-edge region (A_1, A_2 and A_3), and result from excitations to crystal field split 3d states as well as non-local excitations.[176] When Ti is in a 6-coordinate environment, the first peak (A_1) results from a $1s \rightarrow 3d\text{-}t_{2g}$ excitation while feature A_2 results from a $1s \rightarrow 3d\text{-}e_g^*$ excitation. The third peak (A_3) is a result of a non-local (intersite hybrid) excitation, which results from a transition of 1s electrons to 3d states of a next-nearest neighbour transition metal through O 2p-states and the Ti 4p-states of the absorbing atom.[161]

The intensity and energy of feature A_2 in the pre-edge region of the Ti K-edge spectra from $Yb_2Ti_{2-x}Fe_xO_{7-\delta}$ (*Inset* of Figure 2.6) changes with increasing x. The increase in intensity is

a result of a decrease in the Ti CN.[129,131,178,179] The pre-edge intensity changes for the same reasons provided above when discussing the Fe K-edge XANES spectra (Section 3.2).[129,131,157,178] The small shift of feature A_2 to lower energy with increasing Fe incorporation is a result of greater final-state relaxation resulting from a change in the screening of the final state core-hole with decreasing CN.[129,159,178,179] The absolute reason for the shifts in energy of the pre-edge peaks observed in the Ti K-edge spectra but not in Fe K-edge spectra is not known, but it may be due to the poorer screening of the core-hole by the empty Ti 3d states compared to that of half-filled Fe 3d states.[160,165]

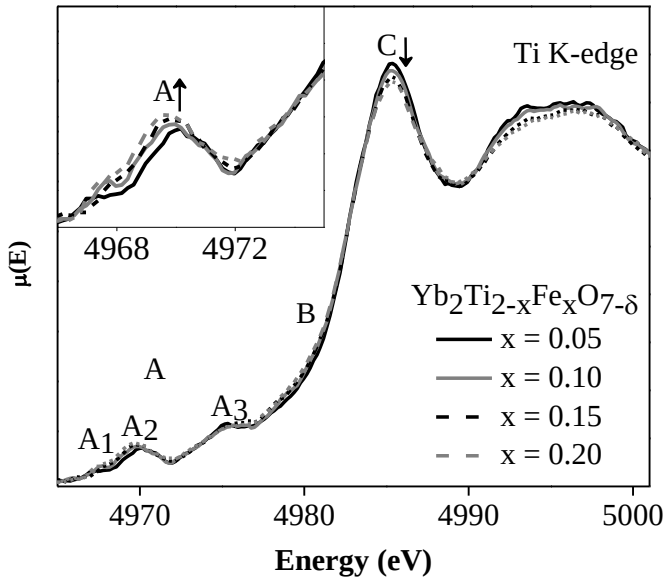

Figure 2.6 Ti K-edge spectra from the $Yb_2Ti_{2-x}Fe_xO_{7-\delta}$ series. Feature A represents the pre-edge region, and features B and C represents the main-edge region. An expanded view of the pre-edge region is shown in the inset.

The main-edge absorption peak (features B and C) results from a dipolar transition of 1s electrons to 4p states.[161,177] The decrease in intensity and energy of the main-edge with increasing Fe incorporation is a result of a decrease in the Ti CN. These changes occur for

similar reasons described about with respect to the Fe K-edge XANES spectra (Section 2.3.2).[158,162,163,169]

2.3.5 Ti $L_{2,3}$-edge XANES

Ti $L_{2,3}$-edge spectra were also collected from the $Yb_2Ti_{2-x}Fe_xO_{7-\delta}$ series to probe the Ti CN. The Ti L_3-edge XANES spectra are shown in Figure 2.7 and result primarily from 2p→3d excitations.[170,180] The spectral peaks are broadened by final-state interactions, including multiplet interactions.[170,181] The splitting of the most intense peaks is due to the crystal field splitting of Ti 3d states.[180] Assuming that Ti has an octahedral coordination in $Yb_2Ti_2O_7$, the Ti 3d t_{2g} orbitals are not involved in bonding and this gives rise to a single sharp peak in the L_3-edge (Feature D in Figure 2.7). If the TiO_6 octahedra are distorted, as is the case in $Yb_2Ti_2O_7$, then this results in the splitting of the e_g^* states into nondegenerate states, which leads to the asymmetric e_g^* peak (feature E) that is shown in Figure 2.7.[182-184] To understand how the Ti CN changes with Fe incorporation in $Yb_2Ti_{2-x}Fe_xO_{7-\delta}$, the Ti L_3-edge spectra can be compared to previously reported spectra from systems having well defined Ti coordination environments.[180] If the intensity ratio of features D and E is large (D:E ~1:3), then this is indicative of the presence of Ti having a CN of 5; however, the D:E intensity ratio is much smaller when the CN is 6 or 4.[180] The line shape and intensity ratio (~ 1:1) of features D and E from the Ti L_3-edge presented in Figure 2.7 is indicative of either 6-coordinate Ti or Ti having both 4- and 6-coordinate environments (i.e., no 5-coordinate Ti appears to be present). As the coordination environment of Ti is reduced from octahedral to tetrahedral, the ratio of unoccupied 3d states (D:E) changes from 3:2 (t_{2g}:e_g^*) to 2:3 (e:t_2^*). As shown in Figure 2.7, the decrease in intensity of feature D with greater Fe incorporation in the $Yb_2Ti_{2-x}Fe_xO_{7-\delta}$ series (and the more symmetric nature of feature E) implies that the Ti CN decreases from 6 to a mixture of 4 and 6.[180,183,185] This explanation is further

verified by the shift of feature E to lower energy with greater Fe incorporation. This shift in energy is a result of the lower crystal field splitting energy of Ti^{4+} when it is in a tetrahedral environment compared to an octahedral environment. These observations indicate that the Ti CN decreases with greater Fe incorporation in $Yb_2Ti_{2-x}Fe_xO_{7-\delta,}$ and are consistent with the Ti K-edge spectra presented above.

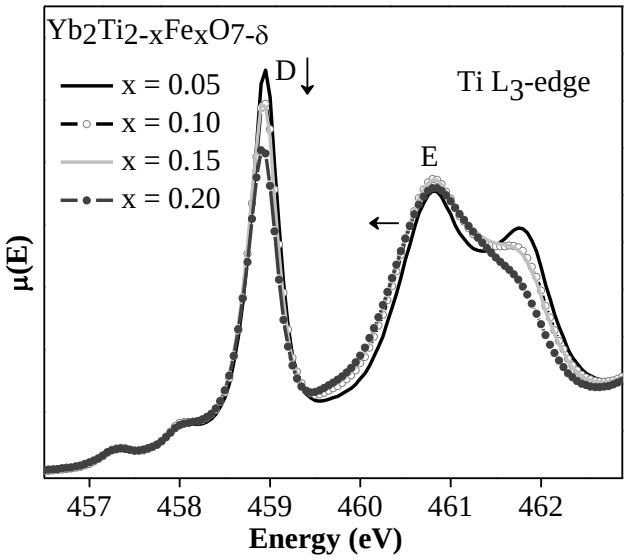

Figure 2.7 Ti L_3-edge XANES spectra from $Yb_2Ti_{2-x}Fe_xO_{7-\delta.}$ The arrows show the change in intensity of feature D and the change in energy of feature E that occurs as Fe substitutes for Ti.

2.4 Conclusions

The $Yb_2Ti_{2-x}Fe_xO_{7-\delta}$ system was synthesized by a solid state reaction and the phase purity and lattice parameters were analyzed using powder XRD. A slight decrease in the unit cell with greater Fe content was observed in the $Yb_2Ti_{2-x}Fe_xO_{7-\delta}$ series. These systems were thoroughly studied by XANES to investigate the change in oxidation state and CN of the transition-metals upon substitution of Fe. Examination of Fe K-edge XANES spectra revealed that Fe adopts an oxidation state of 3+ rather than 4+ in $Yb_2Ti_{2-x}Fe_xO_{7-\delta}$, and that the CN of Fe decreases with

greater x. The decrease in CN of Fe from ~6 to between 6 and 4 with increasing Fe content was observed by the investigation of Fe L_3-edge spectra from $Yb_2Ti_{2-x}Fe_xO_{7-\delta}$. Analysis of Ti K- and L_3-edge XANES spectra from $Yb_2Ti_{2-x}Fe_xO_{7-\delta}$ revealed that the Ti CN decreases with greater Fe incorporation. These spectra also showed that Ti appears to be present in 6- and 4-coordination environments but not in a 5-coordination environment. The presence of only Fe^{3+} in this system allows the chemical formula to be written as $Yb_2Ti_{2-x}Fe_xO_{7-x/2}$. A greater understanding of these oxygen deficient materials has been achieved, which will be useful if they are to be developed for solid oxide fuel cell and/or nuclear waste immobilization applications.

Chapter 3

An X-ray absorption spectroscopic study of the effect of bond covalency on the electronic structure of $Gd_2Ti_{2-x}Sn_xO_7$*

3.1 Introduction

The titanate and stannate pyrochlores have a wide range of technologically important properties, which are related to their remarkable compositional diversity and structural flexibility.[64,79,137,141,186,187] These compounds can exhibit resistance to radiation induced structural damage, making them useful for nuclear waste sequestration applications.[87,88,188] Systematic ion beam irradiation studies of rare-earth titanate and stannate pyrochlores have demonstrated the importance of the electronic structure and metal-oxygen bond interactions to the ability of these materials to resist radiation induced structural damage.[87-89,188] Investigations of $Y_2Ti_{2-x}Sn_xO_7$ and $La_2(Sn,Ti)_2O_7$ have shown that the resistance to radiation induced amorphization appears to increase with greater Sn substitution.[65,189] $Gd_2Ti_{2-x}Sn_xO_7$ compounds have also been found to exhibit fast ionic conduction, making them viable in solid oxide fuel cells.[79,137] Studies of $Gd_2Ti_{2-x}Sn_xO_7$ (and $Y_2Ti_{2-x}Sn_xO_7$) have suggested that the high ion conductivity is due the presence of anti-site disorder, as is found in $Gd_2Ti_{2-x}Zr_xO_7$.[79,190] This is expected due to the similar ionic radii of Gd (and Y) and Sn cations.[79,186] However, Rietvield analysis of powder XRD and powder neutron data from $Gd_2Ti_{2-x}Sn_xO_7$ and $Y_2Ti_{2-x}Sn_xO_7$ have shown that there is no significant anti-site disorder in stannate materials, which has been ascribed to the covalent character of the Sn-O interactions.[89,191] The presence of Sn-O covalent bond interactions has been shown to lead to the lattice adopting an ordered pyrochlore structure rather than the disordered defect fluorite structure, which would affect the resistance to radiation

* A version of this Chapter has been published. Reprinted with permission from Aluri, E. R.; Grosvenor, A. P. *Phys. Chem. Chem. Phys.* **2013**, *15*, 10477. © 2013 The Royal Society of Chemistry doi: 10.1039/c3cp51250a

induced structural damage of these materials.[89,191] Therefore, it is important to understand how the substation of elements having different electronegativity values influence the bonding interactions between metal and oxygen.

X-ray absorption near-edge spectroscopy (XANES) is a technique that can be used to study changes in the electronic structure and local environment of atoms within a material because of variations in bond length and covalency of metal-oxygen bonds upon substitution.[121,125] XANES is also sensitive to changes in the local coordination environment of atoms in materials.[159,192,193] For example, in the previous Chapter, it was shown that the coordination number (CN) of both Ti and Fe decreases in $Yb_2Ti_{2-x}Fe_xO_7$, which adopts the pyrochlore-type structure, as Fe^{3+} replaces Ti^{4+}. In the current Chapter, XANES spectra from the Ti K-, Sn L_3-, Sn K-, and Gd L_3-edges have been collected to investigate how the electronic structure changes upon varying Sn content in the $Gd_2Ti_{2-x}Sn_xO_7$ system ($0 \leq x \leq 2$). Partial density of states (DOS) calculations have also been performed for $Y_2Ti_{2-x}Sn_xO_7$ to aid in the interpretation of the Sn L_3- and Ti K-edge XANES spectra. Additionally, Sn L_3- and Ti K-edge spectra from $Y_2Ti_{2-x}Sn_xO_7$ have been examined to confirm these calculations.

3.2 Experimental

3.2.1 Synthesis

The $Gd_2Ti_{2-x}Sn_xO_7$ ($x = 0.0, 0.5, 1.0, 1.5, 2.0$) materials were synthesized by the ceramic method. Gd_2O_3 (Alfa Aesar, 99.99%), TiO_2 (Alfa Aesar, 99.9%), and SnO_2 (Alfa Aesar, 99.9%) powders were mixed in stoichiometric amounts and pressed into pellets uniaxially at 6 MPa. These pellets were placed in aluminum crucibles and heated in air at 1400^{o}C over 9 days with intermediate grinding and pelleting until phase-pure materials were formed. All materials were

quench cooled in air. The $Y_2Ti_{2-x}Sn_xO_7$ (x = 0.0, 1.0, 2.0) and $La_2Sn_2O_7$ samples were synthesized using the ceramic method as described above to support the interpretation of the XANES spectra. Stoichiometric amounts of Y_2O_3 (Alfa Aesar, 99.99%), TiO_2 (Alfa Aesar, 99.9%), and SnO_2 (Alfa Aesar, 99.9%) were used in the synthesis of $Y_2Ti_{2-x}Sn_xO_7$, and La_2O_3 (Alfa Aesar, 99.99%) and SnO_2 (Alfa Aesar, 99.9%) powders were mixed in stoichiometric amounts to prepare $La_2Sn_2O_7$. The phase purity of all samples was confirmed by powder X-ray diffraction (XRD). Powder XRD patterns from each sample were collected using a PANalytical Empyrean X-ray diffractometer and a Cu $K\alpha_{1,2}$ X-ray source operating at 45 kV and 40 mA. The lattice constants from the $Gd_2Ti_{2-x}Sn_xO_7$ and $Y_2Ti_{2-x}Sn_xO_7$ systems were determined using the HighScore Plus Software package and were found to increase linearly with greater Sn content, in agreement with Vegard's law.[150,194]

3.2.2 XANES

The Ti K-, Sn L_3-, Sn K- and Gd L_3-edge XANES spectra from $Gd_2Ti_{2-x}Sn_xO_7$ were collected using the Pacific Northwest Consortium/X-ray Science Division Collaborative Access Team (PNC/XSD-CAT, Sector 20) bending magnetic beamline (20BM) located at the Advanced Photon Source (APS), Argonne National Laboratory.[195] Additionally, Sn L_3- and Ti K-edge XANES spectra from the $La_2Sn_2O_7$ and $Y_2Ti_{2-x}Sn_xO_7$ (x = 0.0, 1.0 and 2.0) samples were also collected. A Si (111) double crystal monochromator with harmonic rejection was used, providing a photon flux of $\sim 10^{11}$ photons/s. The spectral resolution is 0.5 eV at 3929 eV (Sn L_3-edge), 0.7 eV at 4966 eV (Ti K-edge), 1.0 eV at 7000 eV (Gd L_3-edge), and 4.1 eV at 29200 eV (Sn K-edge).[151,195] The spectra were recorded in transmission mode using ionization chambers filled with $He_{(g)}$ and $N_{2(g)}$ (70%:30% for the Ti K-edge; 80%:20% for the Sn L_3-edge; and 0%:100% for the Gd L_3- and Sn K-edges) to achieve optimal absorption edge step heights and signal to

noise ratios. The fluorescence yield spectra were collected using either a 13-element Ge detector ($Gd_2Ti_{2-x}Sn_xO_7$) or a single element Vortex detector ($Y_2Ti_{2-x}Sn_xO_7$ and $La_2Sn_2O_7$). Only the spectra collected in transmission mode are reported here. Samples were prepared by finely grinding the materials and sealing the powder between layers of Kapton tape. The thickness of these samples was varied by adding or removing layers of powder between tape to maximize the absorption-edge step height.

XANES data were collected using a 0.15 eV per step through the Ti K-, Sn L_3-, and Gd L_3-edges, and 1.5 eV per step through the Sn K-edge. Energy calibrations were performed by simultaneously collecting spectra from the respective metal and metal oxides, and setting the edge energies to known values. The Ti K-edge spectra were calibrated using Ti metal (4966 eV), the Sn L_3-edge spectra were calibrated using Sn metal (3929 eV), and the Sn K-edge spectra were also calibrated using Sn metal (29200 eV).[151] The Gd L_3-edge spectra were calibrating using Gd_2O_3 (7243 eV) and the absorption-edge energy of Gd_2O_3 was determined by calibrating the spectrum from this oxide using Fe metal foil, which has an absorption-edge energy of 7110 eV.[151] Calibration and normalization of all of the spectra analysed was performed using the Athena software program.[152]

3.2.3 Electronic structure calculations

Electronic structure calculations were performed to aid in the interpretation of the Ti K- and Sn L_3-edge XANES spectra using the self-consistent tight-binding linear-muffin-tin orbital model and the atomic spheres approximation (TB-LMTO-ASA).[196] These calculations were performed for $Y_2Ti_{2-x}Sn_xO_7$ because of the difficulties in performing these calculations on systems having partially occupied f-orbitals (e.g., $Gd_2Ti_{2-x}Sn_xO_7$). The density of states (DOS) were calculated for the $Y_2Ti_2O_7$ and $Y_2Sn_2O_7$ pyrochlore-type oxides using previously reported structural parameters.[197] To calculate the DOS for Y_2TiSnO_7, a super cell was created that

contained two pyrochlore unit cells joined along the *a*-axis with an equal number of Ti and Sn atoms being placed in alternating sites. This new unit cell allocates the Ti and Sn atoms individually into the B sites, and the space group of the new unit cell was determined using the symmetry reduction program provided with the TB-LMTO-ASA calculation package.[196] The Brillouin zone integration was performed over a total of 512 *k*-points. The total DOS and partial DOS for Sn, Ti, and O orbitals were calculated.

3.3 Results and discussion

3.3.1 Structure

The powder XRD patterns from the $Gd_2Ti_{2-x}Sn_xO_7$ series ($0.0 \leq x \leq 2.0$) are shown in Figure 3.1. All materials were phase-pure and the powder patterns compare well to calculated powder patterns for $Gd_2Ti_2O_7$ and $Gd_2Sn_2O_7$, which adopt the pyrochlore-type structure.[191,198] The lattice constants (Table 3.1) were found to increase linearly as Sn is incorporated into the Ti-site of $Gd_2Ti_{2-x}Sn_xO_7$, in agreement with Vegard's law.[193] The observed increase in the lattice constant with greater Sn content is due to the larger ionic radii of 6-coordinate Sn^{4+} (r_{Sn4+} = 0.690 Å) as compared with Ti^{4+} (r_{Ti4+} = 0.605Å).[155] The intensities of the super structural peaks (odd lattice planes) observed in the powder patterns from these pyrochlore-type oxides were observed to decrease with greater Sn incorporation. The decrease in the intensities of the super structural peaks is mainly caused by the progressive decrease in the difference in the average scattering power between the A- and B-site ions with increasing Sn incorporation.[89,193] Previous studies of stannate pyrochlores (e.g., $Gd_2Ti_{2-x}Sn_xO_7$ and $Y_2Ti_{2-x}Sn_xO_7$) have determined the site occupancies of the metal sites by performing a Rietvield analysis of powder XRD data. These studies have shown that the amount of cation anti-site disorder experienced in stannate materials

is considerably less (~ 5 % in $Gd_2Sn_2O_7$) than is found in zirconate pyrochlore materials (~30% in $Gd_2Zr_2O_7$).[89,199,200] The lack of significant cation anti-site disorder has been attributed to the covalency of the Sn-O interaction in the B-site, which is supported by the examination of XANES spectra (*vide infra*). The powder diffraction patterns of $Y_2Ti_{2-x}Sn_xO_7$ are shown in Figure A1.1 (Appendix 1 information) and the lattice constants (Table A1.1; Appendix 1) were also found to increase with greater Sn content.

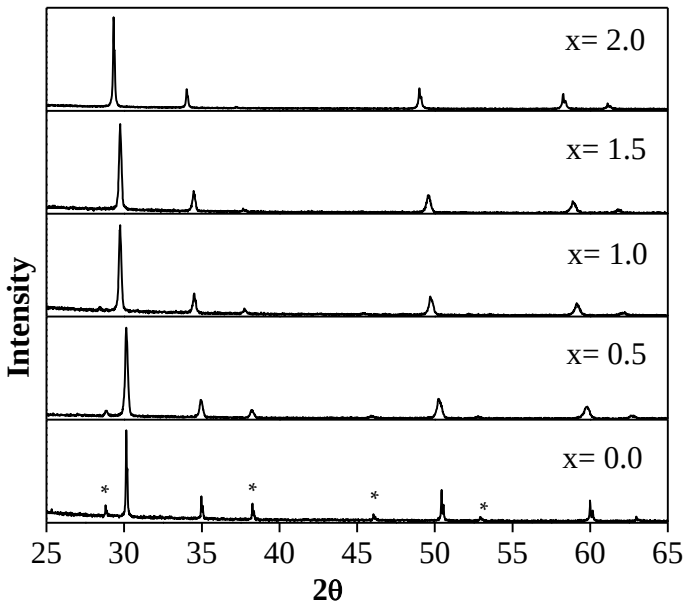

Figure 3.1 XRD patterns from the $Gd_2Ti_{2-x}Sn_xO_7$ series are shown. The diffraction peaks shift to lower 2θ with increasing Sn content. The odd lattice planes (super structural peaks) are marked by stars.

Table 3.1 Lattice constants from the $Gd_2Ti_{2-x}Sn_xO_7$ series

$Gd_2Ti_{2-x}Sn_xO_7$	
x	a (Å)
0.0	10.1845(2)
0.5	10.2575(6)
1.0	10.3228(7)
1.5	10.3905(5)
2.0	10.4498(2)

3.3.2 Ti K-edge XANES

XANES is sensitive to changes in the electronic structure and crystal structure of materials.[121,125] The examination of these spectra has allowed for a study of the influence of metal substitution on covalency, bond length, and the overall electronic structure of the $Gd_2Ti_{2-x}Sn_xO_7$ system. The normalized Ti K-edge spectra from $Gd_2Ti_{2-x}Sn_xO_7$ are presented in Figure 3.2 and compare well to previously reported K-edge XANES spectra from oxides containing Ti^{4+} in a 6-coordinate environment.[159,192] These spectra result from 1s→3d (quadrapolar; pre-edge (A)) and 1s→4p (dipolar; main-edge (B)) transitions.[159,177] Three features (A_1, A_2 and A_3) are observed in the pre-edge region and result from both local and non-local excitations.[161,176] Feature A_1 in the pre-edge region results from pure local 1s→3d-t_{2g} excitations. The low energy region of feature A_2 results from local 1s→3d-e_g^* excitations, while the higher energy region results from non-local (intersite-hybrid) excitations of 1s electrons to d- states of next-nearest neighbour atoms that overlap with Ti 4p states of the absorbing atom *via* O 2p states.[176] Feature A_3 is a result of pure non-local (intersite-hybrid) excitations.[161,176] Feature C in

the high energy region of the spectra is most likely a result of multi-scattering resonances. Multi-scattering peaks occur when the core electron is ejected from the atom and is backscattered by multiple neighbouring atoms (i.e., EXAFS; extended X-ray absorption fine structure), resulting in constructive and destructive interference.[201] All of the features observed in the spectra (A, B, C) change in a systematic way with substitution of Ti for Sn. The changes in the pre-edge region (A) are discussed first, followed by a discussion of why the main-edge (B) region shifts in energy. The shifts in energy of the main-edge (B) region with varying composition are discussed below by comparing the Ti K-edge XANES spectra from $Y_2Ti_{2-x}Sn_xO_7$ to those from $(Y,Gd)_2Ti_2O_7$, and to the calculated partial DOS for the $Y_2Ti_{2-x}Sn_xO_7$ compounds.

The intensity of feature A_1 does not change considerably in the spectra from $Gd_2Ti_{2-x}Sn_xO_7$ (Figure 3.2a); however, the intensities of feature A_2 and feature A_3 do change dramatically depending on composition. As was stated above, feature A_1 (and the low-energy side of feature A_2) result from local 1s→ 3d transitions. The intensity of pre-edge features resulting from local excitations change considerably because of changes in CN or distortion of the local coordination environment.[129,159,202] As the CN changes, the variation in the amount of overlap between Ti 3d and Ti 4p states can change the dipolar character of the transition, leading to changes in the intensity of these features.[129,178] As limited anti-site disorder is present in these materials, the Ti CN remains fairly constant regardless of composition and is the reason for why the intensity of feature A_1 does not change in these materials.[89,199] The intensities of feature A_3 and feature A_2 (particularly the high-energy side of this feature) change because of variations in the intersite-hybrid transitions.[176,203] The decrease in intensity of these two features with greater Sn content is related to the concentration of unoccupied next-nearest neighbour d orbitals.[203] As

Sn is substituted for Ti, fewer unoccupied next nearest neighbour Ti 3d states are available for 1s electrons from the absorbing atom to be excited to, resulting in a decrease in the intensity of feature A_3 and the high energy region of feature A_2. The observation of a reduction of the intensity of intersite-hybrid peaks because of a decrease in the number of unoccupied next-nearest neighbour d-states has not been observed often.[203]

Examination of the first derivative of the spectra from $Gd_2Ti_{2-x}Sn_xO_7$ (Figure 3.2b) shows that the main-edge energy (feature B) shifts to higher energy with greater Sn incorporation. A shift in the absorption energy can result from both ground-state and final state effects. Final-state effects occur due to the relaxation of electrons towards the core-hole produced during the excitation and are sensitive to changes in the chemical environment.[174,204] For example, a lower CN results in greater final state relaxation effects due to the presence of fewer electrons in the first coordination shell that are available to screen the core-hole.[130,174] Ground-state effects, on the other hand, mainly occur due to changes in the charge and bonding environment of the absorbing atom, leading to a change in the screening of the nuclear charge of the absorbing atom. For example, feature B could shift to higher energy due to the development of a more positive charge on Ti with greater Sn substitution in $Gd_2Ti_{2-x}Sn_xO_7$ ($\chi_{Sn} = 1.8 > \chi_{Ti} = 1.5$).[205] A more positive charge on a Ti ion would cause a more attractive potential to act on the core electrons; leading to a positive shift in absorption energy. Feature B could also shift by varying the distance from the surrounding atoms to the absorbing atom (bond-length). The average Ti-O bond length increases with increasing Sn content owing to the increased ionic radius of Sn^{4+} compared to Ti^{4+}, and could result in a decreased screening of the Ti nuclear charge by the electrons from the oxygen anions in the first coordination shell.[155]

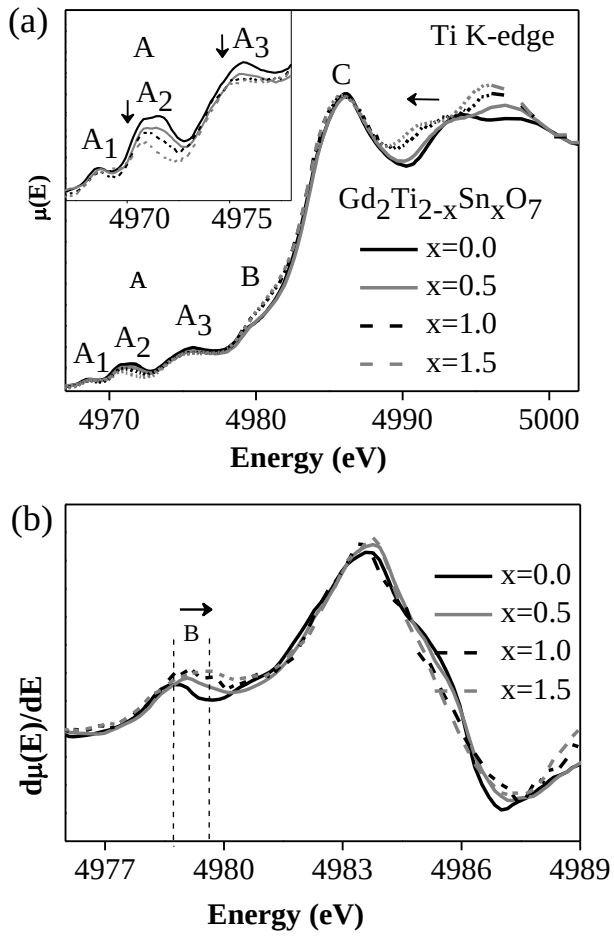

Figure 3.2 (a) Ti K-edge XANES spectra from the $Gd_2Ti_{2-x}Sn_xO_7$ system. Feature A (A_1, A_2, and A_3) represents the pre-edge region and arises from 1s→3d excitations. Features B and C represent the main-edge region and result from 1s→4p transitions. (The separation between the pre- and main-edge regions is represented by a dashed-line.) The pre-edge region is shown in the inset. Arrows mark the changes observed in the spectra with increasing Sn content. The multi-scattering peak (feature C) shifts to lower energy, decreases in intensity, and becomes broader with increasing Sn content. The increase in the Ti-O bond distance causes a longer multi-scattering resonance path length, leading to a shift of this feature to lower energy.[201] (b) The first derivative of the Ti K-edge XANES spectra from $Gd_2Ti_{2-x}Sn_xO_7$ is shown. The first derivative of the spectra has been smoothed, and the vertical dashed lines represent the peak energies of feature B from the $Gd_2Ti_{2-x}Sn_xO_7$ series when x = 0.0 and 1.5.

The Ti K-edge XANES spectra from $Y_2Ti_{2-x}Sn_xO_7$ were compared to the calculated partial DOS for these materials to confirm if the shifts observed in the Ti K-edge XANES spectra from $Gd_2Ti_{2-x}Sn_xO_7$ result from final-state or ground-state effects (Figures 3.3 and 3.4). The intensity and absorption energy of the features found in the Ti K-edge spectra from the $Y_2Ti_{2-x}Sn_xO_7$ series vary with Sn composition (Figure 3.3). The intensity of the pre-edge features (A_2 and A_3) decrease with greater Sn incorporation in $Y_2Ti_{2-x}Sn_xO_7$, as was observed for $Gd_2Ti_{2-x}Sn_xO_7$, and is a result of fewer unoccupied next-nearest neighbour d-states being available to excite 1s electrons to (*vide supra*). The first derivative of the main-edge region of the Ti K-edge XANES spectra from $Y_2Ti_{2-x}Sn_xO_7$ is shown in Figure 3.3b and the peak maximum (feature B) is observed to shift to higher energy (~0.8 eV) with increasing Sn substitution. The reason for why the absorption energy of feature B shifts to higher energy in $Y_2Ti_{2-x}Sn_xO_7$ with increasing Sn content can be analysed by examination of the calculated partial DOS from $Y_2Ti_{2-x}Sn_xO_7$ (Figure 3.4). Feature A in the XANES spectra (Figure 3.3) is assigned to the region of the Ti 3d partial DOS found between 1 and 5 eV (Figure 3.4b), whereas the main-edge region (feature B; Figure 3.3) of the Ti K-edge XANES spectra is assigned to the region of the Ti 4p partial DOS found between 9 and 14 eV (Figure 3.4a). The Ti 3d and 4p conduction states shown in Figure 3.4 are involved in Ti-O anti-bonding interactions. The small negative shift in energy observed for the Ti 3d partial DOS (~ -0.3 eV) and the significant shift to higher energy observed for the Ti 4p partial DOS (~ +0.8 eV) with greater Sn content is in agreement with the Ti K-edge XANES spectra from $Y_2Ti_{2-x}Sn_xO_7$ (*c.f.* Figures 3.3 and 3.4). The DOS calculation confirms that ground-state effects are at least primarily responsible for the changes observed in the spectra reported in this study, as the effect of a core-hole (i.e., final-state effects) was not considered during calculation.

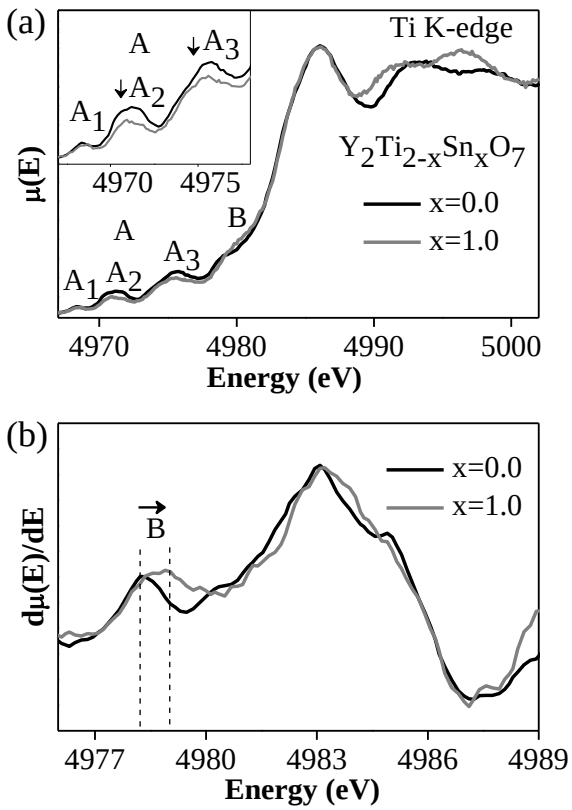

Figure 3.3 (a) Ti K-edge XANES spectra from $Y_2Ti_2O_7$ and Y_2TiSnO_7 are shown. The changes in the intensity and energy of the various features with increasing Sn content are marked by arrows. (b) The first derivative of the Ti K-edge XANES spectra from $Y_2Ti_2O_7$ and Y_2TiSnO_7 are shown. The vertical dashed lines represent the energies of feature B in the spectra from these materials.

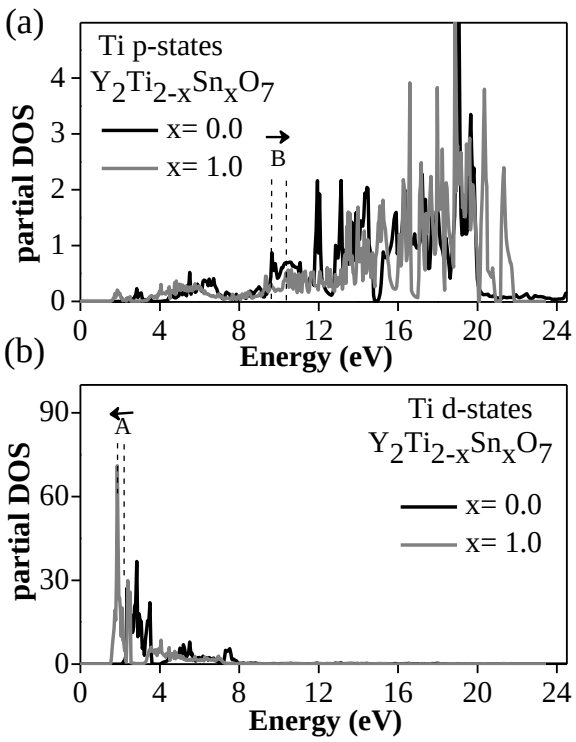

Figure 3.4 (a) The partial DOS calculations of the Ti 4p states from $Y_2Ti_{2-x}Sn_xO_7$ are presented, and have been plotted relative to the Fermi level (0 eV). The Ti 4p states found between 9 and 14 eV were observed to shift to higher energy (~ +0.8 eV) with increasing Sn content which is marked by vertical lines. (b) The Ti 3d partial DOS calculations from $Y_2Ti_{2-x}Sn_xO_7$ are presented. The Ti 3d states were observed to shift by ~ -0.3 eV with increasing Sn incorporation, which is significantly smaller than the shift observed for the Ti 4p states.

As was explained above, an increase in the average Ti-O bond length with increasing Sn content could play a role in shifting the main-edge region to higher absorption energy because of ground-state effects. This was investigated by comparing the Ti K-edge XANES spectra of $Y_2Ti_2O_7$ and $Gd_2Ti_2O_7$ (Figure 3.5). The Ti-O bond length was observed to increase on going from $Y_2Ti_2O_7$ to $Gd_2Ti_2O_7$ by comparison of previously reported crystal structure data (Table 3.2) and Ti K-edge EXAFS data examined in this present study (not shown).[198,206] As the Ti-O bond length increases, a very slight shift (~0.3 eV) to higher energy was observed from the first derivative of the main edge region of the Ti K-edge XANES spectra from $Y_2Ti_2O_7$ and $Gd_2Ti_2O_7$

(Figure 3.5b). However, the shift to higher absorption energy with increasing bond length is much smaller than the shift observed in the spectra from $Y_2Ti_{2-x}Sn_xO_7$ (~0.8 eV) even though the percent change in the Ti-O bond length is similar. Because of this, it is proposed here that the shift in energy of feature B observed in the Ti K-edge XANES spectra from $Y_2Ti_{2-x}Sn_xO_7$ is primarily a result of a change in the covalency of the Ti-O bond. As the Sn content increases in $Y_2Ti_{2-x}Sn_xO_7$, the more covalent Sn-O interaction leads to an increase in the ionic strength of the Ti-O bond to ensure charge balance, as Sn is more electronegative than Ti ($\chi_{Sn} = 1.8 > \chi_{Ti} = 1.5$).[205] As the ionic character of the Ti-O bond increases with greater Sn content, a more positive charge develops on Ti. This results in a reduced ground-state screening of the nuclear charge and is observed as a shift to higher energy with greater Sn incorporation of region B in the Ti K-edge XANES spectra.[203] No significant shifts were observed in the pre-edge region (feature A) of the Ti K-edge XANES spectra from $Y_2Ti_{2-x}Sn_xO_7$ with greater Sn content (Figure 3.3). It is hypothesized here that a change in the covalency of the Ti-O bond influences the energy of the Ti 3d – O 2p antibonding states to a smaller degree than the Ti 4p – O 2p antibonding states, which is in agreement with the calculated partial DOS from these materials (Figure 3.4).

Table 3.2 Ti-O and Sn-O bond lengths from $RE_2Ti_2O_7$ (RE = Y and Gd) and $RE_2Sn_2O_7$ (RE = Y, Gd, and La) determined using previously reported crystallographic information.[198,201,206]

RE	$RE_2Ti_2O_7$ Ti-O (Å)	$RE_2Sn_2O_7$ Sn-O (Å)
Y	1.955	2.043
Gd	1.977	2.050
La	-	2.074

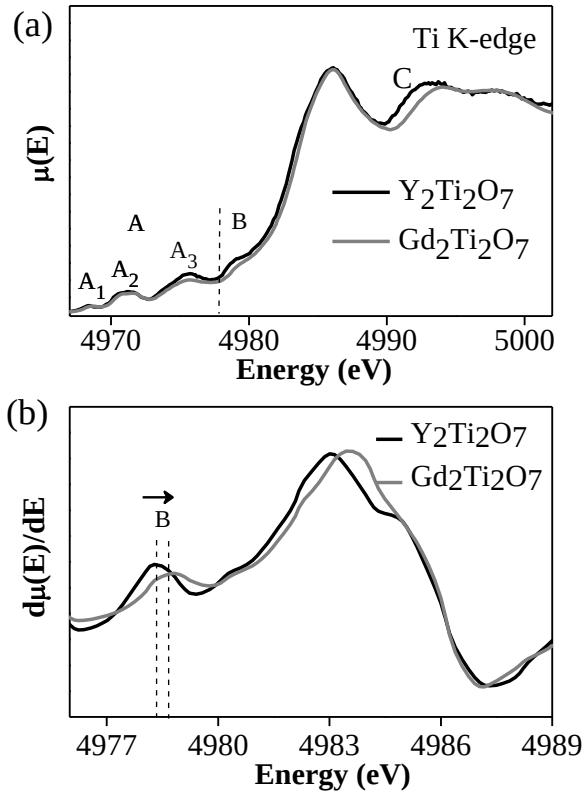

Figure 3.5 (a) Ti K-edge XANES spectra from $Y_2Ti_2O_7$ and $Gd_2Ti_2O_7$ are shown. (b). The first derivative of the Ti K-edge XANES spectra from $Y_2Ti_2O_7$ and $Gd_2Ti_2O_7$ are shown. The vertical dashed lines represent the peak energies from $Y_2Ti_2O_7$ and Gd_2Ti_2O. An increase in the energy of feature B with increasing Sn incorporation is marked by an arrow.

The shifts in absorption energy observed in the Ti K-edge XANES spectra from the $Gd_2Ti_{2-x}Sn_xO_7$ series were compared to the shifts from $Y_2Ti_{2-x}Sn_xO_7$. The first derivative of the main-edge region from the Ti K-edge XANES spectra of $Gd_2Ti_{2-x}Sn_xO_7$ are shown in Figure 3.2b. The peak maximum (feature B) is observed to shift to higher energy (~0.9 eV) over the range of substitution, which is in good agreement with the shift in energy observed for the $Y_2Ti_{2-x}Sn_xO_7$ series with greater Sn content. This implies that feature B in the Ti K-edge XANES

spectra from these $Gd_2Ti_{2-x}Sn_xO_7$ materials also shift because of a change in the Ti charge (i.e., increase in the ionic character of the Ti-O bond) as more Sn is substituted into the system.

3.3.3 Sn L_3-edge XANES

The normalized Sn L_3-edge spectra from the $Gd_2Ti_{2-x}Sn_xO_7$ series were collected to probe the effects of covalency on Sn as the composition was varied and are presented in Figure 3.6. The Sn L_3-edge spectra exhibit two features that result from $2p_{3/2} \rightarrow 5s$ (Feature A) and $2p_{3/2} \rightarrow 5d$ (Feature B) excitations, respectively.[207-209] The shape, position, and intensity of feature B change with varying Sn concentration while feature A does not change. The line shape and position of feature B (and A) in the $Gd_2Ti_{2-x}Sn_xO_7$ spectra are interpreted below by first comparing the Sn L_3-edge spectra from $Y_2Ti_{2-x}Sn_xO_7$ and $RE_2Sn_2O_7$ (RE=Y, Gd, and La), and by comparing the spectra from $Y_2Ti_{2-x}Sn_xO_7$ to the calculated partial DOS from these compounds. A broader peak (C) is also observed at higher energy in all of these spectra (~3960 eV) and is presumed to result from multi-scattering resonances, as has been suggested previously.[208,209]

The intensity of feature B decreases with greater Sn incorporation in the $Gd_2Ti_{2-x}Sn_xO_7$ system. The observed decrease in intensity is attributed to the change in the covalency of the Sn-O bond, as the Sn-O bond becomes more covalent when Sn is substituted for Ti ($\chi_{Sn} = 1.8 > \chi_{Ti} = 1.5$).[205] With increasing covalency of the Sn-O bond, the Sn 5d states share more electrons with the O 2p states, which results in fewer unoccupied Sn 5d states being available for Sn 2p electrons to be excited to. This effect is observed in the spectra by a decrease in intensity of feature B with increasing Sn content.

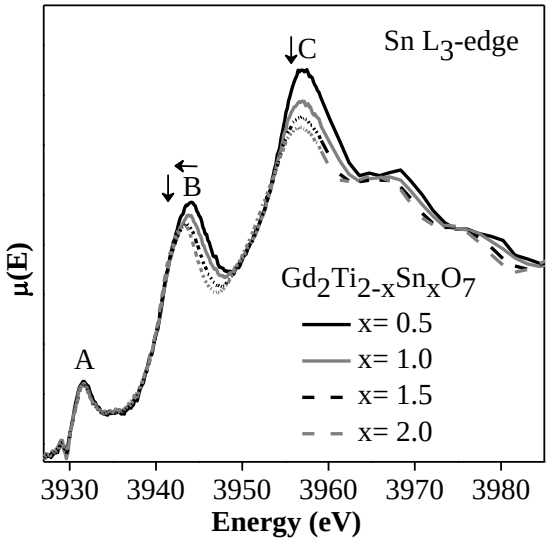

Figure 3.6 Sn L_3-edge spectra from the $Gd_2Ti_{2-x}Sn_xO_7$ series. Feature A and B arise from $2p_{3/2} \rightarrow 4s$ and $2p_{3/2} \rightarrow 5d$ excitations while Feature C (~3960 eV) arises from multi-scattering resonances. The changes in intensity and absorption energy of feature A, B, and C with greater x value are marked by the arrows. The multi-scattering peak (C) decreases in intensity and shifts to lower energy as the Sn substitutes for Ti in $Gd_2Ti_{2-x}Sn_xO_7$, and is a result of an increase in the average Sn-O bond distance.

Feature B was also observed to become narrower to lower energy in the Sn L_3-edge XANES spectra with increasing Sn concentration, resulting in an overall decrease in the average absorption energy of this feature. The decrease in width of this feature and shift in average energy could result from changes in the bond length and/or changes in the charge of the absorbing atom. As Sn is substituted for Ti ($\chi_{sn} = 1.8 > \chi_{Ti} = 1.5$), the average Sn-O bond becomes more covalent, leading to a greater sharing of electrons between the Sn 5d and O 2p states and resulting in a decrease of the cationic charge of Sn.[205] A reduction in Sn charge would lead to greater screening of the nucleus and would be observed as a decrease in the average

absorption energy of this feature. A change in bond-length could also influence the energy of feature B by changing the screening of the Sn nuclear charge.

The shift in energy of features B and A in the Sn L_3-edge XANES spectra from $Gd_2Ti_{2-x}Sn_xO_7$ were studied by comparing the Sn L_3-edge XANES spectra from $Y_2Ti_{2-x}Sn_xO_7$ and $RE_2Sn_2O_7$ (RE = Y, Gd, and La), and by comparing the spectra from $Y_2Ti_{2-x}Sn_xO_7$ to the calculated partial DOS of these materials (Figures 3.7, 3.8, and 3.9). The effect of bond length on the absorption energy of feature B was studied by comparison of the Sn L_3-edge spectra of $RE_2Sn_2O_7$ (RE=Y, Gd, and La) (Figure 3.7). The Sn-O bond length increases as the rare earth metal changes from Y to Gd to La (Table 3.2).[191] This increase in Sn-O bond length would reduce the ability of the electrons from the O anions to screen the Sn nuclear charge, and this would be expected to result in an increase in the Sn absorption energy. The Sn L_3-edge XANES spectra presented in Figure 3.8 clearly show that no change in energy of feature B occurs with varying Sn-O bond length. This observation implies that the shift in absorption energy of feature B in the spectra from $Gd_2Ti_{2-x}Sn_xO_7$ is more likely a result of changes in the covalency of the Sn-O bond.

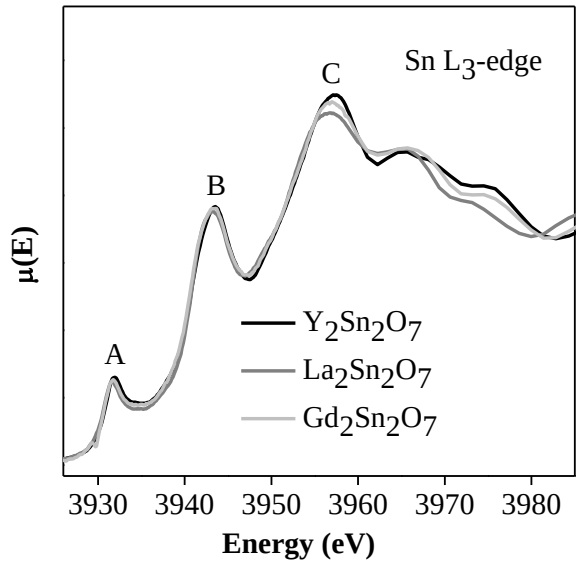

Figure 3.7 Sn L_3-edge spectra from $RE_2Sn_2O_7$ (RE= Y, Gd, and La) are shown. No significant variations in the features from $Y_2Sn_2O_7$, $Gd_2Sn_2O_7$ or $La_2Sn_2O_7$ were observed.

The effect of a change in covalency of the Sn-O bond was further investigated by comparing the Sn L_3-edge XANES spectra from $Y_2Ti_{2-x}Sn_xO_7$ to the calculated partial DOS from these materials. The intensity, position, and shape of feature B varies with Sn composition in the Sn L_3-edge spectra of $Y_2Ti_{2-x}Sn_xO_7$ (Figure 3.8). The intensity of feature B decreases with greater Sn incorporation in $Y_2Ti_{2-x}Sn_xO_7$ and is a result of an increase in the covalency of the Sn-O bond with increasing Sn content, as was discussed above when comparing the Sn L_3-edge XANES spectra from $Gd_2Ti_{2-x}Sn_xO_7$. Further, the line shape of feature B becomes narrower to lower energy and no significant change in feature A with increasing Sn substitution in $Y_2Ti_{2-x}Sn_xO_7$ was observed, as was also the case for $Gd_2Ti_{2-x}Sn_xO_7$. The partial DOS calculations of the Sn 5d states and Sn 5s states are shown in Figure 3.9. Feature B from the Sn L_3-edge XANES spectra (Figure 3.8) corresponds to the region found between 9 and 20 eV in the plot of

the partial DOS and results primarily from Sn 5d states involved in Sn-O anti-bonding interactions (Figure 3.9a). Feature A in the Sn L_3-edge XANES spectra (Figure 3.8) is assigned to the region located between 3 and 9 eV in the plot of the partial DOS and results from 5s states that are involved in Sn-O anti-bonding interactions (Figure 3.9b). The Sn 5d partial DOS calculations show that the width of the Sn 5d states becomes narrower to lower energy with increasing Sn content while the Sn 5s partial DOS show few variations in energy with increasing Sn content. Both of these results are in good agreement with the Sn L_3-edge XANES spectra from $Y_2Ti_{2-x}Sn_xO_7$ (*cf.* Figure 3.8 and Figure 3.9). As was suggested above, the lowering in energy of feature B in the spectra from the quaternary materials studied here ($Y_2Ti_{2-x}Sn_xO_7$ and $Gd_2Ti_{2-x}Sn_xO_7$) is a result of the increased covalency of the Sn-O interaction with greater Sn incorporation, leading to greater screening of the Sn nuclear charge.

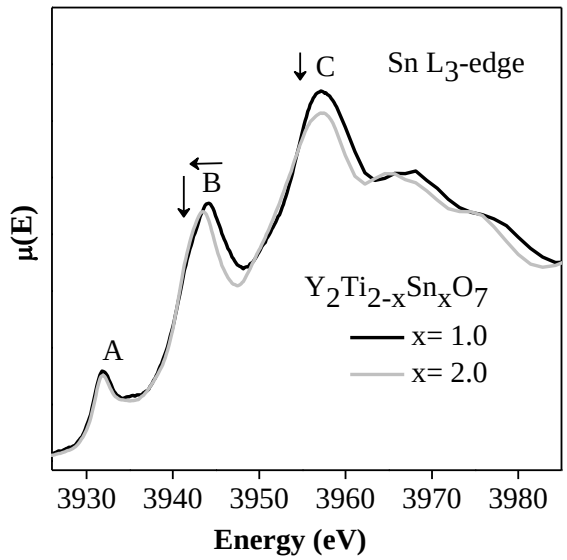

Figure 3.8 Sn L_3-edge spectra from $Y_2Ti_{2-x}Sn_xO_7$ are shown. The changes in intensity and absorption energy of features with greater Sn incorporation are marked by the arrows.

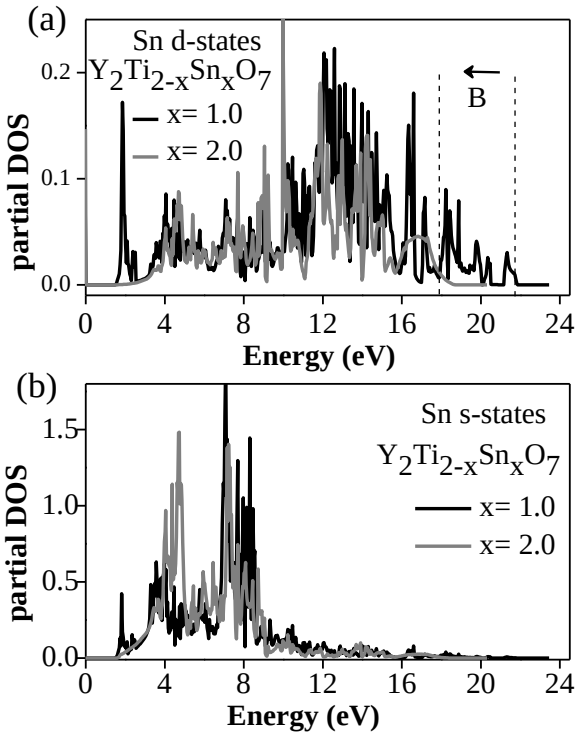

Figure 3.9 The partial DOS calculations of the Sn 5d and Sn 5s states from $Y_2Ti_{2-x}Sn_xO_7$ are shown, and are plotted relative to the Fermi level (0 eV). (a) The Sn 5d states become narrower to lower energy as the Sn concentration increases. (b) The Sn 5s states exhibit no significant change in energy with increasing Sn concentration.

No significant shift in absorption energy of feature A in the Sn L_3-edge XANES spectra from $Gd_2Ti_{2-x}Sn_xO_7$, $Y_2Ti_{2-x}Sn_xO_7$, or $RE_2Ti_2O_7$ (Figures 3.6-3.8) was observed with varying composition. The calculated partial Sn 5s DOS from $Y_2Ti_{2-x}Sn_xO_7$ also showed little change in energy depending on composition (Figure 3.9b). These observations imply that a change in the covalency of the Sn-O bond influences the energy of the Sn 5s-O 2p antibonding states to a much smaller degree than the Sn 5d-O 2p antibonding states.

3.3.4 Sn K-edge XANES

The Sn K-edge spectra from $Gd_2Ti_{2-x}Sn_xO_7$ were collected to further study how the electronic structure of these compounds changes with greater Sn content (Figure 3.10). According to dipole selection rules, the Sn K-edge XANES spectrum results from the excitation of Sn 1s electrons to unoccupied Sn 5p states.[210] Since the Sn 4d states are filled, the Sn K-edge spectrum does not display pre-edge features. (The Sn 5d states are higher in energy than the Sn 5p states.) No significant changes were observed in the XANES spectra from $Gd_2Ti_{2-x}Sn_xO_7$, which is attributed to the poorer resolution of these spectra, as compared to the Sn L_3-edge spectra (see Section 3.2.2).[211]

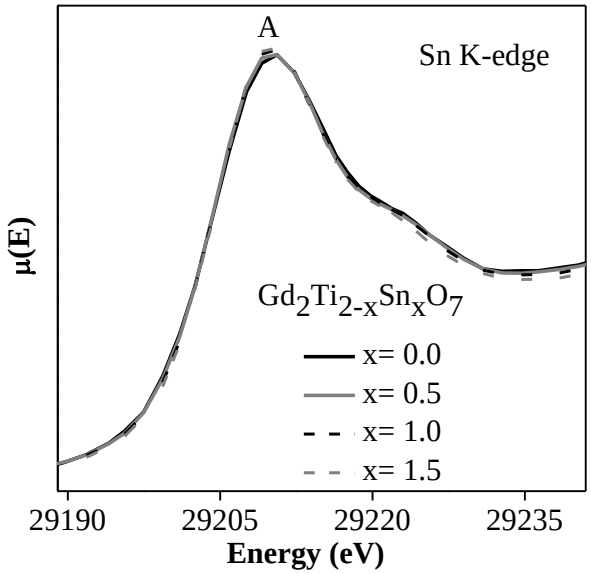

Figure 3.10 Sn K-edge XANES spectra from the $Gd_2Ti_{2-x}Sn_xO_7$ system are presented. Feature A results from a 1s→5p transition. No significant variations in feature A were observed with increasing Sn incorporation.

3.3.5 Gd L_3-edge XANES

Gd L_3-edge XANES spectra were collected to study how the covalency of the Gd-O bond changes upon substitution of Ti for Sn in $Gd_2Ti_{2-x}Sn_xO_7$. The spectra are shown in Figure 3.11 and exhibit a white line that results from a $2p_{3/2} \rightarrow 5d$ excitation.[211,212] The intensity of the white line was observed to increase with greater Sn content and is attributed to an increase in the ionic character of the Gd-O bond, as the electronegativity of Gd is lower than that of either Ti or Sn ($\chi_{Sn} = 1.72 > \chi_{Ti} = 1.32 > \chi_{Gd} = 1.14$).[205] As Sn substitutes for Ti, the ionic character of the Gd-O bond increases and leads to a decrease in sharing of electrons between the Gd 5d and O 2p states. This results in a greater number of unoccupied Gd 5d states being available for Gd 2p electrons to be excited to with increasing Sn content in $Gd_2Ti_{2-x}Sn_xO_7$ and leads to the increase in peak intensity that is observed in Figure 3.11.

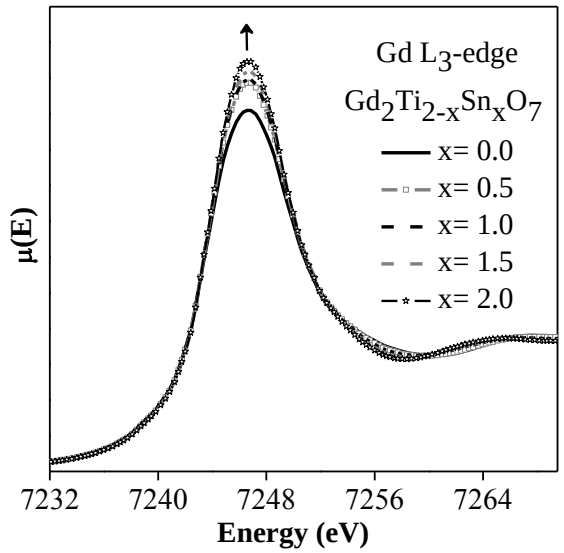

Figure 3.11 Gd L_3-edge spectra from $Gd_2Ti_{2-x}Sn_xO_7$. The intensity of the white line ($2p_{3/2} \rightarrow 5d$) increases with greater Sn content.

3.4. Conclusions

A greater understanding of the effect of covalency of the metal-oxygen bonds on the electronic structure of these pyrochlore-type materials has been achieved by the examination of XANES spectra. The Gd-O and Ti-O bonds become more ionic in the $Gd_2Ti_{2-x}Sn_xO_7$ (and $Y_2Ti_{2-x}Sn_xO_7$) materials with increasing Sn content while the Sn-O bonds become more covalent, leading to changes in energy and intensity of the collected spectra. This information is important to understanding how changes in bonding influence the resistance to radiation induced damage that has been reported for these materials depending on composition.[87,88,186] This investigation has also shown how sensitive the Sn L_3-edge XANES spectra are to variations in the electronic structure of materials compared Sn K-edge XANES spectra, which are more commonly studied. Finally, insights into how the intensity of intersite-hybrid features in transition-metal K-edge spectra can change depending on the concentration of next-nearest-neighbour metal atoms having unoccupied d-states have also been reported.

Chapter 4

An investigation of the electronic structure and structural stability of $RE_2Ti_2O_7$ by glancing angle and total electron yield XANES*

4.1 Introduction

In Chapter 2, the effect of reduced B-site cations and oxygen deficiency on the local coordination environment and oxidation state of transition metal was investigated through a study of $Yb_2Ti_{2-x}Fe_xO_{7-\delta}$. In Chapter 3, the effect of changes in metal-oxygen bond covalency interactions was examined by studying $Gd_2Ti_{2-x}Sn_xO_{7-\delta}$. These previous Chapters discussed how the electronic and structural properties of pyrochlore-type oxides change depending on composition. The next step of this thesis work was to study the structural stability of these materials when exposed to radiation. Various techniques (e.g., TEM) have been used previously to probe the response of a material upon irradiation.[87,102] The present Chapter has mainly focused on how surface sensitive glancing angle and total electron yield XANES (GA-XANES and TEY-XANES) experiments can be used to understand the effect of radiation induced structural damage on the structures of materials.

Crystalline materials have been considered as potential nuclear wasteforms for the long-term storage of radioactive elements, which requires the structure of these materials to remain ordered for thousands of years.[8,9,41,87] A key concern of these materials is the stability of the crystalline structure over thousands of years, which can be affected by the decay of radioactive elements.[32,41,213] This was discussed previously in Section 1.2.1. The incorporated radioactive nuclear waste elements can release α-particles (β- or γ-particles can also be released

* A version of this Chapter has been published. Reprinted with permission from Aluri, E. R.; Grosvenor, A. P. *J. Alloys Comp.* **2014**, *616*, 516-526. © 2014 Elsevier B.V. doi:10.1016/j.jallcom.2014.07.151

depending on the decay mechanism), and be transformed into daughter products during the radioactive decay process.[32,41,45] The α-particles and the daughter products can have sufficient recoil energy to displace other atoms in the structure, leading to metamiction (i.e., the structure becomes amorphous).[46,214] This process can also result in the development of crystal defects and swelling of the structure, which can affect the long-term chemical durability of the nuclear wasteform.[8,41,42] Therefore, it is important to understand how the structure responds to radioactive decay of the incorporated actinide elements. Radiation-induced structural damage can be simulated by implanting the materials with high energy ions (e.g., Au^{-}, Kr^{+}, and Xe^{+}).[41,78,83,87,88,102] High energy (MeV) ion-implantation can produce a thin amorphous (damaged) layer, which is typically a few hundred nm thick.[102]

As was discussed in previous Chapters, XANES is an element-specific method and gives detailed information about the coordination number (CN), oxidation state, and bonding environment of the element of interest.[131,202] The most common measurement methods used to collect XANES spectra are transmission, total electron yield (TEY), and fluorescence yield (FLY).[119,125] The spectra collected using these different detection methods probe different sampling depths.[125] Transmission and fluorescence XANES measurements are inherently bulk sensitive whereas TEY-XANES measurements are surface sensitive.[102,119,120,124] Surface charging can be problematic while recording the TEY-XANES spectra from thick pellets of poorly conductive materials.[215,216] Although hard X-ray XANES spectra are generally bulk sensitive, surface sensitive detection methods such as glancing angle XANES and TEY-XANES measurements can be used to probe only the damaged surface layer of ion-implanted materials.[102,119,124,133,134] In glancing angle XANES (GA-XANES) experiments, the incident X-ray beam angle is set to be just above the critical angle (the angle at which total external

reflection occurs) in order to selectively probe the surface layer. The spectra become more surface sensitive as the glancing angle decreases.

Rare-earth titanate ($RE_2Ti_2O_7$; RE (rare-earth)=La-Lu, and Y) pyrochlore-type oxides have been investigated for the sequestration of nuclear waste due to their resistance to radiation-induced structural damage, which depends on the rare-earth cation present.[87,217,218] $RE_2Ti_2O_7$ crystallites have been examined previously using transmission electron microscopy (TEM) before and after implantation, and this previous study has shown that the resistance to radiation-induced structural damage increases with decreasing radius of the RE cation.[87] Along with stoichiometric materials, oxygen deficient pyrochlore-type materials ($Yb_{1.85}Ca_{0.15}Ti_2O_{7-\delta}$ and $Yb_2Ti_{1.85}Fe_{0.15}O_{7-\delta}$) can also be synthesized by the partial substitution of the A^{3+} or B^{4+} cations by metals that have a lower oxidation state.[142,219] The potential for developing chemically durable pyrochlore-type materials and their ability to reduce radiation-induced structural damage has led to increased interest in the use of these materials for nuclear waste sequestration applications.[78,87,50,198] The objective of the present study was to demonstrate the ability of GA-XANES and TEY-XANES studies to probe the damaged surface layer of rare-earth titanate materials. This study has shown how GA-XANES and TEY-XANES, as well as powder XRD, can be used to study how the structural stability of $RE_2Ti_2O_7$, $Yb_{1.85}Ca_{0.15}Ti_2O_{7-\delta}$, and $Yb_2Ti_{1.85}Fe_{0.15}O_{7-\delta}$ pellets changes depending on composition. An effective way of collecting TEY spectra from thick pellets of poorly conducting pyrochlore-type oxides has also been tested and is discussed.

4.2 Experimental

4.2.1 Synthesis

RE_2O_3 (Alfa Aesar, 99.99 %) and TiO_2 (Alfa Aesar, 99.9%) powders were used to synthesize the $RE_2Ti_2O_7$ (RE=Sm, Eu, Gd, Ho, Yb, Y) materials by the ceramic method and the synthesis process was described in previous Chapters (Sections 2.2.1 and 3.2.1). The materials were heated in air at 1400 ^oC over 6-9 days, with intermediate grinding and repelleting until phase purity was achieved. Yb_2O_3, TiO_2, and $CaCO_3$ (EMD, >99%) powders were mixed and first heated to 900 ^oC to decompose the carbonate before being heated to 1400 ^oC and then quench cooled in air to synthesize $Yb_{1.85}Ca_{0.15}Ti_2O_{7-\delta}$. The method used to synthesize $Yb_2Ti_{1.85}Fe_{0.15}O_{7-\delta}$ was discussed in Chapter 2 (Section 2.2.1). The phase purity of the synthesized materials was confirmed by powder X-ray diffraction (XRD) using a PANalytical Empyrean X-ray diffractometer and a Cu $K\alpha_{1,2}$ X-ray source. A Rietveld refinement of the powder XRD patterns from some of the synthesized (undamaged) $RE_2Ti_2O_7$ materials was performed using the High Score Plus Software package.[150] The lattice constants, the x-coordinate of O in the 48f position (x_{48f}), the overall thermal factor, and the line shape were all refined during analysis (Table A2.1 in Appendix 2). The phase-pure samples were repelleted at 8 MPa after being examined by powder XRD and heated at 1400 ^oC for 3 days to increase the hardness of these pellets before being implanted by Au^- ions.

4.2.2 Ion beam implantation

Ion implantation of $RE_2Ti_2O_7$ (RE=Sm, Eu, Gd, Ho, Yb, Y), $Yb_{1.85}Ca_{0.15}Ti_2O_{7-\delta}$, and $Yb_2Ti_{1.85}Fe_{0.15}O_{7-\delta}$ was performed using the 1.7 MeV Tandetron accelerator located at Interface Science Western (ISW), University of Western Ontario. The ion beam was aligned normal to the

pellet surface during ion-implantation. All materials were implanted by 2 MeV Au^- ions to a dose of 5×10^{14} ions/cm^2 at room temperature.

The Stopping and Range of Ions in Matter (SRIM-2013) software package was used to calculate the depth profiles and defect per ion profiles of the implanted $RE_2Ti_2O_7$ (RE=Sm, Gd, Yb), $Yb_{1.85}Ca_{0.15}Ti_2O_{7-\delta}$, and $Yb_2Ti_{1.85}Fe_{0.15}O_{7-\delta}$ samples.[220] The densities (ρ) of $Sm_2Ti_2O_7$, $Gd_2Ti_2O_7$, $Yb_2Ti_2O_7$, $Yb_{1.85}Ca_{0.15}Ti_2O_{7-\delta}$, and $Yb_2Ti_{1.85}Fe_{0.15}O_{7-\delta}$ used in the calculations were 6.17 g/cm^3, 6.57 g/cm^3, 7.16 g/cm^3, 6.89 g/cm^3, and 7.46 g/cm^3, respectively.[198,219] Ion implantation depth profile calculations were performed using five thousand (5000) 2 MeV Au^- ions and by assuming that the target displacement energies were 25 eV for RE/Ti/Fe/Ca and 28 eV for O. These calculations (Figure 4.1a and Figure A2.1) predicted that the ions penetrate to a depth of ~100-450 nm for all samples. Profiles of the number of vacancies produced per Au^- ion are shown in Figure 4.1b and Figure A2.2. These calculations showed that the number of vacancies produced in the material reach a maximum at a depth of ~200 nm, and that the number of vacancies decreases dramatically at deeper depths.

4.2.3 Micro powder X-ray diffraction

Micro powder XRD (μ-XRD) patterns from the ion implanted samples were collected using the PANalytical Empyrean X-ray diffractometer described in Section 4.2.1. The diffraction patterns were collected to analyze the changes that occur in the long-range crystal structure of these titanate pyrochlore-type oxides after ion-implantation. μ-XRD analysis was performed by reducing the X-ray beam spot size to 200 μm using a mono-capillary collimator. Each implanted pellet was placed on a goniometer stage which permits translation in x-, y- and z-axis directions as well as tilting of the goniometer head. The surface of the implanted pellets was aligned to the

incident X-ray beam using a microscope and diffraction patterns were collected in the 2θ range of 10-55^{o}.

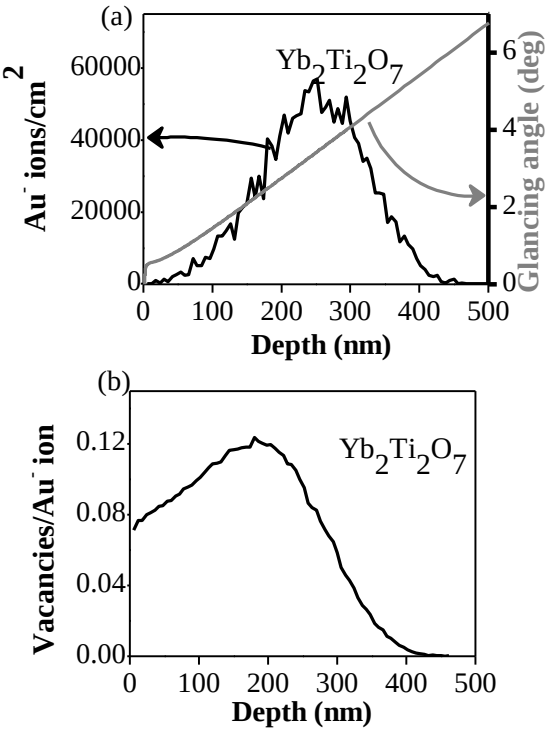

Figure 4.1 (a) A plot of the ion beam implantation depth profile from $Yb_2Ti_2O_7$ calculated using SRIM-2013 is shown. The calculation was performed using 5000 Au^- ions with the ion beam energy being 2 MeV. A plot of glancing angle *versus* X-ray attenuation depth for $Yb_2Ti_2O_7$ is also included in the figure and was calculated for photons having an energy of 4966 eV (Ti K-edge). (b) A plot of the number of vacancies produced per Au^- ion (defect per ion profile) in $Yb_2Ti_2O_7$ by a 2 MeV beam of 5000 Au^- ions is presented.

4.2.4 XANES

The Soft X-ray Microcharacterization Beamline (SXRMB, 06B1-1) located at the Canadian Light Source (CLS) was used to collect the Ti K-edge XANES spectra from the damaged and undamaged $RE_2Ti_2O_7$ (RE=Sm, Eu, Gd, Ho, Yb and Y), $Yb_{1.85}Ca_{0.15}Ti_2O_{7-\delta}$, and

$Yb_2Ti_{1.85}Fe_{0.15}O_{7-\delta}$ materials using a Si(111) monochromator.[153] The resolution of the beamline and sample preparation were discussed in Chapter 2 (Section 2.2.2). The ion-implanted (i.e., damaged) $RE_2Ti_2O_7$ (RE=Sm,Gd,Ho,Yb), $Yb_{1.85}Ca_{0.15}Ti_2O_{7-\delta}$, and $Yb_2Ti_{1.85}Fe_{0.15}O_{7-\delta}$ pellets (~1-2 mm thick) were mounted on the Cu sample holder using carbon tape, and silver paint was used to place the surface of the pellets in electrical contact with the sample holder. All spectra were collected in total electron yield (TEY) mode using a step size of 0.15 eV through the absorption-edge. The angle between the X-ray beam and the implanted pellet was ~85^o during these measurements.[153] The spectra were calibrated using the K-edge spectrum from Ti metal (4966.0 eV).[151]

Ti K-edge GA-XANES spectra from damaged pellets of $RE_2Ti_2O_7$ (RE=Sm, Gd, and Yb), $Yb_{1.85}Ca_{0.15}Ti_2O_{7-\delta}$, and $Yb_2Ti_{1.85}Fe_{0.15}O_{7-\delta}$ were collected using the Pacific Northwest Consortium/X-ray Science Division Collaborative Access Team (PNC/XSD-CAT, Sector 20) bending magnetic beamline (20BM) located at the Advanced Photon Source (APS).[195] A Si (111) double crystal monochromator with harmonic rejection was used, providing a photon flux of ~10^{11} photons/s and a resolution of 0.7 eV at 4966 eV.[151,195] GA-XANES analysis of the ion implanted pellets was performed using a vertically focused X-ray beam with a height of 45 μm and a beam width of 2 mm. The X-ray beam angle of incidence on the surface of the pellets was changed using a motor driven Huber (goniometer) stage that permits x-, y-, and z-axis translation as well as rotation of the glancing angle (α) between the X-ray beam and the surface of the sample. The glancing angle (α) was set to the desired value with an accuracy of 0.1^o to reach different depths of the implanted pellets during GA-XANES analysis. A web-based program was used to calculate the glancing angles required to reach specific X-ray attenuation depths for photons having energies of 4966 eV (Ti K-edge; Figure 2a and Table 4.1).[221] Partial fluorescence

yield spectra were collected using a single element vortex silicon drift detector. (The Ti K-edge partial fluorescence spectra collected at different glancing angles were not found to be influenced by absorption effects, which will be discussed in Chapter 5 (Section 5.3.1).) Spectra were recorded by stepping the energy in 0.15 eV increments through the absorption edge and calibrated against Ti metal (4966.0 eV).[151] All XANES spectra discussed here were normalized, calibrated, and analyzed using the Athena software program.[152]

Table 4.1 Calculated glancing angles required to give specific X-ray attenuation depths for photons having energies of 4966 eV (Ti K-edge).

	Ti K-edge (4966 eV)	
Sample	X-ray attenuation depth (nm)	Glancing angle (^{o})
$Sm_2Ti_2O_7$	100	1.0
	450	3.8
	4835	45
$Gd_2Ti_2O_7$	100	1.1
	450	4.5
	4088	45
$Yb_2Ti_2O_7$	100	1.5
	450	6.1
	3013	45
$Yb_2Ti_{1.85}Fe_{0.15}O_{7-\delta}$	100	1.5
	450	6.4
	2889	45
$Yb_{1.85}Ca_{0.15}Ti_2O_{7-\delta}$	100	1.4
	450	5.8
	3187	45

4.3 Results and discussion

4.3.1 Powder X-ray diffraction before and after ion implantation

Bulk powder XRD and μ-XRD patterns from $RE_2Ti_2O_7$ (RE=Sm, Eu, Gd, Ho, Yb and Y), $Yb_{1.85}Ca_{0.15}Ti_2O_{7-\delta}$, and $Yb_2Ti_{1.85}Fe_{0.15}O_{7-\delta}$ before (bulk powder XRD) and after (μ-XRD) being implanted by Au^- ions to a dose of 5×10^{14} ions/cm^2 are presented in Figure 4.2 and Figure A2.3. The XRD patterns of the undamaged materials in this study are in good agreement with those reported previously, where the $RE_2Ti_2O_7$ (RE=Sm, Eu, Gd, Ho, Yb and Y) materials adopt the pyrochlore-type structure.[87,198] The lattice constants of the ternary materials (Table 4.2) were found to decrease with decreasing ionic radius of the RE cation.[155] The lattice constant of $Yb_{1.85}Ca_{0.15}Ti_2O_{7-\delta}$ was found to be larger than that of $Yb_2Ti_2O_7$ because of the larger ionic radius of Ca^{2+} compared to Yb^{3+} (r_{Ca2+}=1.120 Å> r_{Yb3+} = 0.985 Å).[155] As was studied previously in Chapter 2 (Section 2.3.1), the lattice constant of $Yb_2Ti_{1.85}Fe_{0.15}O_{7-\delta}$ was found to be smaller than that of $Yb_2Ti_2O_7$ because of the decrease in Ti and Fe CN upon Fe^{3+} substitution.[155]

Cation anti-site disorder can be observed in these materials, and is related to the ratio of the A and B cationic radii. As the ionic radii ratio (r_A/r_B) approaches ~1.46, the A-site and B-site cations may undergo anti-site disorder which can result in a phase transition from the pyrochlore to the defect fluorite structure.[41,64,87,200] The super structural peaks (odd planes) from the XRD patterns were used to differentiate the pyrochlore-phase materials from the defect-fluorite phase materials.[192,200,222,223] A decrease in the intensity of the superstructural peaks is generally indicative of cation anti-site disorder; however, the intensities of these peaks relative to the other peaks are also affected by the differences in the scattering power between the A- and B-site cations.[193] Rietvield refinement results of the powder XRD patterns collected from some of the

undamaged $RE_2Ti_2O_7$ (RE=Sm,Gd,Yb) materials are presented in Figure A2.4 and Table A2.1 in Appendix 2. The refinement results confirmed that all three $RE_2Ti_2O_7$ materials studied in this manner adopted the pyrochlore-type structure. The refinement parameters show that a small decrease in the x_{48f} position of the oxygen anions was observed with decreasing radius of the RE cation (Table A2.1). In pyrochlore-type materials, the TiO_6 octahedral shape is sensitive to the oxygen x_{48f} position parameter.[41,65,87,212] A small decrease in the oxygen x_{48f} position parameter with decreasing radius of the RE cation suggests that a small distortion of the TiO_6 octahedra occurs with decreasing radius of the RE cation.

The examination of diffraction patterns from the $RE_2Ti_2O_7$ (RE=Sm, Eu, Gd, Ho, Yb and Y), $Yb_{1.85}Ca_{0.15}Ti_2O_{7-\delta}$, and $Yb_2Ti_{1.85}Fea_{0.15}O_{7-\delta}$ materials before and after implantation allows for an investigation of how the long-range crystal structure is affected by ion implantation. The lattice parameters did not change because of implantation (Table 4.2); however, the diffraction patterns from the implanted materials (Figure 4.2 and A2.4) clearly show a broadening of the diffraction peaks (e.g., the (222) diffraction peak; see Table 4.2). The increase in the width of the diffraction peaks could be a result of a decrease in the average crystallite size, but these peaks can also broaden because of the production of defects.[105] The presence of the small hump located near the (222) diffraction peak (~30^o) in the diffraction patterns from the implanted $RE_2Ti_2O_7$, $Yb_2Ti_{1.85}Fe_{0.15}O_{7-\delta}$, and $Yb_{1.85}Ca_{0.15}Ti_2O_{7-\delta}$ materials (shown in Figure 4.2 and A2.4, respectively) indicates that these materials become partially amorphous after ion implantation. The intensity of the amorphous hump located at ~30^o in the diffraction patterns from the implanted $RE_2Ti_2O_7$ materials gradually decreases with decreasing ionic radii of the RE cation (Sm→Yb).[198,224] It has been previously demonstrated by examination of ion implanted crystallites of $RE_2Ti_2O_7$ by TEM that these materials become less prone to ion-beam induced amorphization with decreasing ionic

radii of the RE cation.[87] As the radius of the RE cation decreases and approaches that of Ti^{4+}, the tendency for the cations to undergo anti-site disorder increases and the materials become more likely to undergo a phase transition from the pyrochlore-type structure to the defect fluorite-type structure because of ion implantation instead of becoming amorphous.[87]

Table 4.2 Lattice constants from the undamaged and damaged materials along with the full width at half maximum (FWHM) of the (222) diffraction peak

		Undamaged		Dose: 5×10^{14} ions/cm^2	
Sample	Average A-site ionic radius (Å)[a]	a (Å)	FWHM of the (222) diffraction peak (^{o})	a Å	FWHM of the (222) diffraction peak (^{o})
$Sm_2Ti_2O_7$	1.079	10.2318(3)	0.0581	10.2390	0.2787
$Eu_2Ti_2O_7$	1.066	10.2043(1)	0.0571	10.2095	0.2800
$Gd_2Ti_2O_7$	1.053	10.1851(1)	0.0878	10.1850	0.3049
$Ho_2Ti_2O_7$	1.015	10.1000(2)	0.0584	10.0845	0.2465
$Y_2Ti_2O_7$	1.019	10.0962(1)	0.0542	10.0340	0.2414
$Yb_2Ti_2O_7$	0.985	10.0296(3)	0.0615	10.0960	0.2552
$Yb_2Ti_{1.85}Fe_{0.15}O_{7-\delta}$	0.985	10.0268(1)	0.0816	10.0350	0.2833
$Yb_{1.85}Ca_{0.15}Ti_2O_{7-\delta}$	1.005	10.0385(6)	0.2476	10.0470	0.2505

[a]The ionic radius of Ti^{4+} is 0.605 Å.[158]

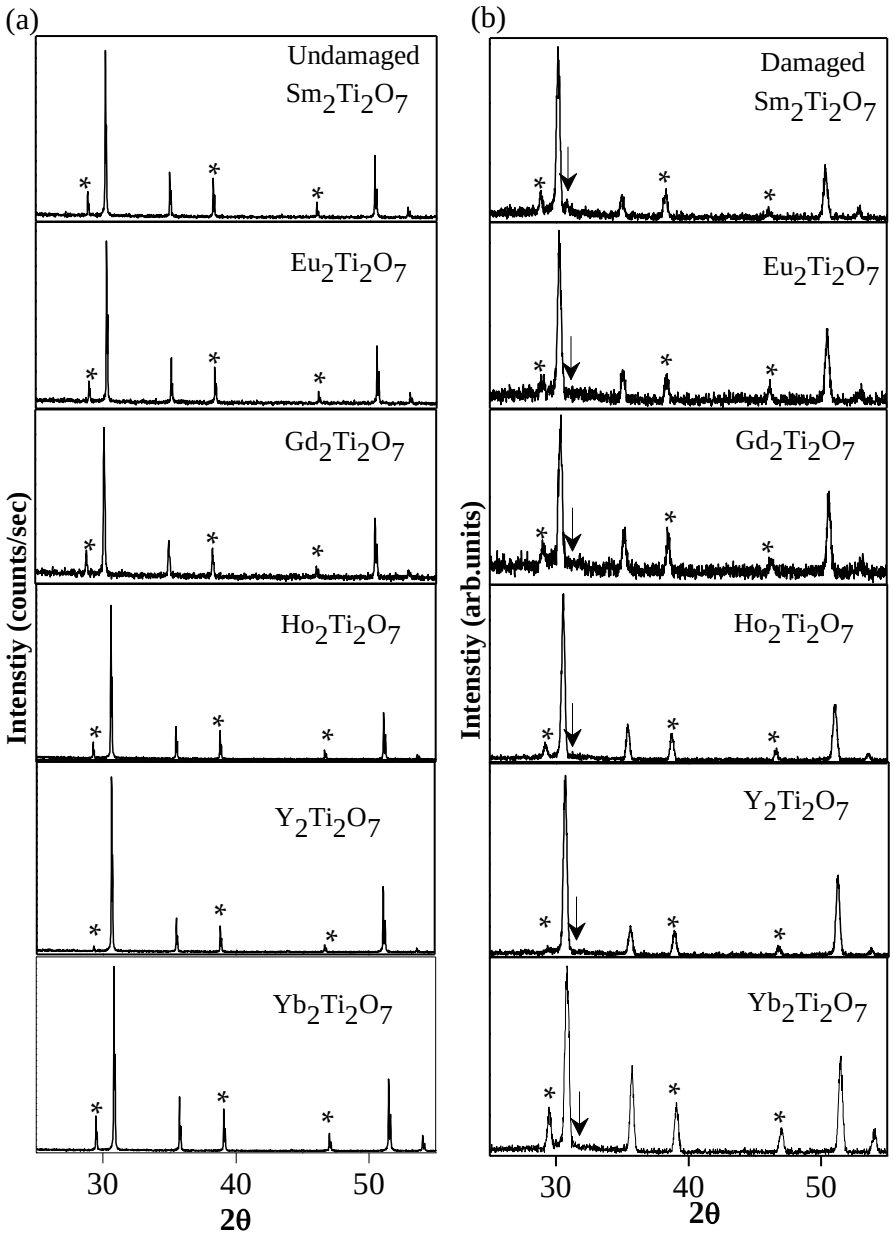

Figure 4.2 Bulk and micro powder XRD patterns from $RE_2Ti_2O_7$ (RE= Sm, Eu, Gd, Ho, Y, and Yb, respectively) are shown before and after the materials were implanted by Au^- ions to a dose of 5×10^{14} ions/cm^2. The odd lattice planes (super structural peaks) from the pyrochlore-type structure are marked by an asterisk (*) and the amorphous hump located near the (222) diffraction peak in the patterns from the damaged materials are indicated by an arrow.

4.3.2 Ti K-edge XANES of the undamaged materials

Normalized Ti K-edge XANES spectra from the undamaged $RE_2Ti_2O_7$ (RE=Sm, Eu, Gd, Ho, Yb, and Y) materials are presented in Figure 4.3. The examination of these spectra has allowed for a study of how the electronic structure of these materials changes depending on composition. The spectra consist of low intensity, quadrapolar (pre-edge; 1s→3d; A) excitations and strong, dipolar (main-edge; 1s→4p; B and C) excitations.[162,180] A detailed explanation of the assignments of these features is given in Section 3.3.2. The features in the spectra have been found to change because of variations in bonding, oxidation state, and CN.[131,202] The changes observed in the pre-edge and main-edge features with varying composition are discussed below.

The intensity and absorption energy of the pre-edge (A) and main-edge features (B and C) in Ti K-edge XANES spectra change with changing CN.[130-131,202,203,225] The pre-edge features (A_1 and A_2) resulting from local excitations are very sensitive to changes in CN or a distortion of the local coordination environment.[129-132,178] Examination of the pre-edge region of Ti K-edge XANES spectra can be useful in determining if the local Ti coordination environment is affected by the radius of the RE cation in $RE_2Ti_2O_7$. As the CN changes and/or the local coordination environment around the Ti ion is distorted, the variation in the amount of overlap between Ti 3d and Ti 4p states can change the dipolar character of the transition.[159,161,129-132] A decrease in Ti CN would result in greater overlap of the Ti 3d and 4p states, which would be observed by an increase in the intensity of the pre-edge peak. However, such changes are not observed in the Ti K-edge spectra (Figure 4.3a) from the undamaged $RE_2Ti_2O_7$ materials as the RE cation is changed. This result is in agreement with the results of the Rietvield refinement of powder XRD data from $Sm_2Ti_2O_7$, $Gd_2Ti_2O_7$, and $Yb_2Ti_2O_7$ (Figure A2.4).

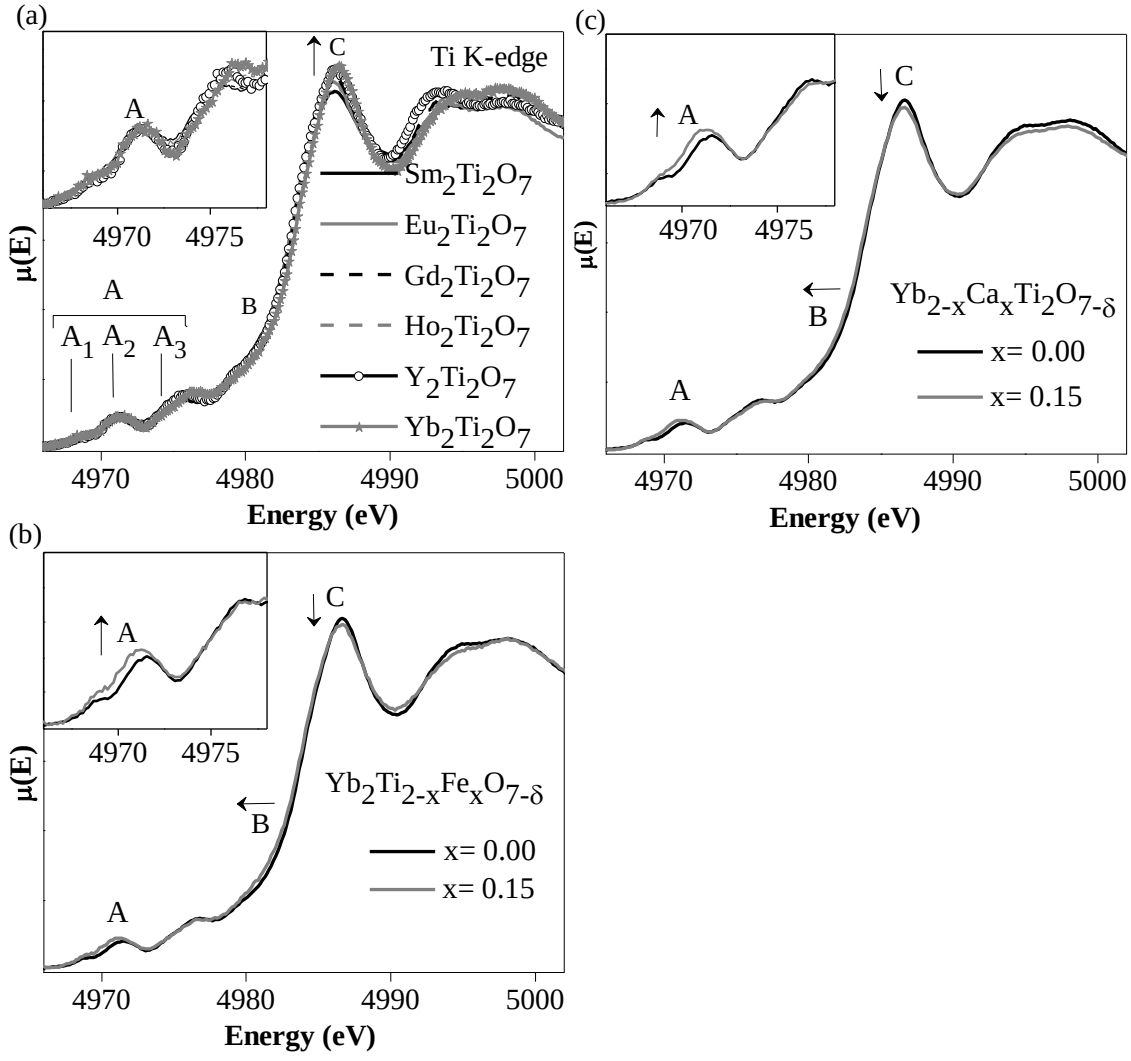

Figure 4.3 (a) Ti K-edge XANES spectra from the $RE_2Ti_2O_7$ system. Feature A represents the pre-edge region and is shown in the inset. Features B and C represent the main-edge region. No changes were observed in the pre-edge region (A) with decreasing radius of the RE cation. The intensity of the main-edge feature (C) increases with decreasing RE ionic radius. The change in intensity of feature C with decreasing radius of the RE cation is indicated by an arrow. (b) Ti K-edge XANES spectra from $Yb_2Ti_{1.85}Fe_{0.15}O_{7-\delta}$ and $Yb_2Ti_2O_7$. The changes of the features (A,B,C) observed in the spectra because of the substitution of Ti^{4+} for Fe^{3+} are marked by arrows. (c) Ti K-edge XANES spectra from $Yb_{1.85}Ca_{0.15}Ti_2O_{7-\delta}$ and $Yb_2Ti_2O_7$. The changes of the features (A,B,C) observed in the spectra because of the substitution of Yb^{3+} for Ca^{2+} are marked by arrows.

The intensity of the main-edge region of the Ti K-edge spectra (C) increases with decreasing radius of the RE cation in the $RE_2Ti_2O_7$ system. The intensity of the main-edge feature (C) changes considerably because of variations in the chemical environment around the Ti atoms.[131,202,203,225] An increase in intensity of feature C can be a result of an increase in the number of Ti 4p final states (or Ti 4p-O 2p states) available for 1s electrons to be excited to. The observed change with decreasing radius of the RE cation could be a result of a change in the bonding environment around the Ti atoms with decreasing Ti-O bond length and/or a distortion of the TiO_6 octahedra. This could lead to an increase in the average number of Ti 4p final states (or Ti 4p-O 2p states) available for 1s electrons to be excited to.

The previously discussed Ti K-edge XANES spectrum (Section 2.3.2) from undamaged $Yb_2Ti_{1.85}Fe_{0.15}O_{7-\delta}$ is presented in Figure 4.3b along with the spectrum from $Yb_2Ti_2O_7$. The observed spectral changes (i.e., an increase in intensity of feature A, a decrease in energy of feature B, and a decrease in intensity of feature C) upon Fe^{3+} substitution are a result of a decrease in the Ti CN upon substitution of Ti^{4+} for Fe^{3+}. Similar spectral changes are observed (Figure 4.3c) in the spectrum from $Yb_{1.85}Ca_{0.15}Ti_2O_{7-\delta}$ upon substitution of Yb^{3+} for Ca^{2+}. The observed decrease in the Ti CN in $Yb_2Ti_{1.85}Fe_{0.15}O_{7-\delta}$ and $Yb_{1.85}Ca_{0.15}Ti_2O_{7-\delta}$ indicates that oxygen vacancies are generated in both systems either by substitution of Ti^{4+} for Fe^{3+} or by substitution of $Yb^{3+}$for Ca^{2+}.

4.3.3 Ti K-edge XANES from ion implanted materials

GA-XANES and TEY-XANES spectra were collected from the ion implanted materials to study how the composition affects the resistance of these materials to structural damage. The 2 MeV Au^- ions penetrate through the surface region to a maximum depth of ~450 nm in these

rare earth titanate materials (Figure 4.1a and Figure A2.1), and defect per ion profiles indicate that the largest number of defects would be generated at a depth of ~200 nm (Figure 4.1b and Figure A2.2). As such, it was necessary to use surface sensitive detection methods to study how the Ti K-edge XANES spectra from these materials change as a result of ion implantation.[102] Examination of these spectra from the implanted $RE_2Ti_2O_7$, $Yb_2Ti_{1.85}Fe_{0.15}O_{7-\delta}$, and $Yb_{1.85}Ca_{0.15}Ti_2O_{7-\delta}$ materials provided important information on the effect of RE ionic radii, metal substitution, and the presence of O-vacancies.

4.3.3.1 GA-XANES

Ti K-edge GA-XANES spectra were collected using glancing angles that provided X-ray attenuation depths of 100 nm and 450 nm to investigate the effect of ion implantation on the local coordination environment of Ti. Normalized Ti K-edge GA-XANES spectra collected at different glancing angles from $RE_2Ti_2O_7$ (RE=Sm,Gd,Yb), $Yb_2Ti_{1.85}Fe_{0.15}O_{7-\delta}$, and $Yb_{1.85}Ca_{0.15}Ti_2O_{7-\delta}$ implanted by Au^- ions to a dose of 5×10^{14} ions/cm^2 are presented in Figure 4.4. These spectra are compared to the Ti K-edge XANES spectra from the undamaged materials collected in TEY mode.

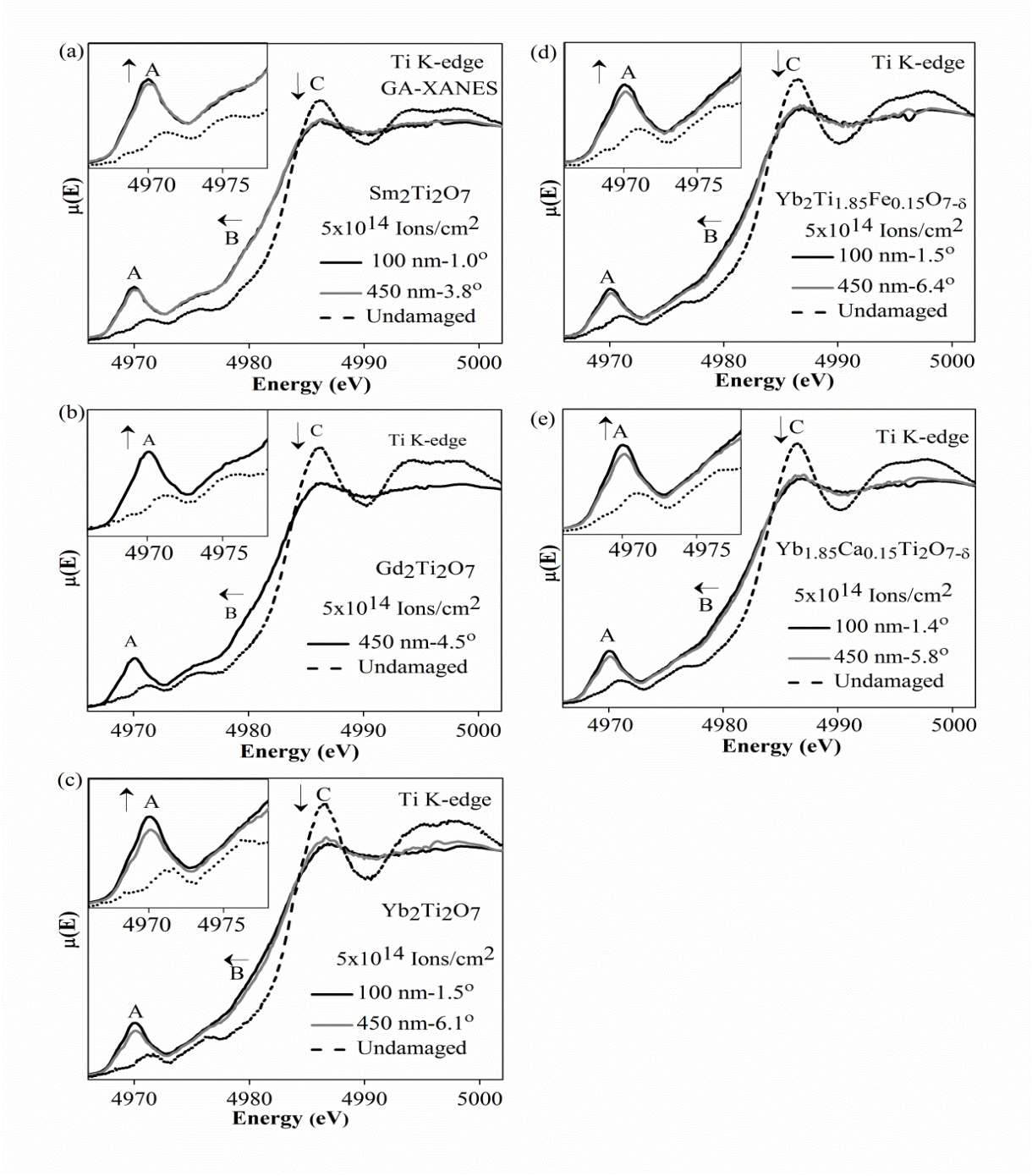

Figure 4.4 Ti K-edge GA-XANES spectra collected at various glancing angles from (a) $Sm_2Ti_2O_7$, (b) $Gd_2Ti_2O_7$, (c) $Yb_2Ti_2O_7$, (d) $Yb_2Ti_{1.85}Fe_{0.15}O_{7-\delta}$, and (e) $Yb_{1.85}Ca_{0.15}Ti_2O_{7-\delta}$ implanted to a dose of 5×10^{14} ions/cm^2 are presented along with the spectra from the undamaged samples. The glancing angles used were chosen so as to attain X-ray attenuation depths of 100 nm and 450 nm. The change in intensity of features A and C, and the change in energy of feature B observed in the spectra with decreasing glancing angle (i.e., decreasing X-ray attenuation depth) are indicated by arrows.

The pre-edge (A) and main-edge features (B,C) in the Ti K-edge GA-XANES spectra from $RE_2Ti_2O_7$ (RE=Sm,Gd,Yb), $Yb_2Ti_{1.85}Fe_{0.15}O_{7-\delta}$, and $Yb_{1.85}Ca_{0.15}Ti_2O_{7-\delta}$ were found to change significantly upon ion implantation (Figure 4.4). The intensity of the pre-edge feature (A) increased while the intensity and energy of the main-edge feature (B,C) decreased as a result of ion implantation. All of these changes are a result of a decrease (and/or distortion) in Ti CN as was described in Section 4.3.2 (and Section 3.2.4).[129-132] The observed decrease in Ti CN does not indicate significant loss of O^{2-} from the materials after ion implantation, but instead suggests that the atoms become disordered in the near surface region of these materials upon ion implantation.

Analysis of the GA-XANES spectra collected at different glancing angles from ion implanted $Sm_2Ti_2O_7$, $Yb_2Ti_2O_7$, $Yb_2Ti_{1.85}Fe_{0.15}O_{7-\delta}$, and $Yb_{1.85}Ca_{0.15}Ti_2O_{7-\delta}$ (Figure 4.4) shows that more damage occurs (i.e., the Ti CN decreases) near the surface (X-ray attenuation depth of 100 nm) compared to deeper into the material (X-ray attenuation depth of 450 nm). This observation is in agreement with the calculated defect per ion profiles presented in Figure 4.1b and Figure A2.2. Examination of the GA-XANES spectra collected from the ion implanted $RE_2Ti_2O_7$ (RE=Sm,Gd,Yb) materials using a glancing angle that provides an X-ray attenuation depth of 450 nm (Figure 4.5a) shows that the $RE_2Ti_2O_7$ materials show an increase in resistance to structural damage with decreasing radius of the RE cation. This assessment is based on the observation of a decrease in intensity of the pre-edge and an increase in the energy and intensity of the main-edge as the RE was changed from Sm to Gd to Yb. As the radius of the RE cation decreases and approaches the radius of Ti^{4+}, the tendency for the cations to undergo anti-site disorder increases and the materials are more likely to undergo a phase transition from the pyrochlore-type structure to the defect-fluorite-type structure because of ion implantation instead

of becoming amorphous.[41,87,198] The observation by GA-XANES that $Yb_2Ti_2O_7$ is more resistant to radiation induced damage compared to $Sm_2Ti_2O_7$ or $Gd_2Ti_2O_7$ is in agreement with previous studies that used TEM to monitor the radiation resistance of crystallites of these materials.[87]

The effect of metal substitution (A-site and B-site substitution) and the presence of oxygen vacancies on the structural stability of $Yb_2Ti_2O_7$ was studied by comparing the GA-XANES spectra from ion implanted $Yb_2Ti_2O_7$, $Yb_2Ti_{1.85}Fe_{0.15}O_{7-\delta}$, and $Yb_{1.85}Ca_{0.15}Ti_2O_{7-\delta}$ (Figure 4.5b). No significant differences in the spectra were observed, which suggests that the number of oxygen vacancies generated by a slight substitution of Ca^{2+} for Yb^{3+} or a slight substitution of Fe^{3+} for Ti^{4+} does not considerably affect the resistance of $Yb_2Ti_2O_7$ to radiation induced structural damage. This result was verified by analysis of Ti K-edge TEY-XANES spectra from the implanted materials (*vide infra*).

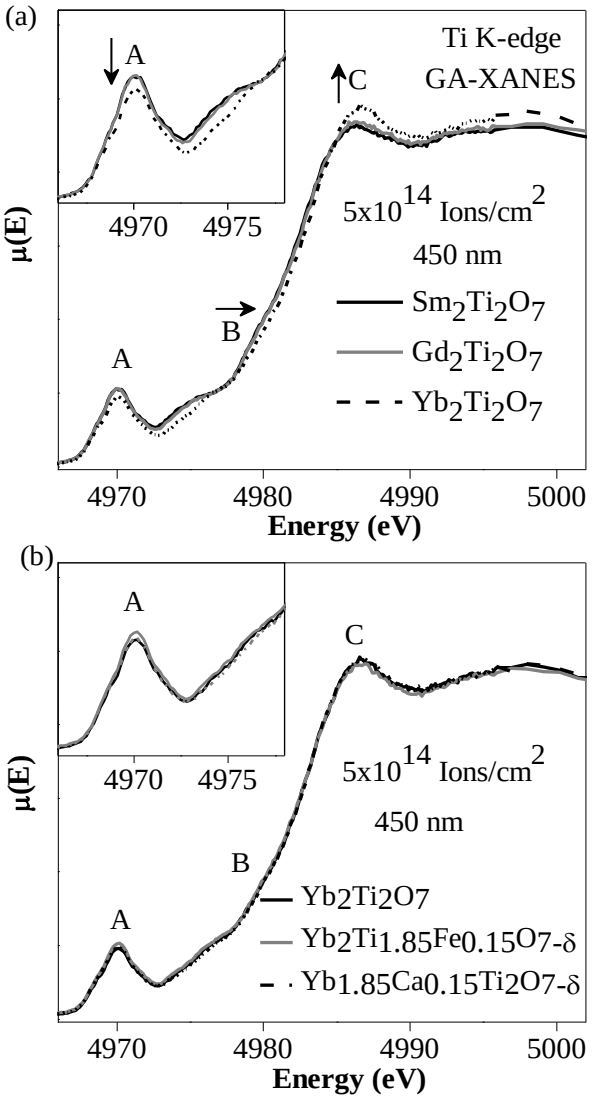

Figure 4.5 (a) Ti K-edge GA-XANES spectra from the implanted $(Sm,Gd,Yb)_2Ti_2O_7$ materials at a glancing angle providing an X-ray attenuation depth of 450 nm are shown. Arrows mark the changes observed in the spectra as the RE was changed from Sm to Gd to Yb. (b) Ti K edge GA-XANES spectra from ion implanted $Yb_2Ti_2O_7$, $Yb_2Ti_{1.85}Fe_{0.15}O_{7-\delta}$, and $Yb_{1.85}Ca_{0.15}Ti_2O_{7-\delta}$ are shown. The glancing angle used to collect these spectra was adjusted to give an X-ray attenuation depth of 450 nm

4.3.3.2 TEY-XANES

Surface sensitive Ti K-edge TEY-XANES spectra were also collected from the implanted materials. The TEY-XANES spectra from the implanted materials have been compared to the spectra from the undamaged materials, and the normalized spectra are shown in Figure 4.6. Charging effects can be problematic while acquiring TEY spectra from thick pellets of insulating materials.[119] These issues can be resolved by mounting the pellet to an electrically grounded sample holder using conductive silver paint to connect the surface of the pellet to the holder to increase the conductivity of the sample.[119,124,226] The effect of this mounting procedure on the quality of the TEY spectra collected is demonstrated in Figure 4.7 by comparison of Ti K-edge spectra before normalization from a pellet of ion implanted $Sm_2Ti_2O_7$ connected to the holder using only carbon tape or using carbon tape *and* silver paint.

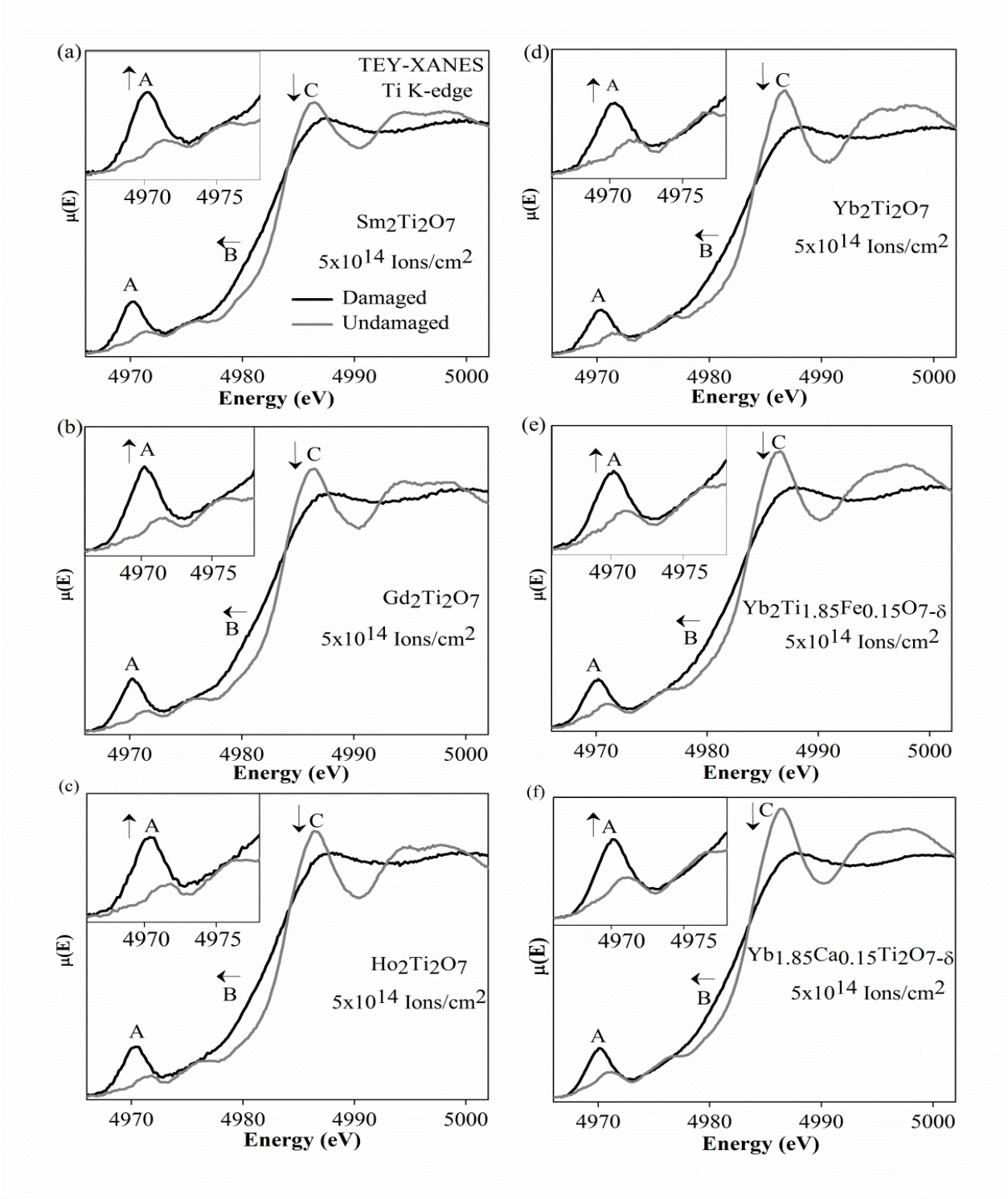

Figure 4.6 Ti K edge TEY-XANES spectra from (a) $Sm_2Ti_2O_7$, (b) $Gd_2Ti_2O_7$, (c) $Ho_2Ti_2O_7$, (d) $Yb_2Ti_2O_7$, (e) $Yb_2Ti_{1.85}Fe_{0.15}O_{7-\delta}$, and (f) $Yb_{1.85}Ca_{0.15}Ti_2O_{7-\delta}$ implanted to a dose of 5×10^{14} ions/cm^2 are shown along with the spectrum from the undamaged materials. The changes observed in the spectra because of implantation are indicated by arrows.

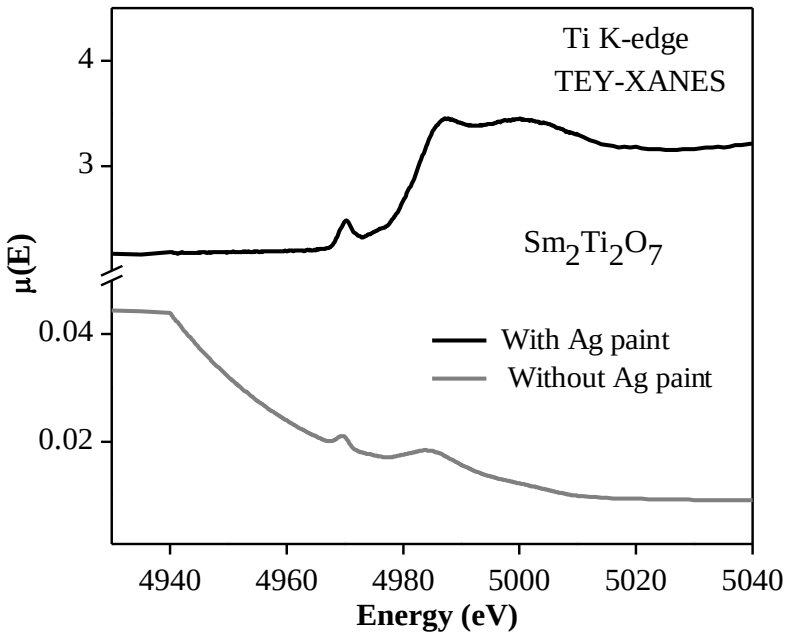

Figure 4.7 Ti K edge TEY-XANES spectra before normalization from a pellet of $Sm_2Ti_2O_7$ implanted to a dose of 5×10^{14} ions/cm^2 and connected to the sample holder using only carbon tape or using carbon tape *and* silver paint. The quality of the TEY spectrum collected was improved by mounting the pellet to the holder using conductive silver paint.

All of the features observed in the Ti K-edge TEY-XANES spectra from $RE_2Ti_2O_7$ (RE=Sm,Gd,Ho,Yb), $Yb_2Ti_{1.85}Fe_{0.15}O_{7-\delta}$, and $Yb_{1.85}Ca_{0.15}Ti_2O_{7-\delta}$ changed upon ion implantation (Figure 4.6). The reasons for the changes in the spectra from the ion-implanted materials are the same as those presented in Section 4.3.3.1, where the changes in the GA-XANES spectra were described. It should be noted that all of the TEY-XANES spectra were collected using the same angle of incidence of the X-rays to the surface of the pellets (~85^o). Because of this, it is difficult to compare how the spectra from the $RE_2Ti_2O_7$ materials changed depending on the RE cation present as the sampling depths were all slightly different. However, the spectra collected from ion implanted $Yb_2Ti_2O_7$, $Yb_2Ti_{1.85}Fe_{0.15}O_{7-\delta}$, and $Yb_{1.85}Ca_{0.15}Ti_2O_{7-\delta}$ *can* be compared, as the

substitution of the A- or B-site cation was minor and it is not expected that this would greatly affect the X-ray attenuation depth or the depth at which electrons would travel through the surface. A comparison of the TEY-XANES spectra from the implanted $Yb_2Ti_2O_7$, $Yb_2Ti_{1.85}Fe_{0.15}O_{7-\delta}$, and $Yb_{1.85}Ca_{0.15}Ti_2O_{7-\delta}$ materials (Figure 4.8) reveals no significant differences as a result of a slight substitution of Ca^{2+} for Yb^{3+} or Fe^{3+} for Ti^{4+}, which is in agreement with the equivalent GA-XANES spectra (see Figure 4.7b). The examination of GA-XANES and TEY-XANES spectra from these rare-earth titanate materials has shown that the damaged surface layer of ion implanted pellets could be studied using either measurement method.

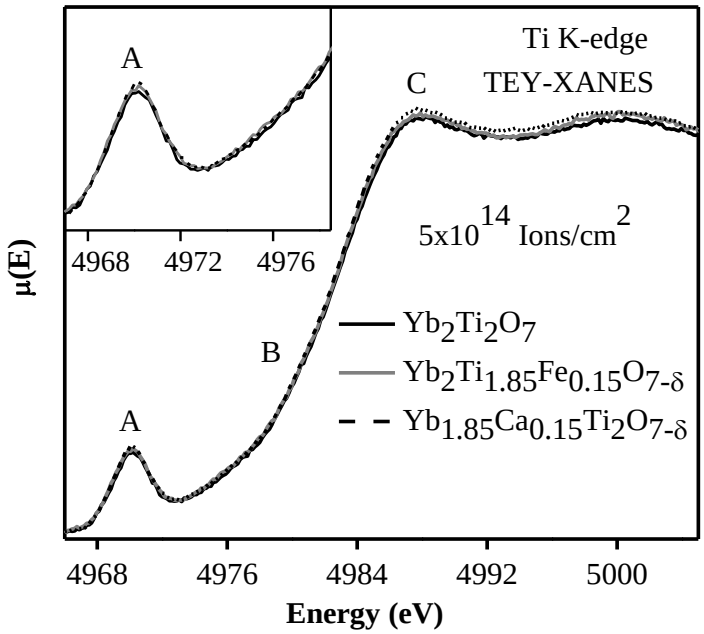

Figure 4.8 Ti K edge TEY-XANES spectra from the implanted $Yb_2Ti_2O_7$, $Yb_2Ti_{1.85}Fe_{0.15}O_{7-\delta}$, and $Yb_{1.85}Ca_{0.15}Ti_2O_{7-\delta}$ materials are shown. No significant changes were observed in the spectra from the implanted materials because of the partial substitution of Ti^{4+} for Fe^{3+} or Yb^{3+} for Ca^{2+}.

4.4 Conclusions

GA-XANES, TEY-XANES, and XRD have been used to study how the structural stability of pyrochlore-type oxides changes depending on composition. The examination of Ti K-edge XANES spectra from the implanted $RE_2Ti_2O_7$ materials has shown that these materials have a greater resistance to ion-induced structural damage with decreasing ionic radii of the RE cation, which is in agreement with the previous TEM study of these materials.[87] This study has also shown that oxygen vacancies generated in the structure of $Yb_2Ti_2O_7$ by a slight substitution of Yb^{3+} for Ca^{2+} or Ti^{4+} for Fe^{3+} does not significantly affect the radiation resistance of this material. An effective sample mounting procedure for collecting high quality TEY-XANES spectra from thick pellets was also reported in this study. This investigation has demonstrated the ability of GA-XANES and TEY-XANES to probe the surface layer materials that have been damaged by ion implantation. These techniques will be useful for the development of materials that can be used to sequester nuclear waste.

Chapter 5

Investigation of the structural stability of ion-implanted $Gd_2Ti_{2-x}Sn_xO_7$ pyrochlore-type oxides by glancing angle X-ray absorption spectroscopy*

5.1 Introduction

The previous Chapter has demonstrated the ability of GA-XANES to probe the surface layer of the materials that have been damaged by ion implantation. The investigation of $RE_2Ti_2O_7$ has shown that these materials have a greater resistance to ion induced structural damage with decreasing ionic radii of the RE ion and also that oxygen vacancies generated in the structure by a slight substitution does not significantly change the resistance. The present Chapter has focused on how the metal-oxygen bond interactions can affect the structural stability of a material upon ion beam implantation. This has been investigated by studying ion implanted $Gd_2Ti_{2-x}Sn_xO_7$. Chapter 3 investigated as-synthesized $Gd_2Ti_{2-x}Sn_xO_7$ and showed that the Gd-O and Ti-O bonds become more ionic while the Sn-O bonds become more covalent with increasing Sn incorporation. In the present Chapter, the changes in metal-oxygen bond interactions on the resistance to radiation induced damage have been investigated systematically from $Gd_2Ti_{2-x}Sn_xO_7$ using GA-XANES.

Rare-earth (RE: (La-Lu) and Y) titanate and stannate pyrochlore-type oxides have been investigated for nuclear waste sequestration applications in the past.[87,88,188] These materials can exhibit varying degrees of resistance to radiation induced structural damage depending on composition.[44,87,88,188] Radiation induced structural damage can be simulated by bombardment

* A version of this Chapter has been published. Reprinted with permission from Aluri, E. R.; Grosvenor, A.P. *J. Phys. Chem. C* **2014**, *118*, 7910-7922. © 2014 American Chemical Society doi**:** 10.1021/jp4095497

(implantation) of the materials using high-energy ion beams (e.g., Au^-, Kr^+, and Xe^+), which was discussed in Section 1.3. The response of $Gd_2Ti_{2-x}Zr_xO_7$, $Y_2Ti_{2-x}Sn_xO_7$, $RE_2Zr_2O_7$, $RE_2Sn_2O_7$ (RE=La-Lu), $RE_2Ti_2O_7$, and $Gd_2Hf_2O_7$ to ion beam implantation has been previously examined by use of one or more of the following techniques: transmission electron microscopy (TEM), X-ray absorption near-edge spectroscopy (XANES), extended X-ray absorption fine structure analysis (EXAFS), and powder X-ray diffraction (XRD).[83,86-88,189,212,227] These investigations have suggested that the resistance to ion beam induced amorphization is not only dependent on the relative sizes of the A- and B-site cations but also on the electronic structure of these materials. Studies of ion implanted $Gd_2Ti_{2-x}Zr_xO_7$ (and $Y_2Ti_{2-x}Sn_xO_7$) have shown that the resistance to ion beam induced structural damage increases with greater Zr content (and Sn content).[83,189,212] This observation shows the effect of cationic radii on the ability of a material to resist radiation induced damage. With increasing radius of the B-site cation, the r_A/r_B ionic radii decreases, which leads to the material becoming more likely to undergo a phase transformation from the pyrochlore-type structure to the defect fluorite structure instead of becoming amorphous after ion beam implantation.[83,189,212] Systematic ion beam implantation studies of $RE_2Zr_2O_7$, $RE_2Sn_2O_7$, and $RE_2Ti_2O_7$ have also demonstrated the importance of the A- and B-site ionic radius and bond covalency to the resistance of materials to radiation induced structural damage.[86-88] To increase the radiation resistance of a material, it is important to understand how both the electronic structure and local chemical environment affect this property.[82,87,88,228,229]

Ion implantation can produce an amorphous layer which is typically only a few hundred nm thick.[102] Hard X-ray XANES (or EXAFS) is not typically surface sensitive, but glancing angle XANES/EXAFS (GA-XANES/EXAFS) can be used to probe the amorphous (damaged) surface layer produced by the implantation of a material by an ion beam.[102,133,134]

GA-XANES and GA-EXAFS allow for the investigation of the bonding environment and the CN of the atoms in the damaged surface layer from these materials.[102,133,134,230] Very few studies have used GA-XANES or GA-EXAFS to study the damaged surface layer of materials (e.g., Pb^{2+} implanted $SrTiO_3$, and Kr^{+} implanted $CaZrTi_2O_7$ and $Gd_2Ti_2O_7$).[102,136,231] A combination of micro powder XRD (μ-XRD) and GA-XANES/EXAFS have been used in this study to investigate how the structural stability of ion-implanted $Gd_2Ti_{2-x}Sn_xO_7$ varies depending on Sn concentration. The primary objective of this study was to understand the importance of bond covalency to the structural stability of materials proposed for nuclear waste sequestration applications. This study has also demonstrated the ability of GA-XANES to identify changes in the local structural environment of transition-metals and main-group metals that are not easily identified by use of X-ray or electron diffraction alone.

5.2 Experimental

5.2.1 Synthesis

$Gd_2Ti_{2-x}Sn_xO_7$ (x = 0.0, 1.0, 2.0) was synthesized using the ceramic method. Gd_2O_3 (Alfa Aesar, 99.99%), TiO_2 (Alfa Aesar, 99.9%), and SnO_2 (Alfa Aesar, 99.9%) powders were mixed in stoichiometric amounts to synthesize $Gd_2Ti_{2-x}Sn_xO_7$, which was described in Chapter 3 (Section 3.2.1). $Gd_2Zr_2O_7$ and $Yb_2Ti_2O_7$ were also synthesized using the solid state reaction method described above to aid in analysis of the GA-XANES spectra and μ-XRD patterns. Gd_2O_3 (Alfa Aesar, 99.99%) and ZrO_2 (Alfa Aesar, 99.978%) powders were used to synthesize $Gd_2Zr_2O_7$ while Yb_2O_3 (Alfa Aesar, 99.9%) and TiO_2 (Alfa Aesar, 99.9%) powders were mixed in stoichiometric amounts to synthesize $Yb_2Ti_2O_7$. Pressed pellets were heated for several days ($Gd_2Zr_2O_7$-17 days; $Yb_2Ti_2O_7$-6 days) until phase purity was achieved. All materials were

quench cooled in air and the phase purity was confirmed by powder X-ray diffraction (XRD). Following examination by powder XRD, the phase-pure $Gd_2Ti_{2-x}Sn_xO_7$ and $Gd_2Zr_2O_7$ materials were repelleted uniaxially at 8 MPa and heated at 1400 ^oC over 3 days to increase the hardness of these pellets prior to ion beam implantation.

Powder XRD patterns from each sample were collected at room temperature using a PANalytical Empyrean X-ray diffractometer and a Cu $K\alpha_{1,2}$ X-ray source. Diffraction patterns used for Rietvield refinement were recorded in the 2θ range of 10-120^o using a step size of 0.008^o. The High Score Plus Software package was employed to perform a Reitvield refinement of the data from the synthesized (undamaged) materials.[150] The lattice constants, the x-coordinate of O in the 48f position (x_{48f}), the overall thermal factor, and the line shape were refined during the analysis. It was found that the best results were determined when the isotropic thermal factors for each atom were constrained to 0.10 $Å^2$ with the overall thermal factor (B overall) being allowed to vary.

5.2.2 Ion beam implantation

Ion beam implantation of $Gd_2Ti_{2-x}Sn_xO_7$ (x = 0.0, 1.0 and 2.0) and $Gd_2Zr_2O_7$ was performed using the 1.7 MeV Tandetron accelerator located at ISW. The sintered pellets of $Gd_2Ti_{2-x}Sn_xO_7$ were implanted at room temperature with 2 MeV Au^- ions to a fluence (dose) of 1×10^{15} and 5×10^{15} ions/cm^2, and the $Gd_2Zr_2O_7$ pellet was irradiated to a fluence of 5×10^{15} ions/cm^2. The ion beam was aligned approximately normal to the pellet surface during implantation, as was discussed in Section 4.2.2.

Ion range and damage event depth profiles of the implanted samples were calculated using the Stopping and Range of Ions in Matter (SRIM-2013) software package.[220] These

calculations were performed using 5000 Au^- ions with the ion beam energy being 2 MeV and by assuming the target (Gd,Ti,Sn,O) displacement energies being 25 eV (Gd,Ti,Sn) and 28 eV (O). The densities (ρ) of $Gd_2Ti_{2-x}Sn_xO_7$ (x = 0.0, 1.0 and 2.0) and $Gd_2Zr_2O_7$ used in depth profile calculations were 6.57 g/cm^3, 7.15 g/cm^3, 7.72 g/cm^3, and 6.91 g/cm^3, respectively.[88,198,200] The calculations predicted that the ion beam implants to a depth of 100-450 nm for all samples (Figure 5.1and Figure A3.1).

5.2.3 Micro X-ray diffraction

The ion implanted $Gd_2Ti_{2-x}Sn_xO_7$ (x = 0.0, 1.0 and 2.0) and $Gd_2Zr_2O_7$ pellets were analyzed using μ-XRD to determine how the long-range structure of these pyrochlore-type materials changed after ion implantation. The μ-XRD patterns were collected using the PANalytical Empyrean X-ray diffractometer described in Section 5.2.1 and diffraction patterns were collected in the 2θ range of 10-55^o. The X-ray beam spot size was reduced to 200 μm using a mono-capillary collimator to perform this analysis. For experimental details on the collection of μ-XRD were discussed in Section 4.2.3.

5.2.4 XANES/EXAFS

The Ti K-, Sn L_3- and Gd L_3-edge GA-XANES spectra (and Ti K-edge GA-EXAFS spectra) were collected from $Gd_2Ti_{2-x}Sn_xO_7$, $Gd_2Zr_2O_7$, and $Yb_2Ti_2O_7$ using the Pacific Northwest Consortium/X-ray Science Division Collaborative Access Team (PNC/XSD-CAT, Sector 20) bending magnetic beamline (20BM) located at the Advanced Photon Source (APS), Argonne National Laboratory.[195] The resolution of the spectra is 0.5 eV at 3929 eV (Sn L_3-edge), 0.7 eV at 4966 eV (Ti K-edge), and 1.0 eV at 7000 eV (Gd L_3-edge).[151,195] The X-ray beam was vertically focused to yield a beam height of 45 μm and slits were used to confine the width of the

beam to 2 mm to perform the GA-XANES/EXAFS analysis of the ion implanted samples. The experimental details for GA-XANES set-up were already discussed in Section 4.2.4. The effect of changing the glancing angle on the attenuation depth of X–rays having specific excitation energies was calculated using the web-based program identified in reference 218 (see Figure 5.1a and Table 5.1). All spectra were collected in fluorescence mode by use of a single element vortex silicon drift detector. The GA-XANES spectra reported here for the implanted materials were collected in fluorescence mode (instead of transmission mode) because of the thickness (~1-2 mm) of the implanted pellets, and because only the near-surface region of the material was damaged by ion implantation. The XANES spectra were collected using a step size of 0.15 eV through the Ti K-, Sn L_3-, and Gd L_3-edges. The Ti K-edge GA-EXAFS spectra from $Gd_2Ti_{2-x}Sn_xO_7$ were collected to k = 13 $Å^{-1}$. The Ti K-edge spectra were calibrated using Ti metal (4966.0 eV); the Sn L_3-edge spectra were calibrated using Sn metal (3929.0 eV); and the Gd L_3-edge spectra were calibrated using Gd_2O_3 (7243.0 eV).[151] The absorption-edge energy of Gd_2O_3 was determined by calibrating the spectrum from this oxide using Fe metal foil, with the Fe K-edge absorption edge energy set to 7110.0 eV.[151]

A Ti K-edge XANES spectrum from a powdered sample of $Yb_2Ti_2O_7$ was also measured using the Soft X-ray Microcharacterization beamline (SXRMB, 06B1-1) at the Canadian Light Source to determine if the Ti K-edge GA-XANES spectra collected in fluorescence mode were affected by absorption effects.[153] The experimental details and sample preparation were discussed in Section 2.2.2. The spectrum was collected in total electron yield mode (TEY). All XANES/EXAFS spectra reported in this study were analyzed using the Athena software program.[152]

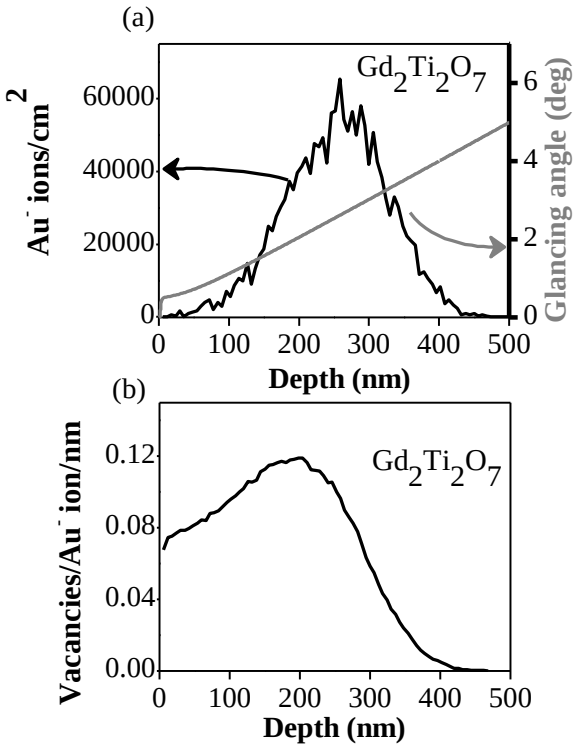

Figure 5.1 (a) An ion beam implantation depth profile and (b) vacancies per ion depth profile of $Gd_2Ti_2O_7$ calculated using SRIM-2013 is shown.[220] The calculation was performed using 5000 Au^- ions with the ion beam energy being 2 MeV and by assuming the target (Gd,Ti,Sn,O) displacement energies being 25 eV (Gd,Ti,Sn) and 28 eV (O).[220] A plot of glancing angle vs. X-ray attenuation depth for $Gd_2Ti_2O_7$ is also included in the figure and was calculated for photons having an energy of 4966 eV (Ti K-edge).[151,221]

Table 5.1 Calculated glancing angles required to give specific X-ray attenuation depths for photons having energies of 3929 eV (Sn L_3-edge), 4966 eV (Ti K-edge), and 7243 eV (Gd L_3-edge)

	Sn L_3-edge (3929 eV)		Ti K-edge (4966 eV)		Gd L_3-edge (7243 eV)	
Sample	X-ray attenuation depth (nm)	Glancing angle (^{o})	X-ray attenuation depth (nm)	Glancing angle (^{o})	X-ray attenuation depth (nm)	Glancing angle (^{o})
$Gd_2Ti_2O_7$	-	-	100	1.1	100	1.2
	-	-	450	4.5	450	5.3
Gd_2TiSnO_7	100	2.6	100	1.7	100	1.3
	450	11.2	450	7.3	-	-
$Gd_2Sn_2O_7$	100	3.2	-	-	100	1.5
	450	14.1	-	-	-	-
					2864	45
$Gd_2Zr_2O_7$	-	-	-	-	100	1.2
					3717	45
$Yb_2Ti_2O_7$	-	-	100	1.5	-	-
	-	-	450	6.1	-	-
	-	-	3013	45	-	-

5.3 Results and discussion

5.3.1 Powder X-ray diffraction before and after ion implantation

Powder XRD and μ-XRD patterns from the $Gd_2Ti_{2-x}Sn_xO_7$ (x = 0.0, 1.0 and 2.0) and $Gd_2Zr_2O_7$ samples before (bulk powder XRD) and after (μ-XRD) being implanted by Au^- ions to a dose of 1×10^{15} ions/cm^2 or 5×10^{15} ions/cm^2 are shown in Figure 5.2. The lattice constants of the undamaged $Gd_2Ti_{2-x}Sn_xO_7$ materials increased with greater Sn^{4+} incorporation, as was described in Chapter 3 (Section 3.3.1). The diffraction patterns of pyrochlore-phase materials differ from those from defect-fluorite phase materials only in the presence of superstructural peaks (odd lattice planes).[192,200,222,223] The intensity of these superstructural peaks is strongly

correlated with site occupancies and atomic positions within the pyrochlore structure, and are also affected by differences in the scattering power between the A- and B-site cations.[89,200,192] A decrease in the intensity of the superstructural peaks is generally indicative of cation anti-site disorder, which results in a phase transition from the pyrochlore to the defect fluorite structure.[200,222] Rietvield refinement results of the powder XRD patterns collected from the undamaged $Gd_2Ti_{2-x}Sn_xO_7$ and $Gd_2Zr_2O_7$ samples are shown in Figure A3.2 and Table A3.1 in Appendix 3. These refinements show that all $Gd_2Ti_{2-x}Sn_xO_7$ materials were single phase and confirmed that the materials adopted the pyrochlore-type structure. However, the low intensities of the superstructural peaks observed in the diffraction pattern of undamaged $Gd_2Zr_2O_7$ (Figure 5.2d) are indicative of a mixture of pyrochlore and defect fluorite phases being present. The concentration of pyrochlore and defect-fluorite phases in the $Gd_2Zr_2O_7$ material was estimated by Rietvield refinement to be 66.1% and 33.9%, respectively (Table A3.1). The refined parameters for the pyrochlore and defect-fluorite structures used to describe $Gd_2Zr_2O_7$ are in good agreement with those reported previously.[83,191,200,232] The amount of cation anti-site disorder observed previously in $Gd_2Sn_2O_7$ is considerably less (~ 5 % in $Gd_2Sn_2O_7$) than that observed in $Gd_2Zr_2O_7$, which is attributed to the covalency of the bond between O^{2-} and the B-site Sn^{4+} ions.[79,89,200] The decrease in intensity of the superstructural peaks in the powder XRD patterns from undamaged $Gd_2Ti_{2-x}Sn_xO_7$ with increasing x (Figure 5.2 and Figure A3.3) is a result of a decrease in the difference in scattering power between the A- and B-site cations with increasing Sn concentration, and is not a result of significant cation anti-site disorder being present.[89,200]

Examination of the diffraction patterns from the $Gd_2Ti_{2-x}Sn_xO_7$ and $Gd_2Zr_2O_7$ materials before and after implantation provides important information on how the structure of these materials is affected by ion implantation (Figure 5.2). The diffraction patterns from the implanted samples clearly show a broadening of the diffraction peaks (e.g., the (222) diffraction peak) when compared to the diffraction patterns from the undamaged materials. The full width at half maximum (FWHW) of the (222) peak from $Gd_2Ti_{2-x}Sn_xO_7$ increases with greater Sn content (see Table 5.2). Diffraction peaks can broaden for multiple reasons, which include the presence of defects.[105] The production of defects in the materials because of ion beam implantation likely contributed to the increased width of the diffraction peaks observed here. However, it would also be expected that the average crystallite size would decrease because of ion beam induced damage, which would also result in an increase in the width of the diffraction peaks. The increase in the intensity of the hump located near the (222) diffraction peak (~30^o) in the diffraction patterns from the implanted $Gd_2Ti_{2-x}Sn_xO_7$ materials also shows that these materials become partially amorphous with increasing dose (i.e., 1×10^{15} ions/cm^2 to 5×10^{15} ions/cm^2).[200] Comparison of the μ-XRD patterns from the $Gd_2Ti_{2-x}Sn_xO_7$ and $Gd_2Zr_2O_7$ samples that were implanted to the same dose (5×10^{15} ions/cm^2; Figure 5.2) shows that $Gd_2Ti_{2-x}Sn_xO_7$ becomes partially amorphous while the diffraction pattern from implanted $Gd_2Zr_2O_7$ does not show an amorphous hump at ~30^o. This observation is a result of the fact that $Gd_2Zr_2O_7$ prefers to undergo a phase transition to the defect fluorite structure upon ion implantation rather than become amorphous.[83] This can be further observed by the loss of the super structural peaks in the diffraction pattern from the damaged (implanted) $Gd_2Zr_2O_7$ sample compared to the diffraction pattern from the undamaged sample (Figure 5.2d).[83]

The decrease in intensity of the super structural peaks observed in the diffraction patterns from the implanted $Gd_2Ti_2O_7$ and Gd_2TiSnO_7 samples (Figure 5.2a,b) suggests that along with becoming partially amorphous, some of the crystallites undergo a pyrochlore to defect fluorite phase transition. However, the diffraction pattern from $Gd_2Sn_2O_7$ implanted to a dose of 5×10^{15} ions/cm^2 shows (Figure 5.2c) peaks that are not easily described by materials having the ordered cubic pyrochlore–type structure. The change in the μ-XRD pattern from $Gd_2Sn_2O_7$ (Figure 5.2c) implanted to a dose of 5×10^{15} ions/cm^2 could be a result of some of the sample decomposing to a mixture of binary oxides. The unidentified peaks were compared to all known structures of oxides containing Gd and Sn, with only the diffraction pattern from SnO being comparable. The Sn oxidation state is 2+ in SnO but the Sn L_3-edge XANES spectra collected from this material suggests that only Sn^{4+} is present (*vide infra*, Section 5.3.2.3), which rules out the presence of this binary oxide. It is also possible that the change in the diffraction pattern from $Gd_2Sn_2O_7$ implanted to a dose of 5×10^{15} ions/cm^2 compared to the undamaged material is a result of the pyrochlore structure being distorted by anion disordering. This would result in a contraction of the unit cell and a shift of the most intense reflection to higher 2θ. This type of disordering has been observed previously during studies of the effect of high pressures on $(Gd,Sm)_2Ti_2O_7$ and $Gd_2Zr_2O_7$.[82,198,233]

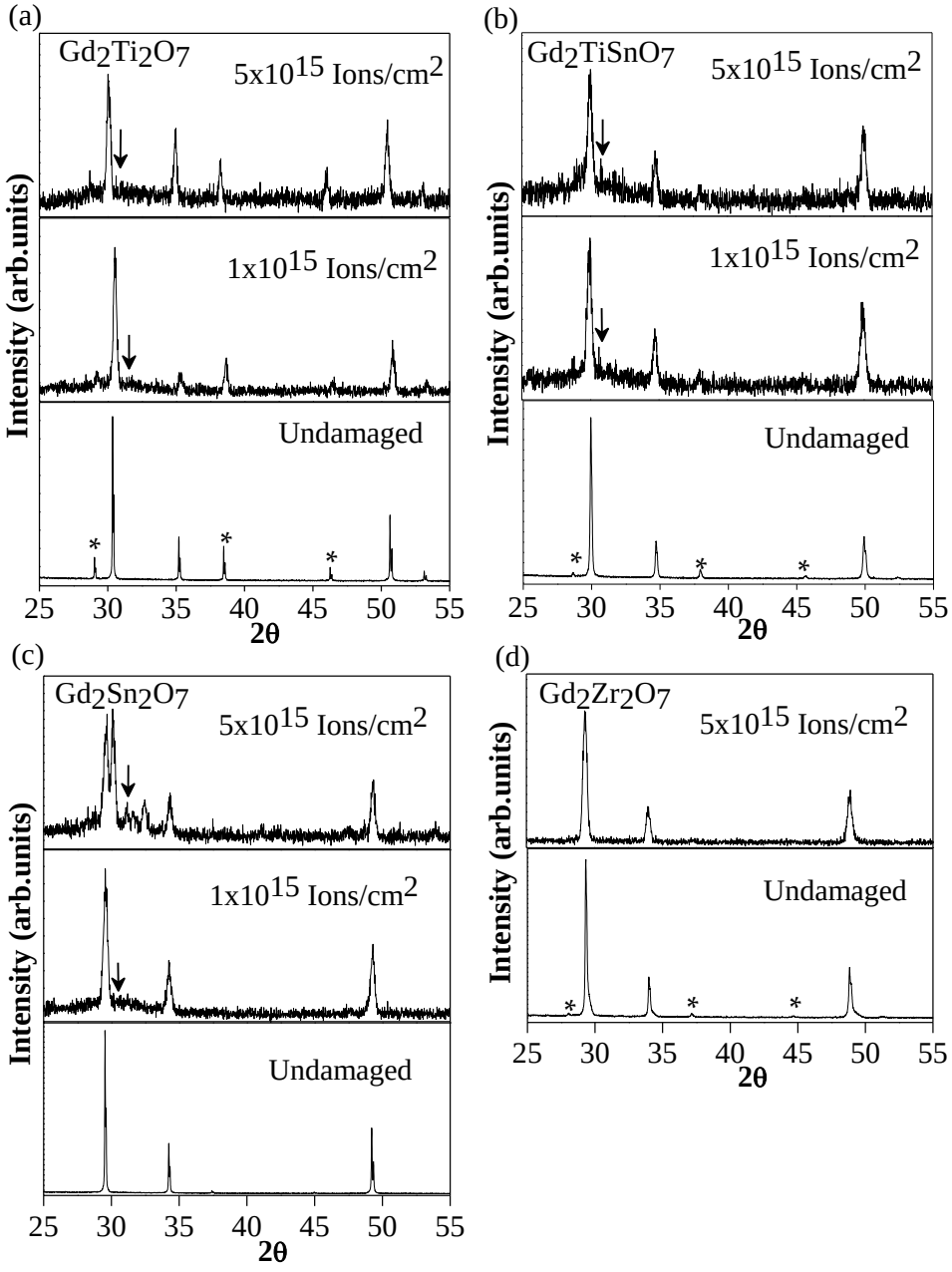

Figure 5.2 Bulk and micro powder XRD patterns from (a) $Gd_2Ti_2O_7$, (b) Gd_2TiSnO_7, and (c) $Gd_2Sn_2O_7$ samples are shown before and after the materials were implanted to a dose of 1×10^{15} ions/cm^2 or 5×10^{15} ions/cm^2 by a beam of Au^- ions. (d) Bulk and micro-powder XRD patterns from $Gd_2Zr_2O_7$ are shown before and after implantation to a dose of 5×10^{15} ions/cm^2 by a beam of Au^- ions. Super structural peaks from the pyrochlore-type structure are marked by an asterisk (*). The amorphous hump located near the (222) diffraction plane is identified by an arrow.

Table 5.2 Lattice constants from the undamaged $Gd_2Ti_{2-x}Sn_xO_7$ and $Gd_2Zr_2O_7$ materials assuming a pyrochlore-type structure are presented along with the full width at half maximum (FWHM) of the (222) peak from the diffraction pattern from the undamaged and damaged materials

	Undamaged		Dose: 1×10^{15} ions/cm^2	Dose: 5×10^{15} ions/cm^2
Sample	a (Å)	FWHM of the (222) diffraction peak (^{o})	FWHM of the (222) diffraction peak (^{o})	FWHM of the (222) diffraction peak (^{o})
$Gd_2Ti_2O_7$	10.1851(4)	0.0440	0.266	0.310
Gd_2TiSnO_7	10.3235(1)	0.1015	0.318	0.353
$Gd_2Sn_2O_7$	10.46066(3)	0.0514	0.358	0.370
$Gd_2Zr_2O_7$	10.5368(1)	0.0914	-	0.347

5.3.2 GA-XANES and GA-EXAFS

Whereas powder XRD allows for an investigation of how the long-range crystal structure changes after ion implantation, GA-XANES and GA-EXAFS allow for an investigation of how the local chemical environment of the atoms in the structure change depending on composition and ion implantation dose.[102,133,134] As was indicated in Section 5.2.2 (and shown in Figure 5.1 and Figure A3.1), the 2 MeV Au^- ions penetrated to a maximum depth of ~450 nm in the $Gd_2Ti_{2-x}Sn_xO_7$ and $Gd_2Zr_2O_7$ pellets. As all of the Au^- ions penetrate through the near-surface region (<100 nm), it would be expected that this region of the samples would experience more damage compared to deeper within the surface where the Au^- ions implant. Ti K-, Sn L_3-, and Gd L_3-edge GA-XANES spectra (and Ti K-edge GA-EXAFS spectra) were collected at glancing angles providing X-ray attenuation lengths of 100 nm and 450 nm (Table 5.1), as well as at 45^o (resulting in a bulk measurement of the sample), to determine the effect of ion implantation on the local coordination environment of the metal ions in $Gd_2Ti_{2-x}Sn_xO_7$.

5.3.2.1 Ti K-edge GA-XANES

Normalized Ti K-edge XANES spectra from $Gd_2Ti_{2-x}Sn_xO_7$ (x = 0,1) samples implanted to a dose of 1×10^{15} ions/cm^2 or 5×10^{15} ions/cm^2 and collected using different glancing angles are presented in Figures 5.3 and 5.4. The spectra from the undamaged materials, which were presented previously in Chapter 3 (Figure 3.2), are also presented in these figures. The Ti K-edge XANES spectra contain both pre-edge and main-edge excitations, which are labeled as features A, B, and C in Figures 5.3 and 5.4. The pre-edge feature (A) arises from weak, quadrapolar 1s→3d transitions and three features are observed in this region (labeled as A_1, A_2, and A_3), which result from both local and non-local excitations.[159,161,176,177] The main-edge (B and C) results from dipole allowed 1s→4p transitions.[159,177] A detailed description for these features were discussed in Section 3.3.2. Above the absorption edge, the core electron is promoted to continuum states and can be back scattered by atoms located in coordination shells surrounding the absorbing atom, resulting in constructive and destructive interference that creates structured oscillations in the spectrum. These oscillations are known as the EXAFS and will be discussed in Section 5.3.2.2.[201]

All GA-XANES spectra reported here for the implanted materials were collected in fluorescence mode (instead of transmission mode) because of the thickness of the implanted pellets (~1-2 mm), and because only the near-surface region of the material was damaged by ion implantation. The intensity of peaks in XANES spectra can be attenuated by absorption effects when collected in this mode, with stronger peaks usually being more attenuated than weaker peaks.[112,120,201] A previous GA-XANES study of ion implanted $Gd_2Ti_2O_7$ suggested that absorption effects could affect Ti K-edge XANES spectra and that the data required correction before analysis.[136] The influence of absorption effects on the Ti K-edge GA-XANES spectra

from the implanted $Gd_2Ti_{2-x}Sn_xO_7$ materials reported here has been tested by comparing GA-XANES spectra from an undamaged pellet of $Yb_2Ti_2O_7$ (Figure 5.5). No significant changes were observed in any of the GA-XANES spectra, even when compared to a spectrum of powdered $Yb_2Ti_2O_7$ collected in total electron yield mode. A comparison of Ti K-edge XANES spectra collected in transmission and fluorescence modes from $Gd_2Ti_2O_7$ (Figure A3.4) also showed little difference between the spectra. These comparisons show that absorption effects do not significantly affect the Ti K-edge GA-XANES spectra and that no data correction is required.

All of the features observed in the Ti K-edge GA-XANES spectra from the $Gd_2Ti_{2-x}Sn_xO_7$ samples changed significantly upon ion implantation (Figures 5.3 and 5.4). The intensity of the pre-edge peak (A) increased while the intensity of the main-edge peak (C) decreased; the absorption energy of feature B also decreased (slightly) upon implantation. All of these changes are indicative of a change in the local coordination environment of Ti.[178,129-132] As was stated above, the pre-edge features result from 1s→3d transitions; however, even a small mixing of p- and d-states can lead to a large increase in the pre-edge intensity by increasing the dipolar character of the transition.[129-132,159,232] It has been observed previously that a decrease in CN and/or a distortion of the local coordination environment can lead to an increased mixing of the p- and d-states, which results in an increase in the pre-edge peak intensity.[53, 62,64,70-74] It could be argued that an increase in the CN from 6 to 8 would also result in greater p-d mixing, which should also result in an increase in the intensity of the pre-edge peak. (This increase in CN could result from the B-site Ti atoms being disordered into the 8-coordinate A-site.) Examination of the main-edge features can be useful when studying the transition-metal K-edge XANES spectra from a series of materials having a similar composition and structure when trying to determine how the CN changes. A decrease in the energy and intensity of main-edge features from

transition-metal K-edge XANES spectra have been shown and described in the previous Chapters (Sections 2.3.2, 2.3.4, and 4.3.3.1) to be a result of a decrease in the CN of the transition-metal being analysed.[130] A decrease in energy and intensity of the main-edge features (B,C) in the spectra presented in Figures 5.3 and 5.4 from the damaged materials implies a decrease in CN with decreasing glancing angle.

The spectral changes observed in Figures 5.3 and 5.4 clearly suggest that the Ti CN decreased in the implanted samples at all doses as compared to the spectra from undamaged $Gd_2Ti_2O_7$ and Gd_2TiSnO_7. The average decrease in CN of these implanted materials can be determined by comparing the spectra to previously reported Ti K-edge XANES spectra from systems having well defined Ti coordination environments.[129-132] Comparison of the intensity and energy of the pre-edge region of the spectra from the implanted materials to previously reported spectra suggests that the local CN of Ti decreased from 6 in the undamaged materials to a mixture of 6- and 5-coordinate Ti, and possibly also 4-coordinate Ti, in the implanted samples.[129-132] (A distortion of the Ti coordination environment could also contribute to the observed change in pre-edge intensity.) It should be noted that as the XANES spectra presented here probe to depths of $\geq$100 nm, it is not believed that significant loss of O^{2-} occurs because of ion implantation. Because of this, the observed reduction of the Ti CN (and likely distortion of the Ti coordination environment) does not suggest that the materials become O-deficient, but instead that the atoms located in the near-surface region of the materials studied become disordered upon ion implantation.

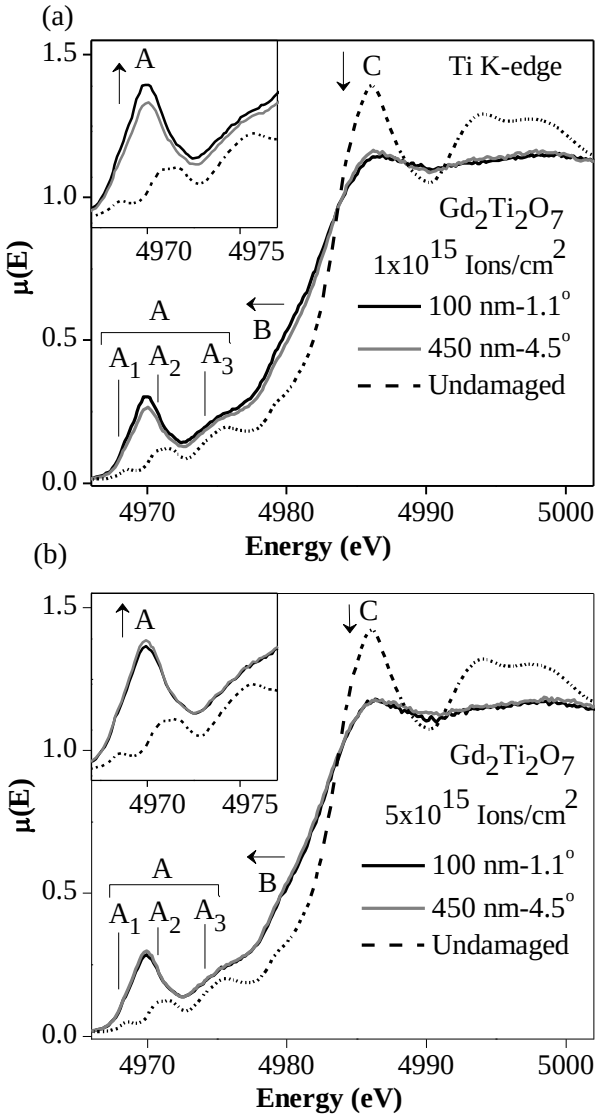

Figure 5.3 (a) Ti K-edge GA-XANES spectra collected at various glancing angles from $Gd_2Ti_2O_7$ implanted to a dose of 1×10^{15} ions/cm^2 are compared to the spectrum from the undamaged sample. The angles listed, 1.1^o and 4.5^o, are the glancing angles used to attain X-ray penetration depths of 100 and 450 nm, respectively. The pre-edge region is shown in the inset. The arrows show the change in intensity of features A and C, and the change in energy of feature B that occurs with decreasing glancing angle (decreasing X-ray attenuation depth). (b) Ti K-edge GA-XANES spectra from $Gd_2Ti_2O_7$ implanted to a dose of 5×10^{15} ions/cm^2 along with the spectrum from the undamaged sample are shown. The changes of the features observed in the spectra with decreasing glancing angle (decreasing X-ray attenuation depth) are marked by arrows.

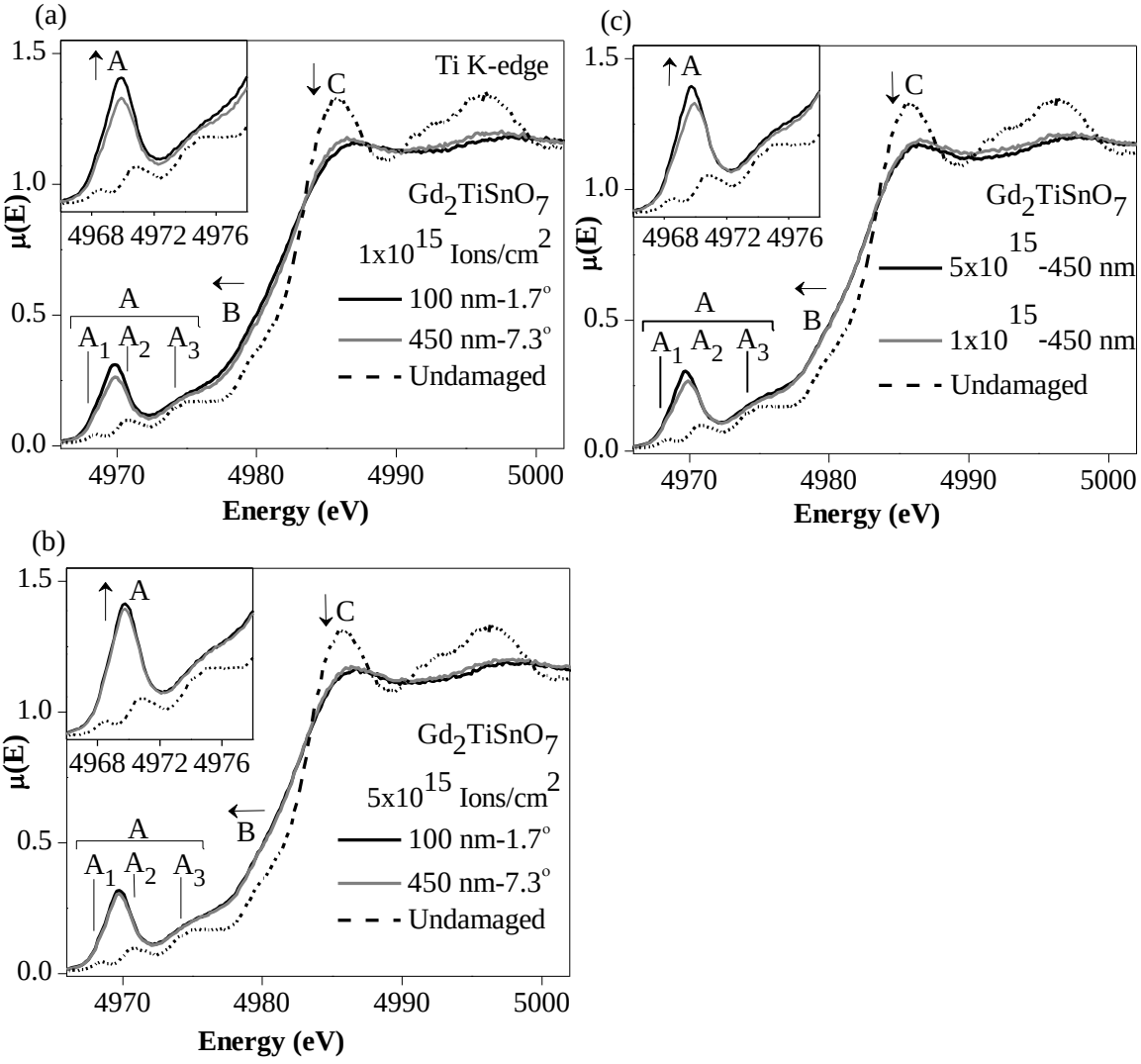

Figure 5.4 (a) Ti K-edge GA-XANES spectra collected at various glancing angles from Gd_2TiSnO_7 implanted to a dose of 1×10^{15} ions/cm^2 are shown along with the spectrum from the undamaged sample. The angles listed, 1.7^o and 7.3^o, are the glancing angles used to attain X-ray penetration depths of 100 and 450 nm, respectively. The changes observed in the spectra with decreasing glancing angle are indicated by arrows. (b) Ti K-edge GA-XANES spectra from Gd_2TiSnO_7 implanted to a dose of 5×10^{15} ions/cm^2 are shown along with the spectrum from the undamaged sample. (c) Ti K-edge GA-XANES spectra from Gd_2TiSnO_7 implanted to a dose of 1×10^{15} ions/cm^2 and 5×10^{15} ions/cm^2 are compared along with the spectrum from the undamaged material. The changes observed with increasing dose are marked by arrows.

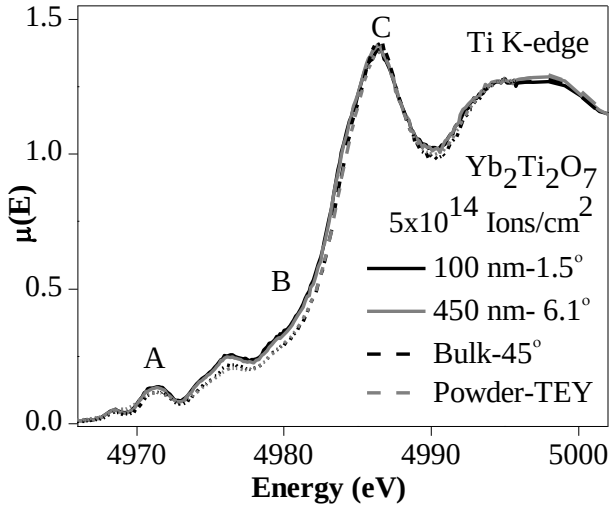

Figure 5.5: Ti K-edge GA-XANES spectra collected at different glancing angles from an undamaged pellet of $Yb_2Ti_2O_7$ and measured in fluorescence mode are shown. The spectra have also been compared to a spectrum from powdered $Yb_2Ti_2O_7$ collected in TEY mode. No significant differences between the spectra were observed.

Examination of the GA-XANES spectra from the $Gd_2Ti_2O_7$ and Gd_2TiSnO_7 materials implanted to a dose of 1×10^{15} ions/cm^2 (Figures 5.3a and 5.4a) shows that more damage occurs near the surface compared to deeper into the material. However, when a higher dose (5×10^{15} ions/cm^2) was used (Figures 5.3b and 5.4b), the spectra collected at glancing angles giving X-ray attenuation depths of 100 nm and 450 nm were very similar (i.e., a higher dose results in more damage occurring at deeper depths). Further, a comparison of the GA-XANES spectra from Gd_2TiSnO_7 implanted to a dose of 1×10^{15} ions/cm^2 and 5×10^{15} ions/cm^2 (Figure 5.4c) shows that the damage experienced by the material increases with greater dose. Examination of the GA-XANES spectra from Gd_2TiSnO_7 and $Gd_2Ti_2O_7$ implanted to a dose of 5×10^{15} ions/cm^2 (Figure 5.6a) also shows that the $Gd_2Ti_{2-x}Sn_xO_7$ system becomes more

susceptible to radiation induced structural damage with increasing Sn concentration, as can be easily observed by the increase in intensity of the pre-edge with increasing Sn concentration. However, it should be noted that a much smaller difference was observed between the GA-XANES spectra from Gd_2TiSnO_7 and $Gd_2Ti_2O_7$ when the materials were implanted to a lower dose (Figure 5.6b).

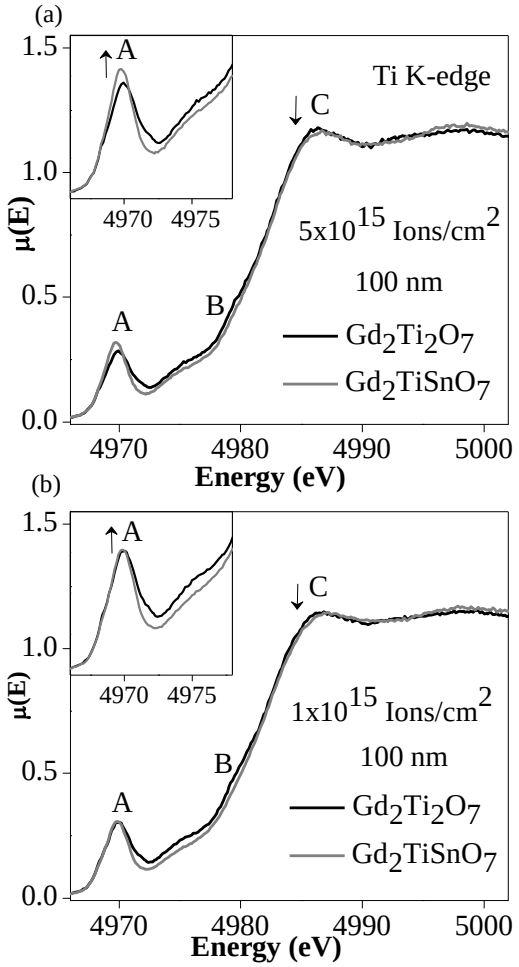

Figure 5.6: (a) Ti K-edge GA-XANES spectra from $Gd_2Ti_2O_7$ and Gd_2TiSnO_7 implanted to a dose of 5×10^{15} ions/cm^2. The glancing angle used to collect these spectra was adjusted to give an X-ray attenuation depth of 450 nm. The changes observed with increasing Sn content are marked by arrows. (b) Ti K-edge GA-XANES spectra from $Gd_2Ti_2O_7$ and Gd_2TiSnO_7 implanted to a dose of 1×10^{15} ions/cm^2 are shown.

5.3.2.2 Ti K-edge GA-EXAFS

Ti K-edge GA-EXAFS spectra were also examined to confirm the effect of ion-beam implantation on the structure of the materials investigated. The Fourier transforms of the Ti K-edge GA-EXAFS spectra collected from the $Gd_2Ti_2O_7$ and Gd_2TiSnO_7 materials implanted to a dose of 1×10^{15} ions/cm^2 or 5×10^{15} ions/cm^2 are shown in Figure 5.7. The intense peak labeled as D results from scattering of electrons by O^{2-} ions in the first coordination shell and the peak labeled as E represents scattering by the second coordination shell, which contains Gd/Ti/Sn. These two features change significantly upon implantation. The spectra presented in Figure 5.7 show a decrease in intensity of the first coordination shell peak (D) and the disappearance of the peak representing scattering from the second coordination shell (E) in the implanted samples at all doses when compared to the spectra from the undamaged materials.[179,212] The disappearance of the second coordination shell peak in the implanted samples confirms the analysis of the μ-XRD patterns (i.e., that the materials become partially amorphous after ion implantation). The decrease in intensity of peak D confirms the observation from the GA-XANES spectra that the Ti CN is reduced after implantation.[176,209] As was suggested in Section 5.3.2.1, the Ti coordination environment may also become distorted as a result of ion implantation, which would contribute to the reduction in amplitude of peak D observed for the EXAFS spectra from the damaged materials compared to the EXAFS spectra for the undamaged materials.

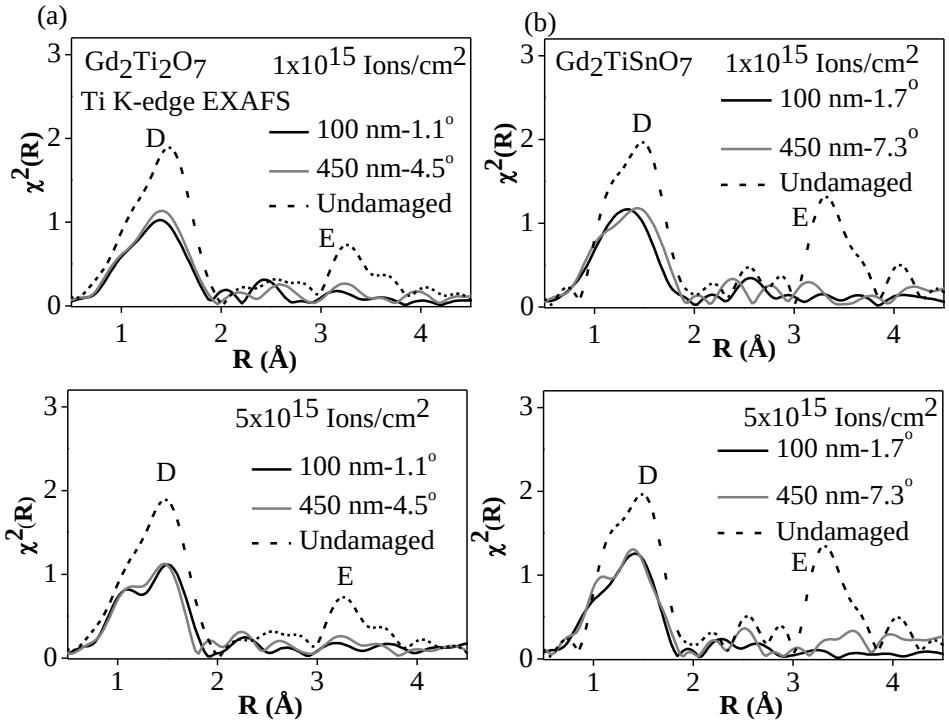

Figure 5.7: (a) Ti K-edge GA-EXAFS spectra from $Gd_2Ti_2O_7$ implanted to a dose of 1×10^{15} ions/cm^2 or 5×10^{15} ions/cm^2 are shown. The intense peak labeled as D arises from scattering by the first coordination shell while the peak labeled as E results from scattering by the second coordination shell, which contains Gd/Ti/Sn. (b) The Ti K-edge GA-EXAFS spectra from Gd_2TiSnO_7 implanted to a dose of 1×10^{15} ions/cm^2 or 5×10^{15} ions/cm^2 are shown.

5.3.2.3 Sn L_3-edge GA-XANES

The effect of ion implantation on the structure of the $Gd_2Ti_{2-x}Sn_xO_7$ materials was further investigated by examination of Sn L_3-edge XANES spectra. The normalized Sn L_3-edge XANES spectra collected at different glancing angles from the $Gd_2Ti_{2-x}Sn_xO_7$ samples implanted by Au^- ions to a dose of 1×10^{15} ions/cm^2 or 5×10^{15} ions/cm^2 are presented in Figures 5.8 and 5.9. The spectra are compared in the figures to the previously discussed XANES spectra (Section 3.3.3, Figure 3.6) from the undamaged materials, which allows for a study of the distortion of the Sn

site that occurs as a result of ion implantation. The spectra primarily result from $2p_{3/2} \rightarrow 5s$ (Feature A) and $2p_{3/2} \rightarrow 5d$ (Feature B) excitations, respectively.[207-209] A broader peak (C) is observed at higher energies (~3960 eV), which has been attributed to multi-scattering resonances.[207-209] Comparison of spectra from the undamaged Gd_2TiSnO_7 material collected in fluorescence and transmission modes (Figure A3.5) show that the fluorescence spectra are not influenced by absorption effects, as was also the case for the Ti K-edge GA-XANES spectra discussed earlier.

The Sn L_3-edge XANES spectra have been found to be very sensitive to changes in the electronic structure of Sn-containing materials. For example, a previous examination of the Sn L_3-edge XANES spectra from $Gd_2Ti_{2-x}Sn_xO_7$ in Chapter 4 (Section 3.3.3, Figure 3.6) has shown that the Sn-O bond becomes more covalent with increasing Sn content. The analysis of Sn L_3-edge GA-XANES spectra from the ion-implanted $Gd_2Ti_{2-x}Sn_xO_7$ materials reported here has provided information on how a change in ordering of the coordination environment affects these spectra. The absorption edge energy of feature A in the spectra from the damaged materials was the same as that found in the spectra from the undamaged $Gd_2Ti_{2-x}Sn_xO_7$ materials, which implies that the Sn oxidation state does not change because of implantation. The line shape and intensity of the features (A,B,C) in the Sn L_3-edge XANES spectra were found to change significantly upon ion implantation (Figures 5.8 and 5.9). The intensity of features B and C decreased upon ion implantation, and all features (A,B,C) became broader.[234] (The widths of the peaks in the spectra from the ion implanted samples were also observed to increase with decreasing glancing angle.) The observed changes in the spectra are attributed to a decrease in the degeneracy of the Sn-O states because of a disordering of the crystal lattice after ion implantation. The features were observed to be broader in spectra from $Gd_2Sn_2O_7$ compared to

spectra from Gd_2TiSnO_7 when the materials were implanted to the same dose (Figure 5.10). This observation implies that $Gd_2Sn_2O_7$ was damaged more than Gd_2TiSnO_7 by the ion beam. These results are in good agreement with analysis of the Ti K-edge GA-XANES spectra and confirm that $Gd_2Ti_{2-x}Sn_xO_7$ becomes more susceptible to radiation induced structural damage with increasing Sn concentration.

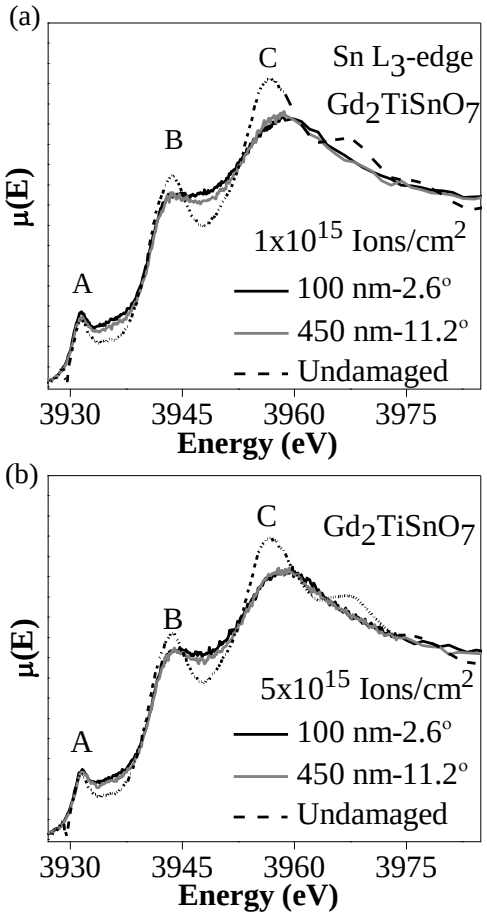

Figure 5.8: (a) Sn L_3-edge GA-XANES spectra from Gd_2TiSnO_7 implanted to a dose of 1×10^{15} ions/cm^2 are shown along with the XANES spectrum from the undamaged sample. The intensities of features B and C decreased with implantation and all features became broader. The widths of the peaks were also observed to increase with decreasing glancing angle. (b) Sn L_3-edge GA-XANES spectra collected from Gd_2TiSnO_7 implanted to a dose of 5×10^{15} ions/cm^2 are shown along with the spectrum from the undamaged material.

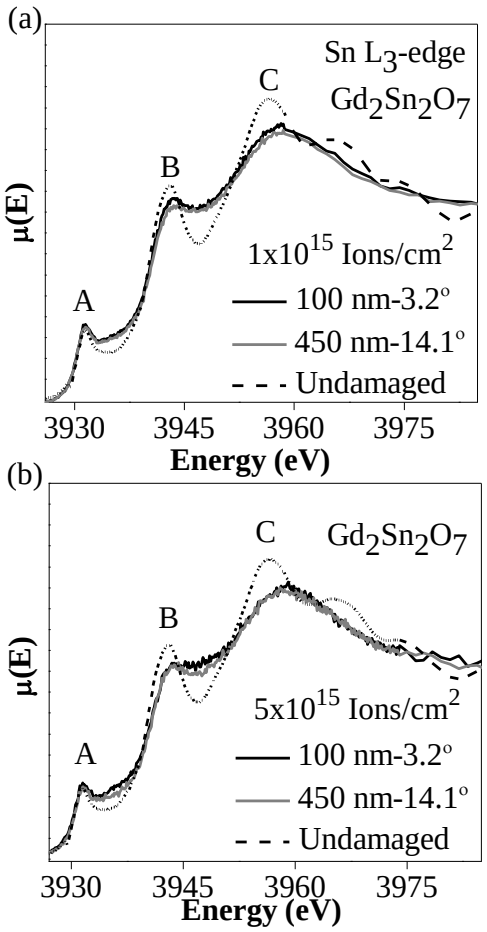

Figure 5.9: (a) Sn L_3-edge GA-XANES spectra from $Gd_2Sn_2O_7$ implanted to a dose of 1×10^{15} ions/cm^2 are shown along with the spectrum from the undamaged material. The intensities of feature B and C decrease and all features become broader in the spectra upon implantation. The features also became broader with decreasing glancing angle. (b) Sn L_3-edge GA-XANES spectra from $Gd_2Sn_2O_7$ implanted to a dose of 5×10^{15} ions/cm^2 are shown along with the spectrum from the undamaged material.

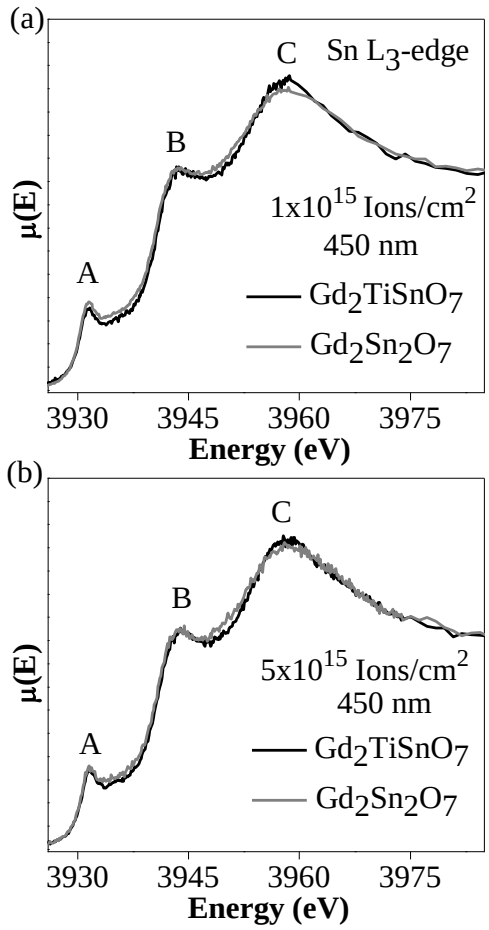

Figure 5.10: (a) Sn L_3-edge GA-XANES spectra from Gd_2TiSnO_7 and $Gd_2Sn_2O_7$ implanted to a dose of 1×10^{15} ions/cm^2 are shown. The glancing angle was adjusted to give an X-ray attenuation depth of 450 nm. Broader features were observed in the spectrum from $Gd_2Sn_2O_7$ compared to in the spectrum from Gd_2TiSnO_7 (b) Sn L_3-edge GA-XANES spectra from Gd_2TiSnO_7 and $Gd_2Sn_2O_7$ implanted to a dose of 5×10^{15} ions/cm^2 collected using glancing angles that give an X-ray attenuation depth of 450 nm are shown.

5.3.2.4 Gd L_3-edge GA-XANES

Gd L_3-edge GA-XANES spectra were also collected from the ion implanted $Gd_2Ti_{2-x}Sn_xO_7$ and $Gd_2Zr_2O_7$ samples to study the effect of ion implantation on the local coordination environment of Gd. The Gd L_3-edge white line XANES spectrum results from a $2p_{3/2} \rightarrow 5d$ excitation and is very intense, which makes this spectrum susceptible to absorption effects when collected in fluorescence mode.[211,212] This can be observed by examining the spectra presented in Figure 5.11 from undamaged $Gd_2Sn_2O_7$ collected in both fluorescence and transmission modes. Algorithms can be used to correct the fluorescence spectra; however, these procedures are not always reliable.[159,235] For this reason, the Gd L_3-edge GA-XANES spectra will not be discussed further.

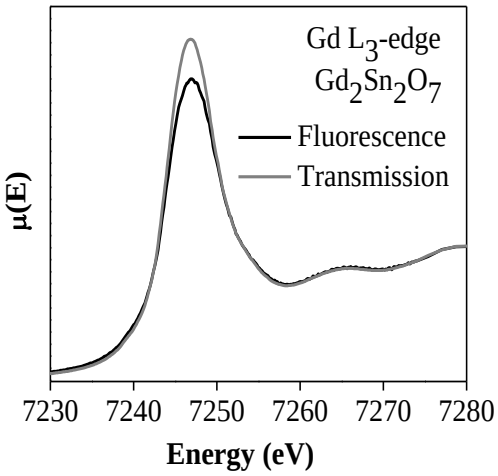

Figure 5.11: Gd L_3-edge XANES spectra from the undamaged $Gd_2Sn_2O_7$ material collected in fluorescence and transmission modes. The fluorescence spectrum is strongly influenced by absorption effects, leading to a decrease in intensity of the main-edge peak.

5.3.3 The effect of Sn substitution on ion beam induced structural damage in $Gd_2Ti_{2-x}Sn_xO_7$

The examination of μ-XRD patterns, GA-XANES spectra, and GA-EXAFS spectra has clearly shown that the $Gd_2Ti_{2-x}Sn_xO_7$ system becomes more susceptible to radiation-induced structural damage upon Sn substitution. As has been stated previously for stannate pyrochlore-type oxides, and confirmed here, it is expected that $Gd_2Ti_{2-x}Sn_xO_7$ is not able to undergo a phase transition from the pyrochlore structure to the defect fluorite structure when the Sn concentration is high because of the covalency of the bond between O^{2-} and the B-site Sn cations.[88,227,228,236] As the Sn-O bond covalency increases, this leads to an increase in the defect formation energy for cation anti-site disorder (i.e., the energy required to disorder the Sn atoms from the 6-coordinate B-site to the 8-coordinate A-site increases), which results in a decreased tendency of the cations to undergo cation anti-site disorder in the structure when the Sn concentration is high. [88,227,228,236] For this reason, the $Gd_2Ti_{2-x}Sn_xO_7$ materials show a greater susceptibility to ion beam induced structural damage with greater Sn content, instead of undergoing an order-disorder phase transition (i.e., from the pyrochlore structure to the defect fluorite structure). However, previous studies of $Y_2Ti_{2-x}Sn_xO_7$ have shown that these materials actually become more resistant to radiation induced structural damage as the Sn content increases.[189] The reason for the different behaviour of these two systems can be explained by examination of the radius ratios between the A- and B-cations in these materials. The cationic radius ratio is lower in $Y_2Sn_2O_7$ ($r_{Y3+}/r_{Sn4+} = 1.48$) than in $Gd_2Sn_2O_7$ ($r_{Gd3+}/r_{Sn4+} = 1.53$).[155] As the A-site ionic radius approaches that of the B-site cation, the ability of the material to undergo cation anti-site disorder and transform from the pyrochlore-type structure to the defect fluorite-type structure is determined by the r_A/r_B radius ratio, with the degree of covalency of the metal-O bond playing a lesser role.[88,228,229] It is because of this that it is believed that $Gd_2Sn_2O_7$

becomes partially amorphous upon ion implantation while $Y_2Sn_2O_7$ remains crystalline and transforms from the pyrochlore structure to the defect fluorite structure.[189] Further, $Gd_2Zr_2O_7$ is also more likely to undergo a phase transition from the pyrochlore structure to the defect fluorite structure after ion implantation instead of becoming amorphous because of the low r_{Gd3+}/r_{Zr4+} radius ratio (r_{Gd3+}/r_{Zr4+} = 1.46) in $Gd_2Zr_2O_7$.[83,155,212] All of these observations indicate the importance of both bond covalency and ionic radii to the ability of a material to resist ion beam induced structural damage, with the ionic radii of A- and B-site cations playing a more important role.[41,86,212]

5.4 Conclusions

Ion beam implantation studies were performed on $Gd_2Ti_{2-x}Sn_xO_7$. A greater understanding of how the structure of these pyrochlore-type materials change in response to ion beam implantation has been gained by analysis of μ-XRD patterns and GA-XANES/EXAFS spectra. The study of Ti K- and Sn L_3-edge GA-XANES spectra has allowed for a detailed investigation of how the Ti and Sn sites change after ion implantation, and has provided a level of detail that cannot be achieved by analysis of X-ray or electron diffraction patterns alone. This investigation has shown that the $Gd_2Ti_{2-x}Sn_xO_7$ materials become more susceptible to ion beam induced structural damage with increasing Sn concentration, which is a result of the covalency of the Sn-O bond. This study has also shown how GA-XANES can be used to understand the effect of ion implantation on the structures of materials.

Chapter 6

A study of the electronic structure and structural stability of $Gd_2Ti_2O_7$ based glass-ceramic composites

6.1 Introduction

Glass-ceramic composites have received attention for the immobilization (i.e., sequestration) of nuclear waste because of the flexible structure of these materials, which can enhance the incorporation of radioactive waste elements.[53,55,237-239] For glass-ceramic composite materials to be a potential nuclear wasteform, they must have a homogeneous distribution of crystalline materials in the bulk of a glass matrix, and the ability to incorporate actinides and other fission products in either the crystalline structure or the glass matrix.[54,98,99,239] The glass in these composites can also act as a secondary barrier for the radioactive waste incorporated in the crystalline material.[98,100,239] Glass-ceramic composite materials can exhibit varying degrees of resistance to radiation induced structural damage depending on the composition of the glass and/or the crystalline material.[32,100,240] The potential for developing glass-ceramic composites containing pyrochlore-type oxides, and the possibility of these materials to be resistant to radiation induced structural damage, has led to an increased interest in using these materials for the sequestration of nuclear waste.[54,98,99,239] Therefore, it is important to understand how the chemistry of these materials affect their resistance to radiation induced structural damage, which can be simulated using high energy ion beam implantation using ions such as Au^-, Kr^+, or Xe^+.[32,45,55,102,240]

[*] A version of this Chapter has been published. Reprinted with permission from Aluri, E. R.; Grosvenor, A. P. *RSC Adv.* **2015**, *5*, 80939. © 2015 The Royal Society of Chemistry doi: 10.1039/c5ra10720b

Borosilicate glass compositions have been proposed in the past for the immobilization of nuclear waste because of the stability and flexibility of the silicate network, which can also incorporate large amounts of radioactive waste elements.[11,32,45,54,55] It has been recently demonstrated that the presence of transition metals (e.g., Fe) in the borosilicate glass can lead to an increased resistance to structural defects caused by β-particles or γ-rays.[242-244] The release of β-particles and γ-rays from radioactive elements can lead to the formation of electron-hole pairs, which can result in a change in the silicate and borate bonding networks.[241,243] Previous reports have suggested that Fe present in the glass matrix can trap the electron-hole pairs because of the redox characteristics of this element.[241,243]

The objective of this study was to understand the interaction of pyrochlore crystallites within a glass matrix, and to investigate how these materials change as a result of ion implantation. Composite materials consisting of a borosilicate (and Fe-Al-borosilicate) glass matrix containing $Gd_2Ti_2O_7$ pyrochlore-type crystallites have been synthesized using different annealing temperatures. Electron microscopy and powder X-ray diffraction (XRD) have been used to study how the $Gd_2Ti_2O_7$ crystallites dispersed in the glass matrix. The interaction of $Gd_2Ti_2O_7$ in the glass matrix has been examined before and after ion implantation by collecting Ti K-edge (GA-)XANES spectra. Si L_3-, Fe K-, and Al L_3-edge XANES spectra were also collected to investigate how the electronic structure of the glass changes depending on $Gd_2Ti_2O_7$ loading, the glass composition, and the annealing temperature used to make these composite materials.

6.2 Experimental

6.2.1 Synthesis

Borosilicate glass (BG), Fe-Al-borosilicate glass (FABG), and glass-pyrochlore composites (BG/FABG-$Gd_2Ti_2O_7$) were synthesized by a conventional solid state method. The compositions of the borosilicate and Fe-Al-borosilicate glasses are listed in Table 6.1. Appropriate amounts of the respective metal oxide powders were mixed using a mortar and pestle and placed in graphite crucibles. The mixtures were annealed at 1100 ^oC for 1 hour in air to produce the glass materials. The amorphous structure was confirmed by examination of powder XRD data. Diffraction patterns from each sample were collected at room temperature using a PANalytical Empyrean X-ray diffractometer and a Co $K\alpha_{1,2}$ X-ray source. The phase analysis was determined using the High Score Plus software package.[150] The synthesized borosilicate glass and Fe-Al-borosilicate glass powders were re-annealed in air at 750 ^oC for 1 hour and the phases of these samples were analysed using powder XRD. Fe-borosilicate glass (FBG) and Al-borosilicate glass (ABG) samples were also synthesized to aid in analysis of the XRD patterns. The compositions of these glasses are also listed in Table. 6.1.

$Gd_2Ti_2O_7$ was synthesized using a simple ceramic method, which was discussed in previous Chapters (Section 3.2.1). Different weight percentages of $Gd_2Ti_2O_7$ (10 wt% to 90 wt%) were mixed with the borosilicate glass (BG) to form the glass-pyrochlore composites. $Gd_2Ti_2O_7$ and BG were ground using a mortar and pestle to produce particles of $\leq$ 100 μm in size, pressed into pellets uniaxially at 6 MPa, and then placed in graphite crucibles. The pellets were heated in air at 1100 ^oC or 750 ^oC for 1 hour. All composite materials were quench cooled in air and were observed to be glass beads after annealing. Similarly, FABG-pyrochlore composites (10 wt% to 90 wt% loadings of $Gd_2Ti_2O_7$) were also formed at different annealing

temperatures (1100 ^{o}C and 750 ^{o}C). The phase analysis of these composite materials was performed using powder XRD. The labels used to name the glasses and glass-ceramic composites studied are listed in Table 6.2.

Table 6.1 Compositions of the different glasses synthesized.

Glass	SiO_2 (mol %)	B_2O_3 (mol %)	Na_2O (mol %)	CaO (mol %)	Fe_2O_3 (mol %)	Al_2O_3 (mol %)
Borosilicate (BG)	63.5	16.9	16.5	3.1	-	-
Fe-Al-borosilicate (FABG)	55.5	16.9	16.5	3.1	3.0	5.0
Fe-borosilicate (FBG)	60.5	16.9	16.5	3.1	3.0	-
Al-borosilicate (ABG)	58.5	16.9	16.5	3.1	-	5.0

Table 6.2 Labels used to name the glasses and glass-ceramic composites studied.

Label	Sample description
BG	Borosilicate glass
FABG	Fe-Al-borosilicate glass
FBG	Fe-borosilicate glass
ABG	Al-borosilicate glass
BG-$Gd_2Ti_2O_7$-1100 ^{o}C/750 ^{o}C	Borosilicate glass- $Gd_2Ti_2O_7$ composite materials annealed at 1100 ^{o}C or 750 ^{o}C
FABG-$Gd_2Ti_2O_7$-1100 ^{o}C/750 ^{o}C	Fe-Al-borosilicate glass- $Gd_2Ti_2O_7$ composite materials annealed at 1100 ^{o}C or 750 ^{o}C

6.2.2 Electron microprobe analysis

Backscattered electron images (BSE) and energy dispersive X-ray spectroscopy (EDX) spectra were collected using a JEOL 8600 electron microprobe instrument. The glass-pyrochlore composite beads were mounted in a polymer resin and the surface of the beads was polished to a smooth surface using diamond paste. The samples were coated with a conductive carbon coating prior to introducing them into the instrument. BSE images were collected from the borosilicate glass composite materials (20 wt% and 40 wt% loading of $Gd_2Ti_2O_7$ annealed at 1100 ^oC; 20 wt%, 40 wt%, and 60 wt % loading of $Gd_2Ti_2O_7$ annealed at 750 ^oC) at 1000X magnification. BSE images were also collected from the composite materials before and after ion implantation using a magnification of 100X. EDX spectra were collected to determine the chemical composition at different locations in each sample.

6.2.3 Ion beam implantation

The borosilicate glass-pyrochlore composites (40 wt% loading of $Gd_2Ti_2O_7$ annealed at 1100 ^oC; 20 wt%, 40 wt%, and 60 wt% loading of $Gd_2Ti_2O_7$ annealed at 750 ^oC) were implanted with high energy (2 MeV) Au^- ions using the 1.7 MV Tandetron accelerator located at Interface Science Western (ISW), University of Western Ontario. The polished side of each glass-ceramic composite bead (see Section 6.2.2) was implanted to a dose of 5×10^{14} ions/cm^2. The ion beam was aligned normal to the glass-ceramic bead surface during implantation. As was stated earlier, the 2 MeV Au^- ions were calculated to implant to a maximum depth of ~450 nm in $Gd_2Ti_2O_7$ (Section 5.2.2). The ion implantation depth profile calculated previously for $Gd_2Ti_2O_7$ (Figure 5.1) was used in this study based on the assumption that pyrochlore crystallites are

located at the surface of the polished glass-ceramic composite beads that were exposed to the Au^- ion beam.

6.2.4 XANES

Ti K- and Fe K-edge XANES spectra were collected from as-synthesized BG-$Gd_2Ti_2O_7$ and FABG-$Gd_2Ti_2O_7$ (20 wt%, 50 wt%, and 80 wt% of $Gd_2Ti_2O_7$) composite materials annealed at 1100 ^oC and 750 ^oC. The spectra were collected using the Canadian Light Source/X-ray Science Division Collaborative Access Team (CLS/XSD, Sector 20) bending magnetic beamline (20BM) located at the Advanced Photon Source (APS), Argonne National Laboratory.[195] The spectral resolution is 0.7 eV at 4966 eV (Ti K-edge) and 1.0 eV at 7112 eV (Fe K-edge).[195] Samples were prepared by sealing finely ground powder between layers of Kapton tape, and the thickness was varied by adding or removing layers of powder between tape to maximize the absorption-edge step height. The spectra were recorded in transmission mode using ionization chambers filled with $He_{(g)}$ and $N_{2(g)}$ (80% He:20% N_2 for the Ti K-edge and 0% He:100% N_2 for the Fe K-edge) to achieve optimal absorption-edge step heights and signal-to-noise ratios. XANES spectra were collected using a step size of 0.15 eV through the Ti K- and Fe K-edges. The Ti K-edge spectra were calibrated using Ti metal (4966 eV), and the Fe-edge spectra were calibrated using Fe metal (7112 eV).[151]

Ti K-edge GA-XANES analysis of the ion implanted pellets of the glass-ceramic composites was also performed (using the 20 BM beamline located at the APS) by vertically focusing the X-ray beam to yield a beam height of 0.15 mm while maintaining the beam width at 1 mm. Ti K-edge GA-XANES spectra were collected in fluorescence mode using a single element vortex silicon drift detector and a step size of 0.25 eV through the absorption edge. The experimental details for GA-XANES measurements were described in Sections 4.2.4 and 5.2.4.

A web based program was used to calculate the glancing angles required to reach specific X-ray attenuation depths for photons having energies of 4966 eV (Ti K-edge; see Table 6.3 (also provided in Table 4.1)).[151]

The Si $L_{2,3}$-edge and Al $L_{2,3}$-edge XANES spectra from the undamaged BG-$Gd_2Ti_2O_7$ and FABG-$Gd_2Ti_2O_7$ composite materials were measured using the Variable Line Spacing-Plane Grating Monochromator (VLS-PGM; 11ID-2) beamline at the Canadian Light Source (CLS).[153] The samples were prepared by placing finely ground powder on carbon tape. The spectra were collected in total fluorescence yield mode (TFY) using a step size of 0.05 eV through the Si absorption edge and 0.025 eV through the Al absorption edge. The spectra were calibrated using elemental Si for the Si $L_{2,3}$-edge (99.40 eV) and Al metal for the Al $L_{2,3}$-edge (72.55 eV).[151] Analysis of all XANES spectra was performed using the Athena software program.[151]

Table 6.3 Calculated glancing angles required to give specific X-ray attenuation depths in $Gd_2Ti_2O_7$ for photons having energies of 4966 eV (Ti K-edge).

Ti K-edge (4966 eV)	
X-ray attenuation depth (nm)	Glancing angle
220	1.4^o
450	4.5^o
4088	45^o

6.3 Results and discussion

6.3.1 Powder X-ray diffraction

Powder XRD patterns from the glasses and glass-pyrochlore composite materials were collected to gain information about the different phases that are present in these materials. The XRD patterns from the composite materials annealed at 1100 ^{o}C and 750 ^{o}C are shown in Figures 6.1 and 6.2, respectively. The patterns from the glasses annealed at 1100 ^{o}C (BG-1100 ^{o}C and FABG-1100 ^{o}C) show only a broad hump in the region of 20-30^{o} (Figure 6.1), which confirms the amorphous structure of these materials. The diffraction pattern from the borosilicate glass annealed at 750 ^{o}C shows peaks representative of quartz (SiO_2) along with a broad amorphous hump (Figure 6.2a), whereas the diffraction pattern from the FABG sample annealed at 750 ^{o}C shows only a broad hump (Figure 6.2b). This observation indicates that quartz (SiO_2) was formed from the amorphous silicate network when the borosilicate glass (BG) was annealed at 750 ^{o}C; however, the amorphous nature of the Fe-Al-borosilicate glass (FABG) was stable when annealed at this temperature (*c.f.* Figure 6.2).[245] The stabilization of the amorphous structure of the FABG sample was assumed to be a result of the presence of Fe and/or Al. The XRD patterns from the Fe- or Al- only containing borosilicate glass (i.e., FBG or ABG) samples annealed at 750 ^{o}C (i.e., FBG-750 ^{o}C, ABG-750 ^{o}C) were collected to aid in the analysis of the stabilization of FABG-750 ^{o}C and these patterns are shown in Figures 6.2c and 6.2d. Diffraction peaks indicating the presence of quartz are observed in the pattern from the FBG sample but not in the pattern from the ABG sample, which indicates that Al_2O_3 is responsible for stabilizing the amorphous structure of the Fe-Al-borosilicate glass regardless of annealing temperature. The small addition of aluminum oxide (Al_2O_3), as a network modifier, can break SiO_4^{4-} tetrahedral bridging bonds and stabilize the amorphous structure of the glass so

as not to allow depolymerization of the glass network to occur.[55,246,247] The presence of Aluminum oxide in the FABG sample helps to stabilize the amorphous structure of this material relative to the BG sample.

Powder XRD patterns were collected from all glass-ceramic composite materials and are shown in Figures 6.1 and 6.2. Diffraction peaks from crystalline $Gd_2Ti_2O_7$ as well as a broad hump are observed in the patterns from the BG-$Gd_2Ti_2O_7$-1100 ^oC, FABG-$Gd_2Ti_2O_7$-1100 ^oC, and FABG-$Gd_2Ti_2O_7$-750 ^oC composite materials (Figures 6.1a, 6.1b, and 6.2b). The patterns from the BG-$Gd_2Ti_2O_7$-750 ^oC materials that contain different loadings of $Gd_2Ti_2O_7$ (Figure 6.2a) contain diffraction peaks from $Gd_2Ti_2O_7$ and quartz, as well as a broad hump that is representative of a glass. The observed decrease in the intensities of the diffraction peaks from quartz with an increase in the loading of $Gd_2Ti_2O_7$ (Figure 6.2a) is mainly caused by the progressive increase in the difference of the average scattering power between materials that contain different loadings of $Gd_2Ti_2O_7$ and quartz.

Examination of the patterns from the composite materials annealed at 1100 ^oC (Figure 6.1) shows that the minimum $Gd_2Ti_2O_7$ loading where the pyrochlore phase peaks started to appear in the diffraction patterns is 40 wt%. This indicates that some of the $Gd_2Ti_2O_7$ crystallites dissolved in the glass when the composite materials were annealed at 1100 ^oC. However, the patterns from the composite materials annealed at 750 ^oC (Figure 6.2) showed diffraction peaks from $Gd_2Ti_2O_7$ in all of the composite materials studied. These observations indicate that the low annealing temperature (i.e., 750 ^oC) favours the formation of a composite material with a negligible amount of pyrochlore dissolving in the glass matrix.

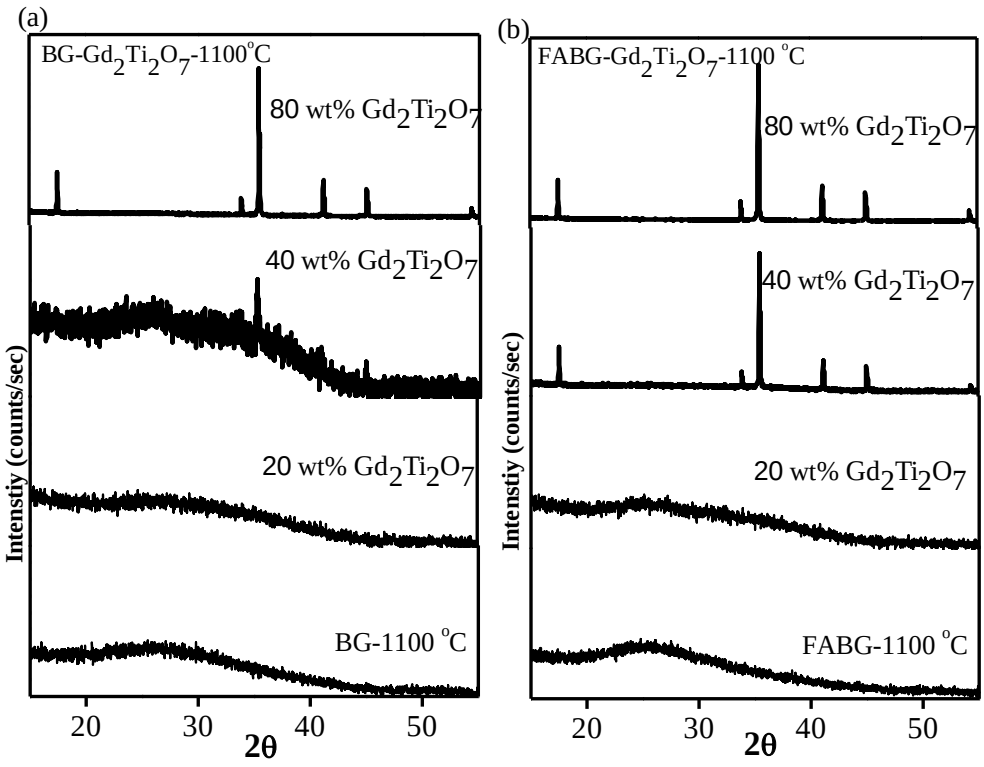

Figure 6.1 XRD patterns from the (a) Borosilicate glass (BG) and the BG-ceramic composite materials annealed at 1100°C and (b) Fe-Al-borosilicate glass (FABG) and the FABG-ceramic composite materials (20 wt%, 40 wt%, and 80 wt% loading of $Gd_2Ti_2O_7$) annealed at 1100°C are shown. The patterns from the glass materials are also shown.

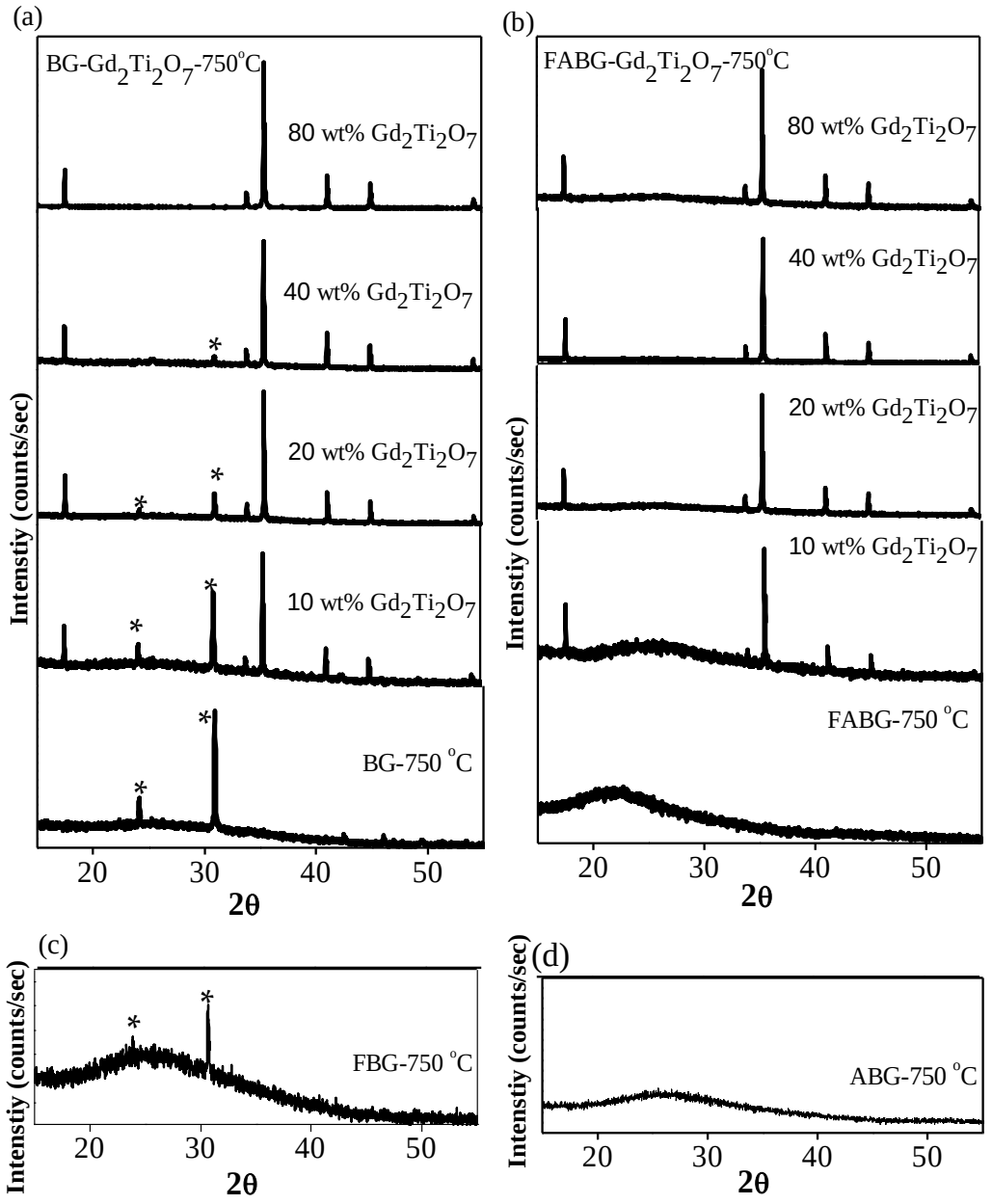

Figure 6.2 XRD patterns from the (a) borosilicate glass and its composite materials annealed at 750°C and (b) Fe-Al-borosilicate glass and its composite materials (10 wt%, 20 wt%, 40 wt%, and 80 wt% loading of $Gd_2Ti_2O_7$) annealed at 750°C are shown. Diffraction peaks from quartz are marked by an asterisk (*). Patterns from (c) Fe-borosilicate glass (FBG) and (d) Al-borosilicate glass (ABG) annealed at 750°C are also shown.

6.3.2 Electron microscopy

Backscattered electron (BSE) images from the borosilicate glass composites annealed at 750 ^{o}C or 1100 ^{o}C are shown in Figure 6.3. BSE images are helpful for obtaining compositional maps of a sample, and for identifying phases depending on the average atomic number.[248] The BSE images from the borosilicate glass composite materials (Figure 6.3) show that the pyrochlore crystallites (bright area) are distributed in the glass matrix (dark area). Pores are observed in the glass matrix because of air bubble formation during annealing.

The BSE images from the composite materials annealed at different temperatures (Figures 6.3a-6.3e) shows that the grain size of the pyrochlore crystallites are smaller in the composite materials annealed at the highest temperature (1100 ^{o}C). The BSE images (Figure 6.3d-e) collected from the composites annealed at 1100 ^{o}C shows that the $Gd_2Ti_2O_7$ crystallites completely dissolved in the glass matrix when the composite contained a low (20 wt %) loading of $Gd_2Ti_2O_7$ while some crystallites remained when a higher (40 wt%) loading of $Gd_2Ti_2O_7$ was present. Examination of EDX spectra (Figure A4.1a in Appendix A4) collected from different locations in the BG-$Gd_2Ti_2O_7$-1100 ^{o}C sample containing a 40 wt% loading of $Gd_2Ti_2O_7$ shows that the regions in the micrographs (see Figure 6.3e) that appear glass-like contain high concentrations of Gd and Ti. The BSE images and EDX spectra (Figure 6.3e and A4.1a) confirm that $Gd_2Ti_2O_7$ crystallites dissolved in the glass matrix after annealing the mixture at 1100 ^{o}C. However, only a small fraction of the $Gd_2Ti_2O_7$ crystallites dissolved in the glass matrix of the composite materials annealed at 750 ^{o}C (see Figures 6.3a-c and A4.1). These observations are in agreement with the powder XRD analysis presented above. BSE images were also collected from the ion implanted composite materials and are compared to those from the as-synthesized materials in Figure A4.2. The morphology and grain size of the $Gd_2Ti_2O_7$ crystallites in the glass

matrix were observed to be similar when comparing the as-synthesized and ion implanted materials.

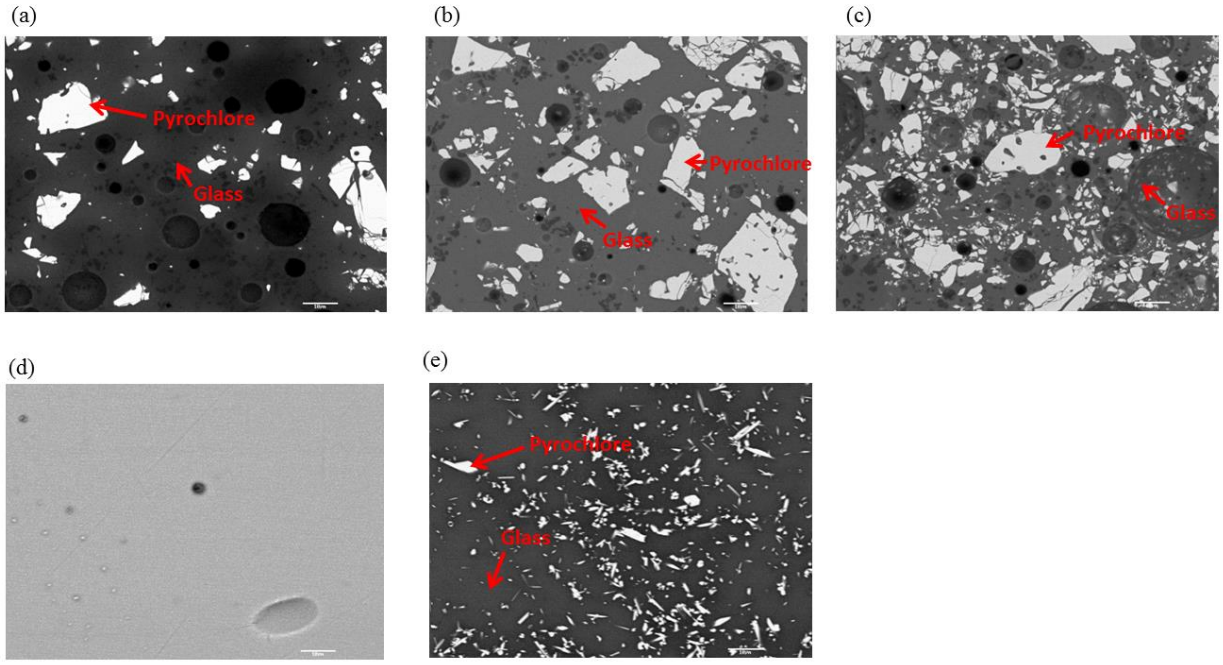

Figure 6.3 (a,b,c) Backscattered images from the borosilicate glass composite materials (20 wt%, 40 wt%, and 60 wt% loading of $Gd_2Ti_2O_7$, respectively) annealed at 750°C. (d,e) Backscattered electron images from the borosilicate glass composite materials (20 wt% and 40 wt% $Gd_2Ti_2O_7$, respectively) annealed at 1100°C. The scale bar in each image is 10 µm.

6.3.3 XANES analysis of the as-synthesized materials

XANES spectra are sensitive to changes in the electronic structure and coordination environment of atoms/ions in materials.[121,125] Examination of Ti K-, Fe K-, Si $L_{2,3}$-, and Al $L_{2,3}$-edge XANES spectra from the glass-ceramic composites has allowed for a study of how the annealing temperature, glass composition, and the loading of $Gd_2Ti_2O_7$ affected the local environment of atoms of these elements.

6.3.3.1 Ti K-edge XANES

The Ti K-edge XANES spectra from the as-synthesized BG-$Gd_2Ti_2O_7$ and FABG-$Gd_2Ti_2O_7$ composite materials (20 wt%, 50 wt%, and 80 wt% loading of $Gd_2Ti_2O_7$) annealed at either 1100 ^oC or 750 ^oC are shown in Figures 6.4 and 6.5, respectively. The spectrum from $Gd_2Ti_2O_7$, which was presented previously (Figure 4.3), is also presented in these figures. Examination of the Ti K-edge spectra has allowed for a study of how changes in the loading of $Gd_2Ti_2O_7$ in the composite materials and the annealing temperature has affected the local coordination environment of Ti. The spectra result from 1s→3d (quadrapolar; pre-edge (A)) and 1s→4p (dipolar; main-edge (B,C)) transitions.[159,161,177] A detailed discussion of these features was presented in previous Chapters (Section 3.3.2, 4.3.2 and 5.3.2.1).

All of the pre-edge and main-edge features (A,B,C) in the spectra were found to change significantly by varying the loading of $Gd_2Ti_2O_7$ in the composite materials or the annealing temperature. The intensity of the pre-edge feature (A) decreased while the energy (B) and intensity (C) of the main-edge feature increased as the loading of $Gd_2Ti_2O_7$ increased in the composite materials (Figures 6.4 and 6.5). These changes in the Ti K-edge XANES spectra have been shown in the previous Chapters (Section 2.3.4 and 5.3.2.1) to be a result of an increase in

the CN of Ti^{4+}.[59,130,131,249] The observed increase in Ti CN suggests that the amount of $Gd_2Ti_2O_7$ dissolved in the glass matrix decreases as the loading of $Gd_2Ti_2O_7$ in the composite materials increases, which is in agreement with the powder XRD and electron microscopy results. The spectra from the composite materials having a low wt% of $Gd_2Ti_2O_7$ show that Ti occupies a low coordinationate environment when $Gd_2Ti_2O_7$ dissolved in the glass. Ti was found to adopt a similar coordination environment in amorphous metal silicates previously investigated by this research group.[131,249]

Examination of the spectra from the borosilicate and Fe-Al-borosilicate glass composite materials containing the same $Gd_2Ti_2O_7$ loading and annealed at 1100 ^oC (Figure 6.6a) shows that less $Gd_2Ti_2O_7$ dissolved in the Fe-Al-borosilicate glass as compared to the borosilicate glass. Only a small change was observed in the spectra from the composite materials annealed at 750 ^oC when compared to the spectra from $Gd_2Ti_2O_7$ (Figure 6.6b). These observations indicate that the FABG glass composition and lower annealing temperature favours the formation of composite materials with a small amount of the pyrochlore crystallites having dissolved in the glass, which is in agreement with the XRD and electron microscopy results.

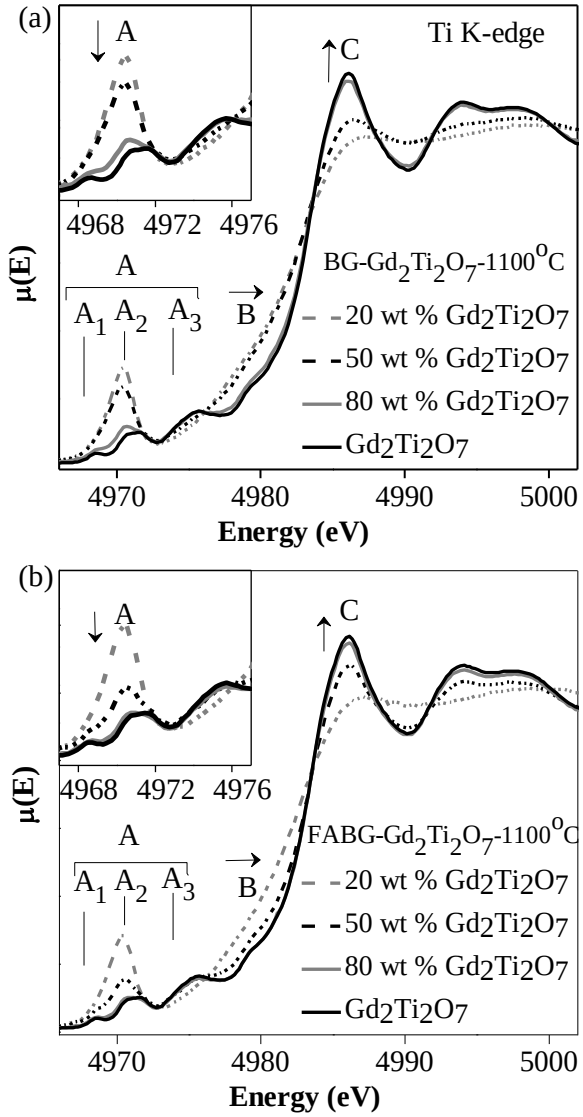

Figure 6.4 Ti K-edge XANES spectra from BG-$Gd_2Ti_2O_7$-1100°C and FABG-$Gd_2Ti_2O_7$-1100°C containing 20 wt% , 50 wt%, and 80 wt% loading of $Gd_2Ti_2O_7$ are shown. The spectra are compared to the spectrum from $Gd_2Ti_2O_7$. Feature A represents the pre-edge region (1s→3d) and is shown in the inset. Feature B and C (1s→4p) represent the main-edge region. The arrows show the changes in intensity and energy of spectral features that occur with increasing loading of $Gd_2Ti_2O_7$.

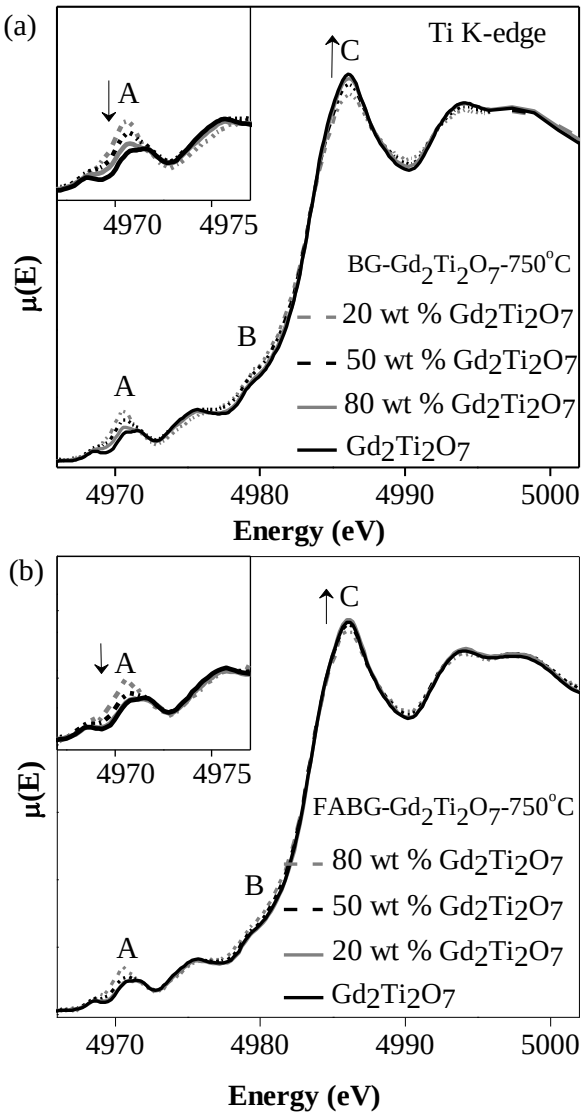

Figure 6.5 Ti K-edge XANES spectra from BG-$Gd_2Ti_2O_7$-750°C and FABG-$Gd_2Ti_2O_7$-750°C containing 20 wt% , 50 wt%, and 80 wt% loading of $Gd_2Ti_2O_7$. The spectra are compared to the spectrum from $Gd_2Ti_2O_7$. Arrows mark the changes observed in the spectra with increasing loading of $Gd_2Ti_2O_7$.

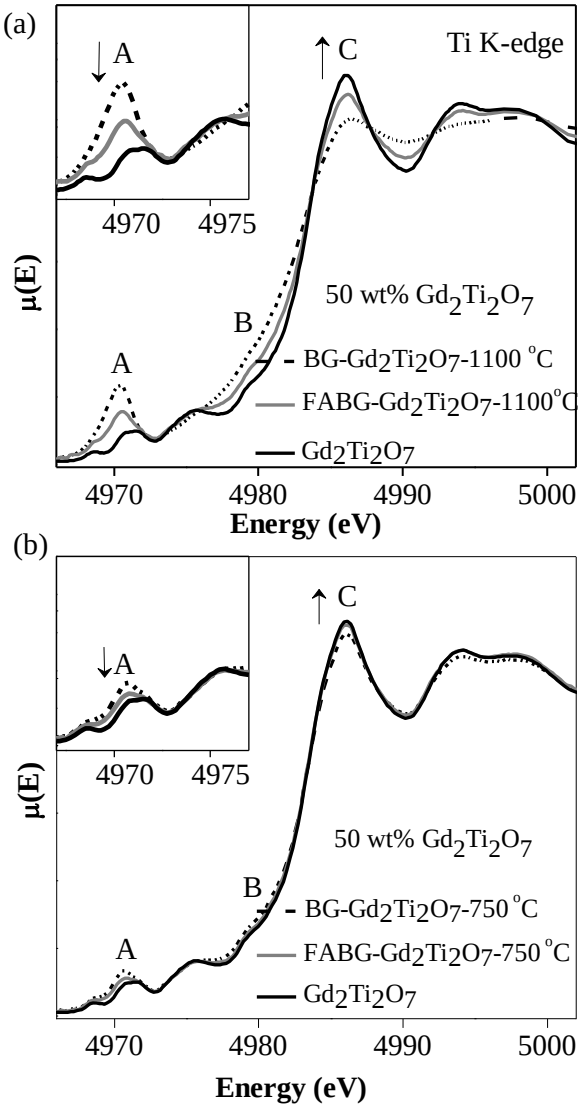

Figure 6.6 (a) Ti K-edge XANES spectra from BG- and FABG- composite materials (50 wt% $Gd_2Ti_2O_7$) annealed at 1100°C are shown. (b) Ti K-edge XANES spectra from BG-$Gd_2Ti_2O_7$-750°C and FABG-$Gd_2Ti_2O_7$-750°C containing the same loading of $Gd_2Ti_2O_7$ are shown. Arrows mark the changes observed in the spectra from the composite materials as compared to $Gd_2Ti_2O_7$.

6.3.3.2 Si $L_{2,3}$-edge XANES

Si $L_{2,3}$-edge XANES spectra were also collected to study how the Si environment was affected by varying the loading of $Gd_2Ti_2O_7$, annealing temperature, and the type of glass used. Normalized Si $L_{2,3}$-edge XANES spectra from the borosilicate glasses annealed at 1100 ^oC or 750 ^oC are shown in Figure 6.7. The spectra are compared to a previously reported spectrum of amorphous SiO_2.[247] The Si $L_{2,3}$-edge spectra exhibit two features that result from $2p \rightarrow 3s$ (Feature D) and $2p \rightarrow 3d$ (Feature E) transitions, respectively.[249] The low-energy region feature (D) is split into two peaks (D_1 and D_2), which result from $2p_{3/2} \rightarrow 3s$ (D_1) and $2p_{1/2} \rightarrow 3s$ (D_2) transitions because of spin-orbit splitting.[162,250-252]

Comparision of the spectra from the borosilicate glasses annealed at 750 ^oC or 1100 ^oC to the spectrum from amorphous SiO_2 (Figure 6.7) reveals a significant difference in the line shapes. Feature D and E become narrower to higher energy in the spectra from the borosilicate glass annealed at 750 ^oC or 1100 ^oC as compared to the spectrum from amorphous SiO_2. Previous studies of various metal containing amorphous silicates and quartzes have shown that these features become narrower to higher energy as the materials change from amorphous silicates to quartzes.[253,255] These changes are attributed to an increase in the degeneracy of the Si-O states because of a more ordered SiO_4^{4-} tetrahedral bond network in the quarz lattice.[252-255] This is also supported by the presence of quartz in the XRD pattern from the borosilicate glass annealed at 750 ^oC (see Figure 6.2a). The width of the features in the spectra from the composite materials were observed to decrease (Figure 6.8 and 6.9) with increasing loading of $Gd_2Ti_2O_7$. The observed changes in the spectra are attributed to changes in the ordering of the glass, including crystallization of quartz, and because of variations in the glass composition as a result of the pyrochlore crystallites dissolving in the glass which may lead to next-nearest-neighbour effects

between the metal cations and Si. [252-255] These observations suggest that both the loading of $Gd_2Ti_2O_7$ in the composite *and* the annealing temperature affect the silicate network in the glass-ceramic composite materials.

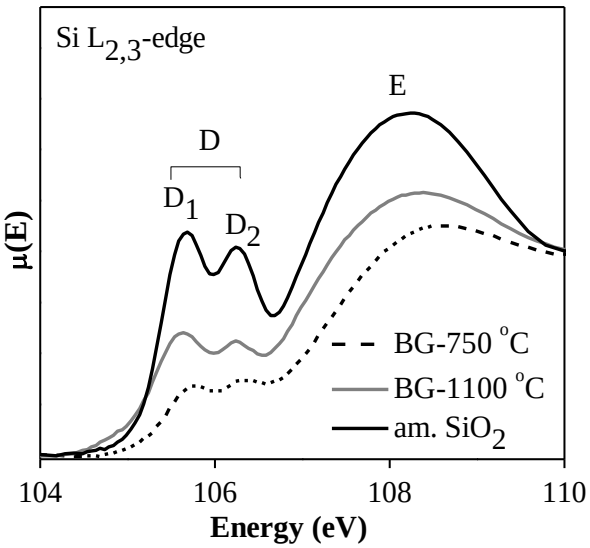

Figure 6.7 Si $L_{2,3}$-edge XANES spectra from the borosilicate glass annealed at 1100 °C or 750 °C are shown. The spectra are compared to the spectrum of amorphous SiO_2 that was reported previously.[249]

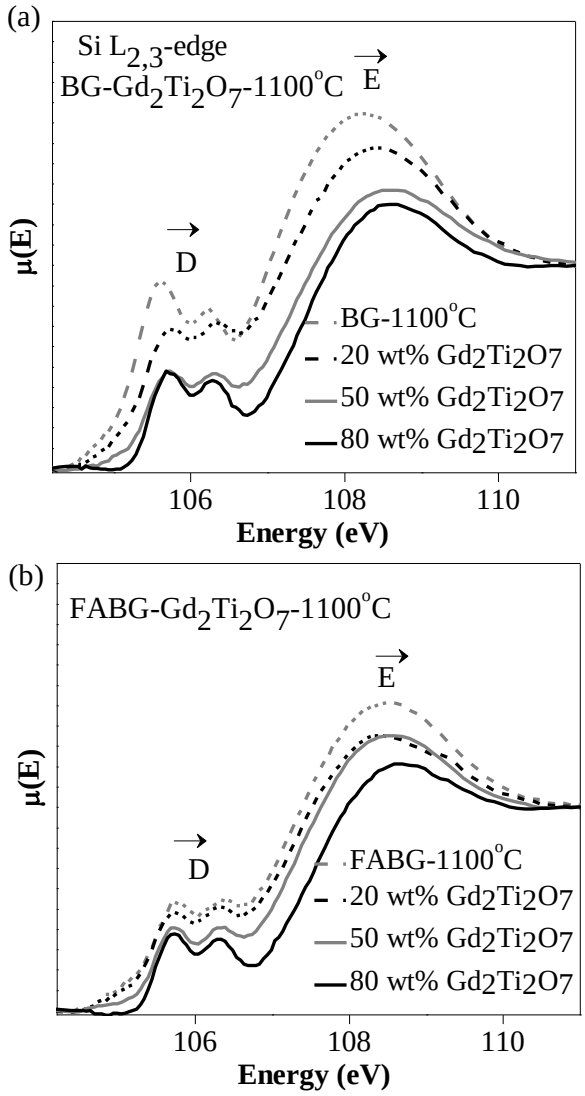

Figure 6.8 Si $L_{2,3}$-edge XANES spectra from (a) BG-$Gd_2Ti_2O_7$-1100 °C and (b) FABG-$Gd_2Ti_2O_7$-1100 °C containing 20 wt% , 50 wt%, and 80 wt% loading of $Gd_2Ti_2O_7$ are shown. The spectra are compared to the spectrum from the corresponding glass. Features C and D become narrower to higher energy with increasing loading of $Gd_2Ti_2O_7$.

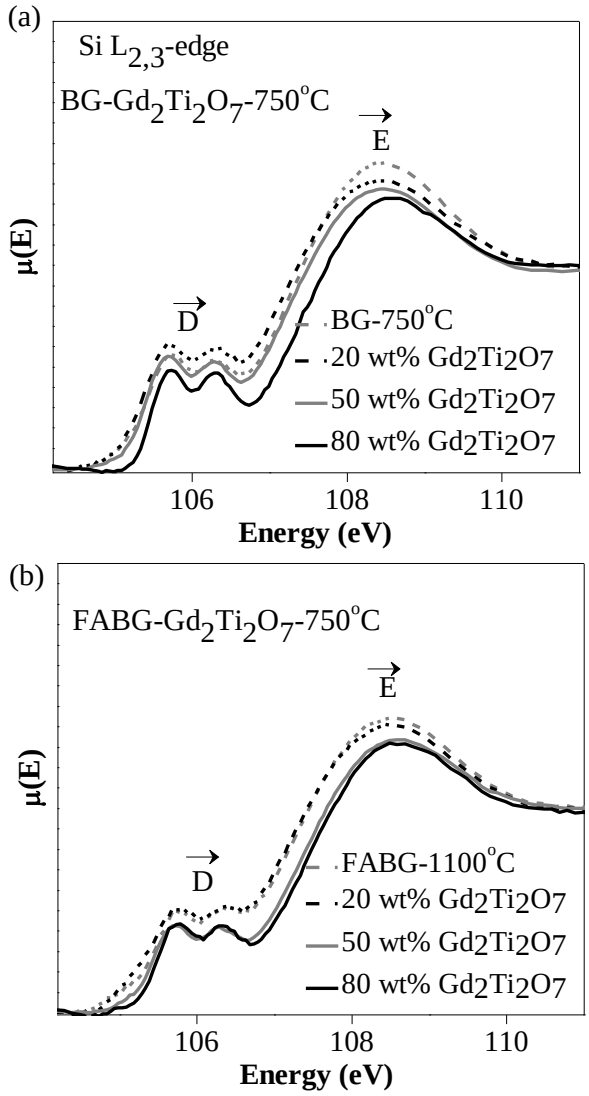

Figure 6.9 Si $L_{2,3}$-edge XANES spectra from (a) BG-$Gd_2Ti_2O_7$-750 °C and (b) FABG-$Gd_2Ti_2O_7$-750 °C containing 80 wt% , 50 wt%, and 20 wt% loading of $Gd_2Ti_2O_7$ are shown. The spectra are compared to the spectrum from the corresponding glass.

6.3.3.3 Fe K-edge XANES

Fe K-edge XANES spectra (Figure 6.10) were collected to study the redox chemistry of Fe in the Fe-Al-glass (FABG) and Fe-Al-glass-ceramic composites (FABG-$Gd_2Ti_2O_7$) when annealed at different temperatures. The spectrum from the FABG sample is compared to the previously reported spectra from FeO (Fe^{2+}) and Fe_2O_3 (Fe^{3+}) in Figure 6.10a.[200,223] The spectra contain both pre-edge (1s→3d) and main-edge (1s→4p) excitations like in the Ti K-edge XANES spectra.[130,157,162] Comparison of the absorption edge energy (Figure 6.10a) of the spectra from FABG, FeO, and Fe_2O_3 shows that both Fe^{3+} and Fe^{2+} exist in the glass.

The spectra from the composite materials (20 wt%, 50 wt%, and 80 wt% loading of $Gd_2Ti_2O_7$) annealed at 1100 ^oC and 750 ^oC are shown in Figures 11b and 11c, and are compared to the spectrum from FABG. The intensity and energy of features A, B, or C do not change considerably in the spectra (Figure 6.10b and 6.10c) when the loading of $Gd_2Ti_2O_7$ was varied. However, the intensity and absorption energy of features A and B do change when comparing the spectra from FABG-$Gd_2Ti_2O_7$-1100 ^oC/750 ^oC to the spectrum from FABG. A shift of the absorption edge to lower energy was observed in the composite materials annealed at 1100 ^oC (Figure 6.10b) whereas the absorption edge shifted to higher energy when the composite materials were annealed at 750 ^oC (Figure 6.10c). The energy of the pre-edge peak (A) in Fe K-edge XANES spectra has been observed previously to not be affected significantly by changes in the Fe CN.[157,162,178,203] Therefore, the observed shifts in energy of both the pre-edge (A) and main-edge (B) features in the Fe K-edge XANES spectra in Figure 6.10 from the composite materials annealed at 750 ^oC or 1100 ^oC are a result of variations in the oxidation state of Fe. Comparision of the spectra from FABG-$Gd_2Ti_2O_7$-750 ^oC and FABG shows that the oxidation state of Fe in the glass matrix is completely oxidized to 3+ when the composite system was

annealed at 750 ^{o}C (*cf.* Figures 6.10a and 6.10c). Further, examination of the spectra from FABG-$Gd_2Ti_2O_7$-1100 ^{o}C and FABG shows that the oxidation state of Fe in the glass was reduced to 2+ when the composite materials were annealed at 1100 ^{o}C (*cf* . Figures 6.10a and 10b). As stated earlier, the intensity of the pre-edge feature (A) in transition metal K-edge XANES spectra can change as a result of a variation of the CN of the metal.[130,157,203] The intensity of the pre-edge feature increased in the spectra from FABG-$Gd_2Ti_2O_7$-750 ^{o}C compared to the spectrum from the as-synthesized FABG sample (Figure 6.10c) while the pre-edge peak intensity in the spectrum from FABG-$Gd_2Ti_2O_7$-1100 ^{o}C was observed to be less intense compared to the spectrum from as-synthesized FABG (Figure 6.10b). The changes observed here suggest that the CN of Fe decreases when the composite materials were annealed at 750 ^{o}C and that the CN of Fe increases when the composite materials were annealed at 1100 ^{o}C.

The observed changes in Fe oxidation state by varying the annealing temperature are a result of a redox reaction between oxygen and Fe. The Fe K-edge XANES spectra show that Fe in the composite materials was reduced to Fe^{2+} when annealed at 1100 ^{o}C and oxidized to Fe^{3+} when the composites were annealed at 750 ^{o}C, which can be described by the following equilibrium reaction: $4Fe^{3+}+2O^{2-} \underset{>T}{\overset{<T}{\rightleftharpoons}} 4Fe^{2+}+O_2$.[256-259] The reduction of Fe^{3+} to Fe^{2+} at 1100 ^{o}C may also be caused by $Gd_2Ti_2O_7$ crystallites dissolving in the glass matrix when the composite materials were annealed at this temperature. These observations indicate that the oxidation state and CN of Fe in the composite materials are strongly affected by the annealing temperature.

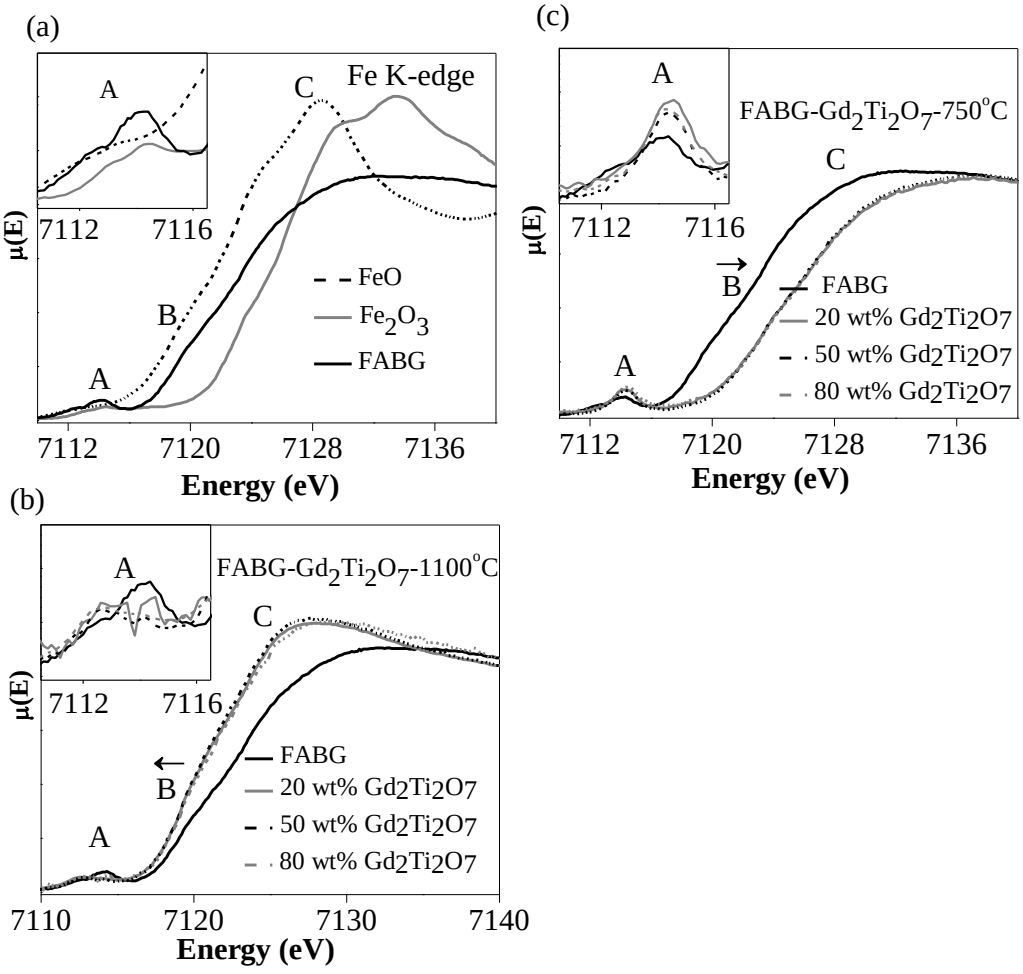

Fgure 6.10 (a). The Fe K-edge XANES spectrum from FABG is compared to the spectra from FeO (Fe^{2+}) and Fe_2O_3 (Fe^{3+}). (b,c) Fe K-edge XANES spectra from FABG-$Gd_2Ti_2O_7$-1100°C and FABG-$Gd_2Ti_2O_7$-750°C containing 20 wt% , 50 wt%, and 80 wt% loading of $Gd_2Ti_2O_7$ are shown. These spectra are compared to the spectrum from FABG. Shifts in the absorption energy of the composite materials annealed at different temperatures as compared to the spectrum from FABG are indicated using arrows.

6.3.3.4 Al $L_{2,3}$-edge XANES

Al $L_{2,3}$-edge XANES spectra were collected from the FABG-composite materials annealed at different temperatures (Figure 6.11). The spectra consist of two features D and E,

which result from 2p→3s and 2p→3d transitions, respectively.[260] Al $L_{2,3}$-edge XANES spectra have been shown previously to be sensitive to changes in the Al CN.[260] Examination of the spectra from the FABG-$Gd_2Ti_2O_7$ composite materials (Figure 6.11) show negligible changes in the spectral features with changes in loading or annealing temperature. These observations indicate that the $Gd_2Ti_2O_7$ loading and annealing temperature do not significantly affect the coordination environment of Al in the composite materials.

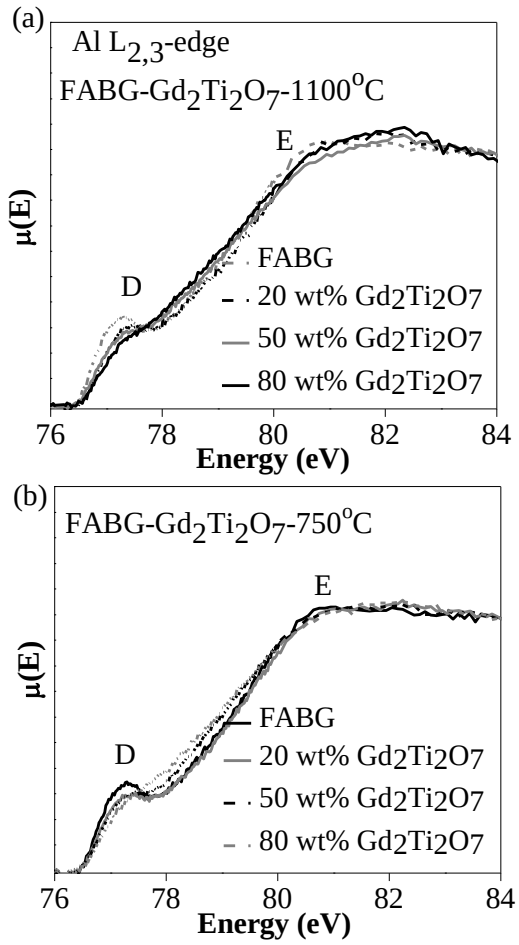

Figure 6.11 Al $L_{2,3}$-edge XANES spectra from (a) FABG-$Gd_2Ti_2O_7$-1100°C and (b) FABG-$Gd_2Ti_2O_7$-750°C are shown.

6.3.4 Ti K-edge GA-XANES of the ion-implanted materials

Glancing angle XANES (i.e., GA-XANES) spectra were collected from ion implanted composite samples to study how the local environment of Ti in the materials change as a result of ion-beam implantation. As was discussed previously (Section 5.2.2), 2 MeV Au^- ions penetrate to a maximum depth of ~450 nm in $Gd_2Ti_2O_7$. Ti K-edge GA-XANES spectra were collected using glancing angles of 1.4°, 4.5°, and 45°, which provide X-ray attenuation depths of 220 nm, 450 nm, and 4088 nm, respectively.

Normalized Ti K-edge GA-XANES spectra from BG-$Gd_2Ti_2O_7$-1100 °C (60 wt% loading of $Gd_2Ti_2O_7$) and BG-$Gd_2Ti_2O_7$-750 °C (20 wt%, 40 wt%, and 60 wt% loading of $Gd_2Ti_2O_7$) implanted using Au^- ions to a dose of 5×10^{14} ions/cm^2 are shown in Figure 6.12. The spectra from the as-synthesized composite materials are also presented. Compared to the spectrum from as-synthesized materials, the intensity of the pre-edge peak (A) increased while the intensity and energy of the main-edge peak (B,C) decreased as a result of ion implantation.[101] These changes are indicative of a decrease in Ti CN because of ion implantation. The observed decrease in Ti CN indicates that ion implantation damages the structure of $Gd_2Ti_2O_7$ in the composite materials.[101] GA-XANES spectra collected at different glancing angles from the ion implanted composite materials annealed at 750 °C or 1100 °C (Figure 6.12) shows that more damage occurs near the surface compared to deeper into the material. A comparision of the spectra collected at a glancing angles providing the same X-ray attenuation depth from ion-implanted BG-$Gd_2Ti_2O_7$-750 °C and $Gd_2Ti_2O_7$ (Figure 6.13) shows that the damage experienced by $Gd_2Ti_2O_7$ in the composite materials was similar to that experienced by the sample that only contained $Gd_2Ti_2O_7$.

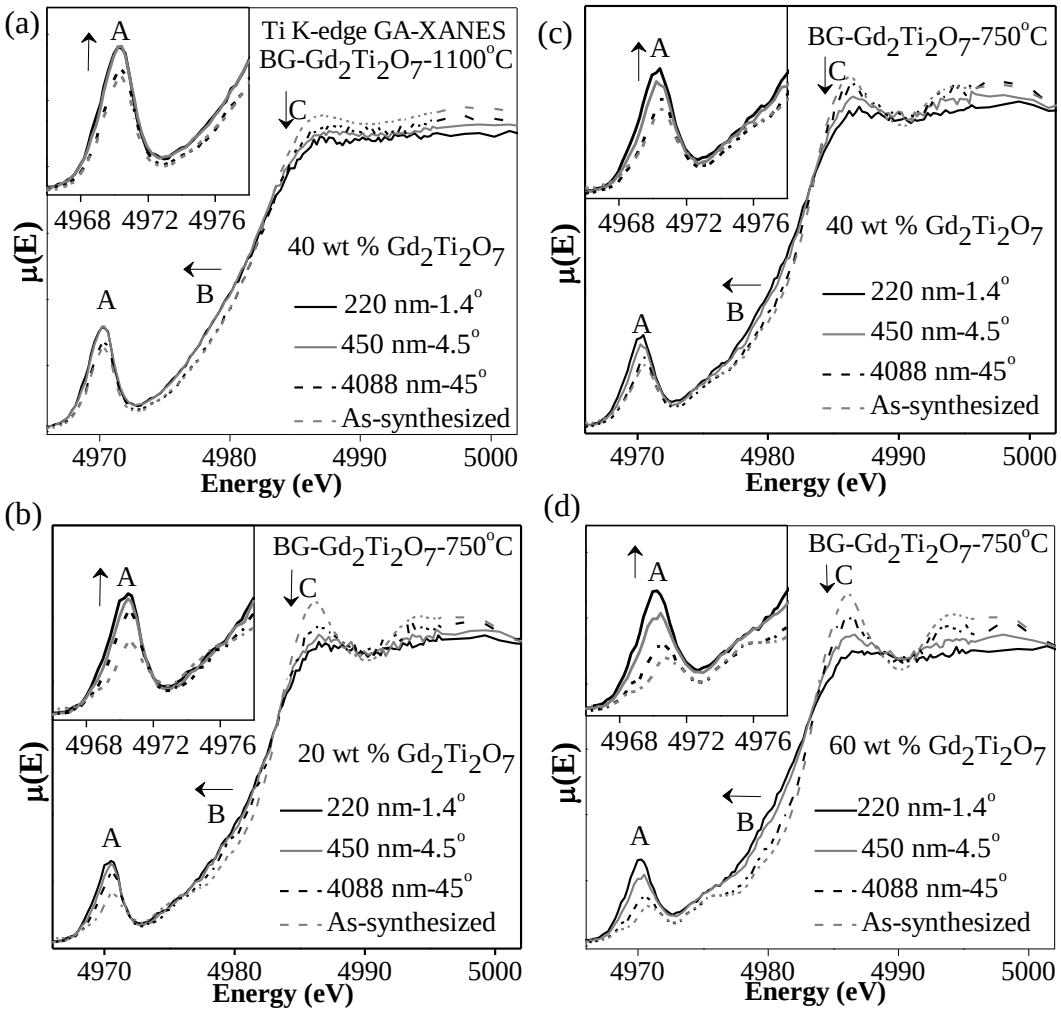

Figure 6.12 Ti K-edge GA-XANES spectra from (a) BG-$Gd_2Ti_2O_7$-1100 °C (60 wt% loading of $Gd_2Ti_2O_7$) and (b,c,d) BG-$Gd_2Ti_2O_7$-750 °C (20 wt%, 40 wt%, and 60 wt% loadings of $Gd_2Ti_2O_7$) implanted using Au^- ions to a dose of 5×10^{14} ions/cm^2 are shown. These spectra are compared to the spectrum from the as-synthesized composite materials. The angles listed, 1.4°, 4.5° and 45°, are the glancing angles used to attain X-ray penetration depths of 220, 450, and 4088 nm, respectively. The changes observed in the spectra with decreasing glancing angle are indicated by arrows.

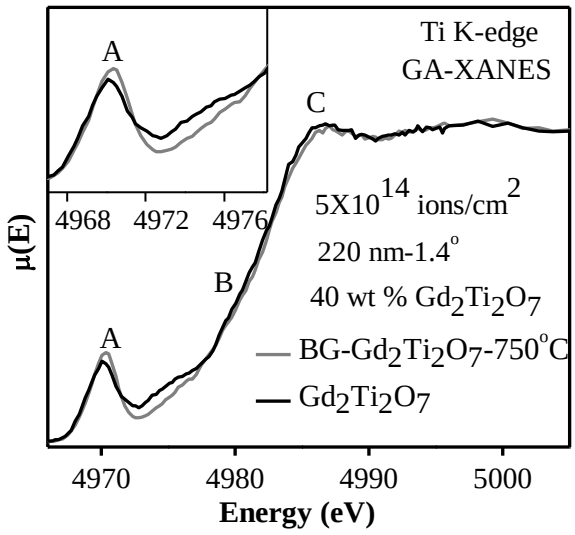

Figure 6.13 (a) Ti K-edge GA-XANES spectra from BG-$Gd_2Ti_2O_7$-750 ^oC (40 wt% loading of $Gd_2Ti_2O_7$) and $Gd_2Ti_2O_7$ implanted to a dose of 5×10^{14} ions/cm^2 are shown. The glancing angle was adjusted for each sample to give an X-ray attenuation depth of 220 nm.

6.4 Conclusions

A greater understanding of glass-ceramic composites has been achieved by the examination of pyrochlore-containing glass-ceramic composite materials by XRD, electron microscopy, and XANES. Glass-ceramic composite materials were synthesized at 1100 ^oC and 750 ^oC; however, $Gd_2Ti_2O_7$ was observed to dissolve significantly in the glass matrix when annealed at 1100 ^oC. Examination of Ti K-edge XANES spectra from the composite materials show that the use of a Fe-Al-borosilicate glass and a lower annealing temperature favours the formation of a composite material with only a small fraction of the $Gd_2Ti_2O_7$ crystallites dissolving in the glass matrix. The Si $L_{2,3}$-edge XANES spectra showed that the ordering of the silicate network changes depending on the glass composition, loading of $Gd_2Ti_2O_7$, and annealing temperature used to form the composite materials. Further, examination of Fe K-edge

XANES spectra from the Fe-Al-borosilicate composites showed that the oxidation state of Fe changed depending on the annealing temperature used to form these composite materials. Examination of Ti K-edge GA-XANES spectra from the ion implanted composite materials has shown that the damage experienced by $Gd_2Ti_2O_7$ in the composite materials *vs* the pure ceramic (i.e., $Gd_2Ti_2O_7$) is similar. The study of these composite materials will be useful for the further development of glass-ceramic composites as potential nuclear wasteforms.

Chapter 7

Conclusions and Directions for Future Research

7.1 Summary of factors affecting resistance to radiation induced damage

The work presented in this thesis has increased our understanding of how changes in electronic properties can influence the resistance to radiation induced damage of materials. These studies are necessary to develop and design materials for nuclear waste immobilization applications. The initial study of this thesis (Chapter 2 and 3) showed how the electronic properties (i.e., bonding environment, coordination number, and oxidation state) of pyrochlore-type oxides change depending on composition. The changes in electronic properties were investigated using XANES. The later part of this thesis (Chapter 4 and 5) discussed how the changes in electronic properties affect the structural stability of materials after ion beam implantation. Surface sensitive TEY-XANES and GA-XANES techniques have been used for this investigation. These studies have demonstrated the ability of TEY-XANES and GA-XANES to identify changes in the local structural environment of transition-metals and main-group metals that are not easily identified by use of X-ray or electron diffraction alone. Finally, the feasibility of combining glass and ceramic materials, and the structural stability of these composite materials, were explored in Chapter 6. The objectives of this thesis (Section 1.5) have been achieved and are summarized in the following sub-sections.

7.1.1 Effect of composition on electronic properties

The effect of elemental substitution on the electronic structure of materials was investigated in Chapters 2 and 3. Chapter 2 discussed the effect of the reduced B-site cation i.e., substituting lower oxidation state metals in the B-site of pyrochlore-type oxides. A series of $Yb_2Ti_{2-x}Fe_xO_{7-\delta}$ ($0 \leq x \leq 0.2$) were synthesized by a conventional solid state reaction method and studied using XANES in order to investigate the changes in coordination number and oxidation state of the transition metal with varying Fe content. The observed changes in transition metal (Ti and Fe) K-edge and L_3-edge XANES spectra indicate that the average CN of Fe and Ti decreased from 6 to a mixture of 4 and 6 with greater Fe content. Analysis of the Fe K-edge XANES spectra shows that Fe adopts an oxidation state of 3+ throughout the series of $Yb_2Ti_{2-x}Fe_xO_{7-\delta}$. The presence of only Fe^{3+} in $Yb_2Ti_{2-x}Fe_xO_{7-\delta}$ results in the material being oxygen deficient. As the Fe^{3+} content increases, a greater oxygen deficiency lowers the metal coordination number, as observed by XANES spectra. This study has achieved a greater understanding of the effect of reduced B-site cations and oxygen deficiency on the local coordination environment and oxidation state of transition metals.

The effect of composition on the metal-oxygen bond covalency was explored by studying a series of $Gd_2Ti_{2-x}Sn_xO_7$ pyrochlore-type oxides in Chapter 3. $Gd_2Ti_{2-x}Sn_xO_7$ (($0 \leq x \leq 2$) was synthesized by the ceramic method and characterized using XANES. To understand the spectral shifts and line shape changes in XANES, partial density of states calculations was performed in this study. The Ti-O bonds become more ionic while the Sn-O bonds becomes more covalent as the Sn content increases and resulted in changes in energy and/or line shape of the Ti K- and Sn L_3-edge XANES spectra. Examination of changes in intensity of the Gd L_3-edge XANES spectra has shown that the ionic character of Gd-O increases with greater Sn content in $Gd_2Ti_{2-x}Sn_xO_7$.

The results presented in this Chapter have shown that the bonding interactions between metal and oxygen in pyrochlore-type oxides vary strongly with composition.

7.1.2 Effect of changes in composition on structural stability

The effect of radiation induced structural damage depending on composition was explored in Chapter 4 and 5. First, the $RE_2Ti_2O_7$ materials were implanted with high-energy (2 MeV) heavy ions (Au^- ions) to mimic radiation induced damage. This can produce an amorphous layer typically a few hundred nm thick. Glancing angle XANES (GA-XANES) and total electron yield XANES (TEY-XANES) were demonstrated in Chapter 4 to be able to study the damaged surface layer of the pellets after being implanted by a beam of high-energy ions. This study investigated the effect of the cationic radii ratio (r_A/r_B) on the structural stability of $RE_2Ti_2O_7$ (RE=La–Lu, Y) using these techniques. $RE_2Ti_2O_7$ (RE=La–Lu, Y) was synthesized by the ceramic method and investigated by Ti K-edge XANES before and after being implanted by 2 MeV Au^- ions. Ti K-edge TEY-XANES and GA-XANES spectra have shown that the local coordination number of Ti decreased i.e., the Ti-site was distorted (damage occurs) after ion beam implantation, and that the degree of damage observed decreases with decreasing radius of the RE ion. These results are in agreement with previous TEM studies of these materials, which show that TEY-XANES and GA-XANES techniques can probe only the damaged surface layer of ion implanted rare-earth titanates.[87] This study has also investigated the effect of oxygen deficiency on the structural stability of $Yb_{1.85}Ca_{0.15}Ti_2O_{7-\delta}$, and $Yb_2Ti_{1.85}Fe_{0.15}O_{7-\delta}$ materials using TEY-XANES and GA-XANES. The spectral analysis has shown that the oxygen vacancies generated by slight substitution of Yb^{3+} for Ca^{2+} or Ti^{4+} for Fe^{3+} in $Yb_2Ti_2O_7$ does not significantly change the resistance of this material to ion induced structural damage. The study

has shown the ability of GA-XANES and TEY-XANES to study the effect of cationic radii ratio (r_{RE}/r_{Ti}) and oxygen vacancies on the structural stability of ion implanted materials.

The effect of metal-oxygen bond covalency on the structural stability of $Gd_2Ti_{2-x}Sn_xO_7$ was explored in Chapter 5. The study presented in Chapter 3 showed that the Gd-O and Ti-O bonds become more ionic while the Sn-O bonds become more covalent in as-synthesized $Gd_2Ti_{2-x}Sn_xO_7$ with increasing Sn incorporation. The $Gd_2Ti_{2-x}Sn_xO_7$ materials were implanted and the damaged surface layer was investigated using GA-XANES/EXAFS. Through the careful analysis of changes in energy and intensity, and line shape of the Ti K-edge and Sn L_3-edge GA-XANES/EXAFS spectra, it has been shown that the Ti-sites and Sn-sites become distorted after ion implantation. The $Gd_2Ti_{2-x}Sn_xO_7$ materials were observed to become more susceptible to ion induced structural damage with increasing Sn concentration, which is attributed to the increased covalency of the bond between O^{2-} and Sn^{4+}. A greater understanding of the effect of bond covalency, cationic radii ratio, and oxygen vacancies of pyrochlore-type oxides on the structural stability has been achieved through the studies presented in Chapters 4 and 5.

7.1.3 Effect of combining the ceramics with glass materials

The final Chapter of this thesis has given more insights into the chemistry (and interaction) of ceramic materials within a glass matrix as well as the structural stability of glass-ceramic composite materials. Borosilicate- and Fe-Al-borosilicate glass-ceramic composites containing $Gd_2Ti_2O_7$ crystallites were synthesized using annealing temperatures of 1100 ^oC and 750 ^oC, and investigated by electron microprobe and XANES. The backscattered electron images collected from the composite materials have shown that the $Gd_2Ti_2O_7$ crystallites dissolved in the glass matrix when annealed at higher temperatures (1100 ^oC), which was also confirmed by

XANES. Analysis of Ti K-edge XANES spectra has shown that the Fe-Al-borosilicate glass composition and a lower annealing temperature (750 ^{o}C) favours the formation of a composite material with only a small fraction of the $Gd_2Ti_2O_7$ crystallites dissolving in the glass matrix. The oxidation state of Fe in the Fe-Al-borosilicate composite materials was reduced to Fe^{2+} when annealed at 1100 ^{o}C and oxidized to Fe^{3+} when annealed at 750 ^{o}C, which was investigated by Fe K-edge XANES. The structural stability of glass-ceramic composite materials after implantation was also explored in this study and was compared with the pure ceramics. The study of ion implanted glass-ceramic materials has shown that the damage experienced by $Gd_2Ti_2O_7$ in the composite materials is similar to pure ceramics (i.e., $Gd_2Ti_2O_7$).

7.2 Significance and implications

The studies presented in this thesis on the pyrochlore-type oxides have provided a better understanding of the effect of composition on electronic properties and the structural stability of these materials. This thesis has also provided a better understanding of how the metal-oxygen bond covalency, cationic radius ratio (r_A/r_B), and oxygen deficiency affect the resistance of these materials. Further, surface sensitive GA-XANES and TEY-XANES techniques have been successfully demonstrated to probe the damaged surface layer of a material after being implanted by heavy ions. This will help to investigate how the structure of a material responds to radioactive decay of incorporated nuclear waste elements. GA-XANES and TEY-XANES techniques have provided great insight into the changes in local structural environment of metal atoms that occur as a result of implantation, which are not easily identified by electron diffraction and other spectroscopic studies such as Nuclear Magnetic Resonance (NMR) spectroscopy. Along with this, this thesis has also improved our understanding of the causes of spectral energy shifts, which is critical to the continuing development of XANES as a probe of

electronic structure. These studies and techniques will be useful for the development of materials for nuclear waste immobilization applications.

7.3 Directions for Future Research

A greater understanding of the effect of composition on the electronic properties and structural stability of pyrochlore-type oxides has been achieved in this thesis using XANES. Investigation of glass-ceramic composite materials containing pyrochlore-type crystallites has shown the feasibility of synthesizing composite materials at different annealing temperatures by a simple solid state method. These studies have also provided a better understanding of how the chemistry and interaction of ceramic materials within a glass matrix changes depending on glass (and ceramic) composition and annealing temperature. A few studies have previously investigated the pyrochlore (e.g., $La_2Zr_2O_7$ and $Gd_2Zr_2O_7$) based glass-ceramic composites using back-scattered electron (BSE) images.[100,239] In this thesis, the study of glass-ceramic composites containing $Gd_2Ti_2O_7$ was a good starting point and further exploration is needed in this area to develop a better understanding of the electronic properties and structural stability of these composites depending on the glass and ceramic composition as well as the synthetic conditions used to produce these materials. The proposed direction for future research is the investigation of various glass-ceramic composite systems.

There are many pyrochlore based glass ceramic composite systems that need to be studied; however as a first step in this area, the rare-earth zirconate and titanate pyrochlore-type materials should be studied to understand the effect of ceramic composition on the electronic and structural properties of the composite materials. Previous investigations of the $Gd_2Ti_{2-x}Zr_xO_7$ and $Y_2Ti_{2-x}Zr_xO_7$ (x= 0.0-2.0) pyrochlore ceramic materials have shown that these ceramic materials

exhibit more resistance to radiation induced damage with increasing Zr content. The study of these glass-ceramic composites would provide a better understanding of how the cationic radii ratio affects the interaction of pyrochlore materials within a glass matrix in composite materials. As was reported previously, the $Gd_2Ti_{2-x}Zr_xO_7$ and $Y_2Ti_{2-x}Zr_xO_7$ materials undergo a phase transition from the pyrochlore-type structure to the defect fluorite structure with increasing Zr content.[41,83,234] This order-disorder phase transition would affect the interaction (and dissolving) of pyrochlore crystallites within the glass matrix. It is expected that these changes could potentially affect the electronic structure and local chemical environment of the composite materials, which could be investigated through a systematic study of Ti K-edge and Zr L_3-edge XANES spectra.

The glass composition and annealing temperature of composite materials could affect the chemistry (and interaction) of pyrochlore crystallites within glass matrix. The work done by this group and other groups have shown that small additions of Fe_2O_3 or ZnO to the borosilicate glass composition can enhance the chemical durability of a glass, which would affect the radiation resistance of a material.[242-244,261] Fe-borosilicate and Zn-borosilicate glass composite materials containing $Gd_2Ti_{2-x}Zr_xO_7$ (or $Y_2Ti_{2-x}Zr_xO_7$) pyrochlore crystallites would be chosen to study the effect of glass composition on the electronic properties of the materials using various techniques (e.g., XANES and X-ray Photoelectron Spectroscopy (XPS)). It is expected that the glass composition would affect the interaction of pyrochlore crystallites within the glass matrix of the composite materials.

Once the preliminary studies are complete, these glass-ceramic composite materials would be exposed to high pressures (GPa) using Diamond Anvile Cell. Pressure induced structural damage can mimic radiation induced structural damage.[82,233] A few reports have

investigated the pressure induced structural changes in a material (e.g., $RE_2Ti_2O_7$ and $Gd_2Zr_2O_7$) using in-situ XRD and Raman Spectroscopy.[82,233] The structural damage that caused by applying high pressures would be investigated using in-situ XANES and XRD. It is expected that the degree of damage could vary with varying (glass and ceramic) composition as well as varying the pressure. Pressure induced structural changes in the glass-ceramic composites *vs* pure ceramics would be investigated to understand how the interaction of ceramics within glass material affect the radiation induced structural damage of these materials.

This thesis has investigated pyrochlore-type oxides and glass-ceramic composite materials to provide a better understanding of the effect of varying electronic properties, composition, and morphology on the resistance to radiation induced structural damage depending on composition. The studies outlined for future research could provide more insights into how changes in glass and ceramic composition affect the resistance of these materials to radiation induced damage. In addition to this, these investigations could also provide a better understanding of how to develop and design materials for nuclear waste immobilization applications.

References

1. Lenzen, M. *Energies* **2010**, *3*, 462-591.
2. Lenzen, M. *Ener. Conver. Manage.* **2008**, *49*, 2178–2199.
3. Abu-Khader, M. M. *Prog. Nucl. Ener.* **2009**, *51*, 225–235.
4. Adamantiades, A.; Kessides, I. *Ener. Policy* **2009**, *37*, 5149–5166
5. *World energy Outlook exclusive report 2014*; International Energy Agency: Paris, 2014.
6. Canadian Socio-Economic Information Management System. *Table 127-0002 Electric power generation, by class of electricity producer, monthly (megawatt hour)* [Online], April 1, 2013, pp 10-11. Statistics Canada. http://www.statcan.gc.ca/ (accessed September 1, 2015)
7. *Estimation of global inventories of radioactive waste and Other radioactive materials*, International Atomic Energy Agency: Vienna, 2008.
8. Ewing, R. C. *Canad. Mineral.* **2005**, *43*, 2099-2116.
9. Manning, W. M. *J. Am. Chem. Soc.* **1962**, *84*, 315–315.
10. G. Taubes, *Science* **1964**, *263*, 629
11. Ojovan, M. I.; Lee, W. E. *An Introduction to Nuclear Waste Immobilization*. Elsevier: Amsterdam, 2005.
12. Cohen, B. L. *Rev. Mod. Phys*. **1977**, *49*, 1.
13. Ewing, R. C. *MRS Bull*. **2008**, *33*, 338.
14. Lutze, W.; Ewing, R. C. *Radioactive Waste Forms for the Future.* North Holland: Amsterdam, 1988.
15. Mueller, I.; Weber, W. J. *MRS Bull.* **2001**, *26*, 698.

16. Ewing, R. C. *Mineral. Magaz.* **2011**, *75(4)*, 2359–2377

17. *Inventory of Low-Level Radioactive Waste in Canada*, Annual Report LLRWMO-01613-041-10003; Low-level Radioactive Waste Management Office: Ottawa, 2012.

18. Canadian Nuclear Safety commission. http://nuclearsafety.gc.ca/eng/waste/historic-nuclear-waste/index.cfm

19. Robin, T. *Reprocessing and Recycling of Spent Nuclear Fuel*, Elsevier Ltd: Cambridge, 2015.

20. US Nuclear Regulatory Commission. http://www.nrc.gov/waste/spent-fuel-storage/pools.html

21. Taylor, R. F.; McPhillimy, J.; Pacey, N. R. *Treatment and packaging of waste plutonium and waste actinides for disposal*; Report No. DOE-RW-88.089; Department of the Environment: London, U.K., 1988).

22. *Safety and Security of Commercial Spent Nuclear Fuel Storage: Public Report 2006*, National Research Council of the National Academies, The National Academies Press: Washington, DC, 2006.

23. Canadian Nuclear Safety commission. http://nuclearsafety.gc.ca/eng/waste/index.cfm#Oversight

24. Miller, W.; Alexander, R.; Chapman, N.; McKinley, J. C.; Smellie, J. A. T. *Geological Disposal of Radioactive Wastes and Natural Analogues*, Elseveir Science Ltd; Oxford, UK, 2010, pp 29-51.

25. Ahn, J.; Apted, M. J. *Geological Repository Systems for Safe Disposal of Spent Nuclear Fuels and radioactive waste*. Woodhead publishing limited: Cambridge, UK, 2010, pp 261-271.

26. Ramana, M. V. *Energy Policy* **2013**, *61*, 196–206

27. Melville, J. *Berkely Scienific. J.* **2013**, *17(2)*, 1-8.

28. Brunnengräber, A.; Di Nucci, M. R.; Losada, A. M. I.; Mez, L.; Schreurs, M. A. *Nuclear Waste Governance: An International Comparison*, Springer: Berlin, 2015, pp 47-50.

29. Ewing, R. C.; Von Hippel, F. N. *Science* **2009**, *325*, 151-152.

30. World Nuclear Association. Storage and Disposal Options. http://world-nuclear.org/info/Nuclear-Fuel-Cycle/Nuclear- Wastes/Appendices/Radioactive-Waste-Management-Appendix-2--Storage-and-Disposal-Options/

31. Stefanovsky, S. V.; Yudintsev, S. V.; Gierè, R.; Lumpkin, G. R.; *Energy, Waste, and the Environment: A Geochemical Perspective*, Gierè, R.; Stille, P., Eds.; Special Publication 236; Geological Society of London: London, 2004; pp. 37.

32. Ewing, R. C.; Weber, W. J.; Clinard, F.W. *Prog. Nucl. Energy* **1995**, *29*, 63-121.

33. Weber, W. J.; Navrotsky, A.; Stefanovsky, S.; Vance, E. R.; Vernaz, E. *MRS Bull.*, **2009**, *34 (1)*, 46-53.

34. Hench, L. L.; Clark, D. E.; Campbell, J. *Nucl. Chem. Waste Manage.* **1984**, *5*, 149-173.

35. Ewing, R. C.; *Mineral. Magaz.* **2011**, *75(4)*, 2359–2377

36. Donald, I. W. *Waste Immobilization in Glass and Ceramic Based Hosts*, John Wiley & Sons Ltd: UK, 2010, pp 101-328.

37. Ringwood, A. E.; Oversby, V. M.; Kesson, S. E.; Sinclair, W.; Ware, N.; Hibberson, W.; Major, A. *Nucl. Chem. Waste Manage.* **1981**, *2*, 287-305.

38. Weber, W. J.; Ewing, R. C.; Angell, C. A; Arnold, G. W.; Cormack, A. N.; Delaye, J. M.; Griscom, D. L.; Hobbs, L. W.; Navrotsky, A.; Price, D. L.; Stoneham, M.; Weinberg, M. C. *J. Mater. Res.* **1997**, *12(8)*, 1946-1978.

39. Sickafus1, K. E.; Grimes, R. W.; Valdez, J. A.; Cleave, A.; Tang, M.; Ishimaru, M.; Corish, S.; Stanek, C. R.; Uberuaga, B. P. *Nature Mater*. **2007**, *6*, 217-223.

40. Weber, W. J.; Roberts, F. P. A. *Nucl. Tech.*, **1983**, *60(2)*, 178-198.

41. Ewing, R. C.; Weber, W. J.; Lian, J. *J. Appl. Phys.* **2004**, *95*, 5949-5971.

42. Hobbs, L. W.; Sreeram, A. N.; Jesurum, C. E.; Berger, B. A. *Nucl. Instru. Meth. Phys. Res. B* **1996**, *16*, 18-25.

43. Ewing, R. C.; Chakoumakos, B.C.; Lumpkin, G. R.; Murakami, T.; Greegor, R. B.; Lytle, F. W. *Nucl. Instru. Meth. Phys. Res. B* **1988**, *32*, 487-497.

44. Sickafus, K. E.; Minervini, L.; Grimes, R. W.; Valdez, J. A.; Ishimaru, M.; Li, F.; McClellan, K. J.; Hartmann, T. *Science* **2000**, *289*, 748.

45. Weber, W. J.; Ewing, R. C.; Catlow, C. R. A.; Rubia, T. D.; Hobbs, L. W.; Kinoshita, C.; Matzke, Hj.; Motta, A. T.; Nastasi, M.; Salje, E. K. H.; et al. *J. Mater. Res.* **1998**, *13(6)*, 1434-1484.

46. Ewing, R. C.; Meldrum, A.; Wang, L.; Wang, S. *Rev. Mineral. Geochem*. **2000**, *39(1)*, 319-361.

47. Thome, L.; Garrido, F. *Vacuum*, **2001**, *63*, 619–626.

48. Grambow, B.; *Elements* **2006**, *2*, 357–364.

49. Raj, K.; Kaushik, C. P. *IOP Conf. Series: Mater. Sci. Eng.* **2009**, *2*, 012002

50. Donald, I. W.; Metcalfe, B. L.; Taylor, R. N. J. *J. Mater. Sci.* **1997**, *32*, 5851–5887.

51. Lutze, W.; Ewing, R. C. *Radioactive waste forms for the future*, Lutze, W.; Ewing, R. C.,eds. North-Holland: Amsterdam, 1988, pp. 699–740.

52. Marples, J. A. C. *Glass Technol*. **1988**, 29, 230

53. Lee, W. E.; Ojovan, M. I.; Stennett, M. C.; Hyatt, N. C. *Adv. Appl. Ceram.* **2006**, *105 (1)*, 1-12.

54. Pace, S.; Cannillo, V.; Wu, J.; Boccaccini, D. N.; Seglem, S.; Boccaccini, A. R. *J. Nucl. Mater.* **2005**, *341*, 12–18.

55. Caurant, D.; Loiseau, P.; Bardez, I.; Gervais, C. *J. Mater. Sci.* **2007**, *42*, 8558–8570.

56. Paul, A. *Chemistry of Glasses*. Chapman & Hall: New York, ed. 2, 1990.

57. Lumpkin, G. R. *Elements* **2006**, *2*, 365–372.

58. Montel, J. *Comp. Rend. Geosci.* **2011**, *343*, 230–236.

59. Ewing, R. C. *Canad. Mineral.* **2001**, *39*, 697-715.

60. Ewing, R. C.; Jercinovic, M. J. *MRS Proc.* **1986**, *84*, 67.

61. Clarke, D. R. *Ann. Rev. Mater. Sci.* **1983**, *13*, 191-218.

62. Wang, L.; Liang, T. *J. Adv. Ceram.* **2012**, *1(3)*, 194-203

63. Strachan, D. M.; Scheele, R. D.; Buck, E. C.; Icenhower, J. P.; Kozelisky, A. E.; Sell, R. L.; Elovich, R. J.; Buchmiller, W. C. *J. Nucl. Mater.* **2005**, *345*, 109–135.

64. Subramanian, M. A.; Aravamudan, G.; Rao, G.V. S. *Prog. Solid State Chem.* **1983**, *15*, 5.

65. Lumpkin, G. R.; *J. Solid State Chem.* **2007**, 180, 1512–151

66. Chakoumakos, B. C. *J. Solid State Chem.* **1984**, *53*, 120.

67. Chakoumakos, B. C.; Ewing, R. C. *Mater. Res. Soc. Symp. Proc.* **1985**, *44*, 641.

68. Sohn, J. M.; Kim, M. R.; Woo, S. I. *Catal. Today* **2002**, *83*, 289-297.

69. Sarohan, P.; Hwan, H. J.; Moon, J. *Catal. Lett.* **2003**, *87*, 3–4.

70. Lee, S. H.; Yoon, C. B.; Seo, S. B.; Kim, H. E. *J. Mater. Res.* **2003**, *18(8)*, 1765-1770.

71. Bongers, P. F.; Van Meurs, E. R. *J. Appl. Phys.* **1967**, 38, 944.

72. Shimakawa, Y.; Kubo, Y.; Manako, T. *Nature* **1966**, *379*, 53-55.

73. Abrantes, J. C. C.; Levchenko, A.; Shlyakhtina, A.V.; Shcherbakova, L. G.; Horovistiz, A. L.; Fagg, D. P.; Frade, J. R. *Solid State Ionics* **2006**, *177*, 1785.

74. Todorov, I. T.; Purton, J. A.; Allan, N. L.; Dove, M. T. *J. Phys.: Condens. Matter.* **2006**, *18*, 2217–2234.

75. Chakoumakos, B. C. *J. Solid State Chem.* **1984**, *53*, 120-129.

76. Momma, K.; Izumi, F. *J. Appl. Crystallogr.* **2008**, *41*, 653–658.

77. Harvey, E. J.; Whittle, K. R.; Lumpkin, G. R.; Smith, R. I.; Redfern, S. A. T. *J. Solid State Chem.* **2005**, *178*, 800–810.

78. Wang, S. X.; Begg, B. D.; Wang, L. M.; Ewing, R. C.; Weber, W. J.; Kutty, K. V. G. J. *Mater. Res.* **1999**, *14*, 4470.

79. Wuensch, B. J.; Eberman, K. W.; Heremans, C.; Ku, E. M.; Onnerud, P.; Yeo, E. M. E.; Haile, S. M.; Stalick, J. K.; Jorgensen, J. D. *Solid State Ionics* **2000**, *129*, 111–133.

80. Kharton, V. V.; Kovalevsky, A. V.; Tsipis, E. V.; Viskup, A. P.; Naumovich, E. N.; Jurado, J. R.; Frade, J. R. *J. Solid State Elec. Chem.* **2002**, *7*, 30-36.

81. Minervini, L.; Grimes, R. W.; Sickafus, K. E. *J. Am. Ceram. Soc.* **2000**, *83*, 1873–1878.

82. Zhang, F. X.; Manoun, B.; Saxena, S. K.; Zha, C. S. *Mater. Lett.* **2006**, *60*, 2773-2776.

83. Sattonnay, G.; Moll, S.; Thomé, L.; Decorse, C.; Legros, C.; Simon, P.; Jagielski, J.; Jozwik, I.; Monnet, I. *J. Appl. Phys.* **2010**, *108*, 103512.

84. Lian, J.; Wang, L.; Chen, J.; Sun, K.; Ewing, R. C.; Farmer, J. M.; Boatner, L. A. *Acta Materialia* **2003**, *51*, 1493-1502.

85. Petrykin, V. V.; Goodilin, E. A.; Hester, J.; Trofimenko, E. A.; Kakihana, M.; Oleynikov, N. N.; Tretyakov, Y.D. *Physica C* **2001**, *357-360*, 388-392

86. Lian, J.; Zu, X. T.; Kutty, K. V. G.; Chen, J.; Wang, L. M.; Ewing, R. C. *Phys. Rev. B* **2002**, *66*, 054108.

87. Lian, J.; Chen, J.; Wang, L. M.; Ewing, R. C. *Phys. Rev. B* **2003**, *68*, 134107.

88. Lian, J.; Helean, K. B.; Kennedy, B. J.; Wang, L. M.; Navrotsky, A.; Ewing, R. C. *J. Phys. Chem. B* **2006**, *110*, 2343-2350.

89. Eberman, K. W. Crystallographic Origins of Fast-ion Conduction in Pyrochlore. Ph.D. Thesis, Massachusetts Institute of Technology, June 1998.

90. Ringwood, A. E.; Kesson, S. E.; Ware, N. G.; Hibberson, W. O.; Major, A. *Geochem. J.* **1979**, *13*, 141.

91. A.E. Ringwood, S.E. Kesson, N.G. Ware, W.O. Hibberson, A.Major, Immobilisation of high level nuclear wastes in SYNROC, Nature 278, 1979, 219-223

92. Ringwood, A. E.; Kelly, P. M.; Bowie, S. H. U.; Kletz, T. A. *Philos. Trans. Royal Soc. London, Ser. A*, **1986**, *319*, 63-82.

93. Solomah, A. G.; Richardson, P. G.; Mcllwain, A. K. *J. Nucl. Mater.* **1987**, *148*, 157-165.

94. Solomah, A. G.; Sridhar, T. S.; Jones, S. C. *Adv. Ceram.* ***1986****, 20, 259*

95. Sridhar, T. S.; Solomah, A. G. *Nucl. Tech.* **1989**, *85(1)*, 89-97.

96. Yang, J.; Tang, B.; Luo, S. *MRS Proc.* **2000**, *663*, 333.

97. Martin, C.; Ribet, I.; Frugier, P.; Gin, S. *J. Nucl. Mater.* **2007**, *366*, 277–287.

98. Zhang, Y.; Zhang, Z.; Thorogood, G.; Vance, E. R. *J. Nucl. Mater.* **2013**, *432*, 545-547.

99. Digeos, A. A.; Valdez, J. A.; Sickafus, K. E.; Atiq, S.; Grimes, R. W.; Boccaccini, A. R. *J. Mater. Sci.*, **2003**, *38*, 1597-1604.

100. Boccaccini, A. R.; Afiq, S.; Grimes, R. W. *Adv. Eng. Mater.* **2003**, *5*, 501-508.

101. Interface Science Western http://www.isw.physics.uwo.ca/facilities_techniques/index.html

102. Reid, D. P.; Hyatt, N. C. *Nucl. Instru. Met. Phys. Res. B* **2010**, *268***,** 1847-1852.

103. Cullity, B. D.; *Elements of X-ray Diffraction.* Addison-Wesley Publishing series: Massachusetts, 1978.

104. Bish, D. L.; Reynolds, R. C. Jr.; *Modern Powder Diffraction.* Bish D. L.; Eds.; Reviews in Mineralogy 20; Mineralogical Society of America: USA, 2004.

105. Singh, A. K. *Advanced X-ray Techniques in Research and Industry*, IOS Press: Amsterdam, The Netherlands, 2005.

106. Willmott, P. *An introduction to synchrotron radiation; Techniques and Applications*. A John Wiley & Sons Ltd: UK, 2011

107. Krinsky, S. *Fundamentals of hard X-ray synchrotron radiation sources.,In Third Generation Hard X-ray Synchrotron Radiation Sources*; Mills, D. M.,Eds.; John Wiley & Sons: New York, 2002; pp 1–41.

108. Crease, R. P. *Phys. Perspect.* **2008**, *10*, 438–467.

109. Margaritondo, G. *Phys. Today* **2008**, *61*, 37–43.

110. Mills, D. M. *Third Generation Hard X-ray Synchrotron Radiation Sources; Source properties, optics, and experimental techniques.* John Wiley & Sons: New York, 2002; pp 41–100.

111. Brown, G.; Halbach, K.; Harris, J.; Winick, H. *Nucl. Instr. Meth. Phys. Res.* **1983**, *208*, 65–77.

112. Bunker, G. *Introduction to XAFS: a practical guide to X-ray absorption fine structure spectroscopy*, Cambridge University Press: Cambridge, U.K., 2010.

113. Jiang, D. T.; Chen, N.; Zhang, L.; Malgorzata, K.; Wright, G. *AIP Conf. Proc.* **2007**, *882*, 893.

114. Paterson, D. J.; Boldeman, J. W.; Cohen, D. D.; Ryan, C. G. *AIP Conf. Proc.* **2007**, *879*, 864–867.

115. Regier, T.; Krochak, J.; Sham, T. K.; Hu, Y. F.; Thompson, J.; Blyth, R. I. R. *Nucl. Instrum. Meth. Phys. Res. A*, **2007**, *582*, 93–95.

116. Kelly, S. D.; Hesterberg, D.; Ravel, B.; *Analysis of soils and minerals using X-ray absorption spectroscopy, in Methods of Soil Analysis—Part 5: Mineralogical Methods*, Soil Sci. Soc. Am. Series 5, Soil Sci. Soc. America: Madison, 2008.

117. Jiang, D. T. *In Synchrotron Radiation: Earth, Environmental and Materials Sciences Applications*; Henderson, G.; Baker, D. R., Eds.; Mineral. Assoc. Canada: Ottawa, 2002; pp 65–98.

118. Newville, M., *Fundamentals of XAFS*, Revision 1.7.; University of Chicago: Chicago, IL, 2004.

119. Achkar, J.; Regier, T. Z.; Wadati, H.; Kim, Y. J.; Zhang, H.; Hawthorn, D. G.; *Phys. Rev. B* **2011**, *83*, 081106-R.

120. Eisebitt, S.; Boske, T.; Rubensson, J. E.; Eberhardt, W. *Phys. Rev. B*, **1993**, *47*, 14103-14109.

121. De Groot, F. M. F. *J. Electr. Spec. Relat. Phenom.* **1994**, *67*, 529-622.

122. Manceau, A.; Marcus, M. A.; Tamura, N. *Rev. Miner. Geochem.* **2002**, *49*, 341-428.

123. Troger, L. Arvanitis, D.; Baberschke, K.; Michaelis, H.; Grimm, U.; Zschech, E. *Phys. Rev. B*, **1992**, *46*, 3283-3289.

124. Achkar, J.; Regier, T. Z.; Monkman, E. J.; Shen, K. M.; Hawthorn, D. G. *Sci. Reports* **2011**, *1*, 18.

125. De Groot, F. M. F. *Chem. Rev.* **2001**, *101*, 1779-1808.

126. Prins, R. Koningsberger, D. C. *X-ray absorption: principles, applications, techniques of EXAFS, SEXAFS, and XANES*, Wiley: New York, 1988.

127. Grunes, L.A.; Leapman, R.D.; Wilker, C.N.; Hoffman, R.; Kunz, A.B. *Phys. Rev. B:Condens. Matter Mater. Phys.* **1982**, *25*, 7157.

128. Wilke, M.; Farges, F.; Petit, P. E.; Brown; G. E.; Martin, F. *Am. Miner.* **2001**, 86, 714-730.

129. Farges, F.; Brown, G. E.; Rehr, J. J. *Phys. Rev. B: Condens. Matt.* **1997**, 56, 1809-1819.

130. Grosvenor, A. P.; Greedan, J. E. *J. Phys. Chem. C* **2009**, *113*, 11366-11372.

131. Gaultois, M. W.; Grosvenor, A. P. *J. Mater. Chem*. **2011**, *21*, 1829–1836.

132. Farges, F.; Brown, G. E.; Rehr, J. J. *Geochim. Cosmochim. Acta*. **1996**, *60*, 3023–3038.

133. Greaves, G. N.; Barrett, N. T.; Antonini, G. M.; Thornley, F. R.; Willis, B. T. M.; Steel, A. *Am. Chem. Soc.* **1989**, *111*, 4313-4324.

134. Waychunas, G. A. *Rev. Mineral. Geo. Chem.* **2002**, *49*, 267.

135. England, K. E. R.; Charnock, J. M.; Pattrick, R. A. D.; Vaughan, D. J. *Mineral. Magazine* **1999**, *63(4)*, 559-566.

136. Stennett, M. C.; Reid, D. P.; Peng, N.; Maddrell, E. R.; Ravel, B.; Hyatt, N. C. *Probing Radiation Damage in Ceramic Wasteforms Using X-ray Absorption Spectroscopy.* Diamond'10 Conference, Budapest, Hungary, Sept 5-9, 2010.

137. Kennedy, B. J. *Physica B* **1998**, *241-243*, 303-310.

138. Vanderah, T. A.; Levin, I.; Lufaso, M. W. *Eur. J. Inorg. Chem.* **2005**, *14*, 2895–2901.

139. Pirzada, M.; Grimes, R.W.; Minervini, L.; Maguire, J. F.; Sickafus, K. E. *Solid State Ionics* **2001**, *140*, 201-208.

140. Horovistiz, A. L.; Boguslavskii, M. V.; Abrantes, J. C. C.; Shlyakhtina, A. V.; Fagg, D. P.; Shcherbakova, L. G.; Frade, J. R. *Solid State Ionics* **2009**, *180*, 774–777.

141. Shlyakhtina, A. V.; Kolbanev, I. V.; Karyagina, O. K.; Shcherbakova, L. G. *Inorg. Mater.* **2005**, *42(5)*, 528–531.

142. Horovisitz, A. L.; Fagg, D. P.; Abrantes, J. C. C.; Frade, J. R. *J. Eur. Ceram. Soc.* **2007**, *27*, 4283-4286.

143. Shlyakhtina, A. V.; Fedtke, P.; Busch, A.; Kolbanev, I. V.; Barfels, T.; Wienecke, M.; Sokolov, A. E.; Ulianov, V. A.; Trounov, V. A.; Shcherbakova, L. G. *Solid State Ionics* **2008**, *179*, 1004–1008.

144. Vračar, M.; Kuzmin, A.; Merkle, R.; Purans, J.; Kotomin, E. A.; Maier, J.; Mathon, O. *Phys. Rev. B* **2007**, *76*, 174107.

145. Waerenborgh, J. C.; Figueiredo, F. M.; Frade, J. R.; Colomer, M. T.; Jurado, J. R. *J. Phys.: Condens. Matter* **2001**, 13, 8171–8187.

146. Haas, O.; Vogt, U. F.; Soltmann, C.; Braun, A.; Yoon, W. S.; Yang, X. Q.; Graule, T. *Mater. Res. Bull.* **2009**, *44*, 1349-1404.

147. Kharton, V. V.; Kovalevsky, A. V.; Tsipis, E. V.; Viskup, A. P.; Naumovich, E.N.; Jurado, J. R.; Frade, J. R. *J. Solid State Elec. Chem.* **2002**, *7*, 30-36.

148. Zheng, Y.; Yu, Z.; Zhuang, Y.; Zhu, S. *Hyperfine Interact.* **1990**, *53*, 439-444.

149. Blasco, J.; Aznar, B.; García, J.; Subías, G.; Martín, J. H.; Stankiewicz, J.; *Phys. Rev. B* **2008**, *77*, 054107.

150. PANalytical B. V. X'Pert HighScore Plus, Version 3.0; Almelo: The Netherlands, 2011.

151. Thompson, A.; Attwood, D.; Gullikson, E.; Howells, M.; Kim, K. J.; Kirz, J.; Kortright, J.; Lindau, I.; Pianetta, P.; Robinson, A.; Scofield, J.; Underwood, J., Vaughan, D.; Williams, G.; Winick, H. X-ray data booklet, Lawrence Berkeley National Laboratory: Berkeley, CA, 2009.

152. Ravel, B.; Newville, M. *J. Synchrotron Rad.* **2005**, *12*, 537-541.

153. Hu, Y. F.; Coulthard, I.; Chevrier, D.; Wright, G.; Igarashi, R. *AIP Conf. Proc.* **2010**, *1234*, 343.

154. Shlyakhtina, A. V.; Knotko, A. V.; Boguslavskii, M. V.; Stefanovich, S. Y.; Peryshkov, D. V.; Kolbanev, I. V.; Shcherbakova, L. G. *Solid State Ionics* **2005**, *176*, 2297-2304.

155. Shannon, R. D. *Acta Crystallogr.* **1976**, *A32*, 751-767.

156. Eberman, K. W.; Wuensch, B. J.; Jorgensen, J. D. *Solid State Ionics* **2002**, *148*, 521-526.

157. Westre, T. E.; Kennepohl, P.; DeWitt, J. G.; Hedman, B. ; Hodgson, K. O.; Solomon, E. I. *J. Am. Chem. Soc.* **1995**, *119*, 6297-6314.

158. Elfimov, I. S.; Anisimov, V. I; Sawatzky, G. A. *Phys. Rev. Lett.* **1999**, *82*, 4264.

159. Yamamoto, T. *X-Ray Spectrom* **2008**, *37*, 572–584.

160. Wong, J.; Lytle, F. W.; Messmer, R. P.; Maylotte, D. H. *Phys. Rev. B* **1984**, *30(10)*, 5596-5610.

161. Cabaret, D.; Joly, Y.; Renevier, H.; Natoli, C. R. *J. Synchrotron Rad.* **1999**, *6*, 258-260.

162. Berlier, G.; Spoto, G.; Bordiga, S.; Ricchiardi, G.; Fisicaro, P.; Zecchina, A.; Rossetti, I.; Selli, E.; Forni, L.; Giamello, E.; Lamberti, C. *J. Catalysis.* **2002**, *208*, 64–82.

163. Toquin, R. L.; Paulus, W.; Cousson, A.; Prestipino, C.; Lamberti, C. *J. Am. Chem. Soc.* **2006**, *128*, 13161–13174.

164. Blasco, J.; Aznar, B.; García, J.; Subías, G.; Martín, J. H.; Stankiewicz, J. *Phys. Rev. B* **2008**, *77*, 054107.

165. Berry, A. J.; Neill, H. C.; Jayasuriya, K. D.; Campbell, S. J.; Foran, G. J. *Am. Mineral.* **2003**, *88*, 967–977.

166. De Groot, F. M. F.; Fuggle, J. C.; Thole, B. T.; Sawatzky, G. A. *Phys. Rev. B* **1990**, *42(9)*, 5459-5468.

167. Van der Laan, G. *J. Elec. Spect. Rel. Phen.* **1997**, *86*, 41-47.

168. Chen, C. L.; Dong, C. L.; Rao, S. M.; Chern, G.; Chen, M. C.; Wu, M. K.; Chang, C. L. *J. Phys.: Condens. Matter*, **2008**, *20*, 255236-255240.

169. Grosvenor, A. P.; Ramezanipour, F.; Derakhshan, S.; Maunders, C.; Botton, G. A.; Greedan, J. E. *J. Mater. Chem.* **2009**, *19*, 9213-9220.

170. Crocombette, J. P.; Pollak, M.; Jollet, F.; Thromat, N.; Soyer, M. G. *Phys. Rev. B* **1995**, *52*, 3143-3150.

171. Ikeno, H.; Tanaka, I.; Miyamae, T.; Mishima, T.; Adachi, H.; Ogasawara, K. *Mater. Trans.* **2004**, *45(5)*, 1414-1418.

172. De Groot, M. F.; Vogel, J.; Fundamentals of X-ray Absorption and Dichroism: The Multiplet Approach. In Neutron and X-ray Spectroscoy [Online]; Hippert, F.; Geissler, E.; Hodeau, J. L.; Lelièvre-Berna, E.; Regnard, J. R. Springer: Netherlands, 2006, pp 3-66.

173. Van Aken, P. A.; Liebscher , B.; Styrsa, V. J. Phys. *Chem. Miner.* **1998**, *25*, 323-327.

174. Gaultois, M. W.; Grosvenor, A. P. *J. Phys. Chem. C* **2010**, *114*, 19822-19829.

175. Cressey, G.; Henderson, C. M. B.; Van der Laan, G. *Phys. Chem. Miner.* **1993**, *20*, 111-119.

176. Cabaret, D.; Bordage, A.; Juhin, A.; Arfaoui, M.; Gaudry, E. *Phys. Chem. Chem. Phys.* **2010**, *12*, 5619-5633.

177. Grunes, L. A. *Phys. Rev. B* **1983**, *27(4)*, 2111-2131.

178. Farges, F.; *Am. Mineral.* **1997**, *82*, 36-43.

179. Farges, F. *J. Non-Cryst. Solids* **1996**, *204*, 53-64.

180. Henderson, G. S.; Liu, X.; Fleet, M. E. *Phys. Chem. Miner.* **2002**, *29*, 32.

181. De Groot, F. M. F. *Coord. Chem. Rev.* **2005**, *249*, 31–63.

182. De Groot, F. M. F.; Figueiredo, M. O.; Basto, M. J.; Abbate, M.; Petersen, H.; Fuggle, J. C. *Phys. Chem. Miner.* **1992**, *19*, 140-147.

183. Ponnusamy, N.; Suntharampillai, T.; Adams, E. M.; Weber, W. J.; Begg, B. D.; Mun, B. S.; Shuh, D. K.; Lindle, D. W.; Gullikson, E. M.; Perera, R. C. C. *J. Phys. Chem. B* **2005**, *109(4)*, 1337-1339.

184. Nemoshkalenko, V. V.; Borisenko, S. V.; Uvarov, V. N.; Yaresko, A. N.; Vakhney, A. G.; Senkevich, A. I.; Bondarenko, T.N.; Borisenko, V. D. *Phys. Rev. B* **2001**, *63*, 075106.

185. Kruger, P. *Phys. Rev. B: Condens. Matter* **2010**, *81*, 125121-1.

186. Yu, T.; Tuller, H. L. *Solid State Ionics* **1996**, *86-88*, 177-182.

187. Jin, D.; Yua, X.; Yanga, H.; Zhua, H.; Wanga, L.; Zheng, Y. *J. Alloys Compd*. **2009**, *474*, 557–560.

188. Whittle, K. R.; Blackford, M. G.; Aughterson, R. D.; Lumpkin, G. R.; Zaluzec, N. J. *Acta Mater.* **2011**, *59*, 7530–7537.

189. Lumpkin, G. R.; Smith, K. L.; Blackford, M. G.; Whittle, K. R. *Chem. Mater.* **2009**, *21*, 2746–2754.

190. Moon, P. K.; Tuller, H. L. *Mat. Res. Soc. Symp. Proc.* **1989**, *135*, 149-155.

191. Kennedy, B. J.; Hunter, B. A.; Howard, C. J. *J. Solid State Chem.* **1997**, *130*, 58-65.

192. Walker, J. D. S.; Hayes, J. R.; Gaultois, M. W.; Aluri, E. R.; Grosvenor, A. P. *J. Alloys Compd.* **2013**, *565*, 44-49.

193. Blanchard, P. E. R.; Clements, R.; Kennedy, B. J.; Ling, C. D.; Reynolds, E.; Avdeev, M.; Stampfl, A. P. J.; Zhang, Z.; Jang, L. Y. *Inorg. Chem.* **2012**, *51*, 13237-13244.

194. Denton, A. R.; Ashcroft, N. W. *Phys. Rev. A* **1991**, *43*, 3161-3164.

195. Heald, S. M.; Brewe, D. L.; Stern, E. A.; Kim, K. H.; Brown, F. C.; Jiang, D. T.; Crozier, E. D.; Gordon, R. A. *J. Synchrotron Rad.* **1999**, *6*, 347–349.

196. Andersen, O. K.; Jepsen, O. *Phys. Rev. Lett.* **1984**, *53*, 2571-2574.

197. Sun, B. J.; Liu, Q. L.; Liang, J. K.; Li, J. B.; Ji, L. N.; Zhang, J.Y.; Liu, Y. H.; Rao, G. H. *J. Alloys Compd.* **2008**, *455*, 265–268.

198. Zhang, Z. L.; Xiao, H.Y.; Zu, X.T.; Gao, F.; Weber, W. J. *J. Mater. Res.* **2009**, *24(4)*, 1335-1341.

199. Yu, T. H. *Electrical properties and structural disorder in Stannate Pyrochlores.* Ph.D. Thesis, M.I.T, Cambridge, Sept 1996.

200. Lee, Y. H.; Sheu, H. S.; Deng, J. P.; Kao, H. C. I. *J. Alloys Compd.* **2009**, *487*, 595-598.

201. Rehr, J. J.; Albers, R. C. *Rev. Mod. Phys.* **2000**, *72*, 621–54.

202. Waychunas, G. A. *Am. Mineral.* **1987**, *72*, 89 – 101.

203. *Sigrist, J. A.; Gaultois, M. W.; Grosvenor, A. P. J. Phys. Chem. A* **2011**, *115*, *1908–1912.*

204. Van Bokhoven, J. A.; Nabi, T.; Sambe, H.; Ramaker, D. E.; Koningsberger, D. C. *J. Phys.: Condens. Matter* **2001**, *13*, 10247-19260.

205. Allred, A. L.; Rochow, E. G. *J. Inorg. Nucl. Chem.* **1958**, *5*, 264-268.

206. Haile, S. M.; Wuensch, B. J.; Prince, E. *Mater. Res. Symp. Proc.* **1990**, *166*, 81-86.

207. Guillot, F.; Dézarnaud-Dandine, C.; Tronc, M. *Chem. Phys.* **1997**, *224*, 281-300.

208. Liu, Z.; Handab, K.; Kaibuchi, K.; Tanaka, Y.; Kawai, J. *J. Electron Spectrosc. Relat. Phenom.* **2004**, *135*, 155–158.

209. Akatsuka, T.; Ushiro, M.; Nagamatsu, S.; Takahashi, Y.; Fujikawa, T. *Polyhedron* **2008**, *27*, 3146-3150

210. Farges, F.; Linnen, R. L.; Brown, G. E. *Canad. Mineral.* **2006**, *44*, 795-810.

211. Materlik, G.; Müller, J. E.; Wilkins, J. W. *Phys. Rev. Lett.* **1983**, *50*, 267-270.

212. Hess, N. J.; Begg, B. D.; Conradson, S. D.; McCready, D. E.; Gassman, P. L.; Weber, W. J. *J. Phys. Chem. B.* **2002**, *106*, 4663-4677.

213. Ewing, R.C. *Nucl. Instr. Meth. Phys. Res. B* **1994**, *91*, 22-29.

214. Pattrick, R. A. D.; Charnock, J. M.; Geraki, T.; Mosselmans, J. F. W.; Pearce, C. I.; Pimblott, S.; Droop, G. T. R. *Mineral. Magazine* **2013**, *77(6)*, 2867-2882.

215. Vlachos, D.; Craven, A. J.; McComb, D. W. *J. Synchrotron Rad.* **2005**, *12*, 224-233.

216. Nakajima, R.; Stohr, J.; Idzerda, Y. U. *Phys. Rev. B* **1999**, *59(9)*, 6421-6428.

217. Chen, J.; Lian, J.; Wang, L. M.; Ewing, R. C. *Appl. Phys. Lett.* **2001**, *79(13)*, 1989-1992.

218. Helean, K.B.; Ushakov, S.V.; Brown, C.E.; Navrotsky, A.; Lian, J.; Ewing, R.C.; Farmer, J.M.; Boatner, L.A. *J. Solid State Chem.* **2004**, *177*, 1858–1866.

219. Shlyakhtina, A. V.; Sokolov, A. E.; Ulyanov, V. A.; Trunov, V. A.; Boguslavski, M. V.; Levchenko, A. V.; Shcherbakova, L. G. *Crystallogr. Reports* **2009**, *54(1)*, 25–30.

220. Ziegler, J. F.; Biersack, J. P.; Ziegler, M. D. *SRIM (The Stopping and Range of Ions in Solids)-2013*, MD: USA, 2013.

221. X-ray Attenuation Length. http://henke.lbl.gov/optical_constants/atten2.html

222. Heremans, C.; Wuensch, B.J.; Stalick, J.K.; Prince, E. *J. Solid State Chem.* **1995**, *117* 108-121.

223. Mandal, B. P.; Pandey, M.; Tyagi, A. K. *J. Nucl. Mater.* **2010**, *406*, 238–243.

224. Li, Y. H.; Wang, Y. Q.; Zhou, M.; Xu, C. P.; Valdez, J. A.; Sickafus, K.E. *Nucl. Instru. Met. Phys. Res. B* **2011**, *269*, 2001–2005.

225. Hayes, J. R.; Grosvenor, A.P. *J. Phys.: Condens. Matter* **2011**, *23*, 465502.

226. Kim, K.H.; Akase, Z.; Suzuki, T.; Shindo, D. *Mater. Trans.* **2010**, *51(6)*, 1080-1083.

227. Lian, J.; Ewing, R. C.; Wang, L. M.; Helean, K. B. *J. Mater. Res.* **2004**, *19(5)*, 1575-1580.

228. Chen, Z. J.; Xiao, H. Y.; Zu, X. T.; Gao, F. *J. Appl. Phys.* **2008**, *104*, 093702.

229. Panero, W. R.; Stixrude, L.; Ewing, R. C. *Phys. Rev. B* **2004**, *70*, 054110.

230. England, K. E. R.; Charnock, J. M.; Pattrick, R. A. D.; Vaughan, D. J. *Miner. Magazine* **1999**, *63(4)*, 559-566.

231. Greegor, R. B.; Lytle, F. W.; Arnold, G. W.; Ewing, R. C. *J. Non-Cryst. Solids* **1990**, *122*, 121-132.

232. Moskal, G.; Swad´zba, L.; Hetmanczyk, M.; Witala, B.; Mendala, B.; Mendala, J.; Sosnowy, P. *J. Eur. Ceram. Soc.* **2012**, *32*, 2025–2034.

233. Zhang, F. X.; Lian, J.; Becker, U.; Ewing, R. C.; Hu, J.; Saxena, S. K. *Phys. Rev. B* **2007**, *76*, 214104.

234. De los Reyes, M.; Whittle, K. R.; Zhang, Z.; Ashbrook, S. E.; Mitchell, M. R.; Jang, L.; Lumpkin, G. R. *RSC Adv.* **2013**, *3*, 5090–5099.

235. Carboni, R.; Giovannini, S.; Antonioli, G.; Boscherini, F. *Physica Scripta* **2005**, *T115*, 986-988.

236. Chen, Z. J., Xiao, H. Y.; Zu, X. T.; Wang, L. M.; Gao, F.; Lian, J.; Ewing, R. C. *Comput. Mater. Sci.* **2008**, 42, 653–658.

237. Amoroso, J.; Marra, J. C.; Tang, M.; Lin, Y.; Chen, F.; Su, D.; Brinkman, K. S. *J. Nucl. Mater.* **2014**, *454*, 12–21.

238. Loiseau, P.; Caurant, D. *J. Nucl. Mater.* **2010**, *402*, 38-54.

239. Boccaccini, A. R.; Bernardo, E.; Blain, L.; Boccaccini, D. N. *J. Nucl. Mater.* **2004**, *327*, 148-158.

240. Northrup, C. J. M.; Arnold, G. W.; Headley, T. J. *MRS Proc.* **1980**, *6*, 667.

241. McGann, O. J.; Bingham, P. A.; Hand, R. J.; Gandy, A. S.; Kavcic, M.; Itnik, M. Z.; Bucar, K.; Edge, R.; Hyatt, N. C. *J. Nucl. Mater.* **2012**, *429*, 353-367.

242. Malchukova, E.; Boizot, B.; Petite, G.; Ghaleb, D. *Eur. Phys. J. Appl. Phys.* **2009**, *45*, 10701.

243. McGann, O. J.; Gandy, A. S.; Bingham, P. A.; Hand, R. J.; Hyatt, N. C. *MRS Proc.* **2013**, *1518*, 41-46.

244. Magnien, V.; Neuville, D. R.; Cormier, L.; Roux, J.; Hazemann, J. L.; Pinet, O.; Richet, P. *J. Nucl. Mater.* **2006**, *352*, 190-195.

245. Kihara, K. *Eur. J. Mineral.* **1990**, *2*, 63-77.

246. Singh, J.; Singh, D.; Singh, S. P.; Mudahar, G. S.; Thind, K. S. *Mater. Phys. Mech.* **2014**, *19*, 9-15.

247. Petrescu, S.; Malki, M.; Constantinescu, M.; Anghel, E. M.; Atkinson, I.; State, R.; Zaharescu, M. *J. optoelectron. Adv. Mater.* **2012**, *14*, 603-612

248. Krinsley, D. H; Kenneth, P.; Boggs, S; Tovey, N. K. *Backscattered scanning electron microscopy and image analysis of sediments and sedimentary rocks.* Cambridge University Press: Network, 1998.

249. Gaultois, M. W.; Grosvenor, A. P. *Phys. Chem. Phys. Chem.* **2011**, *21*, 1829-1836.

250. Li, D.; Bancroft, G. M.; Fleet, M. E. *Am. Mineral.* **1996**, *81*, 111-118.

251. Li, D.; Bancroft, G. M.; Kasrai, M.; Fleet, M. E.; Feng, X. H.; Tan, K. H.; Yang, B. X. *Solid State Commun.* **1993**, *87*, 613-617.

252. Li, D.; Bancroft, G. M.; Kasrai, M.; Fleet, M. E.; Feng, X. H.; Tan, K. H. *Am. Mineral.* **1994**, *79*, 785-788.

253. Garvie, L. A. J.; Buseck, P. R. *Am. Mineral.* **1999**, *84*, 946-964.

254. G. R. Harp, D. K. Saldin and B. P. Tonner, *I. Phys.: Condens. Matter* **1993**, *5*, 5377-5388.

255. Li, D.; Bancroft, G. M.; Kasrai, M.; Fleet, M. E.; Secco, R. A.; Feng, X. H.; Tan, K. H.; Yang, B. X. *Am. Mineral*. **1994**, *79*, 622-632.

256. Mehdikhani, B.; Borhani, G. H. *Proc. Appl. Ceram.* **2013**, *7*, 117–121.

257. Magnien, V.; Neuville, D. R.; Cormier, L.; Roux, J.; Hazemann, J. L.; De Ligny, D.; Pascarelli, S.; Vickridge, I.; Pinet, O.; Richet, P. *Geo. Cosmo. Acta*. **2008**, *72*, 2157-2168.

258. Magnien, V.; Neuville, D. R.; Cormier, L.; Roux, J.; Hazemann, J. L.; Pinet, O.; Richet, P. *J. Nucl. Mater.* **2006**, *352*, 190-195.

259. Kukkadapu, R. K.; Li, H.; Smith, G. L.; Crum, J. D.; Jeoung, J.; Poisl, W. H.; Weinberg, M. C. *J. Non-Cryst. Solids* **2003**, *317*, 301-318.

260. Walker, J. D. S.; Grosvenor, A. P. *Inorg. Chem.* **2013**, 52, 8612-8620.

261. Zhang, H.; Corkhill, C. L.; Heath, P. G.; Hand, R. J.; Stennett, M. C.; Hyatt, N. C. *J. Nucl. Mater.* **2015**, *462*, 321–328.

Appendix 1

Supporting information for Chapter 3

Table A1.1 Lattice constants from the $Y_2Ti_{2-x}Sn_xO_7$ series

$Y_2Ti_{2-x}Sn_xO_7$	
x	a (Å)
0.0	10.0969(2)
1.0	10.2389(5)
2.0	10.3731(1)

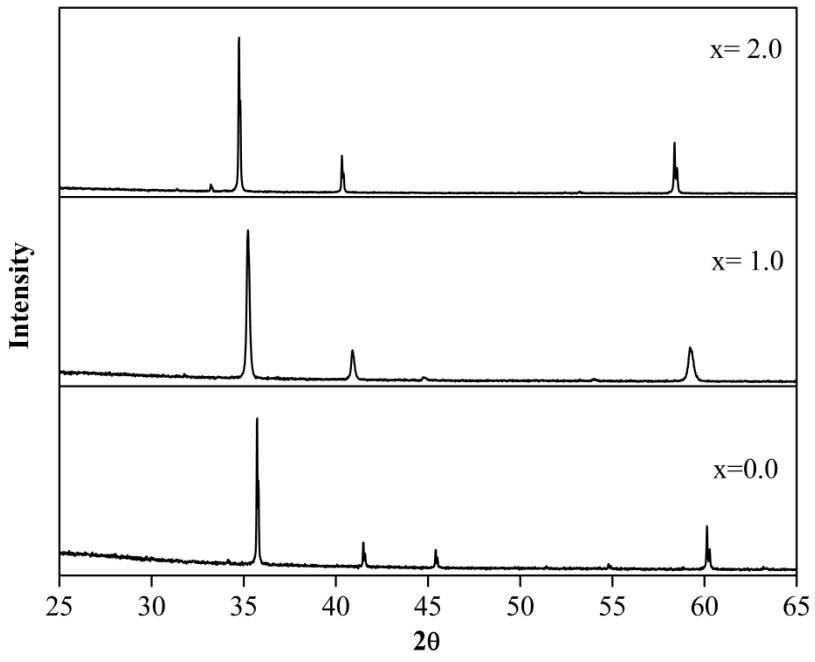

Figure A1.1 XRD patterns from the $Y_2Ti_{2-x}Sn_xO_7$ series are shown. The diffraction peaks shift to lower 2θ with increasing Sn content.

Appendix 2

Supporting information for Chapter 4

Table A2.1. Rietveld refinement results of powder XRD patterns from the undamaged $(Sm,Gd,Yb)_2Ti_2O_7$ materials*

	$Sm_2Ti_2O_7$	$Gd_2Ti_2O_7$	$Yb_2Ti_2O_7$
Crystal structure	Pyrochlore[a] ($Fd\bar{3}m$)	Pyrochlore ($Fd\bar{3}m$)	Pyrochlore ($Fd\bar{3}m$)
a (Å)	10.2318(3)	10.1851(1)	10.0296(3)
x_{48f}	0.4288(3)	0.4252(2)	0.4223(3)
B overall ($Å^2$)	0.80(2)	0.21(1)	0.48(1)
R_p (%)	3.46	5.89	2.73
R_{wp} (%)	7.22	6.90	9.05
GOF	4.33	1.37	10.97

*a = Lattice constant; x_{48f} = x-coordinate of the oxygen anions occupying the 48f site, B overall = Overall isotropic thermal factor. R_p = Refinement profile, R_{wp} = Weighted refinement profile, GOF = Goodness of fits (R_{wp}/R_{exp}); R_{wp} and R_{exp} are the weighted refinement and expected profiles, respectively.

[a]Atomic positions for the pyrochlore-type structure: RE:16c (0 0 0); Ti:16d (½ ½ ½); O:8a (⅛ ⅛ ⅛); and O':48f (x ⅛ ⅛).

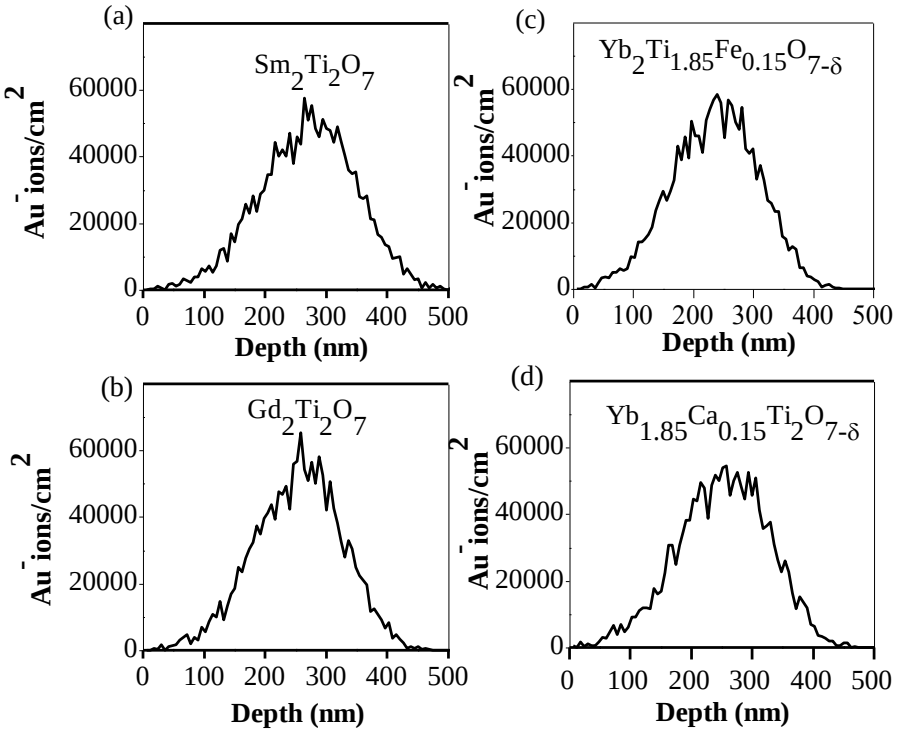

Figure A2.1 Ion beam implantation depth profiles from (a) $Sm_2Ti_2O_7$, (b) $Gd_2Ti_2O_7$, (c) $Yb_2Ti_{1.85}Fe_{0.15}O_{7-\delta}$, and (d) $Yb_{1.85}Ca_{0.15}Ti_2O_{7-\delta}$ calculated using SRIM-2013.[220] These calculations were performed using 5000 Au^- ions with the ion beam energy being 2 MeV.

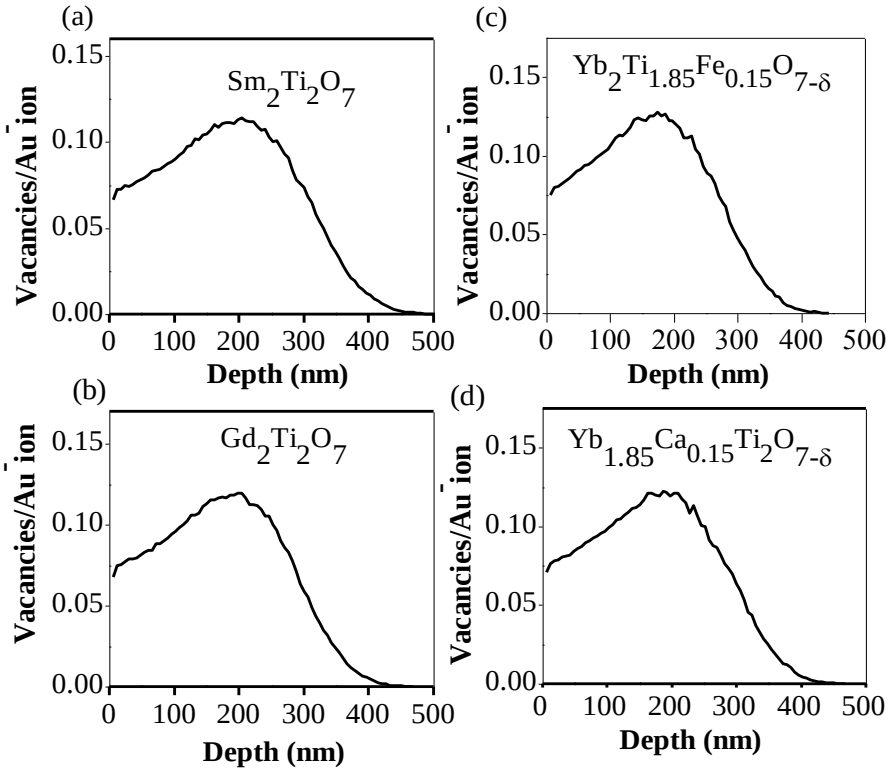

Figure A2.2 Defect-per-ion profiles from (a) $Sm_2Ti_2O_7$, (b) $Gd_2Ti_2O_7$, (c) $Yb_2Ti_{1.85}Fe_{0.15}O_{7-\delta}$, and (d) $Yb_{1.85}Ca_{0.15}Ti_2O_{7-\delta}$ calculated using SRIM-2013.[220] These calculations were performed using 5000 Au^- ions with the ion beam energy being 2 MeV.

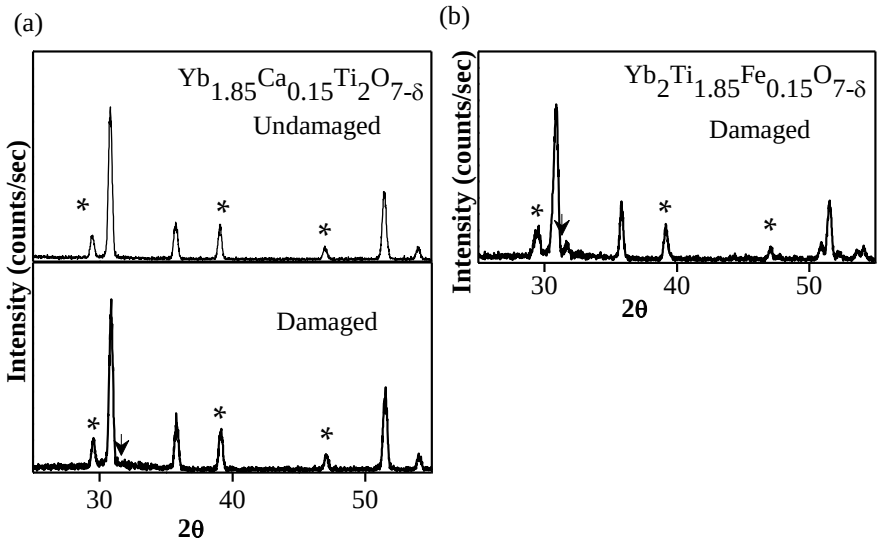

Figure A2.3 Micro powder XRD patterns from the $Yb_2Ti_{1.85}Fe_{0.15}O_{7-\delta}$ and $Yb_{1.85}Ca_{0.15}Ti_2O_{7-\delta}$ materials implanted to a dose of 5×10^{14} ions/cm^2 are shown. The diffraction pattern from undamaged $Yb_{1.85}Ca_{0.15}Ti_2O_{7-\delta}$ is also presented while the diffraction pattern from undamaged $Yb_2Ti_{1.85}Fe_{0.15}O_{7-\delta}$ was presented in Section 2.3.1.

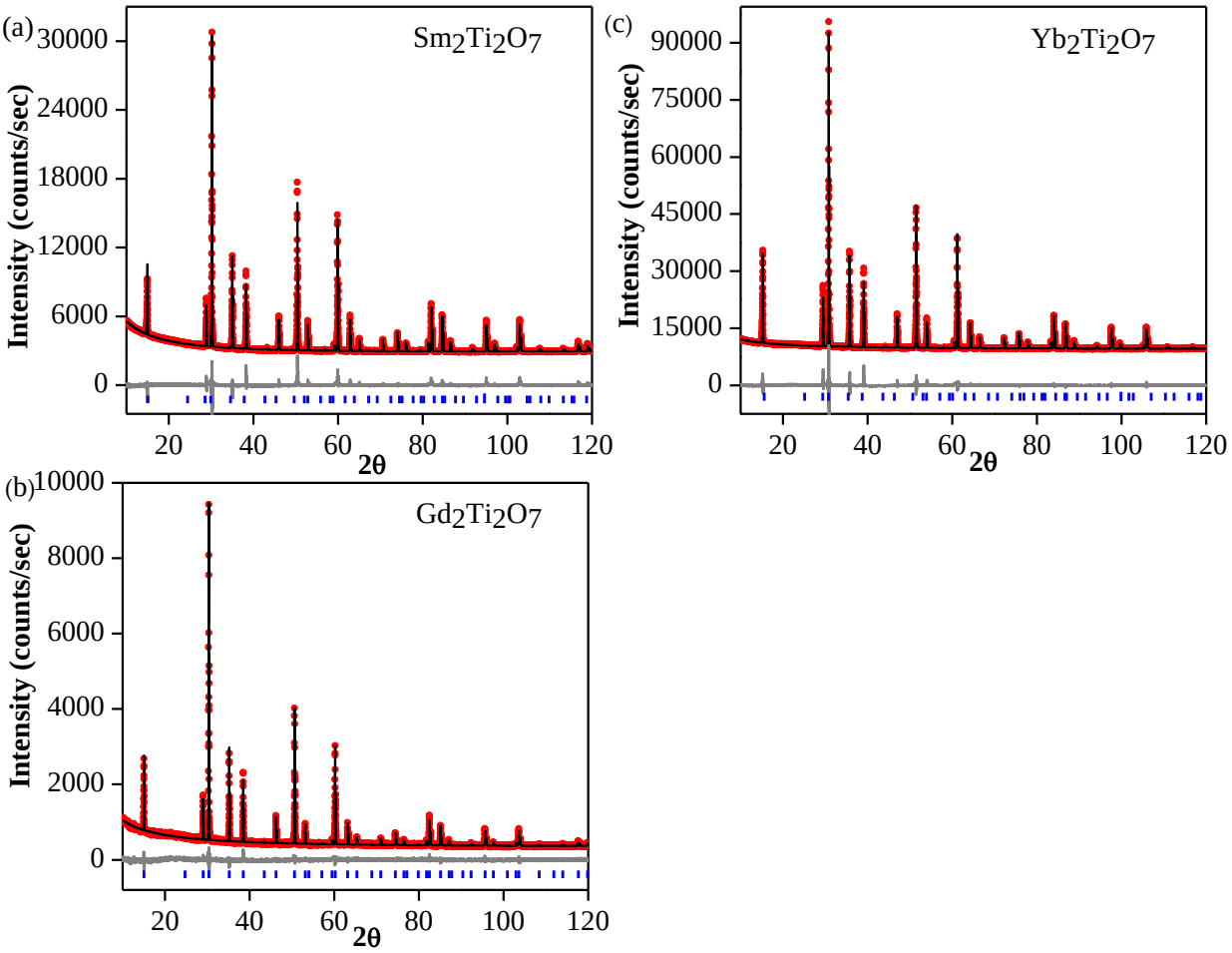

Figure A2.4 Rietvield refinement results of the powder XRD patterns collected from some of the undamaged $RE_2Ti_2O_7$ materials: (a) $Sm_2Ti_2O_7$, (b) $Gd_2Ti_2O_7$, and (c) $Yb_2Ti_2O_7$. The data points are represented by red triangles. The refinement (black line) and the difference plot (gray line) between the observed and calculated patterns are also shown. Peak positions from the pyrochlore-type crystal structure are indicated by blue vertical marks.

Appendix 3

Supporting information for Chapter 5

Table A3.1 Rietveld refinement results of powder XRD patterns collected from the undamaged $Gd_2Ti_{2-x}Sn_xO_7$ and $Gd_2Zr_2O_7$ materials*

	$Gd_2Ti_2O_7$	Gd_2TiSnO_7	$Gd_2Sn_2O_7$	$Gd_2Zr_2O_7$	
Crystal structure	Pyrochlore[a] ($Fd\bar{3}m$)	Pyrochlore ($Fd\bar{3}m$)	Pyrochlore ($Fd\bar{3}m$)	Pyrochlore ($Fd\bar{3}m$)-66.1%	Defect-Fluorite[c] ($Fm\bar{3}m$)-33.9%
a (Å)	10.1851(4)	10.3235(1)	10.46066(3)	10.5368(1)	5.2444(6)
x_{48f}	0.4252(4)	0.421(5)	0.4143(5)	0.407(5) 0.341(7)[b]	
B overall (Å^2)	0.85(5)	0.62(2)	0.21(5)	0.38(9)	
R_p (%)	5.38	5.38	5.17	4.12	
R_{wp} (%)	7.00	6.62	7.41	5.36	
GOF	1.41	1.24	1.55	0.98	

*a = Lattice constant; x_{48f} = x-coordinate of the oxygen anions occupying the 48f site, B overall = Overall isotropic thermal factor. R_p = Refinement profile, R_{wp} = Weighted refinement profile, GOF = Goodness of fits (R_{wp}/R_{exp}); R_{wp} and R_{exp} are the weighted refinement and expected profiles, respectively.

[a]Atomic positions for the pyrochlore-type structure: Gd:16c (0 0 0), Ti/Sn/Zr:16d (½ ½ ½), O:8a (⅛ ⅛ ⅛), and O':48f (x ⅛ ⅛).

[b]x-coordinate of the oxygen anions occupying the 48f site when the atomic positions for the $Gd_2Zr_2O_7$ pyrochlore-type structure are Gd:16d (½ ½ ½), Zr:16c (0 0 0), O:8a (⅛ ⅛ ⅛), and O':48f (x ⅛ ⅛).

[c]Atomic positions for the defect-fluorite-type structure: Gd: 4a (0 0 0), Zr: 4a (0 0 0), and O: 8c (¼ ¼ ¼).

Table A3.2 Calculated electronic and nuclear stopping parameters at 2 MeV for the $Gd_2Ti_{2-x}Sn_xO_7$ and $Gd_2Zr_2O_7$ materials

Sample	Electronic stopping parameter (dE/dx) eV/nm	Nuclear stopping parameter (dE/dx) eV/nm
$Gd_2Ti_2O_7$	2684	4786
Gd_2TiSnO_7	2669	4961
$Gd_2Sn_2O_7$	2667	5145
$Gd_2Zr_2O_7$	2535	4823

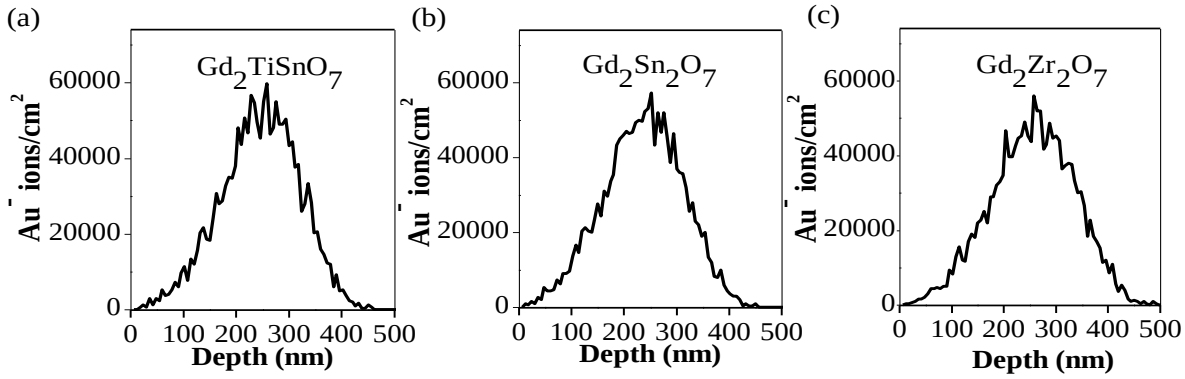

Figure A3.1 Ion beam implantation depth profiles from (a) Gd_2TiSnO_7, (b) $Gd_2Sn_2O_7$, and (c) $Gd_2Zr_2O_7$ calculated using SRIM-2013.[220] These calculations were performed using 5000 Au^- ions with the ion beam energy being 2 MeV MeV and by assuming the target (Gd,Ti,Sn,O) displacement energies being 25 eV (Gd,Ti,Sn) and 28 eV (O).[220]

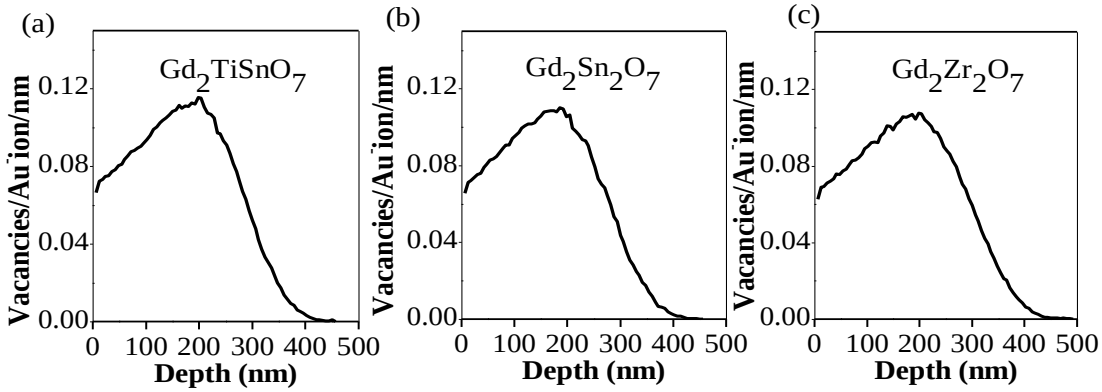

Figure A3.2 Vacancies per ion depth profiles from (a) Gd_2TiSnO_7, (b) $Gd_2Sn_2O_7$, and (c) $Gd_2Zr_2O_7$ calculated using SRIM-2013.[220] These calculations were performed using 5000 Au^- ions with the ion beam energy being 2 MeV MeV and by assuming the target (Gd,Ti,Sn,O) displacement energies being 25 eV (Gd,Ti,Sn) and 28 eV (O).[220]

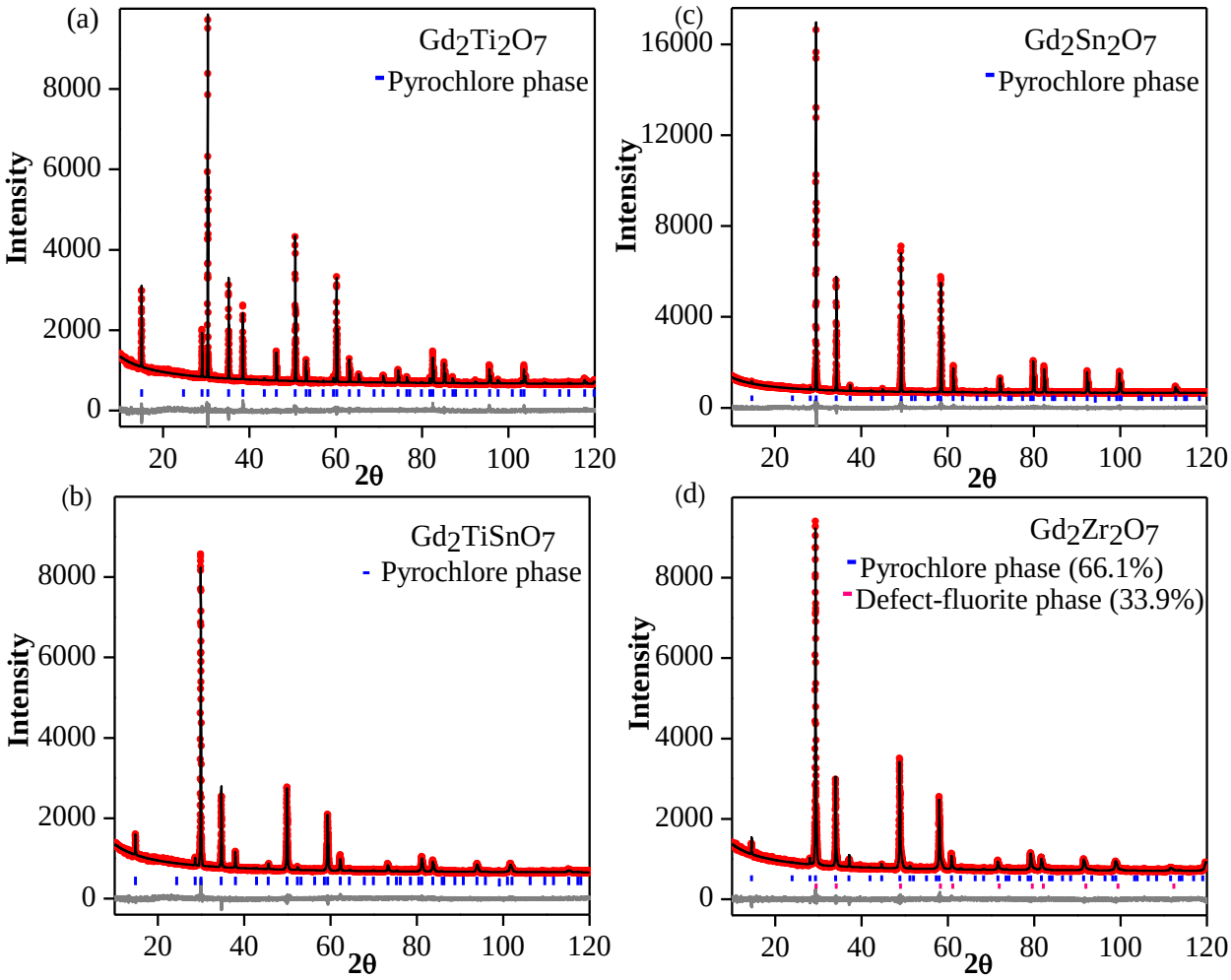

Figure A3.3 Rietveld refinement results of the powder XRD patterns collected from the undamaged materials: (a) $Gd_2Ti_2O_7$, (b) Gd_2TiSnO_7, (c) $Gd_2Sn_2O_7$, and (d) $Gd_2Zr_2O_7$. The data points are represented by red triangles. The refinement (black line) and the difference plot (gray line) between the observed and calculated patterns are also shown. Peak positions from the pyrochlore (blue) and defect-fluorite (pink) crystal structures are indicated by vertical marks.

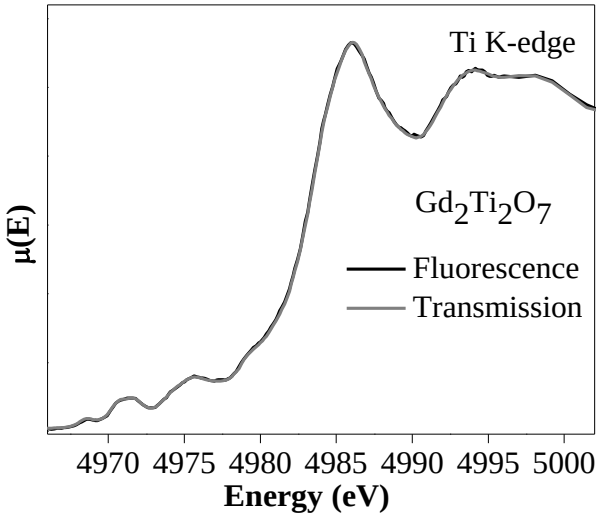

Figure A3.4 Ti K-edge XANES spectra from the undamaged $Gd_2Ti_2O_7$ material collected in fluorescence and transmission modes. No significant changes were observed between the spectra.

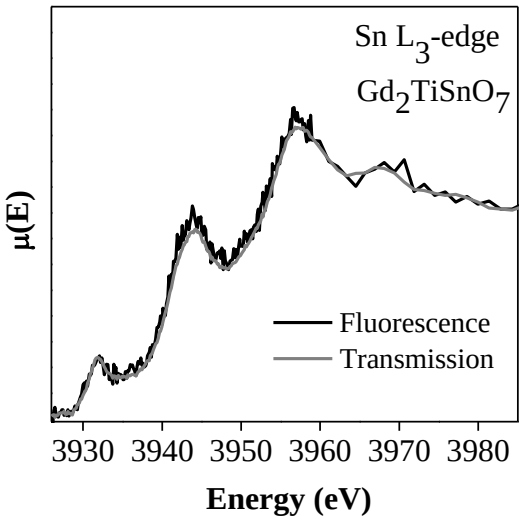

Figure A3.5 Sn L_3-edge XANES spectra from the undamaged Gd_2TiSnO_7 material collected in fluorescence and transmission modes. No significant changes were observed between the spectra.

Appendix 4

Supporting information for Chapter 6

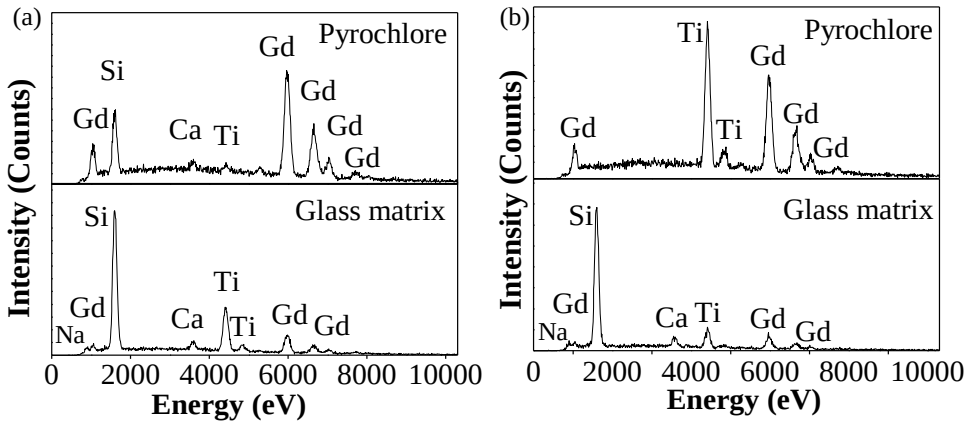

Figure A4.1 EDX spectra from (a) BG-$Gd_2Ti_2O_7$-1100^oC and (b) BG-$Gd_2Ti_2O_7$-750^oC containing 40 wt% loading of $Gd_2Ti_2O_7$ are shown.

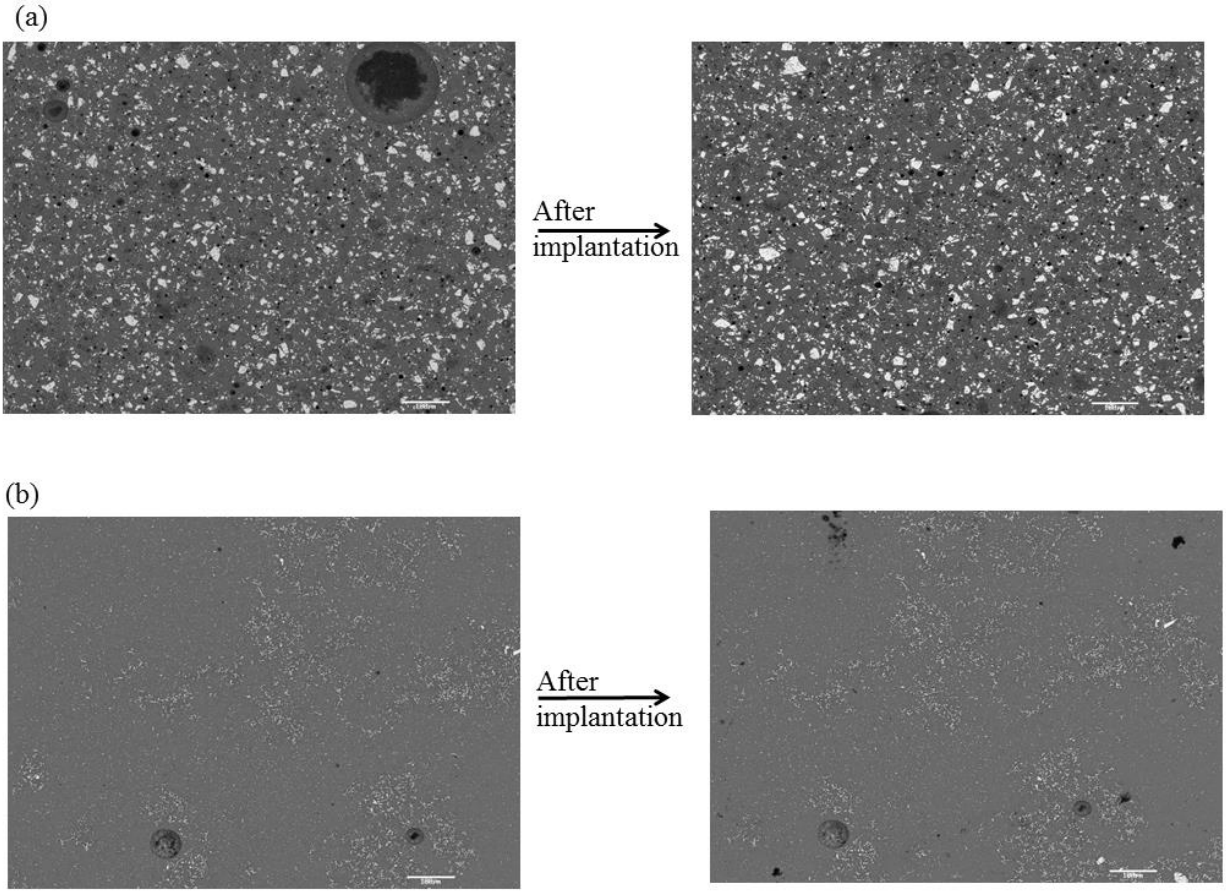

Figure A4.2 (a,b) Backscattered images from the borosilicate glass composite materials (40 wt% loading of $Gd_2Ti_2O_7$) annealed at 750^{o}C and at 1100^{o}C, respectively, before and after implantation. There are no changes in morphology and grain size of pyrochlore-type (brighter area) crystallites in the composite materials upon implantation. The images were collected at 100X magnification and a scale bar of 100 μm.